The Initiation of Rain-Triggered Lahars

Robert John Jones

Submitted in accordance with the requirements for the

degree of Doctor of Philosophy

University of Leeds

School of Earth and Environment

October 2016

The candidate confirms that the work submitted is his own, except where work which has formed part of jointly authored publications has been included. The contribution of the candidate and the other authors to this work has been explicitly indicated below. The candidate confirms that appropriate credit has been given within the thesis where reference has been made to the work of others.

Chapter 3 includes work from the following jointly authored publication in *Geomorphology*:

Jones, R., Thomas, R.E., Peakall, J., Manville, V. 2016. Rainfall-Runoff Properties of Tephra: Simulated Effects of Grain-size and Antecedent Rainfall. Geomorphology, 282, 39-51. 10.1016/j.geomorph.2016.12.023

The development of the research methods, collection of required field samples, undertaking of the experiments, interpretation of results and manuscript composition (text and figures) within the above manuscript are attributable to the candidate. Co-Authors assisted in research method development (All co-authors), experimental construction (R.E. Thomas), interpretation of results (All co-authors) and the editing of the manuscript (All co-authors).

Chapter 4 includes work from the following jointly authored publication in *Bulletin of Volcanology*:

Jones, R., Manville, V., Andrade, D., 2015. Probabilistic analysis of rain-triggered lahar initiation at Tungurahua volcano. Bulletin of Volcanology, 77(8). 10.1007/s00445-00015-00946-00447.

The development of the research methods, execution of the data analysis, interpretation of results and manuscript composition (text and figures) within the above publication are attributable to the candidate. Co-Authors assisted in collecting and sharing the raw datasets (D. Andrade) and in the editing and refining of the manuscript and the interpretation of results (V. Manville).

Chapter 5 includes work from a jointly authored manuscript which has previously been submitted to *Geology:*

Jones, R., Manville, V., Peakall, J., Froude, M., Odbert, H. Real-time prediction of rain-triggered lahars: incorporating seasonality and catchment recovery.

The development of the research methods, data analysis, interpretation of results and manuscript composition (text and figures) within the above manuscript are attributable to the candidate. Co-Authors collected and provided the lahar and rainfall data (M. Froude and H. Odbert) and assisted with the formation and refinement of the manuscript (V. Manville, J. Peakall & M. Froude).

Acknowledgements

Academic Assistance and Advice During PhD

Firstly, I would like to thank my supervisors at the University of Leeds Dr. Vern Manville and Professor Jeff Peakall for their advice and help over the past four years. I have been tremendously fortunate to have been affiliated with the STREVA project during the course of this PhD, and this has provided me the opportunity to work and interact with many fantastic people across a multitude of disciplines. I am particularly thankful to Jenni Barclay, Jeremy Phillips and Anna Hicks for their help and advice at various workshops, meetings and conferences. The STREVA forensic workshop in Ecuador was a particular highlight, and one of the many STREVA events which continually motivated me and reminded me why I was undertaking this research.

I would also like to thank IGEPN and specifically Patty Mothes, Daniel Andrade, Marco Almeida and Stefy Almeida for their invaluable assistance during initial fieldwork and subsequent research in Ecuador. Their generosity in sharing both their academic insight and practical assistance was absolutely invaluable and for that I am tremendously grateful. Similarly, I am thankful to Rebecca Astbury for her fieldwork assistance at Calbuco and to Angelo Castruccio and Jorge Clavero for sharing their local knowledge of the area. Alvaro Amigo and everyone else at SERNAGEOMIN made us feel hugely welcome and went the extra mile to ensure the fieldwork was both successful and enjoyable.

Many thanks to Rob Thomas and Gareth Keevil for their long-running and patient support in designing, constructing and undertaking experimental work at the Sorby lab at the University of Leeds. Also to Mel Froude for sharing some of

her extensive knowledge of Belham Valley lahars and for allowing me to use her associated lahar database. Similarly, I would like to acknowledge the Montserrat Volcano Observatory (MVO) for allowing me to use rainfall and lahar data within my research. Finally, I would like to acknowledge the Natural Environment Research Council (NERC) for providing the funding through the STREVA project which allowed me to undertake this PhD.

Family & Friends

Firstly, I would like to thank Tor, without your unwavering support I would never have been able to get anywhere near this point, you are amazing.

Secondly, thanks to Mum and Dad for always being there and for helping out no matter how big or small the problem. To Richie for providing the inspiration for everything and for being the best brother and friend anyone could ask for. And to Monty for helping me to escape the PhD-bubble and for being an absolute dude.

Thirdly, thanks to friends in Leeds. Thanks to Mike, the lunches in Pickards and one-too-many-pint Tuesday nights were more valuable than you know. Thanks to Hollie, Sarah and Luke for being awesome office-mates, and for reminding me that I was not alone.

Thanks to everyone else who has helped fill the last few years with amazing experiences. Thanks to Mark, Karen, Zak, Holly, Maya, Lola, Sam, Pete and Erin for so many fun weekends and to Matt for all the vaguely irresponsible Cricket, Rugby and American Football excursions.

And finally to Craig, always remembered, Go Ducks!

Abstract

Rain-triggered lahars are a significant secondary hazard at volcanoes where unconsolidated pyroclastic material is exposed to intense rainfall, frequently occurring for years to decades after the initial eruptive activity affects proximal areas or primary hazard zones. Mechanisms of rain-triggered lahar initiation are often inferred from downstream flow observations, whilst rain-triggered lahar risk mitigation typically relies on ground-based flow detection. As a result, increasing knowledge of the physical processes involved in rain-triggered lahar initiation and enhancing the use of underutilised instrumental networks are key areas in the development of lahar risk mitigation techniques. This thesis examined rain-triggered lahar initiation in three primary ways: (i) The field-based examination of factors influencing the nature of the rain-triggered lahar hazard following the April 2015 eruption of Calbuco; (ii) The development of quantitative rainfall simulation experiments examining the effects of grain size distribution and antecedent rainfall; and (iii) The analysis of rainfall data and instrumental lahar records to devise new methods of rain-triggered lahar prediction and forecasting.

Parameters identified at Calbuco as dictating the spatial variability and magnitude of the post-eruption rain-triggered lahar hazard included the volume and grain-size of emplaced pyroclastic material, vegetation coverage, pre-eruption ice and snow cover, topography and rainfall characteristics. Subsequent laboratory-based rainfall simulation experiments featuring man-made tephra beds examined the quantitative effects of factors including the grain-size of surface tephra and antecedent rainfall upon rain-triggered lahar initiation processes. Increased surface runoff was demonstrated during periods

of heightened antecedent rainfall and as a result of reduced surface grain size. Reduced surface grain size also induced the formation of surface crusts, further enhancing runoff.

Real-time telemetered rainfall data have been utilised as an effective basis for the creation and development of lahar forecasting models, with peak rainfall intensity acting as the optimal rainfall parameter for predicting lahar occurrence. The demonstrated increased warning times provided by such real-time predictive models illustrates their value both alongside existing lahar detection networks and as an alternative where such resources are unavailable. The incorporation of antecedent rainfall data has been shown to increase model performance, as has the integration of catchment recovery proxies at locations in periods of eruptive quiescence. The probabilistic models developed within this thesis also facilitate the continuous temporal calibration and adjustment of predictions as the databases used to generate lahar forecasts expand and evolve. The quantitative examination of factors driving rain-triggered lahar initiation processes within this thesis and the development of new techniques of lahar forecasting and prediction provide a platform for enhanced lahar risk mitigation. Further research should aim to integrate quantitative lahar magnitude thresholds into the developed lahar forecasting models, facilitating probabilistic inundation modelling and enhanced inter-location lahar comparisons.

Contents

List of Figures

List of Tables

Chapter 1: Introduction

1.1. Lahars

Lahar is a term of Javanese origin which literally translates as "mudstream" and describes the same process as the Philippine phrase *baha nin dugi* which translates as "floods of mud" (Rodolfo, 1989; Rodolfo et al., 1989; Rodolfo and Arguden, 1991; Lavigne et al., 2000b; Lavigne and Suwa, 2004; Barclay et al., 2007; Lavigne et al., 2007; Dumaisnil et al., 2010). The term lahar was first utilised in English literature in 1922 by Escher (Neall, 1976), subsequently by Scrivenor in 1929 (Rodolfo, 1989; Rodolfo and Arguden, 1991; Lavigne et al., 2000b), and was defined in 1949 by Van Bemmelen as "a mudflow containing debris and angular blocks of chiefly volcanic origin" (Van Bemmelen, 1949; Rodolfo and Arguden, 1991; Lavigne et al., 2000b). The definition of such flows continued to evolve with time, encompassing such definitions as "a flowing mixture of rock debris and water", "flows involving a mixture of volcanic debris and water occurring on and around volcanoes" and "mass flows of varying proportions of water and solids originating at a volcano" (Neall, 1976; Fagents and Baloga, 2006; Barclay et al., 2007). However, Smith & Fritz (1989) defined a lahar as a flow event which involves "a rapidly flowing mixture of rock debris and water (other than normal streamflow) from a volcano" and this definition has been widely utilised in the subsequent published literature (e.g. Rodolfo and Arguden, 1991; Van Westen and Daag, 2005; Capra et al., 2010; de Bélizal et al., 2013). Lahars have caused 17% of historical volcano-related fatalities (Fig. 1.1) (Auker et al., 2013), with approximately 30,000 lahar related fatalities during the 20th Century (Witham, 2005); emphasising their nature as a persistent, lethal and globally significant volcanic hazard.

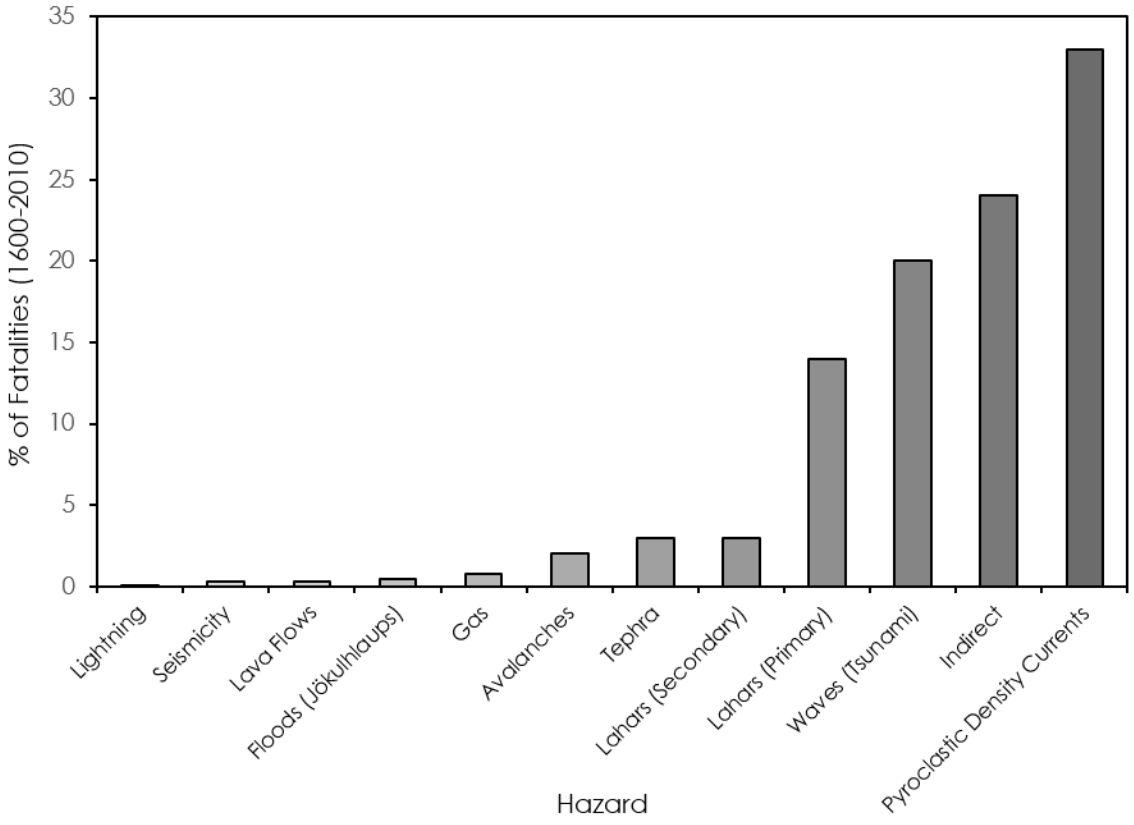

Figure 1.1: Distribution of volcanic fatalities by causal hazard (1600-2010). Data from Auker et al. (2013).

As a product of its historical use by the inhabitants of Indonesia, largely without a specific need to make precise rheological distinctions, *Lahar* is a wide ranging term which can sufficiently describe the entirety of an individual, complex event with multi-phase rheology (Rodolfo, 1989; Rodolfo et al., 1989; Rodolfo and Arguden, 1991; Major et al., 1996; Doyle et al., 2009; Dumaisnil et al., 2010; Doyle et al., 2011). In modern literature lahars are typically segregated into several categories based on flow characteristics. Debris flows are frequently designated as those flows containing above 60% sediment by volume or 80% sediment by weight; hyperconcentrated flows as those with 20-60% sediment by volume; streamflows as those with less than 20% sediment by volume and mudflows as a distinct class of cohesive, fine rich flows with 20-40% sediment by volume (Rodolfo, 1989; Rodolfo and Arguden, 1991; Major et al., 1996; Cronin et

al., 1999; Lavigne et al., 2000b; Lavigne and Thouret, 2003; Lavigne and Suwa, 2004; Van Westen and Daag, 2005; Fagents and Baloga, 2006; Barclay et al., 2007; Lavigne et al., 2007; Doyle et al., 2009; Doyle et al., 2010; Dumaisnil et al., 2010).

Debris flows are identified as generally appearing to flow like wet concrete and are capable of holding gravel in suspension at low velocities and whilst stationary (Pierson, 2005; Fagents and Baloga, 2006). These flows possess a significantly higher yield stress than hyperconcentrated flows and their flow mechanism has been described as "plug flow", "viscous fluid flow" and "modified granular flow" (Cronin et al., 1999; Barclay et al., 2007; Doyle et al., 2011). The viscosity of such flows decreases as velocity increases, with debris flows capable of achieving velocities twice that of water flows of comparable depth and slope (Pierson, 1995; Lavigne and Thouret, 2003). Velocities of debris flows typically peak at 15-30 km hr^{-1}, at which stage they are capable of carrying extremely large boulders in suspension (Neall, 1976; Pierson, 2005). Debris flow deposition occurs en masse or via incremental accretion, with grain-by-grain settling prevented by the increased particle-particle interactions as a result of the elevated sediment concentration (Neall, 1976; Lavigne and Thouret, 2003; Barclay et al., 2007; Doyle et al., 2011). Hyperconcentrated flows are often identified as appearing to flow "like a liquid", have a small yet measurable yield strength and can raise the level of the underlying channel bed by several m hr^{-1} through grain-by-grain settling at flow velocities of up to approximately 20 km hr^{-1} (Pierson, 1985; Rodolfo et al., 1989; Cronin et al., 1999; Fagents and Baloga, 2006). Such flows are thought to typically be vertically stratified, comprising a boulder bearing bedload region and an upper dilute, fine grained suspension region (Cronin et al., 1999; Barclay et al., 2007; Doyle et al., 2011). These

classifications are arbitrary and do not correspond to specific lahar behaviour thresholds, with flow rheology being controlled by the continuum of liquid-solid interactions (Barclay et al., 2007; Lavigne et al., 2007).

The described liquid-solid interactions of the various lahar flow types are typically highly variable on both a spatial and temporal scale due to erosional and depositional processes including bulking (the increase in flow volume by erosion and entrainment of material), debulking (volume loss by selective deposition), dilution (the increase in flow volume by interaction with a water source) and infiltration (the loss of liquid into permeable substrates) (Fagents and Baloga, 2006; Doyle et al., 2009; Doyle et al., 2011). The efficiency of bulking depends upon on the erodibility of the channel, the shear stress applied by the flow to the channel surface, the pore pressures within underlying substrates and the total volume of sediment available for erosion (Pierson, 1995; Lavigne and Thouret, 2003; Doyle et al., 2011). Turbulence in lahars typically decreases as sediment concentration increases due to the dampening effects of the suspended sediment (Rodolfo et al., 1989; Rodolfo and Arguden, 1991), and increased sediment concentration can result in a change from Newtonian to quasi-plastic or Bingham plastic flow rheologies (Neall, 1976). The subsequent laminar flow-type associated with high sediment concentration lahars decreases shear stress at the flow margins and thus reduces erosive capacity (Jakob and Hungr, 2005). As such, a lower sediment concentration flow of comparable velocity gradient has a heightened erosive capacity compared with a higher sediment concentration flow; illustrating a factor which prevents the perpetual increase in erosive capacity of lahars at stable gradients (Caruso and Pareschi, 1993; Doyle et al., 2011). Debulking is a product of a reduction in lahar energy and basal shear stress driven by factors including flow velocity, depth, sediment

concentration, density and channel topography (Fagents and Baloga, 2006); whilst lahar interaction with streamflow acts to dilute the flow and reduce sediment concentration, as identified at Ruapehu in 1995 (Cronin et al., 1999). The degree of infiltration into underlying permeable substrates during the flow depends on the permeability and the degree of saturation of the channel bed (Doyle et al., 2011), as well as the permeability and compressibility of the flow itself (Major and Iverson, 1999).

The structure of a lahar and the location of the maximum sediment concentration within the flow is highly variable. In some examples lahars are identified as having a streamflow front (Cronin et al., 1999; Manville et al., 2000a; Jakob and Hungr, 2005; Doyle et al., 2011; Lube et al., 2012), whilst in other locations boulder dam structures are located at the front of the flow (Lavigne and Suwa, 2004; Okano et al., 2012). Lahars also frequently travel as a surge of pulses (Lavigne and Thouret, 2003; Lavigne and Suwa, 2004); primarily attributed to fluctuations in rainfall, breaks in slope or the effects of temporary dams. The increased velocity potential of high sediment concentration parts of the flow indicates that under uniform conditions such regions would migrate to the front of the flow (Doyle et al., 2011). The structure of a lahar is thus a function of the initiation mechanism (discussed below), degree of interaction with streamflow, channel profile, bulking efficiency and the grain size distribution of entrained material.

1.1.1. Lahar Initiation Mechanisms

Lahar initiation requires three primary factors; a supply of volcaniclastic material, a moisture source and adequate relief. These three

factors can combine in a variety of environments, resulting in numerous potential lahar initiation mechanisms. Primary, syn-eruptive lahars are initiated when eruptive material rapidly comes into contact with a moisture source (Neall, 1976). The ejection of crater lake material is one such initiation method; examples of this process occurred during the 1975, 1995 and 2007 eruption sequences at Mt Ruapehu, New Zealand as expelled Crater Lake water, sediment and fresh ejecta interacted with the seasonal snow pack, ice and underlying sediment to form lahars (Neall, 1976; Nairn et al., 1979; Cronin et al., 1997; Cronin et al., 1999; Fagents and Baloga, 2006; Graettinger et al., 2009; Manville et al., 2009a; Massey et al., 2009; Kilgour et al., 2010). Lahars triggered by crater lake ejection are also common at Mt. Kelud, Indonesia, with an eruption in 1919 expelling 38×10^6 m^3 of water, triggering lahars that covered 131 km^2, inundated 104 villages, and killed 5100 people (Thouret et al., 1998). Another initiation mechanism of syn-eruptive lahars involves the melting of ice and snow due to pyroclastic density current (PDC) and lava flow activity. Significant examples of this lahar initiation mechanism have occurred at Cotopaxi Volcano in Ecuador where major lahars have been triggered in 1534, 1742-44, 1766, 1768 and 1877 (Aguilera et al., 2004; Kumagai et al., 2009), and at Nevado del Ruiz Volcano in Columbia where 25,000 fatalities occurred as a result of such flows in 1985 (Lowe et al., 1986; Pierson et al., 1990; Thouret, 1990; Pierson, 1995). Where volumes of snow and ice are particularly large, snow-slurry lahars containing entrained snow, fragments of glacier and river ice form, such as those produced during the 2009 eruption of Redoubt Volcano, Alaska (Waythomas et al., 2013; Waythomas, 2014). Subglacial melting of ice and the release of sub-glacial reservoirs as a result of eruptive activity produces a type of lahar/glacial outburst flood known in Iceland as a jökulhlaup (Jónsson et al., 1998; Snorrason et al., 2002). Primary lahars have

the potential to be hot as a product of the temperature of the eruptive products that trigger them. (e.g. Arguden and Rodolfo, 1990; Pierson et al., 1996).

The transformation of debris avalanches as a result of dewatering or interaction with streamflow is another mechanism of syn-eruptive lahar occurrence (e.g. Vallance and Scott, 1997; Capra et al., 2002). Such lahars occurred during the 1980 eruption of Mt. St. Helens (Pierson, 1985) and this process has also been inferred from the deposits of the Osceola Mudflow, Mt. Rainier which occurred approximately 5,600 years ago during a period of phreatomagmatic activity (Vallance and Scott, 1997). Lahars created as a product of debris avalanche transformation are often amongst the largest and most mobile lahars due to the large magnitude of the initial debris avalanches (Arguden and Rodolfo, 1990; Rodolfo and Arguden, 1991; Vallance and Scott, 1997; Capra et al., 2002; Fagents and Baloga, 2006).

In addition to primary, syn-eruptive lahars there are several initiation mechanisms of secondary, post-eruptive lahars; with a persistent lahar hazard often generated for over a decade at a single location after a major eruption (Major et al., 2000; Gran and Montgomery, 2005; Van Westen and Daag, 2005; Barclay et al., 2007). The breaching or displacement of lakes is one such initiation method and lahars of this nature can be highly destructive due to the potentially large volumes of released water (Neall, 1976). Such lakes can be located inside or outside the crater and be permanent or transient in nature (Manville et al., 2009a). Examples of lahar formation as a result of crater lake breaching include the 1953 and 2007 events at Mt Ruapehu in New Zealand, the former event resulting in the Tangiwai Rail Disaster (Neall, 1976; Fagents and Baloga, 2006; Graettinger et al., 2009; Massey et al., 2009; Carrivick et al., 2010; Lube et al.,

2012); and the 1541 burial of Ciudad Vieja, Guatemala as a result of a crater lake outburst lahar from Volcán de Agua (Neall, 1976). Transient lakes are a common feature of volcanic landscapes and are often formed as a result of drainage obstruction due to PDC, lahar and tephra deposits (e.g. Umbal and Rodolfo, 1996). Lahars can form as the lake level overtops the drainage obstruction or as flows such as landslides or PDCs enter the lake, displacing the lake water (Umbal and Rodolfo, 1996; Manville and Cronin, 2007). Examples of such lahars occurred at Mt Pinatubo after the 1991 eruption when the formation of Lake Mapanuepe initiated a cycle of lake level increase and lake-breach lahars (Tungol and Regalado, 1996; Umbal and Rodolfo, 1996; Lavigne and Thouret, 2003).

The lahar initiation mechanism of primary focus within the context of this thesis is rainfall triggering. Identified as *Murgangs* by Escher in 1922 (Neall, 1976), these lahars occur when rainfall interacts with pyroclastic material and are largely post-eruptive. The initiation of rain-triggered lahars typically occurs via either shallow landsliding of saturated tephra layers above basal décollement surfaces (Rodolfo and Arguden, 1991; Hodgson and Manville, 1999; Manville et al., 2000b; Scott et al., 2005; Mead et al., 2016), runoff induced rill erosion (Nammah et al., 1986; Leavesley et al., 1989; Yamakoshi and Suwa, 2000; Lavigne and Thouret, 2003; Major and Yamakoshi, 2005; Barclay et al., 2007) or particle detachment as a result of rainsplash erosion followed by subsequent transport by overland flow (Segerstrom, 1950; Waldron, 1967). As a result, factors which impact the frequency and magnitude of rain-triggered lahars include the grain size distribution (Pierson et al., 2013), thickness (Janda et al., 1996; Scott et al., 1996a; Manville et al., 2000b) and volatile content (Waldron, 1967) of pyroclastic material; vegetation coverage (Yamakoshi and Suwa, 2000; Barclay et al., 2007; Ogawa et al., 2007; Alexander et al., 2010) and type (Capra et al., 2010); rainfall

intensity and duration (Rodolfo and Arguden, 1991; Lavigne et al., 2000b; Van Westen and Daag, 2005; Hikida et al., 2007; Okano et al., 2012; Mead et al., 2016); slope angle (Pierson et al., 2013) and initial moisture content (Lavigne et al., 2000b; Barclay et al., 2007; Okano et al., 2012; Jones et al., 2015); all of which are temporally and spatially variable. With approximately 46% of the world's volcanoes situated in the high-rainfall global tropical belt, rain-triggered lahar hazard is widespread; with Merapi (e.g. de Bélizal et al., 2013), Mayon (e.g. Paguican et al., 2009), Colima (e.g. Capra et al., 2010), Pinatubo (e.g. Van Westen and Daag, 2005), Irazu (e.g. Waldron, 1967), Tungurahua (e.g. Jones et al., 2015), Santiaguito (e.g. Harris et al., 2006), Sakurajima (e.g. Hikida et al., 2007), Semeru (e.g. Thouret et al., 2014), Unzen (e.g. Yamakoshi and Suwa, 2000) and Mt St. Helens (e.g. Major and Yamakoshi, 2005) amongst the most widely studied sites of recent rain-triggered lahar activity.

1.2. Rain Triggered Lahars

1.2.1. Emplacement of Pyroclastic Material

The nature of the emplacement of pyroclastic material within drainage basins following a volcanic eruption dictates the magnitude and distribution of the post-eruption hydrologic response. The potential emplacement mechanisms, namely tephra fall, pyroclastic density currents (PDCs), lava flows, debris avalanches and/or primary lahars, in combination with the magnitude of the eruption and proximity to the volcano determine the degree of catchment disturbance (Pierson and Major, 2014). Figure 1.2 displays the degree of such landscape disturbance relative to pre-eruption conditions (Fig. 1.2A) after the February 14th 2014 eruption of Kelud, illustrating the emplacement of valley-fill

PDC deposits, widespread vegetation damage and the mantling of topography with tephra and co-PDC fall deposits (Fig. 1.2B).

Tephra fall mantles topography downwind of an eruption, often in an elliptical pattern when syn-eruptive wind direction is consistent, with exponential decay of deposit thickness and median grainsize with increased distance downwind evident in simple eruptions (Pyle, 1989). In addition to the distance from the vent, the nature of the resultant tephra deposits are a product of the magnitude and characteristics of the eruption, with tephra fall typically the most widespread mechanism of pyroclastic deposition (Ayris and Delmelle, 2012). As a result of their mantling of topography, tephra deposits impact both hillslopes and valley floors within the affected region (e.g. Pierson et al., 2013). Tephra fall damages or destroys vegetation via burial, abrasion, interference with leaf surface metabolic activity, overloading of tree canopies and chemical damage; factors which are dependent on the grain-size distribution, thickness and volatile content of the tephra deposits, as well as the type of the affected vegetation (Ayris and Delmelle, 2012; Swanson et al., 2013; Pierson and Major, 2014). Tephra deposition and the burial of vegetation act to decrease surface roughness (Barclay et al., 2007) and infiltration rates (e.g. Major and Yamakoshi, 2005; Pierson et al., 2013) within catchments relative to pre-eruption conditions, whilst also providing a source of unconsolidated, easily erodible material (Janda et al., 1996; Gran and Montgomery, 2005).

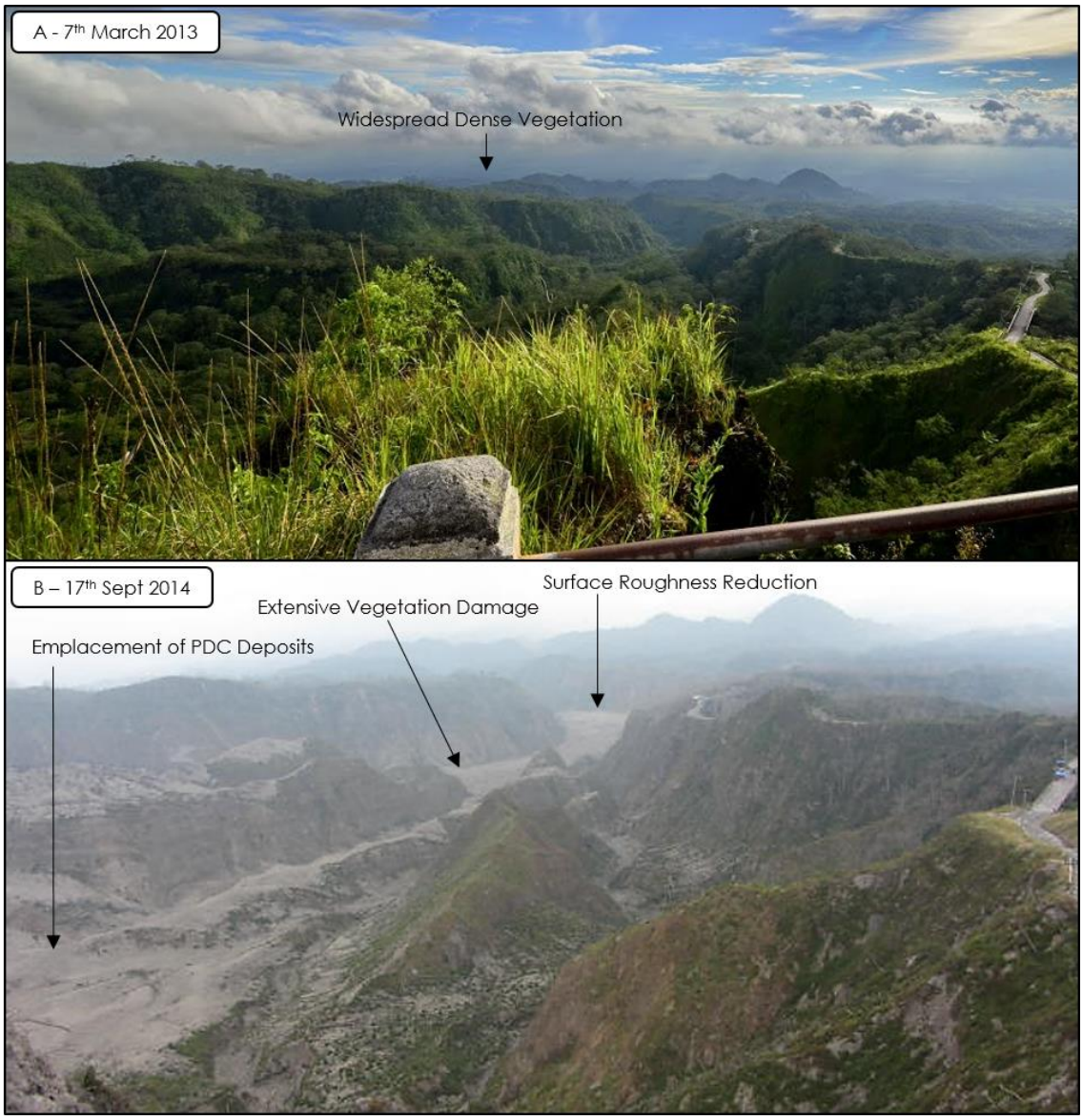

Figure 1.2: Landscape disturbance caused by the February 14th 2014 Eruption of Kelud, Indonesia. A: Pre-eruption image taken in March 2013 facing downstream in the Bladak river to the west of the volcano displaying dense, tropical vegetation. B: Post-eruption image taken in September 2014 of the same area displaying spatially variable vegetation damage, valley-fill PDC deposits, topography mantling tephra and co-PDC fall deposits.

Pyroclastic Density Currents (PDCs) are formed by eruption column collapse (e.g. Shea et al., 2011), lateral blasts (e.g. Druitt, 1992) or lava dome collapse (e.g. Sparks et al., 2002) and these high velocity (>10 ms^{-1}) flows have the potential to emplace high temperature (100°C-700°C) pyroclastic deposits across inundated regions (Pierson and Major, 2014) with typical runout distances

of up to 20 km and extreme runout distances >100 km (Sparks, 1976; Cole et al., 2002; Shea et al., 2011; Hall et al., 2013; Major et al., 2013). In common with tephra fall deposits, PDC deposits cause widespread vegetation damage by abrasion and burial, however PDCs also have the potential to strip and burn vegetation (e.g. Edmonds et al., 2006; Major and Mark, 2006) and can be highly erosive in regions proximal to their source (Scott et al., 1996b). PDCs are generally valley confined (e.g. Fig. 1.3), except in extreme examples (e.g. Scott et al., 1996b), and can fill valleys with flat-topped deposits and substantially alter drainage networks (Scott et al., 1996b; Major and Mark, 2006). Such thick valley-fill deposits can provide a long-term sediment supply, generating a multi-decadal rain-triggered lahar hazard after large eruptions (Major et al., 2000; Major and Yamakoshi, 2005; Van Westen and Daag, 2005). PDC deposits can provide a source of easily erodible material, however large, high temperature deposits may feature welded, lithified zones of less-erodible material (Sparks, 1976). The grain-size distribution of PDC deposits depends on the nature of the flow, ranging from coarse, massive block-and-ash flow deposits to finer-grained ash- or pumice-rich surge deposits (Cole et al., 2002; Stinton et al., 2014). Fine-grained surface layers are common as a product of ashfall from buoyant lifting of the flow (Sparks et al., 2002).

Although less common than PDCs and tephra dispersal, debris avalanches (Siebert, 1984) and large, primary lahars (Pierson, 1995) are processes which can also alter catchment hydrology and emplace voluminous volcaniclastic deposits. Both processes can be highly erosive proximal to their source, stripping soil and vegetation (Pierson and Major, 2014), although primary lahars are more channel-confined than the typically larger debris avalanches. Deposits from both processes are composed of a range of material including

juvenile products and source edifice fragments. Debris avalanche deposits are often "hummocky" in appearance and can provide a multi-decadal sediment source due to their potentially large volumes (≥1 km^3) (Capra et al., 2002).

1.2.2. Rain-Triggered Lahar Initiation Mechanisms

The initiation of rain-triggered lahars typically occurs via either shallow landsliding of saturated tephra layers above basal décollement surfaces (Hodgson and Manville, 1999; Manville et al., 2000b; Pareschi et al., 2000; Scott et al., 2005; Mead et al., 2016), runoff induced rill erosion (Nammah et al., 1986; Leavesley et al., 1989; Yamakoshi and Suwa, 2000; Lavigne and Thouret, 2003; Major and Yamakoshi, 2005; Barclay et al., 2007) or particle detachment as a result of rainsplash erosion followed by subsequent transport by sheet wash (Segerstrom, 1950; Waldron, 1967). Manville et al. (2000b) describe a lahar initiation mechanism at Ruapehu consisting of the sliding above a detachment layer created by two superposed tephra layers with contrasting grain size distributions. This concept is echoed by Pierson et al. (1996) who describe a fine surface deposit at Pinatubo created by co-ignimbrite fallout as easily liquefiable compared to the coarser underlying substrates. This initiation mechanism involves an increase in pore fluid pressures due to infiltration of rainfall, which reduces inter-granular friction and increases deposit density until shear failure and liquefaction occur (Manville et al., 2000b; Mead et al., 2016). This indicates that under certain conditions decreased infiltration could delay lahar initiation as pore fluid pressure would increase more slowly.

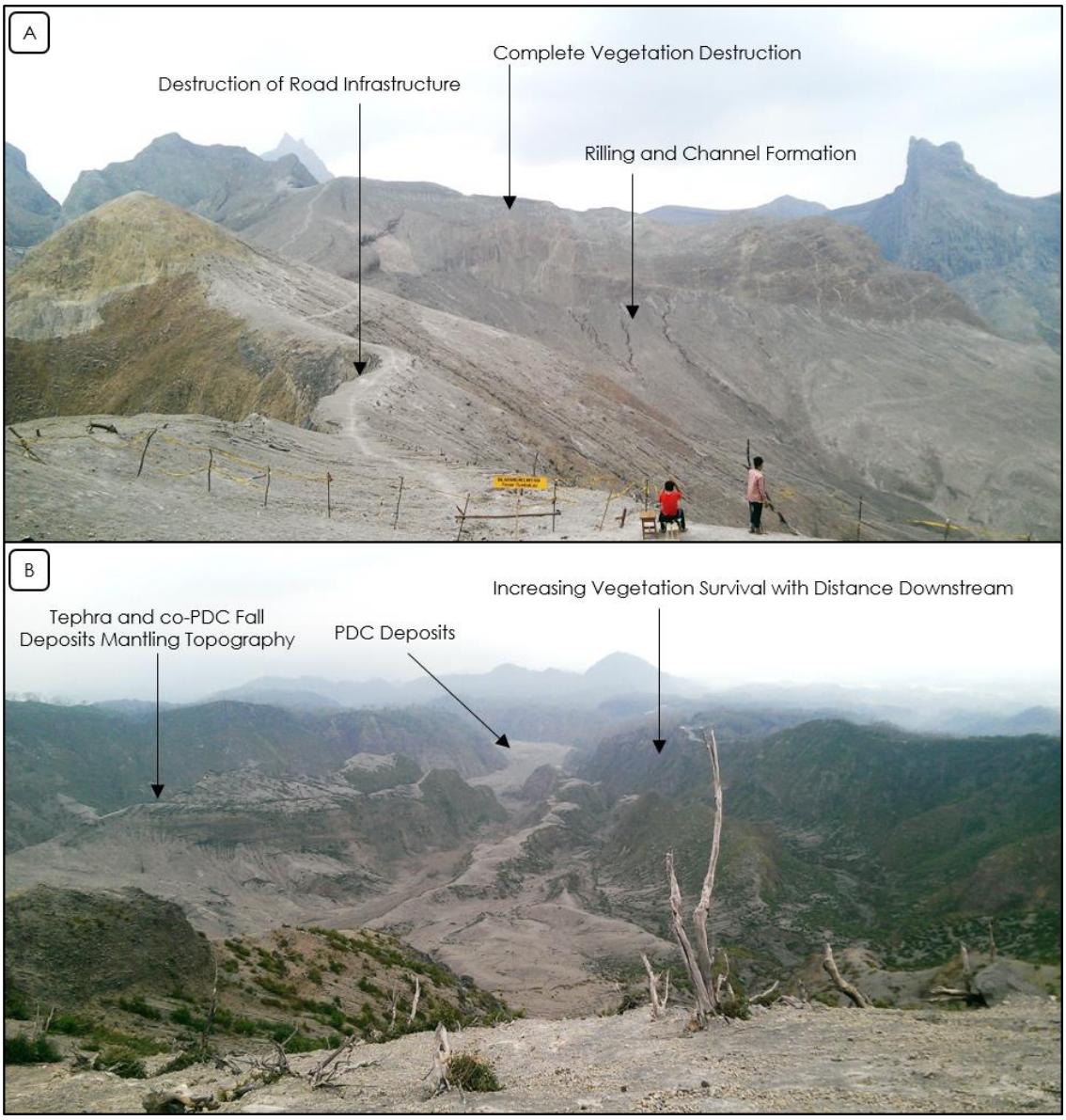

Figure 1.3: Impacts of the 14th February 2014 eruption of Kelud, Indonesia in the upper catchment of the Bladak river to the west of the volcano. A: Proximal eruption impacts displaying complete vegetation destruction, the emplacement of pyroclastic material and the development of post-eruption rill and channel networks. B: Downstream view indicating increasing vegetation survival with distance downstream, valley-fill PDC deposits and the mantling of topography with tephra and co-PDC fall deposits.

Rill erosion and sheet wash are the dominant hillslope erosion mechanisms of pyroclastic material as a result of post-eruption precipitation (Fig. 1.3A) (Pierson and Major, 2014). These processes are heavily interrelated, with areas of particle detachment and sheet wash progressively invaded by headward-eroding gullies (Fig. 1.4), as a product of cumulative rainfall after an eruption (Segerstrom, 1950).

Rill formation is initiated by the exceedance of a critical fluid shear stress or unit stream power threshold (Nearing et al., 1989; Gilley et al., 1993). Fluid shear stress is a function of flow depth and slope angle, while unit stream power is a function of flow depth, velocity and slope angle. As a result, increased surface runoff heightens the potential for rill initiation for a given slope angle (Gomez et al., 2003), indicating that the relationship between rainfall and runoff is a key factor in rain-triggered lahar initiation. For non-cohesive substrata, the threshold value required to initiate rilling for a given slope angle is controlled by particle size, shape and mass density (Gilley et al., 1993). Headward and lateral growth of rill networks with time is frequently identified after the emplacement of pyroclastic material (Segerstrom, 1950; Waldron, 1967; Collins and Dunne, 1986; Gran and Montgomery, 2005). Both the development of rill networks (Fig. 1.3) and extensive sheetwash act to expose underlying substrates, altering surface permeability and erodibility (Collins and Dunne, 1986).

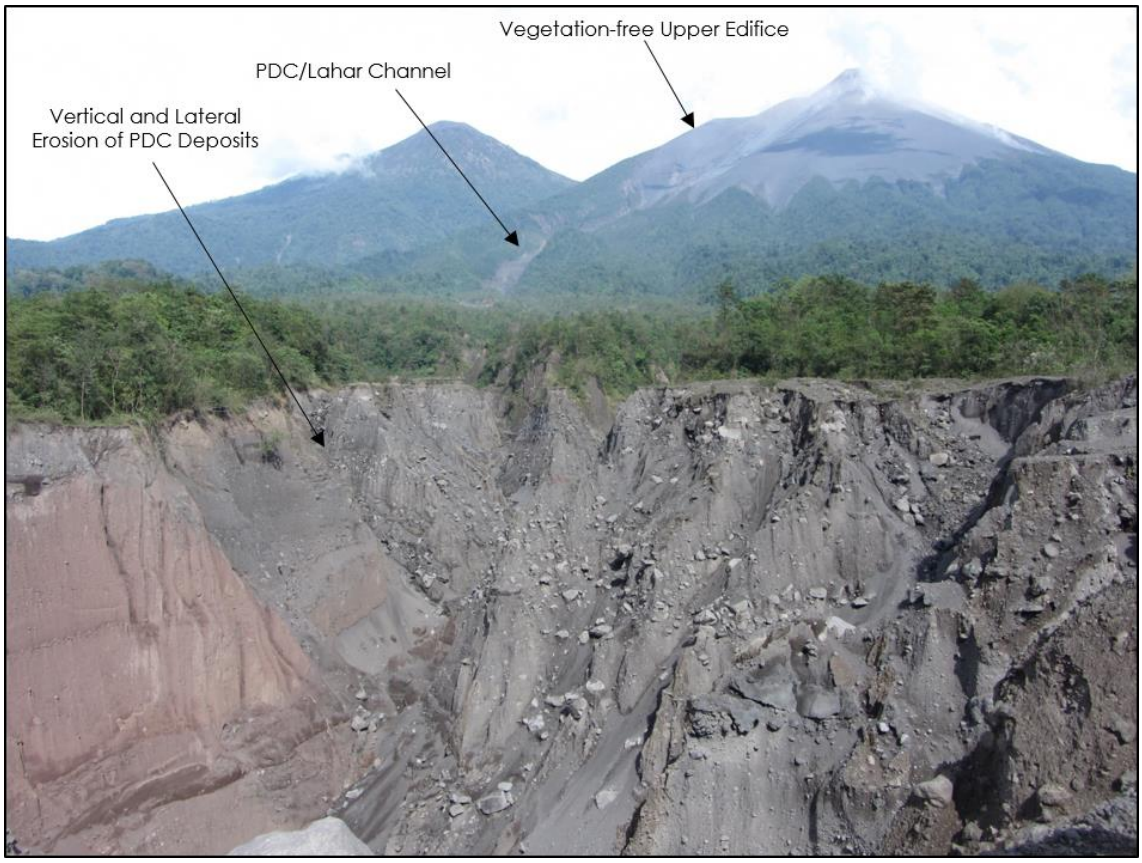

Figure 1.4: Rain-triggered lahar erosion of PDC deposits in the Santa Teresa Baranca, Volcán de Fuego, Guatemala (Feb 2012). Visible in the image are the vegetation-free, tephra covered upper edifice of Fuego and the lahar-driven vertical (≈60 m) and lateral (≈50 m) erosion of PDC deposits emplaced during the January 8th 2003 eruption of Fuego 6.5 km downstream of the active crater.

1.2.3. Grain Size Distribution

The grain size distribution of pyroclastic material, a function of its eruption style, proximity to its source and emplacement mechanism, strongly influences its permeability and this has a significant impact on the magnitude of the potential rain-triggered lahar hazard (Shepherd, 1989; Major and Yamakoshi, 2005). A reduction in pore space typically accompanies a reduction in particle size and this decreases infiltration rates, making the grain size distribution of source material an important factor in the evaluation of rain-triggered lahar hazard (Shepherd, 1989). Reduced infiltration rates promote overland flow, enhancing

rill and sheet erosion when exposed to rainfall and increasing the probability of rain-triggered lahar generation (Leavesley et al., 1989; Ogawa et al., 2007; Pierson et al., 2013). The runoff-enhancing impacts of fine ash layers are described at Pinatubo (Pierson et al., 1996), Montserrat (Alexander et al., 2010), Chaitén (Pierson et al., 2013) and Unzen (Yamakoshi and Suwa, 2000), with an increase in lahar initiation thresholds due to relatively coarse ash layers described at Mayon (Rodolfo and Arguden, 1991) and Merapi (Lavigne et al., 2000a). Fine particles are also more likely to be displaced and detached by rainsplash than coarser particles (Collins and Dunne, 1986). As such, it is typically accepted that finer ash layers will result in lower initial rain-triggered lahar initiation thresholds than analogous coarser deposits.

1.2.4. Vegetation, Surface Roughness and Topography

The extent of vegetation damage and destruction in addition to the rate at which this vegetation recovers are important factors in the frequency and magnitude of rain-triggered lahars. Vegetation loss reduces infiltration, interception, evapotranspiration and surface roughness enhancing post-eruption runoff rates (Yamakoshi and Suwa, 2000; Barclay et al., 2007; Ogawa et al., 2007; Alexander et al., 2010). The area and degree of vegetation destruction is broadly controlled by the magnitude of an eruption and the proximity of the affected area to the active crater (Figs. 1.2 & 1.3), with large eruptions including Pinatubo in 1991 (Pierson et al., 1996) and Mt. St. Helens in 1980 (Major and Mark, 2006) resulting in catchment-wide destruction, whilst smaller eruptions only cause vegetation damage in very proximal areas (Fig. 1.4) (e.g. Thouret et al., 2014). Vegetation damage and recovery is identified as a primary control on

catchment behaviour and the variability of lahar initiation thresholds under specific rainfall conditions at locations including Mt. St. Helens (Major and Yamakoshi, 2005), Unzen (Yamakoshi and Suwa, 2000) Soufrière Hills (Alexander et al., 2010) and Pinatubo (Gran and Montgomery, 2005). Re-vegetation directly increases interception and evapotranspiration, whilst the development of root networks both increases the permeability of deposits and stabilises them, increasing infiltration rates and reducing erodibility respectively (Major and Mark, 2006). Surface roughness is also enhanced upon revegetation, impeding runoff and reducing its erosive potential (Barclay et al., 2007). The potential runoff reduction and deposit stabilisation provided by re-vegetation are two reasons why aerial re-seeding has been undertaken at locations such as Mt Unzen (Yamakoshi and Suwa, 2000) in an attempt to mitigate the lahar hazard following eruptions.

Across areas featuring no pre-eruption vegetation, surface roughness is also typically reduced by the emplacement of pyroclastic deposits (Major et al., 1996). PDC deposits have the potential to emplace flat-topped valley-fill deposits above previously complex channel networks, whilst tephra fall can regionally mantle topography (Fig. 1.3). In common with the effects of increased catchment gradient, reduced surface roughness increases runoff velocity and erosive potential and can significantly enhance the rain-triggered lahar hazard (e.g. Pierson et al., 2013).

1.2.5. Crusting, Antecedent Rainfall & Hydrophobicity

Fine ash layers often form runoff-enhancing surface crusts as a result of raindrop compaction induced surface sealing (Leavesley et al., 1989; Watt et al.,

2009) or chemical precipitation of soluble salts (Waldron, 1967). Crust formation is described as heightening runoff at locations including Pinatubo (Pierson et al., 1996), St Helens (Leavesley et al., 1989) and Unzen (Yamakoshi and Suwa, 2000), the latter of which was the site of aerial re-seeding in an attempt to limit the longevity of such crusts. The interaction between rill erosion and surface crusting is therefore an important dynamic in the analysis of rainfall-runoff relationships at fine ash mantled locations (Leavesley et al., 1989; Yamakoshi and Suwa, 2000). The exposure of more permeable substrates after the breakdown of surface crusts and the erosion of surface layers typically increases infiltration rates and lahar initiation thresholds (Yamakoshi and Suwa, 2000). However, Ogawa et al. (2007) described the downward migration of fine ash particles during erosion; a process which can result in the filling of pore spaces between coarse particles by the migrating fine particles, thus reducing infiltration rates within the coarse deposit despite the breakdown of crusts and the erosion of surface layers.

Antecedent rainfall effects the potential infiltration capacity of pyroclastic deposits prior to storm occurrence and is identified as an important factor in rain-triggered lahar initiation (e.g. Barclay et al., 2007; Okano et al., 2012; Jones et al., 2015). The dominant effect of heightened antecedent rainfall is to reduce infiltration capacity, promote surface runoff and thus lower lahar initiation thresholds, as identified at volcanoes including Merapi (Lavigne et al., 2000a), Semeru (Lavigne and Suwa, 2004) and Montserrat (Barclay et al., 2007). At Montserrat lahar frequency increases later in the rainy season due to increased levels of deposit saturation (Barclay et al., 2007). Both the lahar initiation mechanisms of sliding above a detachment surface (e.g. Manville et al., 2000b) and runoff-driven sheet and rill erosion (e.g. Pierson et al., 2013) are enhanced by increased antecedent rainfall. Antecedent impacts are heightened at

locations featuring fine-grained pyroclastic deposits, with negligible antecedent impacts identified at locations featuring coarse-grained material due to the consistently high infiltration rates and effective drainage (Rodolfo and Arguden, 1991; Paguican et al., 2009). The time-scale of studied antecedent rainfall within previous research varies from seven days at Merapi (Lavigne et al., 2007) where rainfall is very high, to three days at Colima where rainfall is lower and evaporation rates high (Capra et al., 2010). At Yakedake increased antecedent rainfall influences not only the hydraulic magnitude of lahars but also the rheology of boulder dam features (Okano et al., 2012), with the likelihood of a slurry matrix within the boulder dam increased if channel floor deposits are pre-saturated. Similarly, heightened saturation within channel floor deposits due to antecedent rainfall has been identified as increasing flow bulking efficiency (Iverson et al., 2010; Reid et al., 2011).

Vegetation-driven hydrophobicity identified by Capra et al. (2010) at Colima displays complexities within the relationship between antecedent rainfall, rainfall-runoff and lahar initiation. This hydrophobicity is identified as the driving factor behind increased lahar frequency early in the rainy season. High levels of hydrophobicity are attributed to the dominant vegetation type and associated high levels of waxes and resins. These hydrophobic compounds can be broken down by sustained rainfall and as such infiltration rates are increased later in the rainy season. Not only is hydrophobicity relevant on a seasonal time scale but it makes 3-day antecedent rainfall a significant consideration at Colima when analysing lahar initiation (Capra et al., 2010). Contrary to most volcanoes, increased antecedent rainfall (breaking down hydrophobic compounds) increases lahar initiation thresholds at Colima.

1.2.6. Rainfall Variation and Type

Rainfall is highly variable on both a spatial and temporal scale in volcanic regions due to orographic effects and disturbance to prevailing weather patterns as a result of the irregular topography (Buytaert et al., 2006). The analysis of lahars and the estimation of rain-triggered lahar initiation thresholds relies heavily on rain gauges and their spatial coverage. At Mt. Mayon (summit elevation 2,462 masl) precipitation analysis relies on a rain gauge at an altitude of 10 m, a location where the recorded rainfall is likely to be substantially lower than the actual rainfall on the upper slopes of the volcano due to orographic effects (Rodolfo, 1989; Rodolfo et al., 1989; Rodolfo and Arguden, 1991; Paguican et al., 2009). Analysis of rain-triggered lahars at Chaitén, Chile by Pierson et al. (2013) relied on distal regional rain gauges due to the sparse network of rain gauges in Northern Patagonia, with the nearest working gauge located 60 km NNE of the volcano. Despite statistical analysis suggesting that total rainfall is similar at Chaitén Volcano to the distal rain gauge, this highlights the need for high resolution temporal precipitation information when analysing lahar initiation. Tungurahua possesses one telemetered rainfall gauge (at an altitude of 2,724 m); this gauge provides rainfall data at a high temporal resolution but does not provide information regarding spatial variation (both lateral and vertical) of rainfall around the dense radial drainage network of the volcano (Jones et al., 2015). A network of 10 rain gauges was installed in 2001 across the island of Montserrat and this helped to display the spatial and temporal rainfall variation when analysing lahars (Barclay et al., 2007). Rainfall gauge coverage is thus a key evaluation when analysing rain-triggered lahar occurrence.

The type of rainfall-delivering weather system and the location and altitude of pyroclastic deposits also influences the nature of the rain–triggered lahar hazard. At Merapi local, orographic rainfall at altitudes >1200 m is often associated with smaller lahars whilst regional migratory weather systems are often associated with large lahars (Lavigne et al., 2000a). This is echoed at Soufrière Hills Volcano, Montserrat where large synoptic weather systems often trigger large flows as a result of sustained catchment-wide rainfall, whilst localised mesoscale convective storms are more associated with the triggering of small lahars (Barclay et al., 2006; Froude, 2015). This pattern is reversed at Semeru volcano, where local orographic effects result in migratory rainfall predominantly occurring at too low of an altitude relative to the location of the source material at the head of lahar-prone drainages to trigger large lahars (Lavigne and Suwa, 2004). This demonstrates that rainfall altitude is an important factor in lahar initiation, with rainfall at different altitudes potentially remobilising different types of deposit. Additionally, rainfall kinetic energy variation provided by the different rainfall types and intensities impacts storm erosivity, with higher intensity rainfall typically more erosive for a given volume of rainfall (Wang et al., 2014).

1.2.7. Catchment Recovery

Post-eruption sediment yields typically decline exponentially with time, in common with other disturbed earth systems such as wildfire affected regions (Graf, 1977). This temporal reduction is associated with the stabilisation of rill networks, a reduction in the volume of easily erodible sediment and vegetation recovery (Collins et al., 1983; Collins and Dunne, 1986; Schumm and Rea, 1995). The time-scale of catchment recovery after an eruption is therefore related

closely to the volume and grain size distribution of deposited material (Janda et al., 1996), amount of precipitation and the vegetation recovery rate (Major and Mark, 2006). Despite this gradual fluvial recovery, after large discreet eruptions sediment yields can remain significantly elevated for multiple decades (Major et al., 2000; Gran and Montgomery, 2005; Major and Yamakoshi, 2005; Van Westen and Daag, 2005).

Post-eruption landslides and secondary pyroclastic flows are two processes which can alter catchment hydrology and thus inhibit catchment recovery (e.g. Torres et al., 1996). Secondary pyroclastic flows caused by explosions within hot pyroclastic deposits and landslides were frequent after the 1991 eruption of Pinatubo (Torres et al., 1996; Hayes et al., 2002; Van Westen and Daag, 2005), and increased the area of some catchments whilst decreasing the area of others by the process of "catchment capture". This process can increase or decrease the lahar hazard in differing catchments due to the change in area, available sediment and vegetation cover, thus altering the typical recovery process (Van Westen and Daag, 2005). A further factor that can inhibit typical catchment recovery is the addition of new pyroclastic deposits due to eruptive activity. This is common at many frequently active volcanoes including Semeru (Dumaisnil et al., 2010; Thouret et al., 2014), Sakurajima (Hikida et al., 2007) and Tungurahua (Williams et al., 2008). Due to the frequent activity at these locations the magnitude of the lahar hazard is more stable with time than after a single discreet eruption as a result of the consistent availability of lahar source material and the prevention of vegetation recovery (Thouret et al., 2014).

1.2.8. Rain-Triggered Lahar Monitoring and Mitigation

As a product of their speed, reach and composition (Pierson et al., 2014), rain-triggered lahars resulted in approximately 7,000 fatalities between 1600 and 2010 (Auker et al., 2013). The extent to which lahars cause physical damage as a result of rock fragment impacts and/or inundation is dictated by the lahar's dynamic characteristics (velocity, depth, sediment concentration and grain size) and the nature of the structure in question (Jenkins et al., 2015a). An example of the impacts of rain-triggered lahars is displayed in Figure 1.5, which illustrates the remnants of the former settlement of El Palmar in Guatemala, which was destroyed due to rain-triggered lahars in the Rio Nima I created by persistent vulcanian activity at Santiaguito and the subsequent rainfall-driven remobilisation of pyroclastic material. In 1982 lahars in the Rio Nima II inundated the western part of the settlement of El Palmar (≈7,000 inhabitants), causing widespread damage and its partial abandonment. El Palmar was completely abandoned in 1998, when further large lahars in the Rio Nima I created a 15 m deep and 50 m wide channel through the middle of the settlement, causing destruction by rock fragment impact and inundation as well as undercutting and channel terrace collapse (Fig. 1.5). Figure 1.5C highlights the continued risk posed to the CA-2 highway bridge over the Rio Samalá 5 km downstream of El Palmar. This bridge is downstream of the confluence of three lahar-prone drainages of Santiaguito and is a site of lahar-driven aggradation and inundation during periods of heavy rainfall. The bridge provides a primary transport link between central Guatemala and Mexico, creating potentially large economic losses if the bridge was destroyed due to rain-triggered lahar activity. The effective assessment of lahar hazard as well as the monitoring of rain-triggered

lahars and the parameters which drive their occurrence are vital components of rain-triggered lahar risk mitigation.

As tephra on steep slopes is generally poorly preserved and proximal-medial lahar deposits are often re-worked by subsequent flows (Manville et al., 2009a), distal lahar deposits are an important resource when reconstructing both eruption and lahar chronologies (Froude, 2015). The importance of this resource is emphasised by the difficulty in accessing rain-triggered lahar initiation zones due to their inherently hazardous nature. The study of distal lahar deposits is thus vital within lahar hazard assessment, yielding information regarding flow extent and magnitude, although it can be challenging to effectively distinguish individual flow events (Froude, 2015).

Figure 1.5: Rain-triggered lahar impacts at Santiaguito, Guatemala (Feb 2012). A: Persistent vulcanian activity and a leveed dacitic lava flow at Santiaguito with visible lahar-prone drainages. B: Damage to the formerly inhabited settlement of El Palmar, 5 km downstream of Santiaguito, due to rain-triggered lahars in the Rio Nima I. C: CA-2 highway bridge over the Río Samalá, 10 km downstream of Santiaguito, a site of lahar-driven aggradation.

Methods of real-time rain-triggered lahar monitoring include the use of Acoustic Flow Monitors (AFMs) (e.g. Marcial et al., 1996; Lavigne et al., 2000b; Williams et al., 2008; Jones et al., 2015), seismometers (e.g. Lavigne et al., 2000b; Davila et al., 2007; Kumagai et al., 2009), rain gauge networks (e.g. Marcial et al., 1996; Lavigne et al., 2000b; Barclay et al., 2007; Capra et al., 2010; Jones et al., 2015), tripwires (Marcial et al., 1996; Lavigne et al., 2000b) and physical observations (e.g. Martinez et al., 1996; Thouret et al., 2007; Stone et al., 2014; Jones et al., 2015). AFMs utilise exploration-class geophones (Hadley and LaHusen, 1995; Marcial et al., 1996) to measure the ground vibration produced by lahars as a result of the frictional interaction both within the flow itself and at the flow margins (Doyle et al., 2011). Once calibrated, AFM recordings can be used to estimate lahar discharges and volumes (Lavigne, 2004; Williams et al., 2008), reconstruct lahar hydrographs (Worni et al., 2011) and differentiate between flow rheologies (Lavigne, 2004). AFMs can be implemented as lahar warning systems, with minimum amplitude threshold values used to alert of flow occurrence (Lavigne et al., 2000b; Van Westen and Daag, 2005). These threshold values are site specific, as instrument type, channel proximity and background noise impact the relationship between recorded instrument amplitude and flow magnitude. Where AFMs are unavailable, seismic networks can also be used to identify lahars (Barclay et al., 2007; Kumagai et al., 2009; Zobin et al., 2009).

Telemetered rain gauges facilitate real-time continuous monitoring of rainfall which may have the potential to trigger lahars (Janda et al., 1996). Telemetered rain-gauges are often tipping-bucket gauges with data collected at pre-defined time intervals (Lavigne et al., 2000b), rainfall thresholds or a combination of the two (Marcial et al., 1996). As discussed previously, increased rainfall gauge coverage both laterally and vertically enhances the potential for

effective lahar hazard assessment (Lavigne et al., 2000b). Tripwires can be installed across lahar-prone channels to provide alerts of lahar transit, but provide no additional information other than location and arrival time (Marcial et al., 1996; Lavigne et al., 2000b). Monitoring of lahars by physical observation typically uses manned observation posts (Waldron, 1967; Martinez et al., 1996; Lavigne, 1999), video monitoring (Thouret et al., 2007; Takeshi, 2011) or volunteer networks (Stone et al., 2014). Lahar monitoring capabilities are highly variable on regional and local scales, typically a function of the financial constraints associated with constructing and maintaining monitoring facilities, with eruptive activity often producing a rain-triggered lahar hazard in areas featuring limited or non-existent lahar monitoring networks.

In addition to flow monitoring, physical lahar hazard mitigation in the form of channelization and the installation of sabo dams is commonly implemented in both Japan and Indonesia (Pierson et al., 2014). Sabo dams encourage deposition of entrained sediment and a reduction in flow velocity and are used at volcanoes including Merapi (Lavigne, 1999; Lavigne and Thouret, 2003), Semeru (Thouret et al., 2007) and Mayon (Paguican et al., 2009). Assessment of likely lahar magnitude is important during the construction of sabo dams, with insufficient structures overwhelmed and rendered useless by large flows such as after the 1991 eruption of Pinatubo (Janda et al., 1996). The construction of man-made debris flow channels designed to constrain and direct lahars towards low-risk regions is expensive but is utilised at locations including Sakurajima (Takeshi, 2011). Sampling systems and load cells can be integrated within these man-made channels in order to enhance the understanding of flow processes (Takeshi, 2011).

Channel avulsion is an important process when attempting to mitigate lahar hazard and risk, with locations including Pinatubo (Major et al., 1996), Chaitén (Pierson et al., 2013) and Merapi (de Bélizal et al., 2013) displaying significant lahar impacts as a product of the avulsion of small flows due to channel-filling aggradation from previous lahars. This process impacts the effectiveness of existing monitoring networks and at Mayon an avulsion created a new 5 km long, 15-70 m wide channel, dramatically altering catchment hydrology (Rodolfo, 1989). The excavation of lahar deposits is a frequently utilised method of increasing lahar channel capacity in order to reduce the potential for flow avulsion (Harris et al., 2006; Orense and Ikeda, 2007). The identification of potential avulsion sites during the lahar hazard assessment process, whether by field-based research or lahar modelling (e.g. Iverson et al., 1998; Darnell et al., 2013; Córdoba et al., 2015; Lee et al., 2015), is important in mitigating future risk. In addition to identifying potential areas of lahar avulsion, lahar modelling has the potential to examine areas of potential flow inundation (Muñoz-Salinas et al., 2009; Córdoba et al., 2015), estimate lahar transit times (Fagents and Baloga, 2005) and recreate past events (Williams et al., 2008).

In conjunction with acting as a basis for hazard and risk mitigation, lahar monitoring networks provide data for rain-triggered lahar research and the development of new mitigation methods. A commonly utilised method within rain-triggered lahar studies is that of rainfall intensity/duration (I/D) analysis (Fig. 1.6). This approach has been undertaken at volcanoes including Pinatubo (Arboleda and Martinez, 1996; Martinez et al., 1996; Rodolfo et al., 1996; Tungol and Regalado, 1996; Van Westen and Daag, 2005), Mayon (Rodolfo and Arguden, 1991) and Merapi (Lavigne et al., 2000b) and involves the production of an equation or range of equations that indicates the anticipated rainfall

intensity required to produce a lahar for a given rainfall duration and vice versa. This analysis typically displays that lahar initiation occurs along a continuum from short duration, high intensity rainfall events to long duration, low intensity events, resulting in a power law relationship (Fig. 1.6) (e.g. Rodolfo and Arguden, 1991; Arboleda and Martinez, 1996; Tungol and Regalado, 1996). I/D analysis attempts to differentiate between "lahar-triggering" and "non-lahar-triggering" rainfall by empirically deriving location-specific relationships using rainfall data and lahar observation/detection.

The incorporation of antecedent rainfall into I/D analysis can help to account for pre-storm deposit moisture content (Lavigne et al., 2000a) or the potential breakdown of hydrophobic compounds (Capra et al., 2010). I/D analysis by Hikida et al. (2007) at Sakurajima helped to derive two thresholds which are illustrated in Figure 1.6; the minimum rainfall required for potential lahar occurrence and the maximum rainfall of non-occurrence. This clarification is beneficial given the inherent uncertainty in I/D analysis, which is illustrated by the overlap of lahar-triggering and non-lahar-triggering rainfall events in Figure 1.6. This uncertainty reflects the lack of consideration of many potential contributing variables such as orographic rainfall and time since eruptive activity. Mead et al. (2016) also indicate that the relative importance of rainfall duration and rainfall intensity upon lahar initiation is dependent on the specific lahar initiation mechanism. Rainfall duration is identified as being more important in shallow-slip lahar initiation, whereas rainfall intensity is identified as more important when considering lahar initiation via runoff-induced rill erosion (Mead et al., 2016).

Estimation of the probability of lahar occurrence given defined rainfall conditions is an alternative approach to lahar hazard assessment which acknowledges the uncertainty in quantifying lahar triggering rainfall (e.g. Barclay

et al., 2006), however such probabilistic approaches have not been widely attempted. Mead et al. (2016) identify the potential benefits of probabilistic lahar hazard assessment via the estimation of initial lahar volume occurrence probabilities. Despite being relatively data intensive, this approach to lahar hazard assessment has the potential to generate probabilistic, quantitative inputs for computational lahar models (Mead et al., 2016).

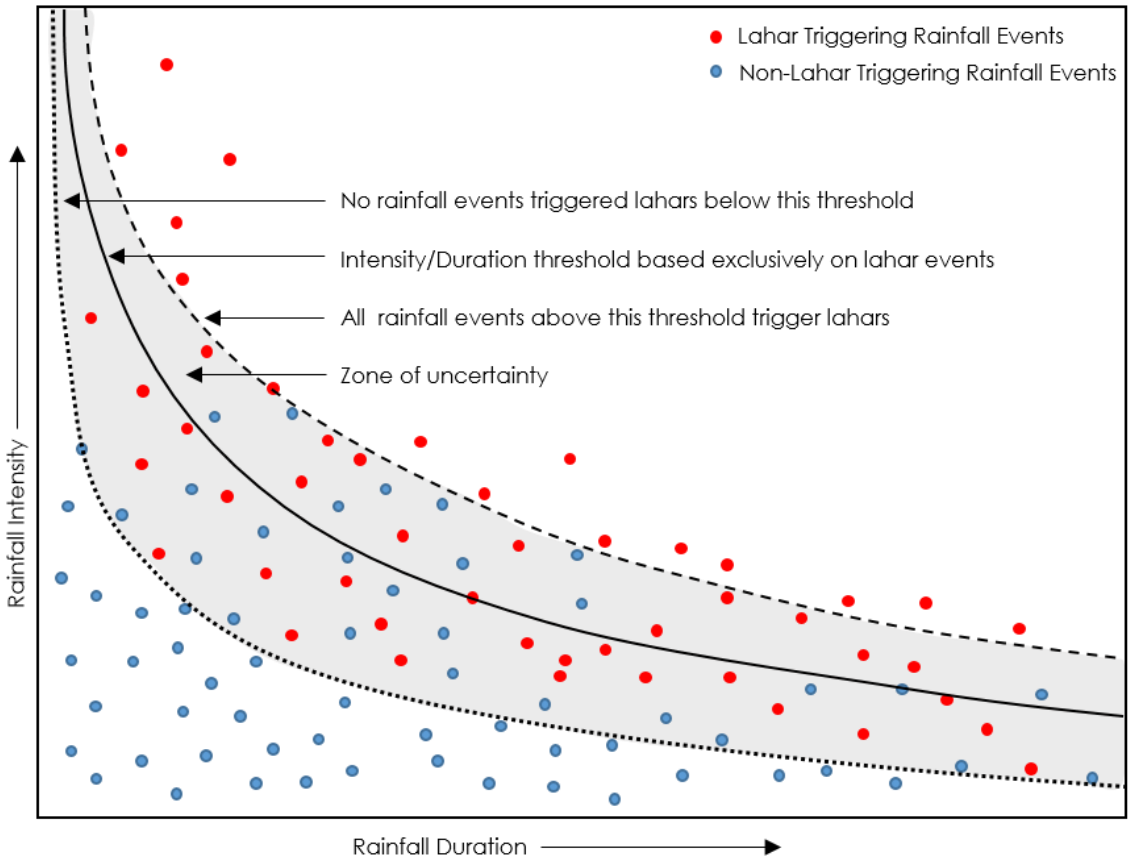

Figure 1.6: A hypothetical example of an Intensity/Duration graph, illustrating the typical characteristics of this type of analysis. Displayed are lahar triggering (red dots) and non-lahar triggering (blue dots) rainfall events as well as three potential output thresholds. (I) The upper threshold indicates the minimum rainfall required to generate a 100% lahar occurrence rate (e.g. Hikida et al., 2007). (II) The lower threshold indicates the maximum rainfall required to generate a 0% lahar occurrence rate (e.g. Hikida et al., 2007). (III) The middle threshold displays a typical lahar initiation threshold, representing the best fit line when focusing exclusively on lahar producing rainfall events (e.g. Rodolfo and Arguden, 1991).

Research has highlighted the globally significant nature of rain-triggered lahar hazards and the complexities involved in both understanding the physical

processes driving lahar occurrence and in implementing effective hazard assessment and risk mitigation strategies. This thesis focuses on both improving knowledge of rain-triggered lahar initiation processes and developing new rain-triggered lahar risk mitigation techniques in order to provide a crucial link between the understanding of the physical components involved in lahar initiation and its practical application within a lahar risk mitigation framework.

1.3. Research Aims and Objectives

This thesis aims to increase insight into the initiation processes of rain-triggered lahars in order to enhance the understanding of these complex, multiphase phenomena. The nature of rain-triggered lahar initiation processes dictates the spatio-temporal variation of lahar occurrence, the development of lahar hydrographs and the resultant lahar hazard and risk. This thesis utilises a combination of field-based research, experimental investigation and the analysis of lahar monitoring data to enhance the understanding of the key parameters driving rain-triggered lahar initiation and to develop real-time lahar forecasting tools based on telemetered rainfall data:

I. Field-based Studies (Chapter 2) – Field work at Calbuco Volcano, Chile was undertaken seven weeks after a significant eruption to examine what eruption-driven catchment disturbance and post-eruption catchment recovery reveal about the initiation of rain-triggered lahars and the magnitude and spatio-temporal variation of the rain-triggered lahar hazard following an eruption. This field-based post-eruption research of rain-triggered lahar hazard aims to physically identify key factors driving rain-triggered lahar initiation.

II. Experimental Research (Chapter 3) – Calibrated simulated rainfall and laboratory-constructed tephra beds are used to study what laboratory-based experiments can reveal about the key physical factors involved in rain-triggered lahar initiation and how this relates to practical lahar hazard and risk assessment. The development of laboratory-based experiments of this nature aims to isolate the effects of individual parameters and to quantitatively examine runoff and infiltration processes from analogous rain-triggered lahar source conditions.

III. Analysis of Lahar Monitoring Data (Chapters 4 & 5) – Rainfall and lahar records from Tungurahua and Soufrière Hills volcanoes are used to develop new tools designed to utilise real-time monitoring data for lahar forecasting. This research approach aims to enhance the use of real-time telemetered lahar monitoring information, including rainfall and AFM data, within a lahar risk mitigation framework.

Chapter 2: Assessing Catchment-by-Catchment Variation in the Post-Eruption Rain-Triggered Lahar Hazard at Calbuco Volcano

Summary

Calbuco Volcano, Chile (-41.33° S, -72.61° W) erupted at 18:05 local time on the 22nd April 2015, producing eruption columns in excess of 15 km in height, dispersing tephra predominantly to the northeast and triggering pyroclastic density currents (PDCs) which travelled down many of the drainages surrounding the volcano. Effective evaluation of the impacts of the eruption throughout the radial drainage network of the volcano is important in identifying the volcano-hydrologic response to the eruption and the magnitude of the potential post-eruption rain-triggered lahar hazard. Exposed terraces in the Rio Blanco Este drainage indicate that PDCs in the catchment occurred during the 6 hour second phase of the eruption. Aerial footage and field-based investigation reveal that in addition to the Blanco Este, PDCs inundated the Rio Tepu, Rio Sur, Rio Blanco Sur, Rio Colorado and Rio Este. In the drainages featuring both PDCs and upstream pre-eruption glaciers, namely the Rio Sur, Rio Blanco Sur, Rio Colorado and Rio Este, snow and ice-melt triggered primary lahars. These primary lahars also affected the Rio Correntoso and at least one flow avulsed from the Rio Blanco Sur across to the Rio Correntoso. Primary lahars scoured upper channels, inundated regions as wide as 150 m in the Blanco Sur and damaged infrastructure including numerous fish farm facilities, bridges, roads and buildings.

A post-eruption rain-triggered lahar hazard was generated in two primary areas, the Rio Blanco Este and southern flanks of the adjacent Osorno Volcano, with smaller flows evident in the Rio Tepu. In the Rio Blanco Este this hazard was generated by the emplacement of widespread unconfined PDC deposits in the upper catchment in combination with tephra deposits. The associated reduction of infiltration rates, rainfall interception by vegetation and surface roughness as well as the addition of easily-erodible pyroclastic material contributed to the generation of this rain-triggered lahar hazard. The rain-triggered lahar hazard on the southern flanks of Osorno was exclusively a product of tephra deposition. These tephra deposits were more fine-grained than those deposited in the proximal drainages of Calbuco such as the Blanco Este and Rio Tepu and thus further reduced infiltration rates. In the Rio Tepu catchment PDC deposits were not sufficiently widespread and tephra deposits were too coarse to generate a significant rain-triggered lahar hazard in the weeks following the eruption.

There was significant catchment-by-catchment variation in the proximal volcano-hydrologic response to the discrete eruption of Calbuco. The pre-eruption snow and ice cover, spatial distribution and volume of PDCs as well as the thickness and grain size of tephra deposits were the most important driving factors behind this variation. Rapid evaluation of these factors in the event of eruptions enhances the effective assessment of post-eruption rain-triggered lahar hazard.

2.1. Introduction

Calbuco Volcano, Chile (-41.33° S, -72.61° W) is located in the Andean Southern Volcanic Zone (SVZ) approximately 30 km NE of the city of Puerto Montt.

The volcano has experienced two Holocene sector collapses, two large explosive eruptions in the past two thousand years and at least eleven basaltic-andesite to andesite (54.8–59.3% SiO_2) producing historical eruptions since 1792; the largest occurring in 1893-95 (Watt et al., 2011; Castruccio and Clavero, 2015; Romero et al., 2016). The slopes of Calbuco feature dense vegetation (Fig. 2.1), largely composed of Valdivian temperate rainforest. Average annual rainfall as recorded at Lago Chapo (234 masl) on the southern flanks of Calbuco is approximately 2115 mm, with peak rainfall in May, June and July. Orographic effects at Calbuco enhance precipitation at higher altitudes and this induces significant spatial variability in recorded rainfall around the volcano.

Prior to 2015, the previous major eruption of Calbuco occurred in 1961, nine months after the M 9.5 Valdivia earthquake, the epicentre of which was 360 km from Calbuco (Romero et al., 2016). The 1961 eruption produced tephra fallout from 12-15 km high eruption columns, lava flows, block-and-ash flows and hot, primary lahars (Klohn, 1963; Castruccio et al., 2010; Castruccio and Clavero, 2015). These primary lahars were triggered by the interaction of block-and-ash flows with ice and snow and were directed to the North (Rio Tepu), South (Rio Blanco Sur) and East (Rio Blanco Este), reaching Lago Llanquihue, Lago Chapo and the Rio Petrohué respectively (Fig. 2.1) (Klohn, 1963; Castruccio et al., 2010; Castruccio and Clavero, 2015). In addition to these hot, primary lahars the widespread dispersal of tephra and deposition of pyroclastic material around the edifice of Calbuco created a spatially variable post-eruption rain-triggered lahar hazard.

An hour-long period of volcano-tectonic (VT) events followed by long-period (LP) events preceded an explosive eruption of Calbuco at 18:05 local

time on the 22nd April 2015, producing eruption columns in excess of 15 km in height. The basaltic-andesite (55% SiO_2) producing eruption consisted of two major pulses, the first (phase 1) lasted approximately 1.5 hours and the second (phase 2) began at 01:08 local time and lasted 6 hours, with tephra predominantly deposited to the northeast of the volcano (Romero et al., 2016). In addition to the predominantly north-easterly distribution of airborne tephra, column collapse-driven pyroclastic density currents (PDCs) with maximum runout distances of 7 km occurred radially, affecting the headwaters of major rivers and triggering a complex sedimentary response within the radial drainage network. The eruption prompted the declaration of a 20 km exclusion zone and the evacuation of over 5,000 inhabitants, with ONEMI advising against access within 200 m of drainages due to potential lahar hazards. A third minor phase of activity began at 23:30 on 23rd April 2015 and produced ash plumes with heights of up to 2 km which were distributed to the east and northeast.

The April 2015 eruption of Calbuco caused substantial perturbation within catchments surrounding the volcano and landscape disturbance of this nature induces long-term geomorphic responses (Pierson and Major, 2014). Despite their persistent, lethal and globally significant nature, rain-triggered lahars are amongst the most poorly understood volcanic hazard. This eruption presented a rare opportunity to investigate lahars as they happen, and this study uses a predominantly field-based approach to examine lahar occurrence seven weeks after the eruption. The aim of this research is to enhance the understanding of key factors required to generate a rain-triggered lahar hazard following significant eruption-driven catchment disturbance. A combination of fieldwork and the examination of aerial photography and video footage is utilised to identify and constrain the factors driving catchment-by-catchment variability

within the volcano-hydrologic response to the eruption and to specifically assess the resultant rain-triggered lahar hazard.

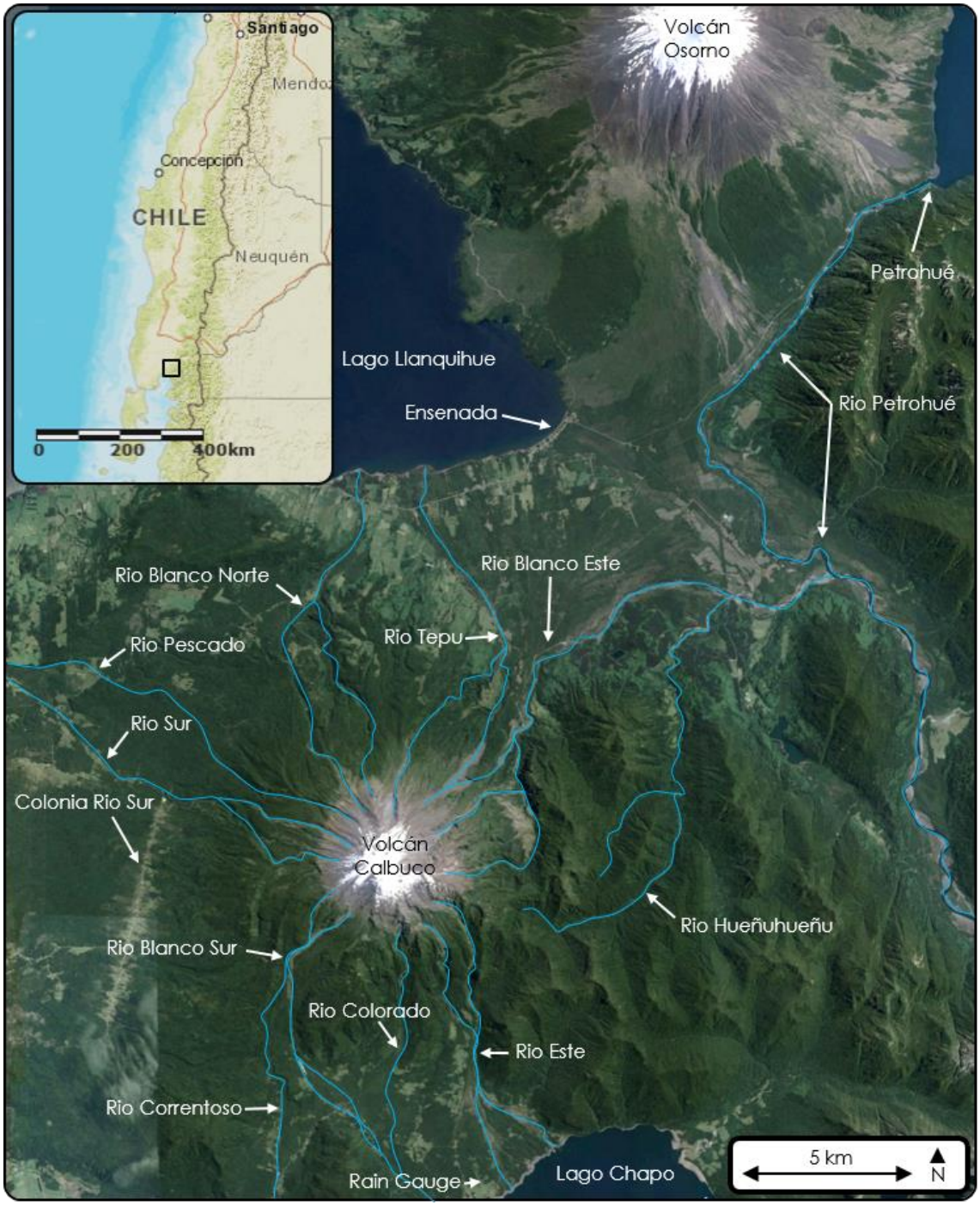

Figure 2.1: Location map of Calbuco Volcano, Chile. Highlighted is the radial drainage network of the volcano and major proximal settlements (GoogleEarth, 2016).

2.2. Methods

The volcano-hydrologic response to the 22nd April 2015 eruption of Calbuco was assessed during a field visit which took place from 7th-22nd June 2015. The analysis of post-eruption conditions during this visit relied upon field investigations of deposit characteristics and stratigraphy, the use of time-lapse cameras and the examination of aerial photographs and video footage taken in the days and weeks following the eruption. Owing to the emplacement of pyroclastic material around the volcano, ground investigations were restricted to accessible regions at the time of the field visit. Where possible, multiple field sites were established along the longitudinal profile of each catchment. This facilitated the examination of the downstream evolution of deposits emplaced both during the eruption and as a result of the post-eruption, rainfall-driven re-mobilisation of pyroclastic material.

Bushnell HD Trophy trail cameras were used to capture both motion-triggered and fixed-interval time-lapse footage of channels during the field visit. The use of these cameras facilitated the identification of any rain-triggered lahar activity and the estimation of the magnitude of flow variation during periods of rainfall as well as illustrating erosion, aggradation and channel migration patterns.

The helicopter-based aerial footage analysed in this study was taken by the Servicio Nacional de Geología y Minería (SERNAGEOMIN) during a series of flights in the days and weeks following the eruption of Calbuco. This footage is used to examine post-eruption deposits in inaccessible upstream regions, identify conditions before the excavation of deposits and to provide evidence as to the volcano-hydrologic response to the eruption prior to the field visit in June 2015.

2.3. Catchment-by-Catchment Post-Eruption Conditions

2.3.1. Rio Blanco Este

The Rio Blanco Este catchment on the eastern slopes of Calbuco encompasses the Rio Frio and Rio Caliente, their confluence to form the single-channel Rio Blanco Este, and the downstream confluences with the Rio Hueñuhueñu and Rio Petrohué (Fig. 2.2). During the April 2015 eruption of Calbuco PDCs flowed down both the Rio Frio and Rio Caliente (Fig. 2.3) and continued past the confluence of the two rivers (41°17'59"S, 72°33'36"W, 423 masl) along the Rio Blanco Este (Fig. 2.2). PDCs filled deep (>20 m) gorges in the upper sections of the Rio Caliente, and the furthest downstream emplacement of PDC deposits within the Rio Blanco Este occurs approximately 7 km (41°17'20"S, 72°33'20"W, 313 masl) from the crater via the Rio Frio channel. The steaming of PDC deposits upstream of this location was visible in all available images taken between the 24th April and 20th June 2015 (Fig. 2.4), with surface temperatures of 60°C measured on June 12th and freshly exposed sub-surface deposits measured at 200°C on the same day at field site BE1 (Table 2.1). Gas release structures occurred across both the whole deposit when freshly emplaced (Figs. 2.4A & 2.4B) and in June on parts of the deposit not yet impacted by channel erosion or terrace collapse. Carbonisation of trees and charring of vegetation was visible both above the surface of the emplaced PDC deposits at the lateral extremities of the eroded region and within the PDC deposits at exposed terrace locations. Flat-topped valley-fill deposits are evident in images of the Rio Blanco Este at field site BE1 on 24th April 2015 shortly after the eruption (Fig. 2.4A). Post-eruption erosion of PDC deposits via streamflow, rain-triggered lahar activity and the undercutting of terraces (Figs. 2.4C & 2.4D)

exposed the stratigraphy at site BE1 by June 11th 2015 and thus the eruption chronology (Fig. 2.5).

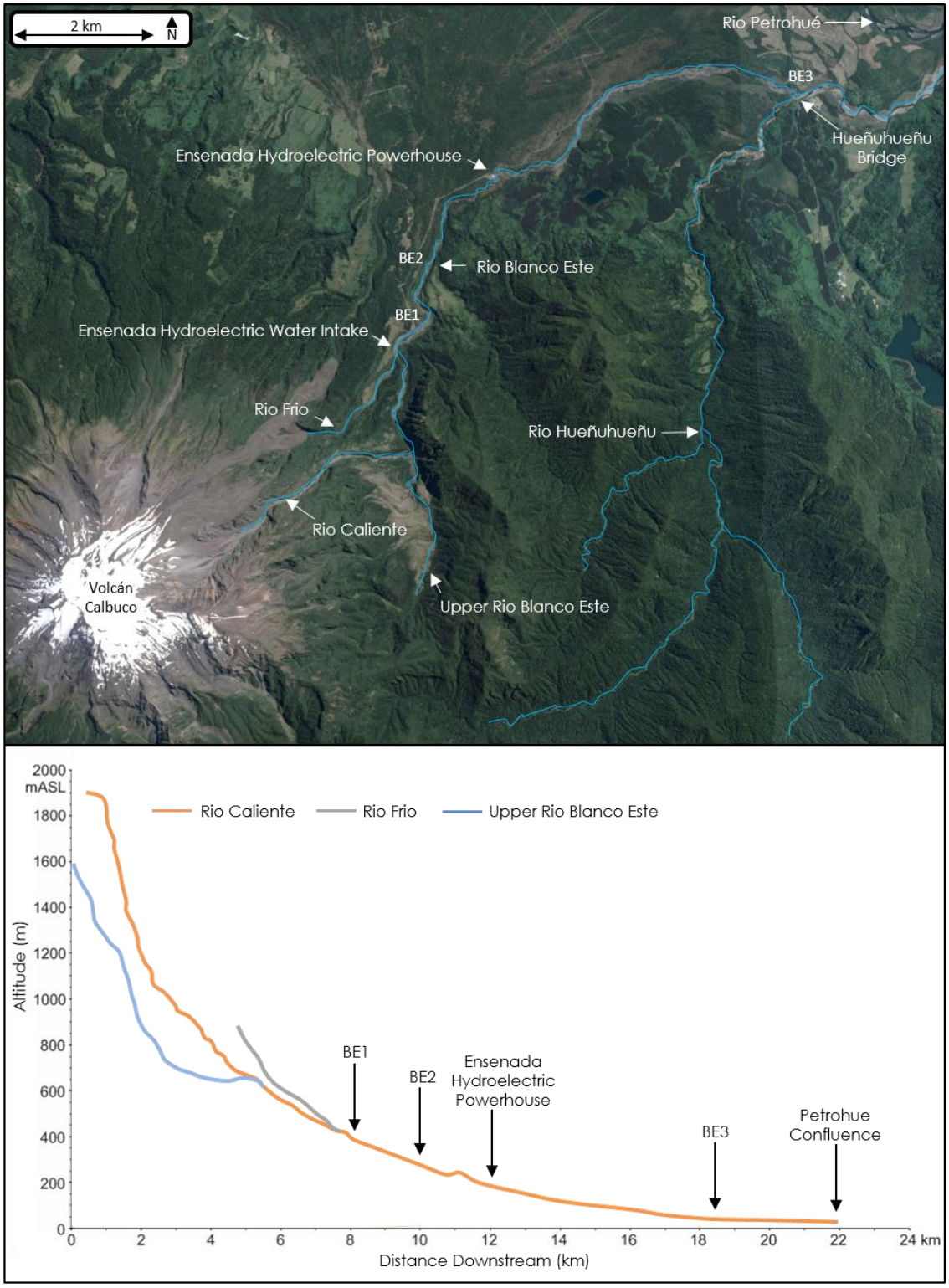

Figure 2.2: Location map (above) and channel profile (below) of the Upper Blanco Este catchment. Highlighted are tributaries, field site locations and notable local infrastructure (GoogleEarth, 2016).

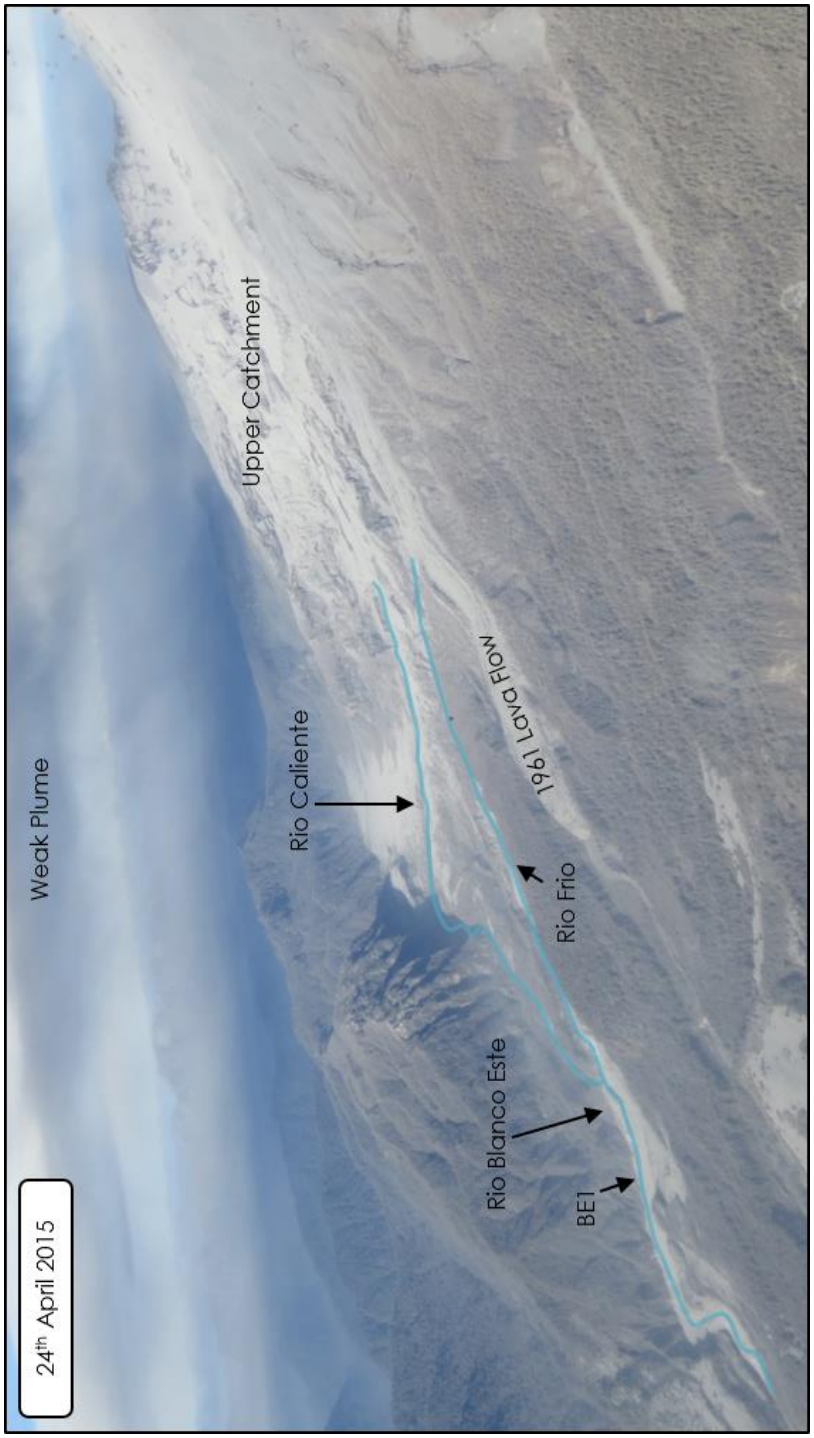

Figure 2.3: Aerial image of the upper catchment of the Rio Blanco Este taken on the 24th April 2015 (SERNAGEOMIN, 2015).

Site Name	Catchment	Latitude			Longitude			Elevation (m)
		Degrees	Minutes	Seconds	Degrees	Minutes	Seconds	
BE1	Blanco (Este)	-41	17	46.6	-72	33	30.7	384
BE2	Blanco (Este)	-41	17	1.4	-72	33	11.8	314
BE3	Blanco (Este)	-41	15	32.2	-72	28	41.1	50
T1	Rio Tepu	-41	16	6.6	-72	33	54.1	205
T2	Rio Tepu	-41	15	54	-72	34	5	182
T3	Rio Tepu	-41	13	57.2	-72	35	44.1	94
S1	Rio Sur	-41	16	59	-72	45	1	225
S2	Rio Sur	-41	17	38	-72	43	58	268
S3	Rio Sur	-41	17	51	-72	43	41	300
S4	Rio Sur	-41	18	10	-72	43	6	344
BS1	Blanco (Sur)	-41	23	23	-72	38	33	447
BS2	Blanco (Sur)	-41	24	15.8	-72	37	36.3	343
BS3	Blanco (Sur)	-41	24	52	-72	36	28	294
C1	Rio Correntoso	-41	25	19	-72	39	0	210
C2	Rio Correntoso	-41	27	8.3	-72	40	21.1	137
A1	Avulsion (BS-C)	-41	23	53.9	-72	33	13.2	382
A2	Avulsion (BS-C)	-41	25	0.6	-72	33	28.2	288
A3	Avulsion (BS-C)	-41	25	23.4	-72	38	52.7	257
O1	Osorno South Flanks	-41	11	38.7	-72	28	32.4	98
O2	Osorno South Flanks	-41	11	27.4	-72	28	17.9	110
O3	Osorno South Flanks	-41	11	3.6	-72	27	55.2	119
O4	Osorno South Flanks	-41	10	48.8	-72	27	44.4	128
O5	Osorno South Flanks	-41	9	12	-72	26	1	179
O6	Osorno South Flanks	-41	8	57	-72	25	51	200
O7	Osorno South Flanks	-41	8	48	-72	25	16	202
O8	Osorno South Flanks	-41	8	36	-72	24	48	206

Table 2.1: Location details of field sites accessed during the June 2015 field visit.

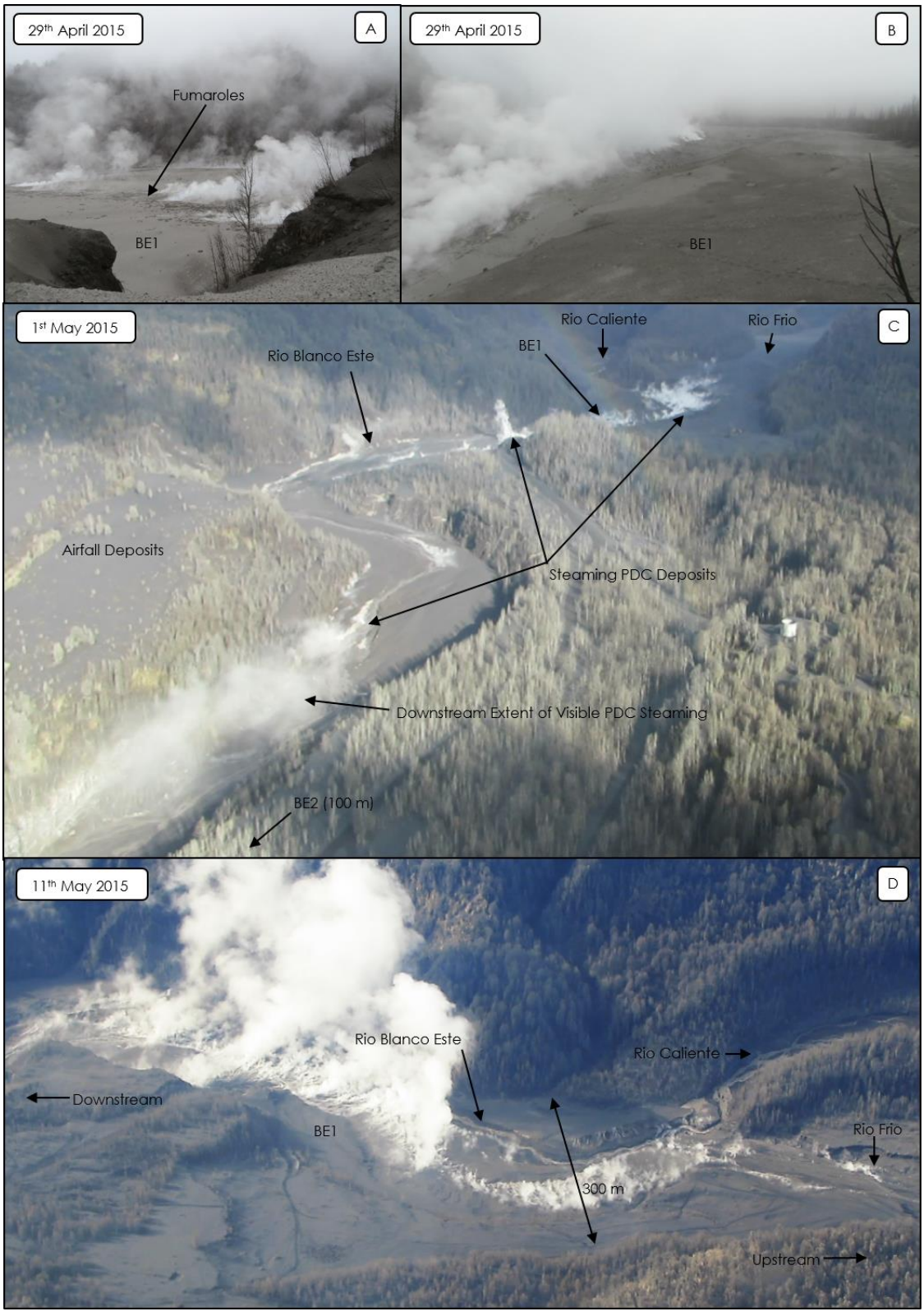

Figure 2.4: Images displaying the post-eruption evolution of Pyroclastic Density Current (PDC) deposits in the Rio Blanco Este (SERNAGEOMIN, 2015). A: Lateral view of degassing of flat-topped PDC deposits at site BE1. B: Upstream view of PDC deposits at site BE1. C: Aerial image displaying initial post-eruption erosion of PDC deposits near site BE1. D: Aerial image displaying continued post-eruption erosion of PDC deposits at site BE1.

Figure 2.5 shows that approximately 60 cm of orange coloured coarse tephra deposits from the 1961 eruption of Calbuco have been exposed at the base of the terraces at site BE1 by the erosion of PDC deposits. These were overlain by 1.5 m thick lahar deposits containing unsorted sub-angular blocks of various sizes up to a maximum diameter of 0.5 m. A fine matrix and unburnt vegetation including tree trunks are present in the upper 1 m of these lahar deposits but not in the lower 0.5 m. These lahar deposits are attributed to either the 1961 or 1972 eruptions of Calbuco. Above these older lahar deposits lies approximately 35 cm of coarse, pumice-rich lapilli associated with the April 2015 eruption. The lowest 10 cm of this airfall deposit (layer A) is light-brown in colour and inversely graded with respect to grain size. Layer A is topped with an additional 10 cm of normally graded, light-brown, coarse, pumice-rich lapilli (layer B). A 15 cm layer of darker brown, very coarse lapilli (Layer C_1) lies above layer B and is topped with a massive, light grey 8-10 m thick PDC deposit (layer P_1). P_1 is composed of a very fine-grained matrix with entrained angular pumice clasts and lithics up to 1 m in diameter. Above layer P_1 is 7 cm of brown, coarse lapilli that becomes less vesicular and darker upwards (layer C_2). Layer C_2 is overlain by 8 cm of dense, coarse, dark grey lapilli (Layer D). In some areas layer D is overlain by up to 10 cm of fine-grained fluvial deposits as a result of initial re-working of upstream PDC deposits and fine-grained airfall deposits. Such fine-grained airfall deposits, likely a product of PDC plume fallout, are seen mantling the topography of the Blanco Este in aerial images taken on April 24th (Fig. 2.3) but were not preserved at Site BE1 during the field visit in June 2015.

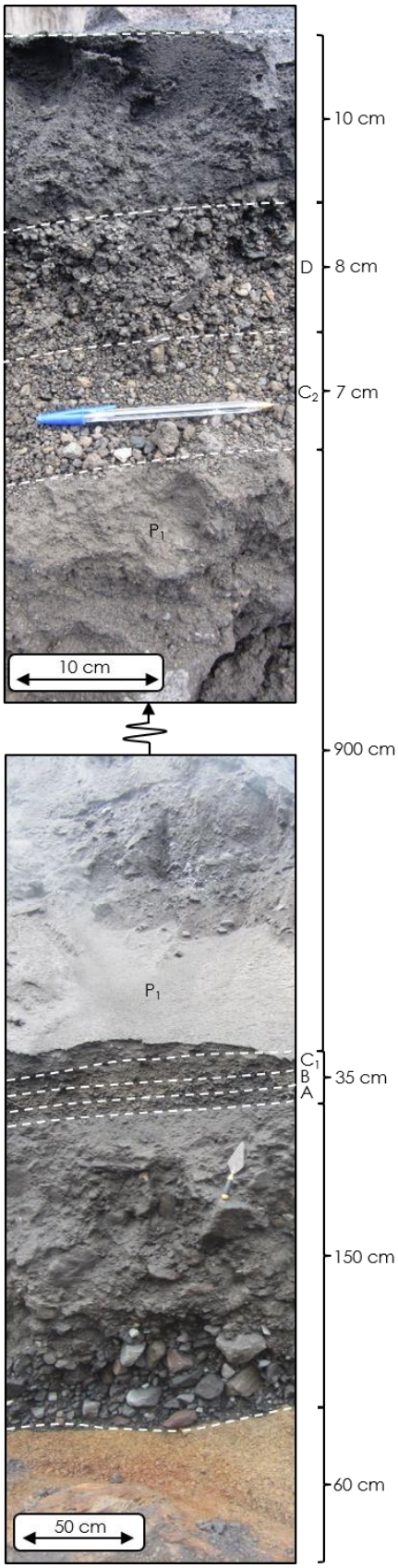

Figure 2.5: Images displaying the stratigraphy of the exposed terraces at field site BE1 in June 2015 detailing pre-eruption deposits and the April 2015 eruption chronology.

Site BE1 is located approximately 100 m downstream of the confluence of the Rio Frio and Rio Caliente and on 11th June 2015 featured an 80 m wide region of PDC erosion with 12-15 m high lateral terraces and a 5-10 m wide and 3-5 m deep central channel with permanent post-eruption streamflow. This permanent streamflow was fed predominantly by the Rio Caliente which also featured permanent pre-eruption streamflow. Rilling and channel formation within PDC deposits was evident in the upper part of the catchment in aerial images taken on the 11th May 2015 (Fig. 2.6). This rill erosion is evidence of excess overland flow induced by a reduction in infiltration rates due to the fine-grained co-PDC fall deposits visible in Figure 2.3. Widening and deepening of the central channel at site BE1 as a result of an individual rain-triggered lahar event was evident between the 15th June 2015 (5 m wide central channel) and 18th June 2015 (20-25 m wide central channel) (Figs. 2.7B & 2.7C). This widening exposed pipeline associated with the destroyed water intake of the Ensenada hydroelectric project (Figs. 2.7C & 2.7D). Exposure of this previously underground pipeline and the 1961 Calbuco tephra deposits (Fig. 2.5) indicates that post-eruption erosion in this part of the catchment has exposed pre-eruption deposits. 12-15 m high terraces composed largely of April 2015 PDC deposits (Fig. 2.5) were located at the lateral extremities of the eroded region in June 2015 and displayed rotational collapse when saturated due to heavy rainfall. Such collapse results in the addition of easily remobilised pyroclastic material to the central channel region.

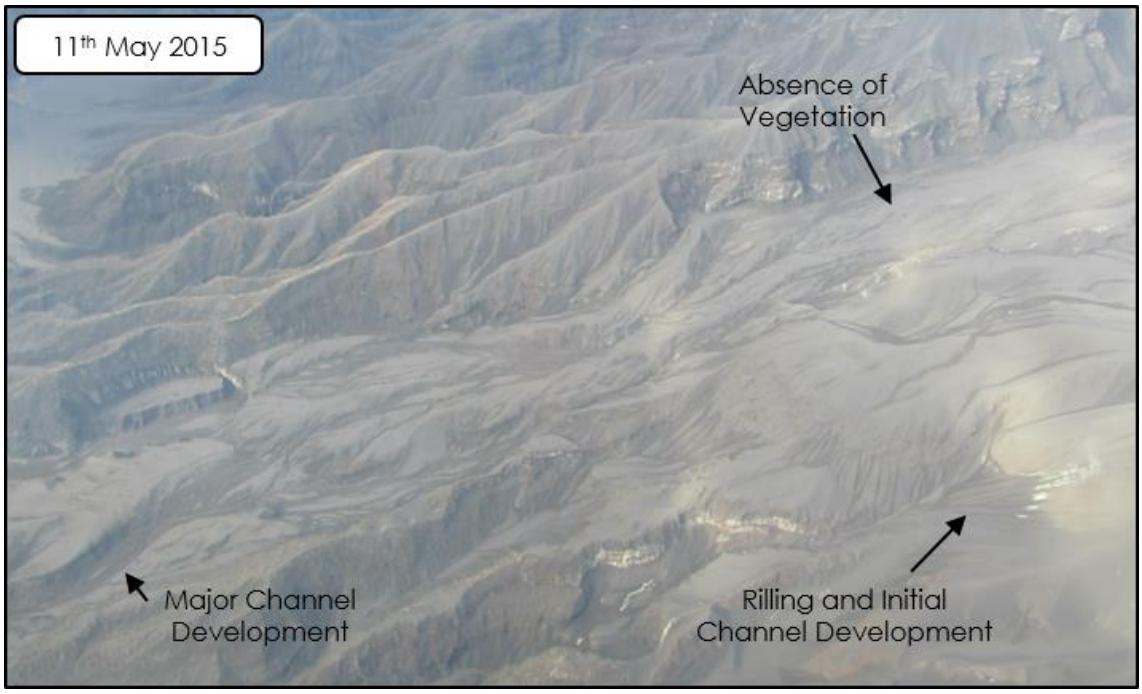

Figure 2.6: Aerial Image of the upper Rio Blanco Este taken on May 11th 2015 displaying post-eruption rill erosion and channel development (SERNAGEOMIN, 2015).

Figures 2.8 & 2.9 illustrate the rainfall-driven flow variability within the Blanco Este at site BE2 during the field visit in June 2015, with corresponding daily rainfall totals in Figure 2.11. These images were captured via both time-lapse footage (Fig. 2.8) and personal site visits (Fig. 2.9) and displayed spatio-temporal flow variation in terms of sediment concentration, discharge and flow type. Active channels at site BE2 migrated continuously during the field visit, frequently changing between braided (Figs. 2.9A & 2.9C) and single-thread flow (Figs. 2.9B & 2.9D). Aggradation was evident at site BE2 during periods of rainfall-driven high-flow (Figs. 2.8A-C) and downcutting during lower flow during dry-periods (Figs. 2.8D-I). Pre-eruption height of the waterfall in Figure 2.9 was 18 m, this height had reduced to approximately 9 m by the 11th June 2015 due to channel aggradation.

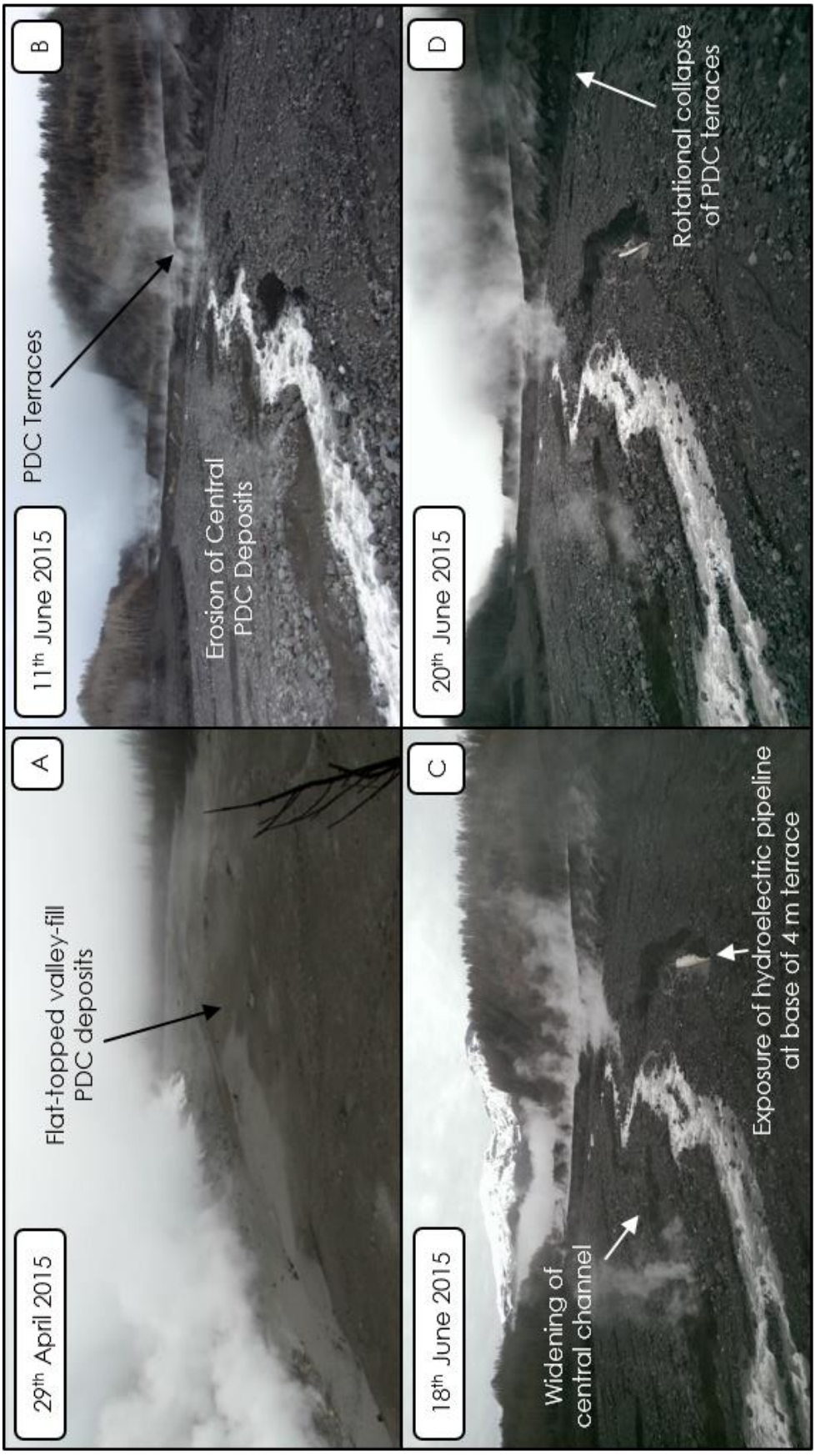

Figure 2.7: Images displaying the evolution and erosion of Pyroclastic Density Current (PDC) deposits at field site BE1 between 29th April 2015 and 20th June 2015.

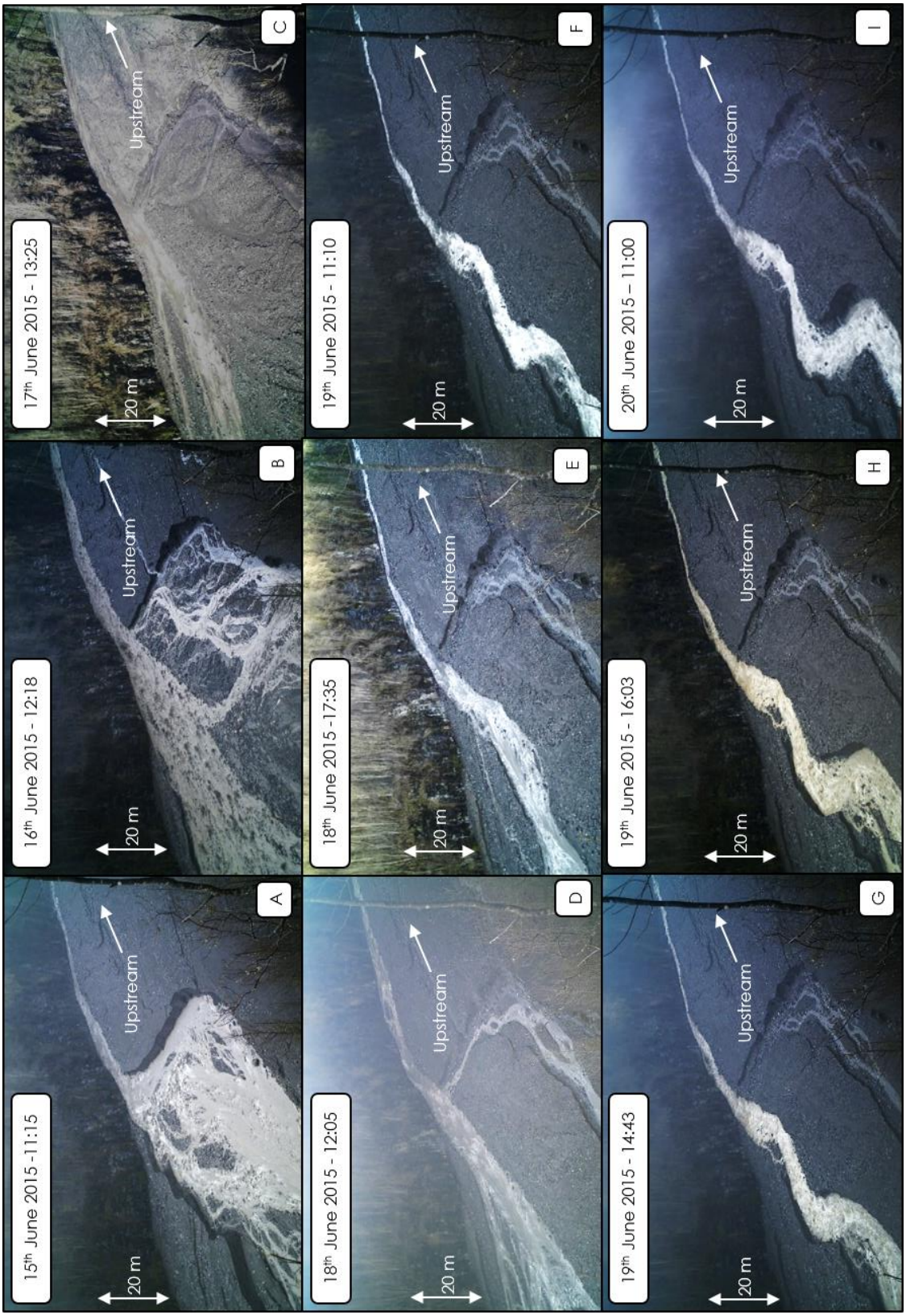

Figure 2.8: Selected time-lapse images illustrating flow variation within the Blanco Este over a 5-day period in June 2015 at field site BE2.

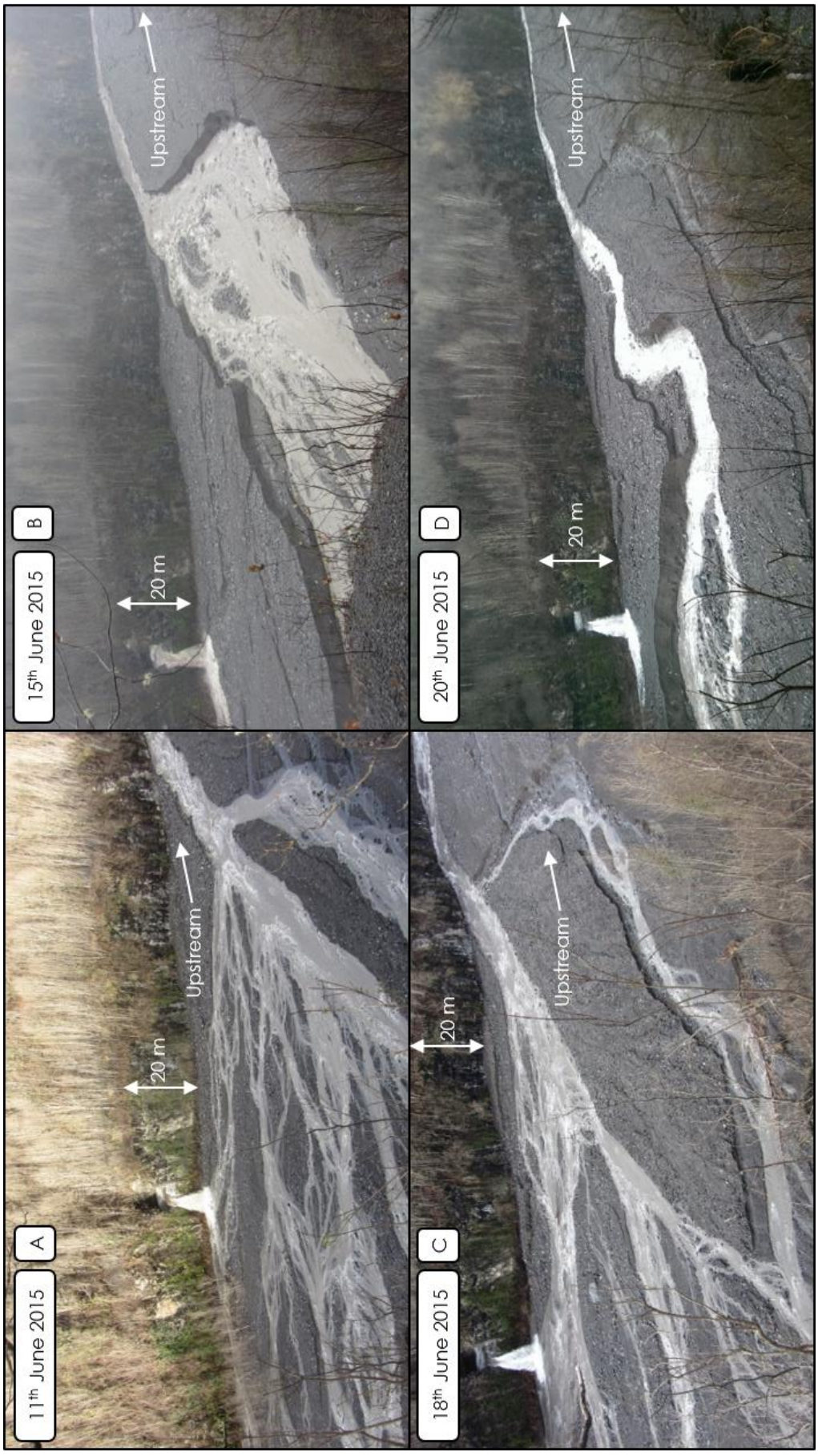

Figure 2.9: Images displaying flow variation within the Blanco Este at field site BE2 between 11th June 2015 and 20th June 2015.

Figures 2.10A-C display the "before and after" images highlighting the initial destruction of the Ensenada hydroelectric powerhouse (41°16'19"S, 72°32'37"W, 201 masl). This structure is located 4.1 km downstream of the confluence of the Rio Frio and Rio Caliente, 2.6 km downstream of the furthest estimated downstream extent of PDC deposits and 6.2 km upstream of the confluence of the Blanco Este and the Rio Hueñuhueñu at site BE3 (Fig. 2.2). Prior to 6th May 2015 (Fig. 2.10A) the channel at this location had aggraded by 1.5 m relative to its pre-eruption condition, and Figures 2.11A-C capture a further 4.5 m of aggradation over the following 12 days which resulted in the inundation of the structure. The regional rainfall record (Fig. 2.11) indicates extensive rainfall (>10 mm) at the Lago Chapo rain gauge (17 km SSW of the Ensenada hydroelectric powerhouse) on the 8th, 16th and 17th May 2015 during this time period, with 36 mm of rainfall recorded on the 16th May 2015. Rapid aggradation of the channel continued over the following weeks, with 4 m of additional aggradation between 18th May 2015 and 29th May 2015. The long-term rate of aggradation slowed over time, with 13.5 m of total aggradation relative to pre-eruption conditions identified on 30th March 2016. The destruction of the Ensenada hydroelectric powerhouse and the continued aggradation of the channel at this location was a product of the deposition of remobilised pyroclastic material due to a reduction in flow energy driven by the lessening of the channel gradient (Fig. 2.2).

Figure 2.10: Images displaying post-eruption impacts due to flow variation in the Blanco Este. A-C: Site of the Ensenada Hydroelectric Powerhouse (SERNAGEOMIN, 2015). D-E: Field Site BE3.

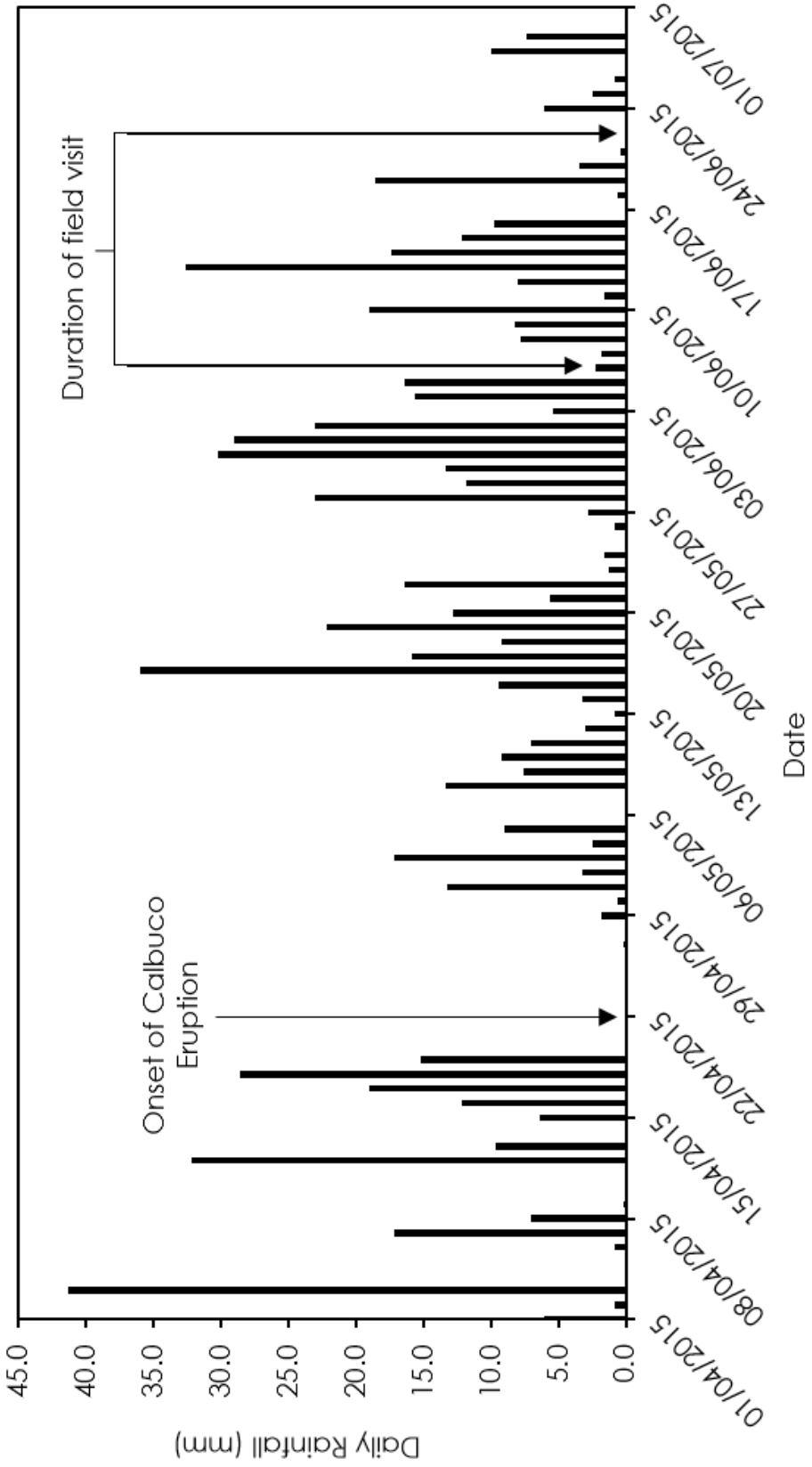

Figure 2.11: Daily rainfall as recorded at the Lago Chapo rain gauge (41°25'47"S, 72°34'35"W – 290 masl) in April, May and June 2015.

The post-eruption sedimentary response at field site BE3, the confluence of the Rio Hueñuhueñu and the Rio Blanco Este, is illustrated in Figures 2.10D &

2.10E. The 6.2 km between the inundated Ensenada hydroelectric powerhouse (Figs. 10A-C) and site BE3 has an average gradient of 2.5% whereas the 4.1 km upstream of the Ensenada Hydroelectric powerhouse to the confluence of the Rio Frio and Rio Caliente features an average gradient of 5.4%. This lessening gradient of the river profile resulted in the deposition of coarse remobilised material upstream of site BE3 and therefore deposits at BE3 were dominated by ash-sized (<2 mm) particles. The Rio Hueñuhueñu drains from a densely vegetated region which experienced no PDC deposits. The dense vegetation increases infiltration, interception and evapotranspiration rates, which minimises tephra remobilisation. Therefore, the flow from the Rio Hueñuhueñu contained very little suspended sediment in June 2015 (Fig. 2.10E). Conversely, the Rio Blanco Este contained large quantities of re-mobilised, suspended fine-grained pyroclastic material and this created a sediment bar at the confluence of the two rivers. When site BE3 was visited after periods of heavy rain the Rio Hueñuhueñu already contained suspended pyroclastic material (Fig. 2.10D) due to the activation of an ephemeral channel a few hundred metres upstream linking the two rivers as a result of aggradation in the Blanco Este. This observed sedimentation posed minimal risk to infrastructure during the field visit as the location of the bridge had been recently heavily excavated due to gradual post-eruption aggradation as a result of rainfall-driven remobilisation of pyroclastic material.

2.3.2. Rio Tepu

The Rio Tepu (Fig. 2.12) on the north/north-eastern flanks of Calbuco is the adjacent drainage to the west of the Rio Blanco Este and flows directly into Lago

Llanquihue. The catchment features two primary contributing upstream channels, hereby known as the western and eastern channels (Fig. 2.12). The confluence of these channels occurs approximately 8.3 km from the active crater of Calbuco and the river then flows as a single channel for a further 6 km until it reaches Lago Llanquihue. The entire catchment of the Rio Tepu was mantled by tephra owing to its position to the NE of the active crater of Calbuco, with visible steaming in the bottom left of Figure 2.13 indicating the presence of PDC deposits. Fine-grained light grey tephra deposits are visible in the upper catchment during ongoing eruptive activity on the 24th April 2015 (Fig. 2.13), but were not preserved until the field study in June 2015.

Figures 2.14A & 2.14B are both aerial images facing upstream towards the upper edifice of Calbuco within the eastern and western channels of the Rio Tepu respectively. Leveed lava flow deposits created during the 1961 eruption of Calbuco (Fig. 2.14B) form the head of the eastern channel (a lobe of this deposit also forms the head of the Rio Frio in the Blanco Este catchment) and this channel displays no visual evidence of PDC transit during the eruption (Fig. 2.14B). Conversely, complete stripping of vegetation within the western channel is indicative of PDC transit (Fig. 2.14A). Figures 2.14C & 2.14D display aerial views looking downstream within the catchment and also illustrate the mantling of the catchment with coarse tephra as well as evidence of streamflow in both the eastern and western channels. The collapsed roofs of structures located in the elevated region between the two channels are evidence of the impacts of the tephra deposits within the catchment (Fig. 2.14D). The structures affected in Figure 2.14D are the highest altitude man-made structures in the catchment (≈430 masl), and most proximal to the active crater.

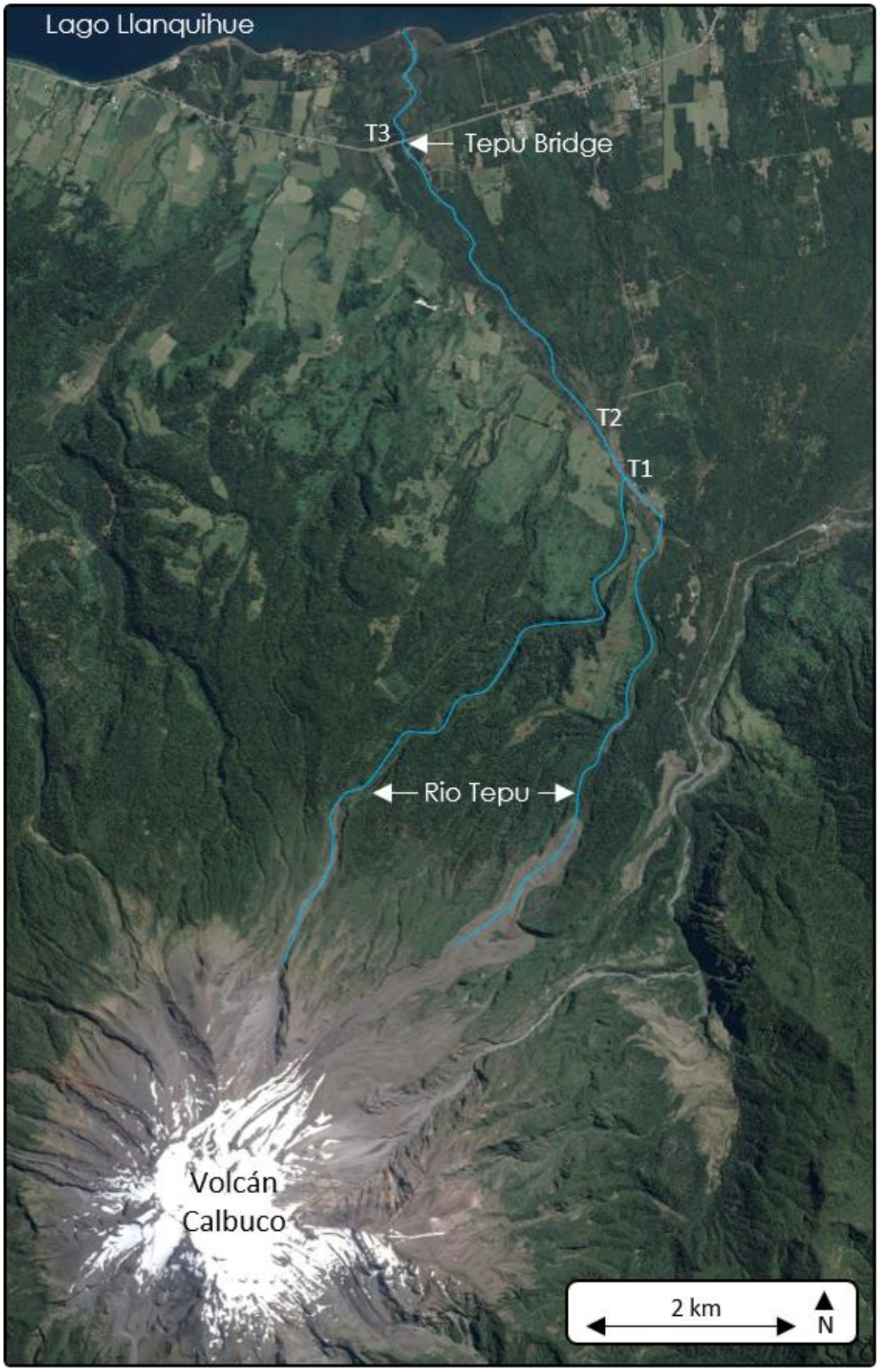

Figure 2.12: Location map of the Rio Tepu catchment and the northern flanks of Calbuco Volcano. Highlighted are contributing channels, field site locations and notable local infrastructure (GoogleEarth, 2016).

Figure 2.13: Aerial Image taken on April 24th 2015 during ongoing eruptive activity displaying the condition of the upper part of the Rio Tepu catchment (SERNAGEOMIN, 2015).

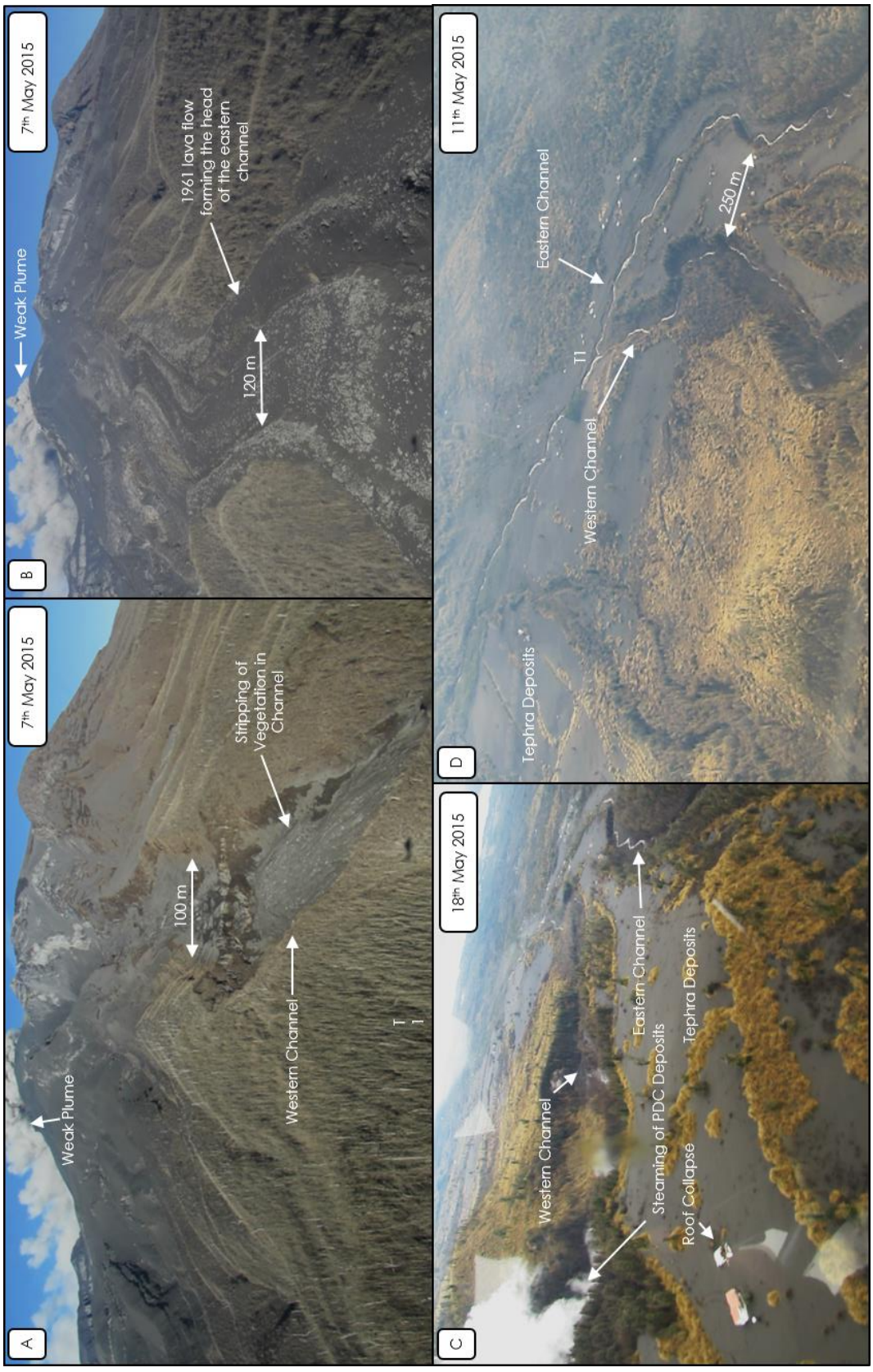

Figure 2.14: Aerial images taken in May 2015 highlighting the post-eruption conditions of the upper catchment of the Rio Tepu (SERNAGEOMIN, 2015).

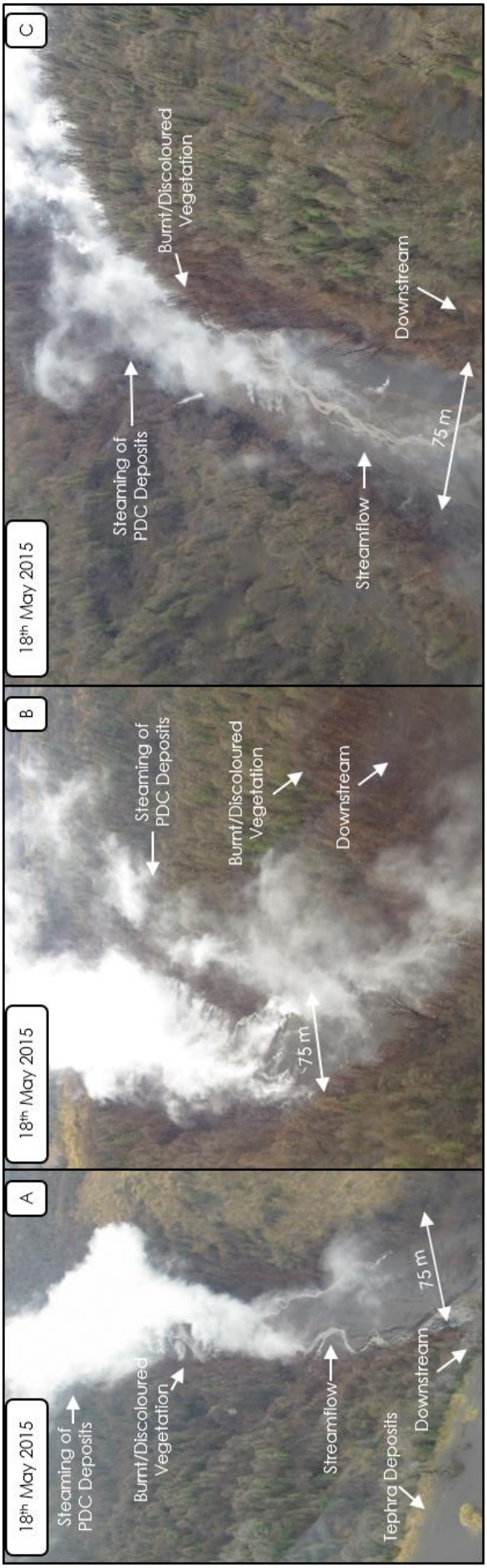

Figure 2.15: Aerial images taken on the 18th May 2015 highlighting the steaming of Pyroclastic Density Current (PDC) deposits in the Western channel of the Rio Tepu and the impacts of these PDCs upon channel vegetation (SERNAGEOMIN, 2015).

Figure 2.15 displays aerial images taken on the 18th May 2015 focused upon the steaming of PDC deposits, permanent streamflow, vegetation removal and lateral vegetation discolouration in the western channel of the Rio Tepu. The approximate downstream extent (41°16'40"S, 72°34'12"W, 280 masl) of steaming and vegetation discolouration in the Western Channel is 7 km downstream of the active crater and 1.3 km upstream of the confluence of the western and eastern channels. Conversely there is no visible steaming in the eastern channel, this is due to the diversion of PDCs in this area down the eastern lobe of the 1961 lava flow deposits, along the Rio Frio and into the Rio Blanco Este. Visible streamflow in Figs. 2.14D & 2.15 illustrates the erosion of PDC deposits in the western channel of the Rio Tepu. These deposits are valley confined and less voluminous than those in the Blanco Este, however the 7 km PDC runout length still provides the potential for remobilisation.

Figures 2.16A & 2.16B display the condition of the eastern channel of the Rio Tepu at field site T1 just upstream of the confluence between the eastern and western channels (Fig. 2.12). Figure 2.16A displays undisturbed tephra-draped terraces approximately 20 cm above the current water level, indicating a lack of any large rain-triggered lahars before June 15th 2015 in the Eastern channel of the Rio Tepu. The lack of damage to the bridge at T1 (bridge support visible in Figure 2.16A) also indicates a lack of significant rain-triggered lahar activity. This bridge was the furthest accessible upstream site in the eastern channel of the Rio Tepu during the field visit in June 2015. At site T2 located immediately downstream of the confluence of the eastern and western channels, flow discharge was increased (Figs. 2.16D & 2.16E) relative to that seen at site T1 (Figs. 2.16A & 2.16B) due to the addition of streamflow from the western channel (Fig 2.16). However, there were still undisturbed bankside tephra terraces 50 cm

above the current water level indicating that no large rain-triggered lahars had occurred in the western channel despite the upstream PDC deposits and the potential for their remobilisation (Fig. 2.15). Flow turbulence is also increased at site T2 (Fig. 2.16D), but there had been no damage to the bridge at this location (Fig. 2.16E).

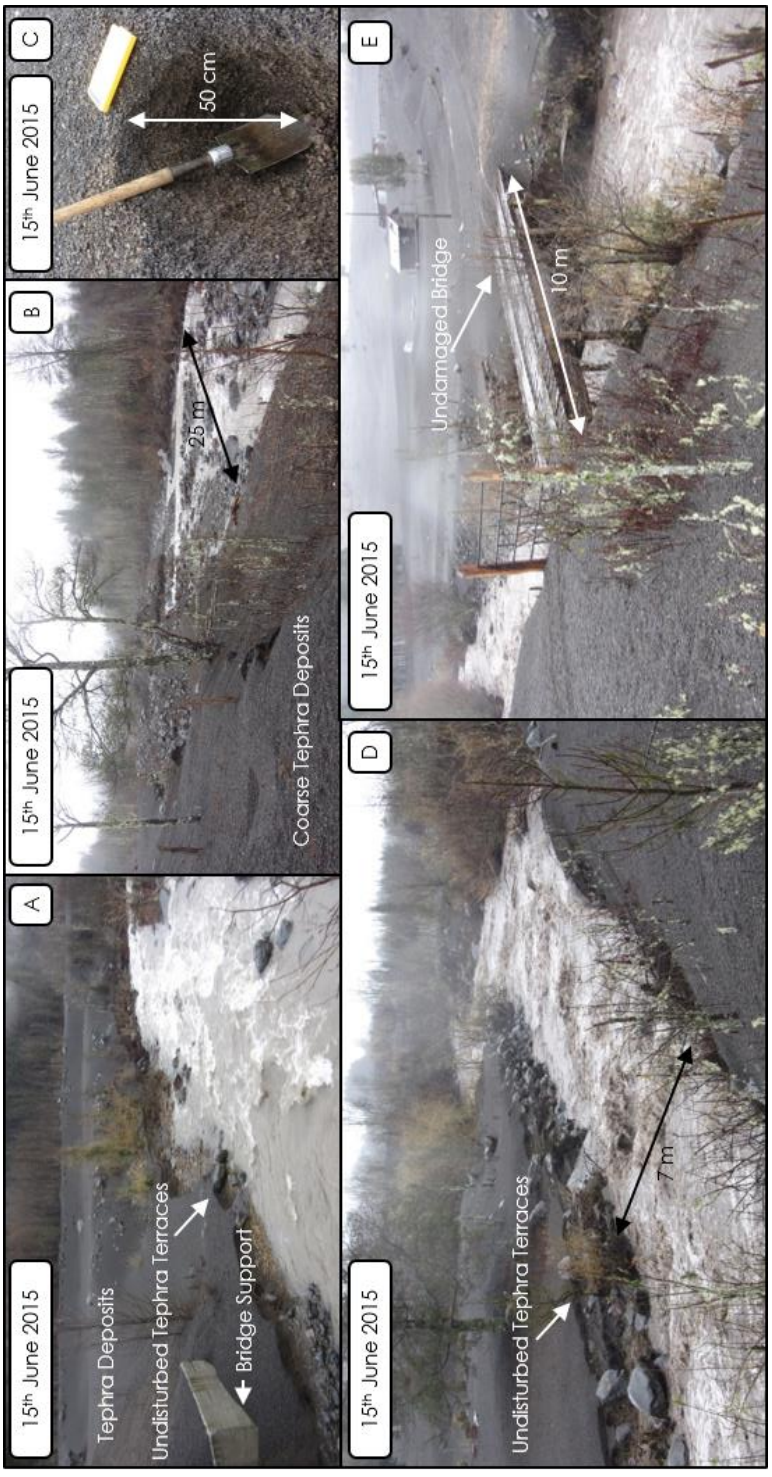

Figure 2.16: Images illustrating the condition of the Rio Tepu at field sites T1 (A-C) and T2 (D-E) on 15th June 2015.

Tephra deposits at site T1 (Fig. 2.16C) were approximately 50 cm thick and consisted of light brown pumice-rich coarse lapilli at the base, which darkens and becomes less vesicular upwards, as identified in the adjacent Blanco Este catchment (Fig. 2.5). As in the Blanco Este, in early post-eruption aerial footage (Fig. 2.13) there is a surface layer of fine-grained light-grey tephra mantling the topography of the Rio Tepu catchment but this was no longer present in June 2015. Further downstream in the Rio Tepu, Figure 2.17B shows the highway bridge linking Puerto Varas and Ensenada near the mouth of the river at site T3. During the field visit in June 2015 this area was continually excavated in order to maintain clearance at the bridge and prevent inundation of the road and surrounding area. The aggradation prompting this excavation was due to the transport and deposition of lapilli and finer material. This gradual aggradation in the downstream reaches of the Rio Tepu is indicative of the transport of pyroclastic material due to rain-triggered lahar activity but there was no evidence at site T3 that lahars had been of sufficient magnitude to cause lateral inundation outside of the primary channel. Ponding of water was evident in the region either side of the highway near site T3 but this was due to the rainfall saturation of tephra deposits in flat regions. Despite the coarse nature of the tephra deposits within the catchment, infiltration and interception rates were reduced across previously densely vegetated regions (Figs. 2.17A & 2.17C). Channel formation subsequently occurred at locations including roads (Fig. 2.17A – T2*)* and open areas where vegetation was buried (e.g. Fig. 2.17C - 41°14'18"S, 72°32'28"W, 107 masl).

Figure 2.17: Images displaying post-eruption conditions at field sites T2 (A) and T3 (B) in June 2015 as well as surface streamflow in other previously vegetated regions (C) of the Rio Tepu catchment.

2.3.3. Rio Sur

The catchment of the Rio Sur (Fig. 2.18) on the north-western flanks of Calbuco was not impacted by tephra deposits to the same degree as the Rio Tepu and the Rio Blanco Este. This is a product of the prevalent wind direction during the eruption, with only the extreme upper catchment (Fig. 2.19) of the Rio Sur significantly affected by airfall deposits. Figures 2.19 & 2.20 display evidence of the stripping and discolouration of vegetation in the contributing channels of the Rio Sur in the area upstream of the college location (Fig. 2.18). This discolouration and stripping of vegetation (e.g. Figs. 2.20B & 2.20E) suggests PDC transit in both the northern and southern channels, whilst further downstream

intermittent vegetation removal with a lack of vegetation discolouration (e.g. Figs. 2.20A, 2.20C & 2.20D) is indicative of primary lahar occurrence.

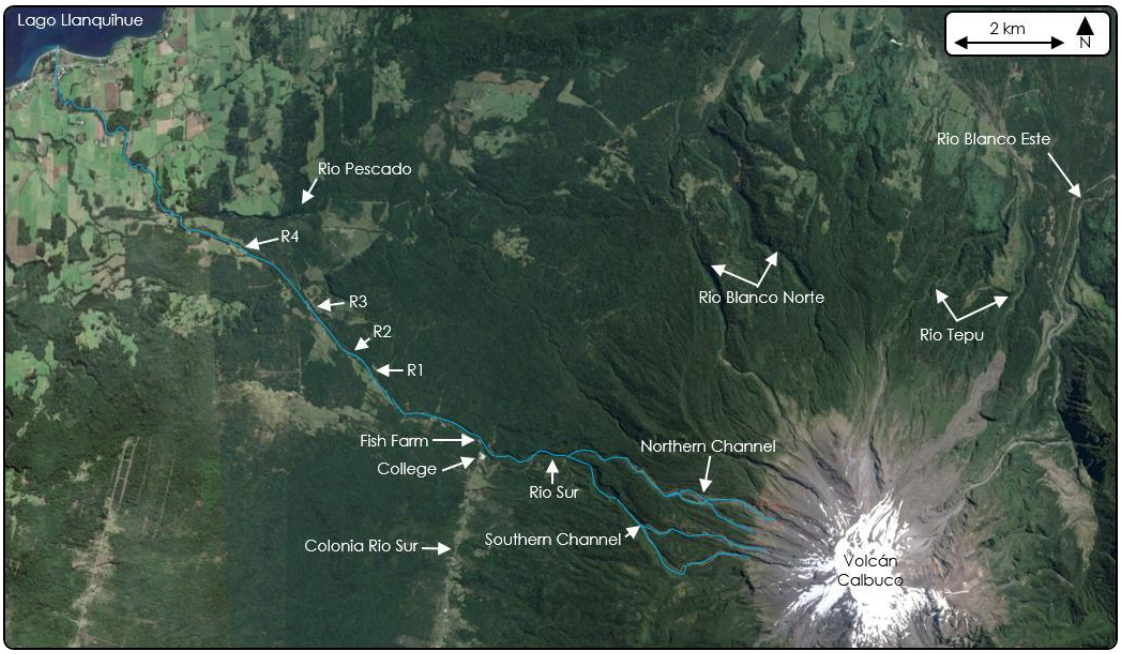

Figure 2.18: Location map of the Rio Sur catchment and the northwestern flanks of Calbuco Volcano. Highlighted are contributing channels, field site locations and notable local infrastructure (GoogleEarth, 2016).

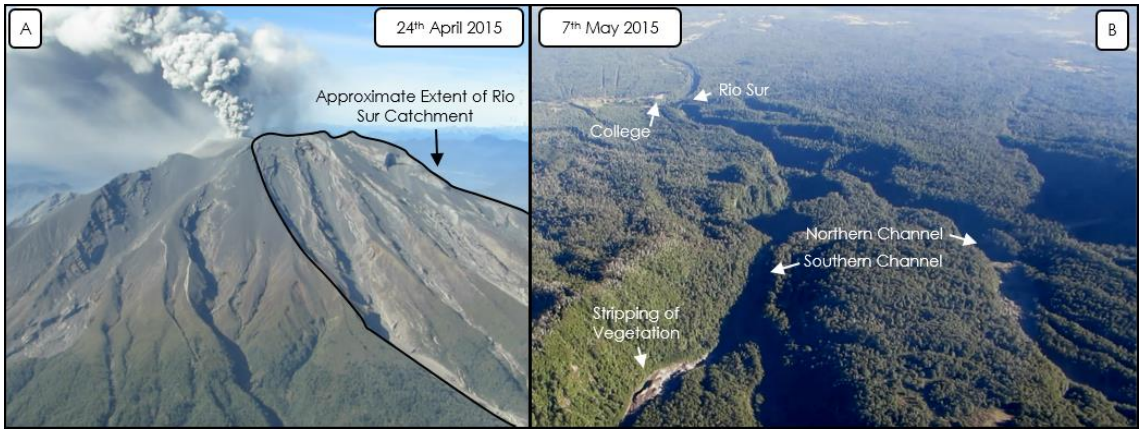

Figure 2.19: Images displaying post-eruption conditions in the upper Rio Sur. A: Delineation of the upper catchment of the Rio Sur in an aerial image taken during ongoing eruptive activity on 24th April 2015 (SERNAGEOMIN, 2015). B: Downstream view of the Rio Sur illustrating the contributing channels of the upper catchment and their confluence near the annotated college location (SERNAGEOMIN, 2015).

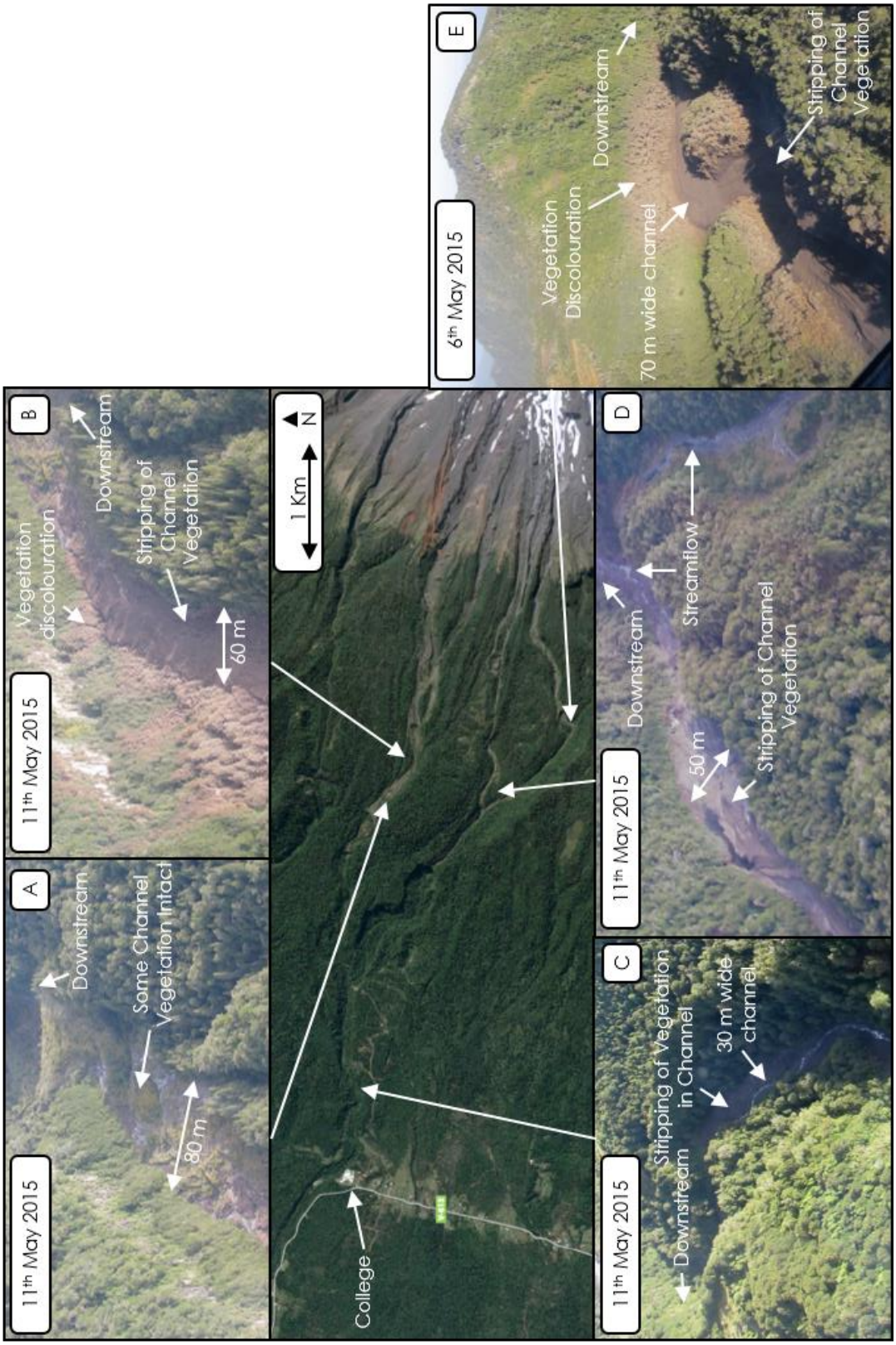

Figure 2.20: Aerial Images of the northern and southern contributing channels of the Rio Sur taken in May 2015 illustrating the occurrence of Pyroclastic Density Currents (PDCs) and primary lahars within the catchment. A central inset satellite image indicates the location of each surrounding aerial photograph (SERNAGEOMIN, 2015; GoogleEarth, 2016).

Figure 2.21 displays the conditions at field site S1 (Fig. 2.18*J* in June 2015 and indicates the destruction of a bridge (9.6 km downstream of the crater) and the emplacement of primary lahar deposits, which have been heavily excavated to prevent flooding. These deposits are characterised by their massive nature, featuring entrained vegetation, damaged material from an upstream fish farm facility and boulders up to 5 m in diameter. Figures 2.21A, 2.21B & 2.21F show excavated terraces of lahar deposits either side of a main channel, whilst immediately upstream of site S1 the channel is less confined (Fig. 2.21E). Fine-grained deposits are present on top of inundated bank regions which have not been covered in excavated material. These fine-grained surfaces triggered ponding and streamflow behind the man-made terraces during periods of rainfall (Fig. 2.21D). Figure 2.21D also displays damaged and transported fish farm equipment from the upstream fish farm facility highlighted in Figure 2.18. A modified shipping container has been mobilised and deposited on top of boulder-rich lahar deposits at this location (Fig. 2.21E). Isolated trees are still standing within the inundated region immediately upstream of site R1 but the majority of the previously dense vegetation proximal to the central channel has been destroyed or buried (Fig. 2.21E). Moss had been stripped from banks, with approximately 2 m of moss stripping above the water level at the time of the field visit (Fig. 2.21C). On 13th-16th June 2015 there was intermittent intense rainfall (Fig. 2.11) and flow discharge and sediment concentration was heightened at site S1 compared to subsequent visits during dry periods. During heavy rainfall boulders with diameters of up to approximately 1 m could be seen and heard rolling within the central channel.

The conditions at site S2 (10.6 km downstream of the crater) in the Rio Sur in June 2015 can be seen in Figure 2.22 and in common with site S1 include the

extensive excavation of lahar deposits in an attempt to channelize streamflow and/or subsequent lahars. Site S2 is also the site of a bridge destroyed by primary lahars as well as large levees constructed of excavated lahar deposits either side of a central channel with a variable width of 5-10 m (Fig. 2.22). There is evidence of felled trees and other vegetation amongst the excavated deposits (Fig. 2.22A), whilst boulders deposited at S2 feature a mixture of sizes up to a maximum diameter of 3 m (Fig. 2.22D). There is no evidence of inundation of the road at S2 which runs adjacent to the river (Fig. 2.22C), although 200 m downstream of S2 there was a partial road collapse due to undercutting by bank erosion. The reduced extent of primary lahar damage at sites S1 and S2 relative to that displayed in Figure 2.20 indicate rapid attenuation of the primary lahar in the Rio Sur with distance downstream. Figure 2.23 shows site S2 at approximately 24 hour intervals over a 6-day period in June 2015 and displays small and gradual fluctuation in flow discharge and sediment concentration. During a period of intense rainfall on 16th June 2015 flow discharge is heightened and has a visibly higher sediment concentration (Fig. 2.23A). In June 2015 this type of gradual fluctuation in flow discharge and sediment concentration appears to be the dominant response mechanism to heightened rainfall as opposed to discreet pulses of rain-triggered lahar activity.

Figure 2.24A displays the collapse of the Puente Zapatero at site S3 (11.2 km downstream of the crater) due to primary lahar activity in the Rio Sur. The ongoing repair work can be seen in an aerial image (Fig. 2.24B) taken on 18th May 2015 and by the field visit in June the replacement bridge was fully operational. In addition to destroying the road bridge, the primary lahar partially inundated a small-scale fish farm facility at this location (Fig. 2.24D). Figures 2.24E & 2.24F display the view downstream and upstream respectively from the

reconstructed bridge. Downstream there are visible mud marks on surviving trees at a height of 3.5-4 m above the current water level. The outside bank has been eroded and undercut both upstream and downstream of the bridge, with bank vegetation removed up to a height of 2 m above the water level. Lahar deposits have been emplaced on inundated regions of the inside bank, although similar to other sites in the Rio Sur these deposits had been heavily excavated prior to June 2015.

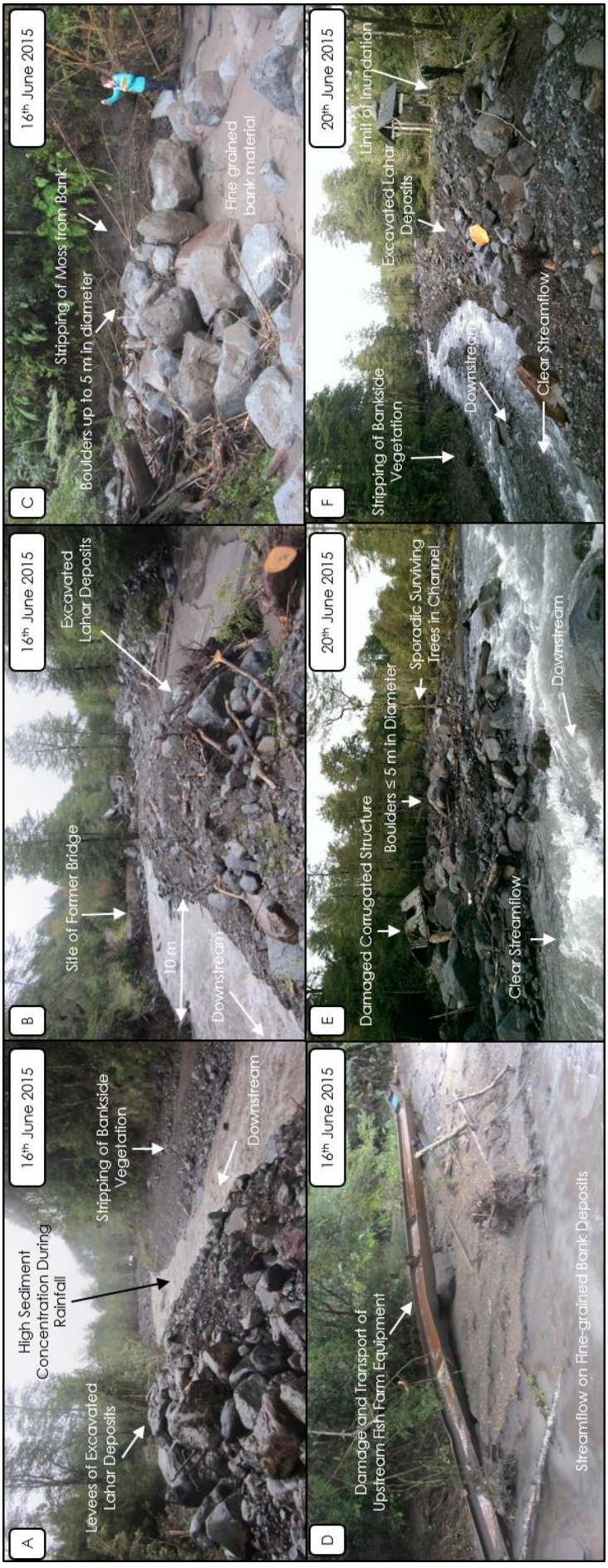

Figure 2.21: Images illustrating the conditions at field site S1 in June 2015 and the associated impacts of the primary lahars generated during the April 2015 eruption.

Figure 2.22: Images illustrating the conditions at field site S2 in June 2015 and the associated impacts of the primary lahars generated during the April 2015 eruption.

At site S4 (13.2 km downstream of the crater), the "Puente Pescado", muddy splash marks were visible on the bridge 1.5 m above the water level in June 2015 (Fig. 2.25B). There was damage to fencing at the channel margins due to undercutting of the banks, with deposits at R4 featuring a wide range of grain sizes with boulders ≤1 m in diameter. A sediment fan at the mouth of the Rio Sur (19.8 km downstream of the crater) is visible in an aerial image taken on 6th May 2015 (Fig. 2.26). Due to the lack of airfall deposits in much of the catchment this sediment fan is a product of primary lahar activity in the catchment and the subsequent remobilisation of pyroclastic material throughout the length of the drainage. The material which reached this sediment fan at the mouth of the Rio Sur is largely fine-grained in nature, with the deposition of larger material evident at sites S1-S4.

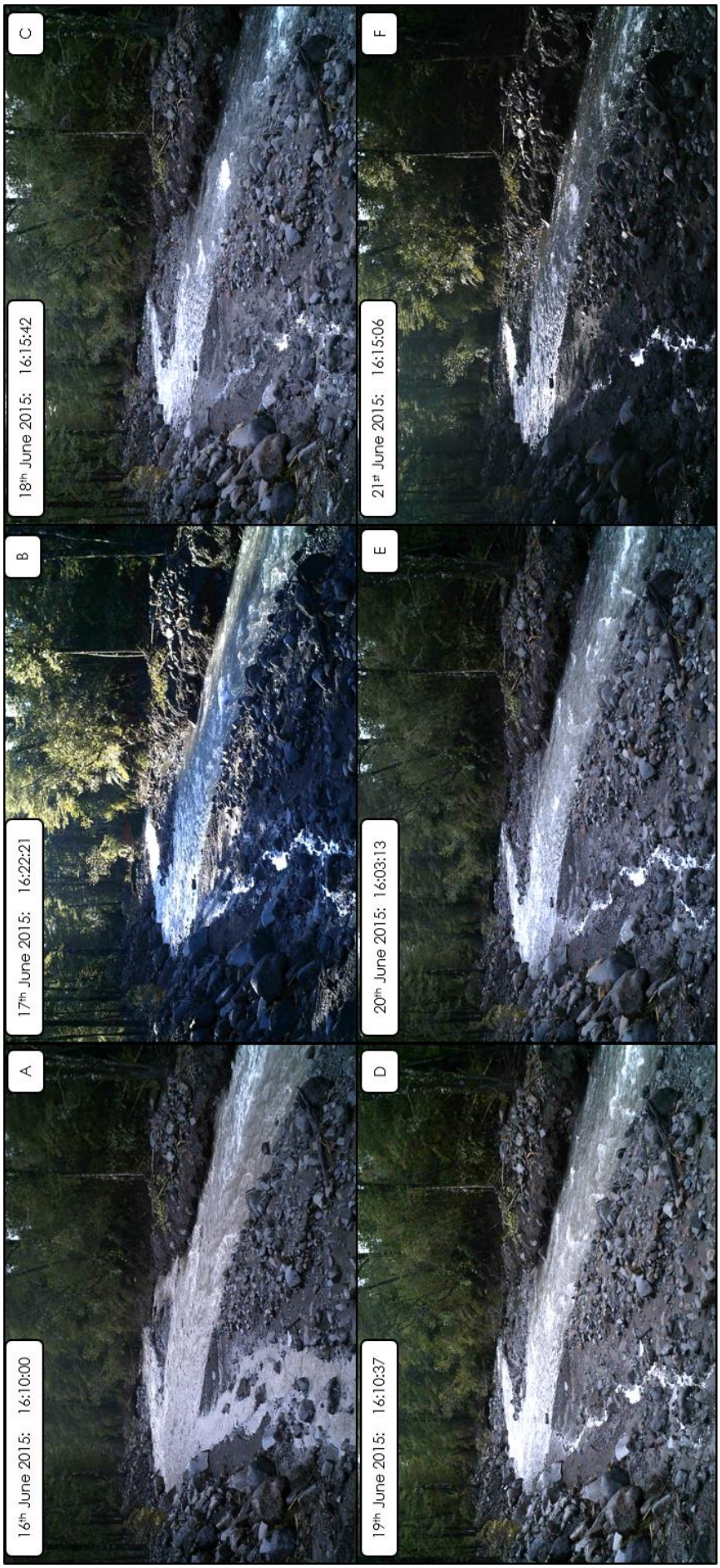

Figure 2.23: Time-lapse images (downstream view) taken at field site S2 over a 5-day period in June 2015.

Figure 2.24: Images displaying the post-eruption conditions at field site S3 taken in the days following the passage of primary lahars (A), during the reconstruction of the Puente Zapatero in Mid-May 2015 (B) and during the field visit in June 2015 (C-F) (SERNAGEOMIN, 2015).

The Rio Sur catchment experienced PDCs in both the Northern and Southern contributing channels upstream of the college location highlighted in Figure 2.18 and the transit of at least one large primary lahar (triggered by PDC-driven snow melt) throughout the course of the Rio Sur. This primary lahar destroyed several bridges and stripped vegetation within the valley to varying extents, with the magnitude of the impacts decreasing with distance downstream from the college location to the mouth of the river. Resultant deposits were extensively excavated in the weeks following the eruption in order to channelize the river after the primary lahar and to prevent flooding. In June

2015 the river showed subdued and gradual responses to rainfall, with only minor fluctuations in flow discharge despite the apparent volume of loose pyroclastic material in the upper reaches of the catchment.

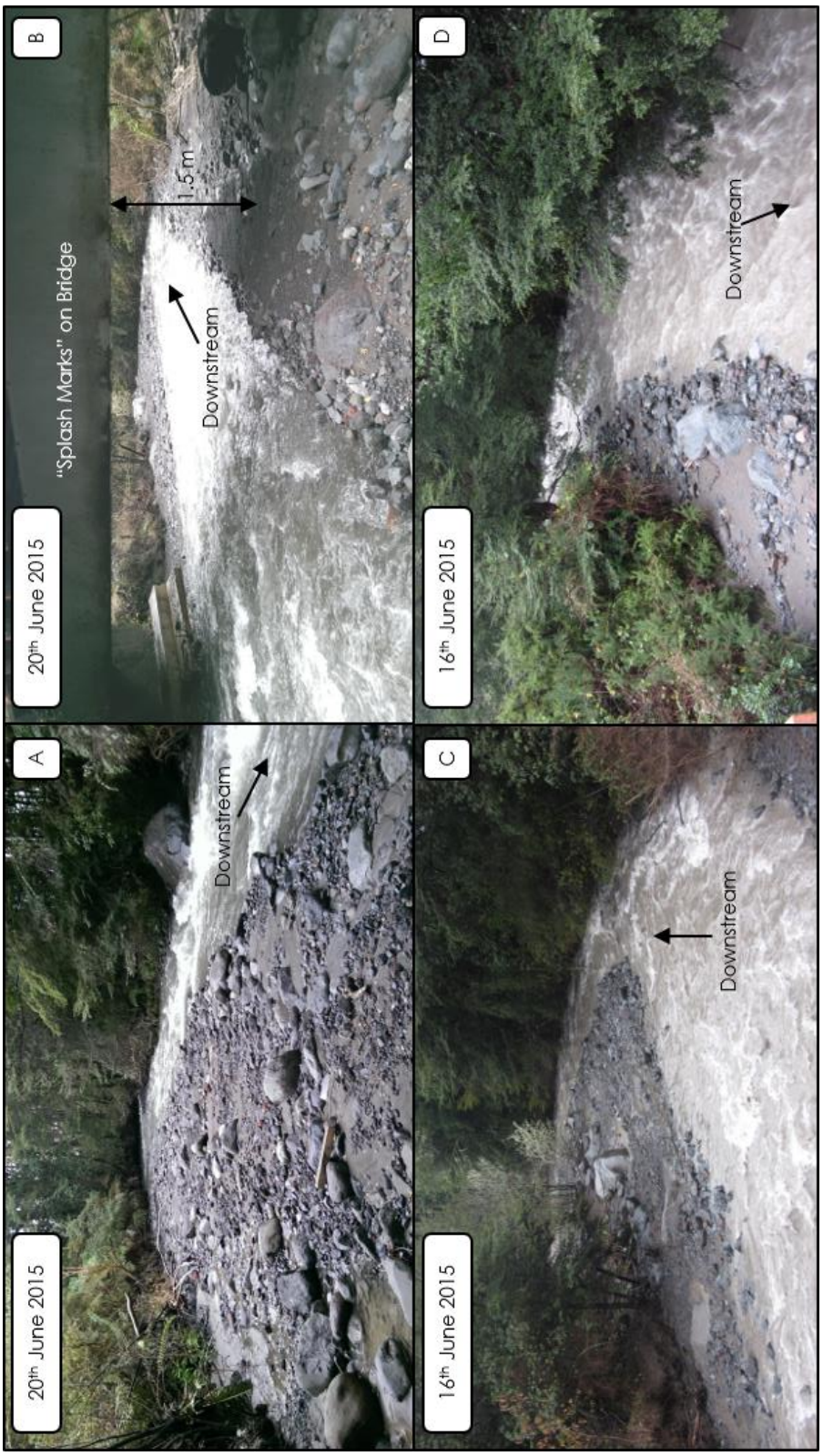

Figure 2.25: Images displaying the conditions at field site R4 (Puente Pescado) in June 2015.

Figure 2.26: Aerial image of the mouth of the Rio Sur on the 6th May 2015 demonstrating deposition of remobilised sediment (SERNAGEOMIN, 2015).

2.3.4. Southern Flanks

The Rio Blanco Sur, Rio Correntoso, Rio Colorado and Rio Este are the primary catchments located on the southern/southwestern flanks of Calbuco (Fig. 2.27). The Rio Correntoso flows into the Rio Chamiza and then west into the Reloncavi Sound east of Puerto Montt whilst the Rio Blanco Sur, Colorado (via the Blanco Sur) and Este all flow into Lago Chapo (Fig. 2.27). There were negligible tephra deposits across the southern flanks of the volcano due to the prevalent south-westerly wind direction during the eruption, however PDCs and primary lahars did affect the southern drainages.

Figure 2.27: Location map of the southern flanks of Calbuco Volcano. Highlighted are the various drainage networks, field site locations and notable local infrastructure (GoogleEarth, 2016).

2.3.5. Rio Blanco Sur

The furthest visible downstream extent of PDC deposits in the Rio Blanco Sur as a result of the April 2015 eruption of Calbuco was approximately 3.8 km downstream of the active crater (Fig. 2.28). Light-grey, steaming PDC deposits were visible in aerial images of the upper catchment in the days following the eruption (Fig. 2.29), whilst fluvial erosion of these deposits can be seen as early as the 24th April 2015 (Fig. 2.29D). There is no visible vegetation remaining in the area inundated by the PDCs, whilst vegetation in the regions adjacent to the flow are significantly discoloured (Fig. 2.29).

The Rio Blanco Sur was severely impacted by large primary lahars triggered by the interaction of partial column collapse PDCs with ice and snow. The furthest upstream evidence of these lahars can be seen at the visible downstream extent of the PDC deposits (Fig. 2.28). Primary lahars in the upper Blanco Sur have completely scoured the inundated area of the valley, resulting in the removal of all vegetation and the exposure of underlying lava flow deposits across a width of approximately 100 m (Fig. 2.28). The resultant channel surface was undulating due to the erosional capacity of the flows (Figs. 2.28 & 2.30). The primary lahars within the Blanco Sur passed over two large waterfalls (Figs. 2.30A & 2.30B), with the second waterfall (height of ≈30 m) approximately 3 km downstream of the furthest visible extent of the late-stage PDC deposits (Fig. 2.28). Throughout this 3 km sub-section of the Blanco Sur primary lahars maintained a straight path and consistent width and removed all vegetation and debris from within the channel.

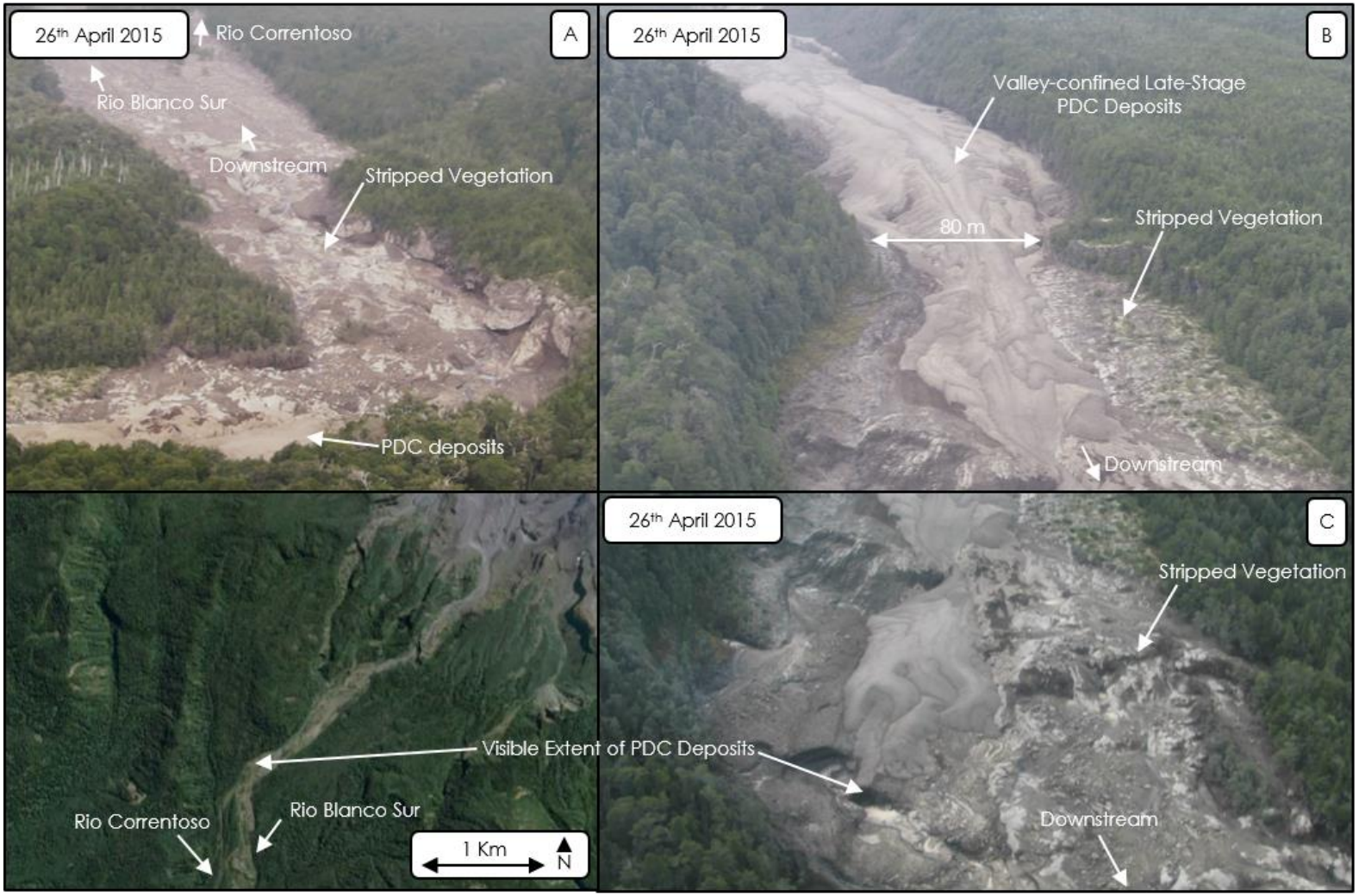

Figure 2.28: Aerial images taken on 26th April 2015 displaying the furthest visible downstream extent of Pyroclastic Density Current (PDC) deposits in the Blanco Sur. Inset satellite image displays the locations of A-C in the upper Rio Blanco Sur (Fig. 2.27) (SERNAGEOMIN, 2015).

The estimated flow width of the Blanco Sur primary lahar as it crossed the second waterfall at field site BS1 is 75 m (Figs. 2.31 & 2.32). 300 m downstream of this waterfall a major fish farm facility was inundated and destroyed (Figs. 2.31 & 2.32). Immediately upstream of the fish farm facility the flow split into two channels (Fig. 2.31A), with both channels continuing towards the settlement surrounding the Puente Blanco Sur at location BS2 (Fig. 2.27). Primary lahar deposits containing boulders with diameters of up to 5 m were present at the location of the destroyed fish farm, which features significant impact damage due to these boulders as well as almost complete inundation. This level of inundation of the fish farm structure indicates flow depths in excess of 7 m. Vegetation was completely removed within the primary channels at BS1, although the presence of the boulder-rich debris flow deposits (Fig. 2.32) rather than completely scoured surfaces (as seen upstream of BS1 in Figs. 2.28 & 2.30) demonstrates the effects of flow widening, decreasing channel gradient and turbulent dissipation of energy as flows passed over the waterfalls. At site A1 approximately 500 m downstream of the destroyed fish farm facility there is evidence of an avulsion from the western of the two Rio Blanco Sur lahar channels. The avulsed flow travelled in a south-westerly direction towards the Rio Correntoso (Fig. 2.27). After the eruption, levees were constructed along the western edge of the Rio Blanco Sur between sites BS1 and BS2 in an attempt to divert any future flows towards Lago Chapo via the primary Blanco Sur channels rather than towards the Rio Correntoso and Rio Chamiza via the course of the avulsion.

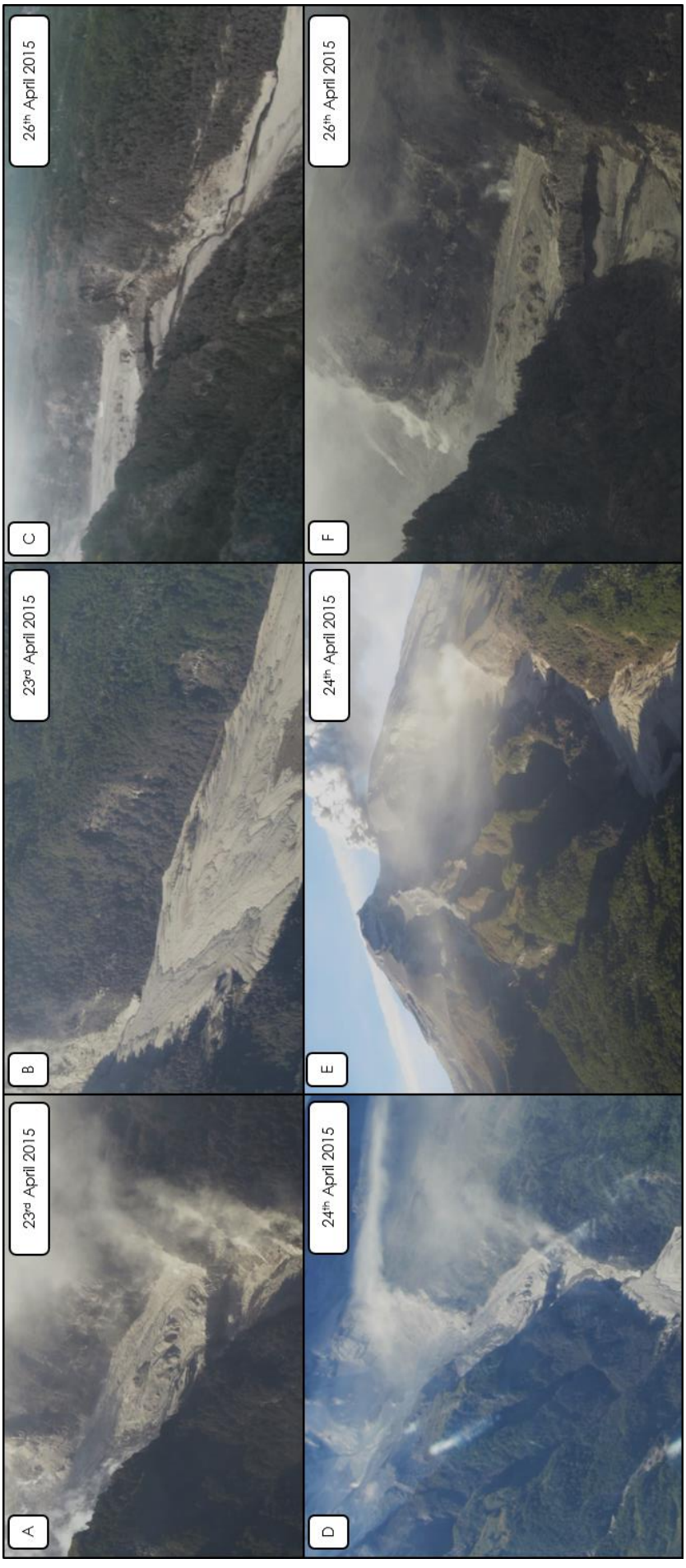

Figure 2.29: Aerial images taken on 23rd-26th April 2015 displaying the nature of the Pyroclastic Density Current (PDC) deposits in the Upper Rio Blanco Sur (SERNAGEOMIN, 2015). The width of the waterfall featured in A, C, D & F is approximately 175 m.

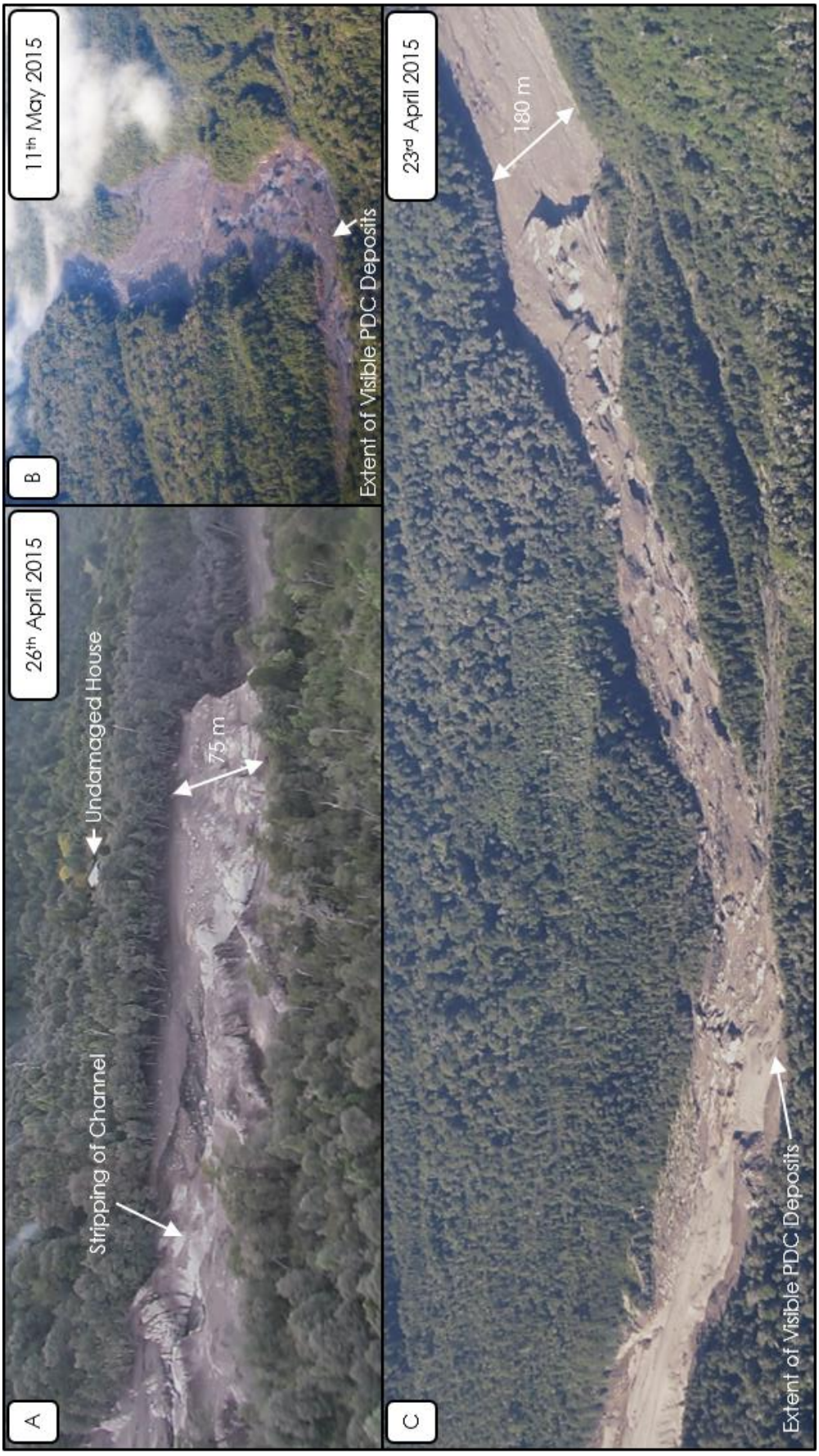

Figure 2.30: Aerial images displaying the condition of the Rio Blanco Sur downstream of the furthest visible downstream extent of Pyroclastic Density Current (PDC) deposits and upstream of site BE1. Evident is the stripping of vegetation and sediment downstream of the PDC deposits due to primary lahar transit (SERNAGEOMIN, 2015).

Figure 2.31: Aerial images taken on 23rd-26th April 2015 displaying primary lahar impacts in the vicinity of field site BS1 in the Blanco Sur and the destroyed fish farm facility (SERNAGEOMIN, 2015).

Figures 2.33 and 2.34A display the primary lahar impacts at site BS2, the location of the former Puente Blanco Sur. At this location several road bridges were destroyed, cutting off road links that connected the communities immediately to the east of the Rio Blanco Sur to the rest of Chile. The primary lahars became less channel confined and inundation was more widespread at site BS2, resulting in the inundation and destruction of houses and other structures in this region (Fig. 2.33). Boulders (≤2 m in diameter) were predominantly deposited in each of the three primary channels of the Blanco Sur at site BS2, with inundated inter-channel regions largely featuring fluvial and hyperconcentrated flow deposits (Fig. 2.33*)*. In these inundated inter-channel regions, the survival rate of vegetation was increased relative to the three primary channels where vegetation was extensively stripped and transported downstream (Fig. 2.33). In addition to vegetation transport, the main concrete structure of the primary road bridge at site BS2 was destroyed and transported over 100 m downstream (Fig. 2.34A).

Figures 2.34C & 2.34D display the primary lahar impacts at site BS3 located approximately 1.5 km downstream of BS2 at the eastern margin of the primary channels of the Blanco Sur, adjacent to the road link to Lago Chapo. At this location, massive to weakly horizontally stratified hyperconcentrated flow deposits are dominant, with the largest clasts being vesiculated, low-density juvenile bombs up to 0.2 m in diameter predominantly located at the flow margins. Deposits fine-upwards (Fig. 2.34D) and have buried but not destroyed fence posts and barbed wire fencing 0.5 m in height. Subsequent streamflow cut channels into these deposits and vegetation was inundated but predominantly still intact. Inundation marks on tree trunks were present 2.75 m above the base of the deposits.

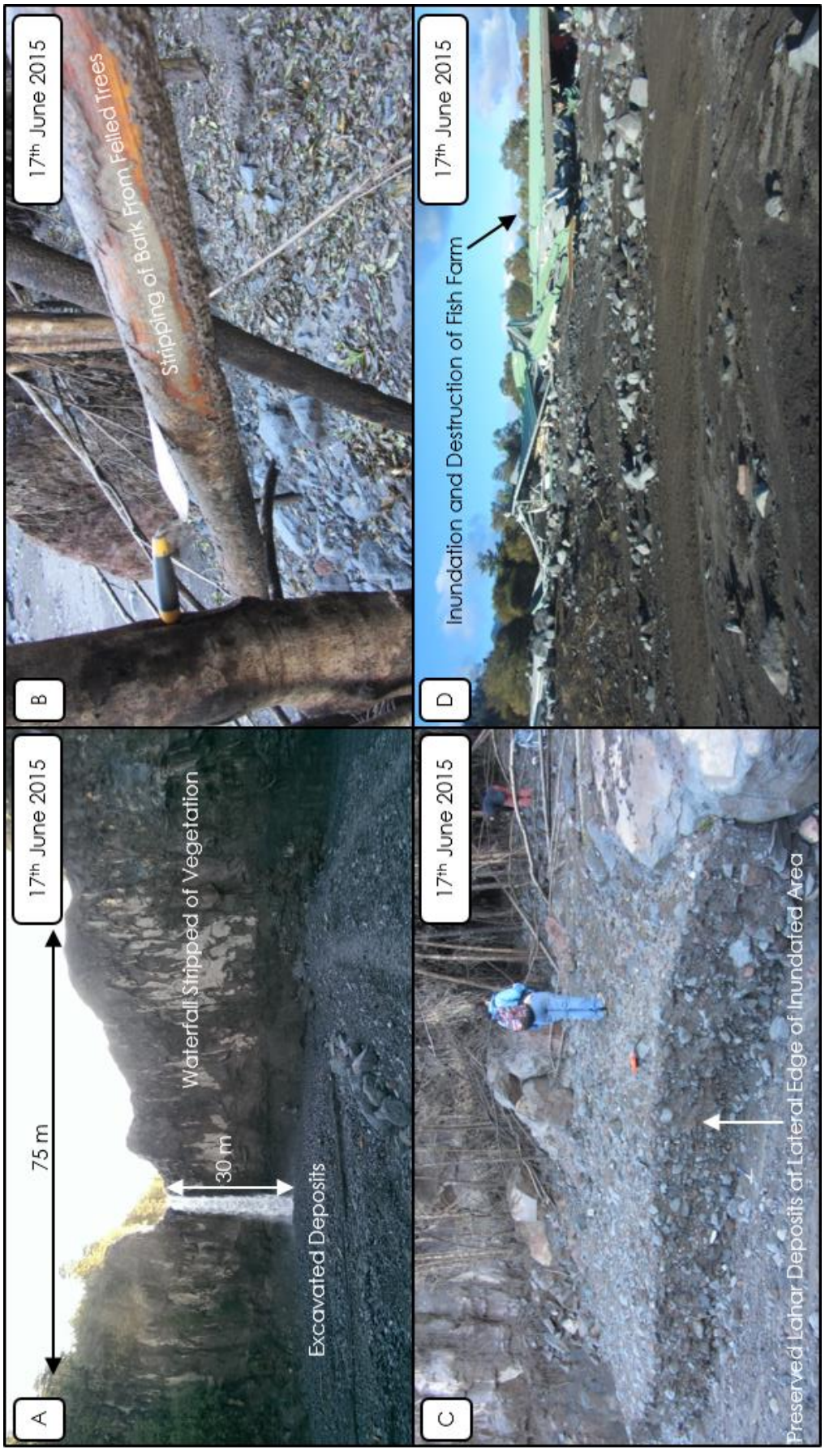

Figure 2.32: Images taken at field site BS1 illustrating the impacts of primary lahar inundation of a large waterfall (A), deposits at the waterfall base (B-C) and the destruction of the fish farm facility (D) at this location.

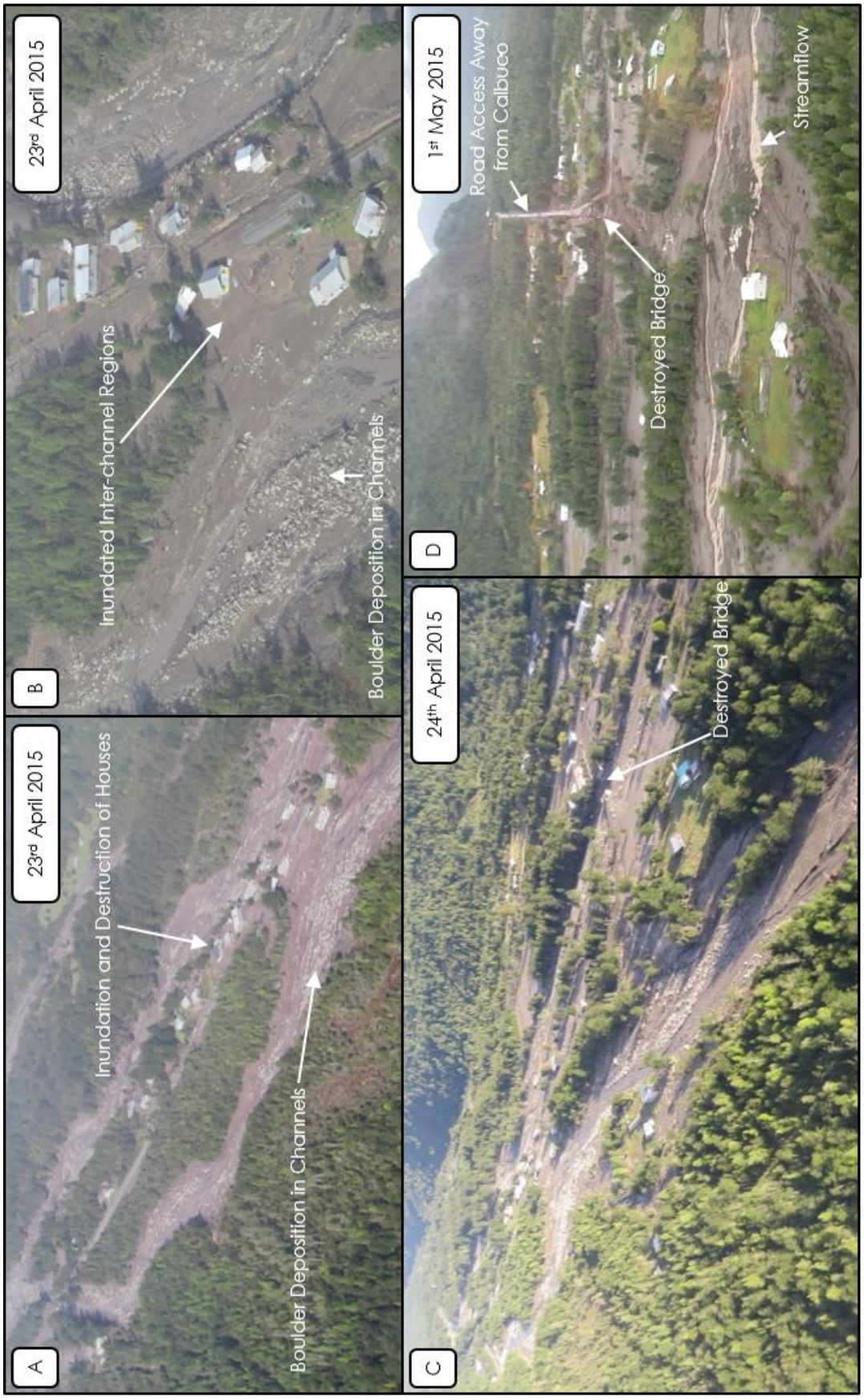

Figure 2.33: Aerial images taken between April 23rd 2015 and May 1st 2015 displaying the primary lahar impacts at field site BS2 (Puente Blanco Sur) including the inundation and destruction of structures in the village, cutting of transport links and variable removal of vegetation (SERNAGEOMIN, 2015).

Figure 2.34: Images taken in June 2015 at field sites BS2 (A+B) and BS3 (C+D) illustrating primary lahar impacts in the Blanco Sur.

Figure 2.35: Aerial images displaying locations near the mouth of the Rio Blanco Sur in the days following the Blanco Sur primary lahars (SERNAGEOMIN, 2015). A & C: Lago Chapo. B & D: The Chamiza Barrier. E: Pre-eruption Google Earth image displaying the characteristics of the Chamiza Barrier location prior to primary lahar inundation (GoogleEarth, 2016).

The furthest downstream extent of the Rio Blanco Sur is the confluence of the river with the Rio Chamiza and Lago Chapo near the Chamiza barrier (Fig. 2.35). Fig. 2.35E uses a satellite image to illustrate the pre-eruption purpose of the Chamiza barrier, to prevent water from the Rio Blanco Sur from flowing down the Rio Chamiza in an uncontrolled manner but instead diverting it into Lago Chapo. The primary lahars of the Rio Blanco Sur resulted in the complete sedimentation of the barrier region with largely fine-grained deposits (Figs. 2.35B & 2.35D). The filling of this region with sediment has resulted in both the westward overtopping of the barrier (enabling lahars to travel down the Rio Chamiza) and the creation of a delta at the confluence with Lago Chapo *(*Figs. 2.35A & 2.35C), which increased in size with time following the eruption.

2.3.6. Rio Correntoso

The Rio Correntoso begins as a distributary of the Rio Blanco Sur at a location several hundred metres downstream of the furthest visible downstream extent of PDC deposits (Fig. 2.28A). There is no evidence of PDCs reaching the Rio Correntoso, however due to the bifurcated nature of the channel at this location any significant lahar activity triggered by PDC transit in the Rio Blanco Sur also impacted the Rio Correntoso. Therefore, the river was affected by the ice and snow melt-triggered primary lahars created by PDCs in the Rio Blanco Sur. In the upper Rio Correntoso (300 m downstream of source) there is evidence of complete stripping of vegetation within the primary channel, but no extensive lateral inundation outside of this primary channel (Fig. 2.36A). This is echoed further downstream at site C1 (Puente Chingue), a location immediately upstream of the confluence of the Rio Correntoso and the avulsion from the

Blanco Sur, which featured stripping of vegetation across a 10 m wide channel (Fig. 2.37A). There is damage to corrugated iron bankside structures at site C1 (Figs. 2.36A & 2.36B), but no evidence of widespread lateral inundation outside of the channel and the Puente Chingue itself (3 m clearance) suffered minimal damage. Significant lateral inundation and spatially variable destruction of bankside vegetation becomes visible downstream of site C1 at two locations (Fig. 2.36C & 2.36D) between the confluence of the Rio Correntoso with the avulsion from the Rio Blanco Sur and site C2 (Puente Correntoso). These deposits suggest the presence of larger flows in the Rio Correntoso downstream of the confluence with the avulsion from the Blanco Sur.

At site C2 (Puente Correntoso) the road bridge was inundated but not destroyed, with deposits spread over an approximately 40 m wide area (Figs. 2.36E, 2.37C & 2.37D). Lahar deposits at C2 had been heavily excavated prior to the field visit in June 2015 in order to channelize streamflow, and the constructed levees featured boulders of diameters up to 2 m. Few trees remained standing within the inundated area to the upstream side of the bridge (Fig. 2.37C), with extensive vegetation being deposited underneath and alongside the bridge. The vegetation survival rate increased within inundated regions immediately downstream of the bridge location (Fig. 2.36E). Channelized lahar deposits and the removal of channel vegetation were visible at the confluence of the Rio Correntoso and Rio Chamiza (Fig. 2.36F), illustrating the extent of primary lahar transit in the Rio Correntoso. At the confluence of the two rivers both boulders and large pieces of vegetation were deposited. The Rio Chamiza contains a high concentration of sediment both upstream and downstream of the confluence, likely as a result of the upstream addition of lahar material from the Rio Blanco Sur at the Chamiza barrier location.

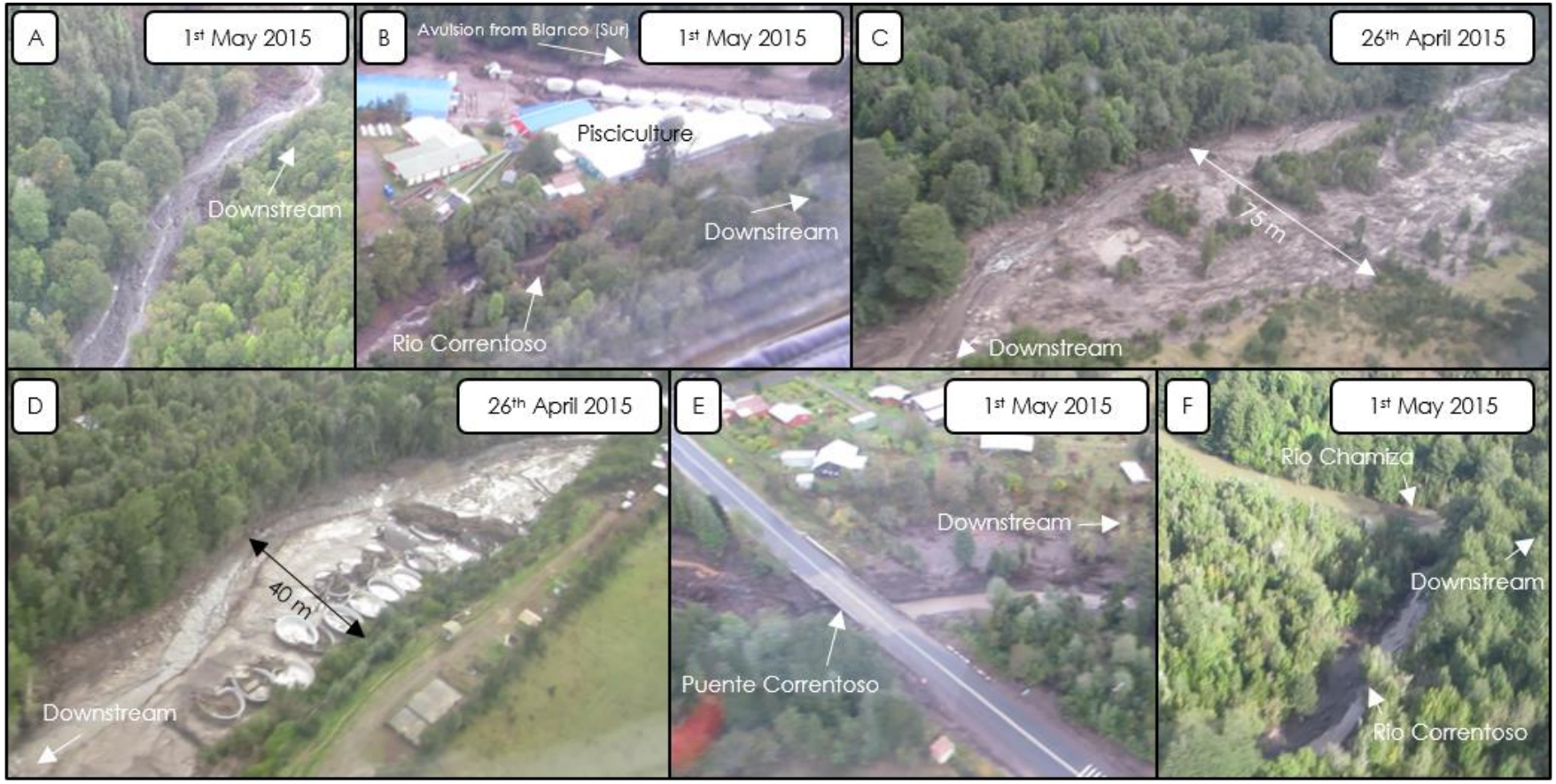

Figure 2.36: Aerial images displaying the primary lahar impacts in the Rio Correntoso with increasing distance downstream (SERNAGEOMIN, 2015). A: 300 m downstream of the divergence from the Rio Blanco Sur. B: Field site C1 (Puente Chingue) and the confluence with the avulsion from the Blanco Sur. C & D: Downstream of the confluence with the avulsion of the Blanco Sur and upstream of the Puente Correntoso. E: Field site C2 (Puente Correntoso). F: Confluence of the Rio Correntoso and Rio Chamiza.

Figure 2.37: Images displaying the primary lahar impacts and conditions at field sites in the Rio Correntoso in June 2015. A & B: Site C1 (Puente Chingue). C & D: Site C2 (Puente Correntoso).

2.3.7. Avulsion: Rio Blanco Sur – Rio Correntoso

The source of the avulsion from the Blanco Sur at site A1 (Figs. 2.38A & 2.39) featured spatially variable removal and burial of vegetation, deposition of boulders ≤3 m in diameter and inundation of an area >50 m wide. An incised central channel with variable depths of up to 4 m was present in the middle of the inundated area at site A1 (Fig. 2.39D), whilst bark was stripped from trees at a height of 4 m above the lahar deposit surface (Fig. 2.39B). In addition to the deposition of boulders and other pyroclastic material, objects from the upstream destroyed fish farm in the Blanco Sur and road barriers were deposited at site A1 throughout the inundated area. Boulders were predominantly distributed in the central region of the inundated area, with lateral regions displaying surface deposits characterised by the fining upwards of material and an absence of large (>5 cm) lithics (Fig. 2.39A). These lateral deposits had weak stratification defined by thin horizontal beds and are indicative of hyperconcentrated flow deposits (Vallance and Iverson, 2015). They were often located above massive, unsorted material containing boulders up to 3 m in diameter characteristic of debris flow deposition (Vallance and Iverson, 2015). The percentage of surviving vegetation in the inundated area increases with distance from the avulsion source as the flows become more channelized and confined (Fig. 2.38A).

Figure 2.38: Aerial images illustrating the impacts of the primary lahar avulsion from the Rio Blanco Sur – Rio Correntoso with increased distance downstream (SERNAGEOMIN, 2015). A: A1 – Avulsion Source. B & C: Conditions between field sites A1 and A2. D: A2 – Road Crossing 2. E: A3 – Road Crossing 1 and the confluence with the Rio Correntoso near a fish farm facility.

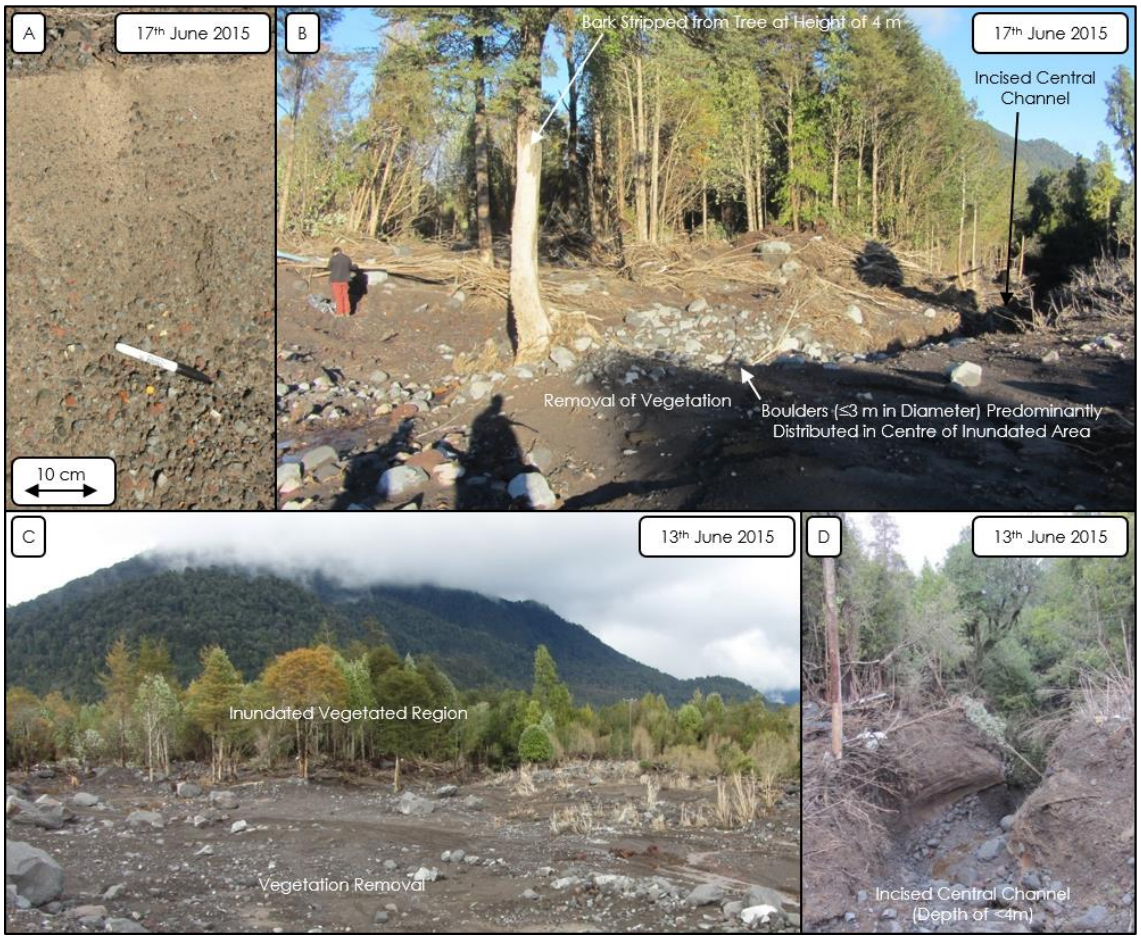

Figure 2.39: Images taken in June 2015 displaying the conditions at field site A1, the source region of the primary lahar avulsion from the Blanco Sur.

The avulsing lahar initially developed into at least two primary channels (Fig. 2.38C), which then merged into a single channel before twice crossing and inundating the road link between the communities of northern Lago Chapo and the rest of Chile. Lahar deposits at sites A2 (Figs. 2.40A-C) and A3 (Fig. 2.40D) had been heavily excavated prior to June 2015 (Figs. 2.39 & 2.40) in order to channelize subsequent streamflow or lahars and restore channel capacity, but aerial footage taken after the eruption helps to examine the post-lahar conditions at sites A2 (Fig. 2.38D) and A3 (Fig. 2.38E). As with the primary lahars in the Blanco Sur the avulsion flows completely stripped vegetation within the channels and deposited boulders with diameters ≤2 m at both of the road crossings (A2 & A3) (Fig. 2.40). Vegetation was removed across a variable width

of 20-40 m at both sites A2 and A3 (Figs. 2.38D, 2.38E & 2.40). Despite a lack of streamflow at site A1 (Fig. 2.39), there is permanent streamflow at sites A2 (Fig. 2.40B) and A3 (Fig. 2.40C) in June 2015. After the passage of the avulsion across the road at site A3 it inundated another fish farm facility, causing damage but not complete destruction, before joining the Rio Correntoso (Fig. 2.38E).

Figure 2.40: Images taken in June 2015 displaying the post-lahar conditions at two locations where the avulsed lahar from the Blanco Sur crossed the primary road linking the communities of northern Lago Chapo to the rest of Chile. A-C: Site A2. D: Site A3.

2.3.8. Rio Colorado

There is evidence of primary lahar activity in the Rio Colorado and the transition of these flows from erosive debris flows towards depositional hyperconcentrated flows with increased distance downstream (Fig. 2.41). The transition from Figure 2.41A-40D displays a reduction in flow energy as the channel gradient lessens with distance downstream. This results in a transition from a wide (>50 m) area of inundation featuring complete removal of vegetation and deposition of boulders (Fig. 2.41A) towards inundation with vegetation survival and deposition of vegetation that was transported from upstream (Figs 2.41C & 2.41D). There is no evidence from either available aerial images or the field visit to site BS3 to suggest flows in this catchment reached either Lago Chapo or the confluence of the Rio Colorado with the Rio Blanco Sur.

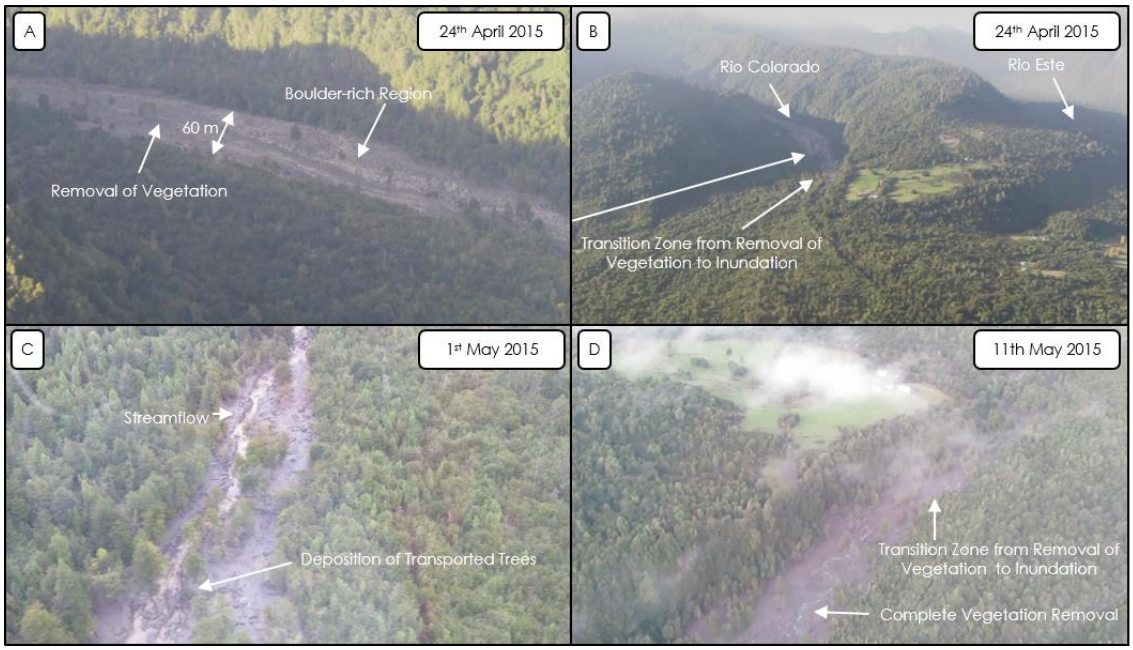

Figure 2.41: Aerial images displaying the post-eruption impacts in the Rio Colorado catchment between 24th April 2015 and 11th May 2015 (SERNAGEOMIN, 2015).

2.3.9. Rio Este

The Rio Este is another drainage on the Southern Flanks of Calbuco featuring evidence of primary lahar occurrence due to the melting of ice and snow. It features two primary channels in its upper reaches, referred to here as the western and eastern channels (Fig. 2.27). The western (Fig. 2.42A) and eastern (Fig. 2.42B) channels feature complete vegetation removal across the inundated regions, with scouring of the outside bends and no visible deposition of boulders. Permanent streamflow is visible in both channels on 11th May 2015 with observed channel widths in excess of 20 m.

At the confluence of the eastern and western channels (Fig. 2.42C) there is a wide (≈100 m) area of inundation featuring no visible vegetation. This single channel region features a wide range of deposits including fluvial (Fig. 2.43B), hyperconcentrated flow (Fig. 2.43C) and debris flow deposits (Fig. 2.43A). There are also examples of areas of complete vegetation removal in the centre of the channel (Fig. 2.43E) and other areas with surviving vegetation and mud marks 1.5 m above the current deposit surface (Fig. 2.43D). The range of deposits indicates temporally and spatially variable lahars in terms of both sediment concentration and inundation extent. Boulders ≤4 m in diameter are visible within the highest sediment concentration debris flow deposits in this single channel part of the Rio Este (Fig. 2.43E).

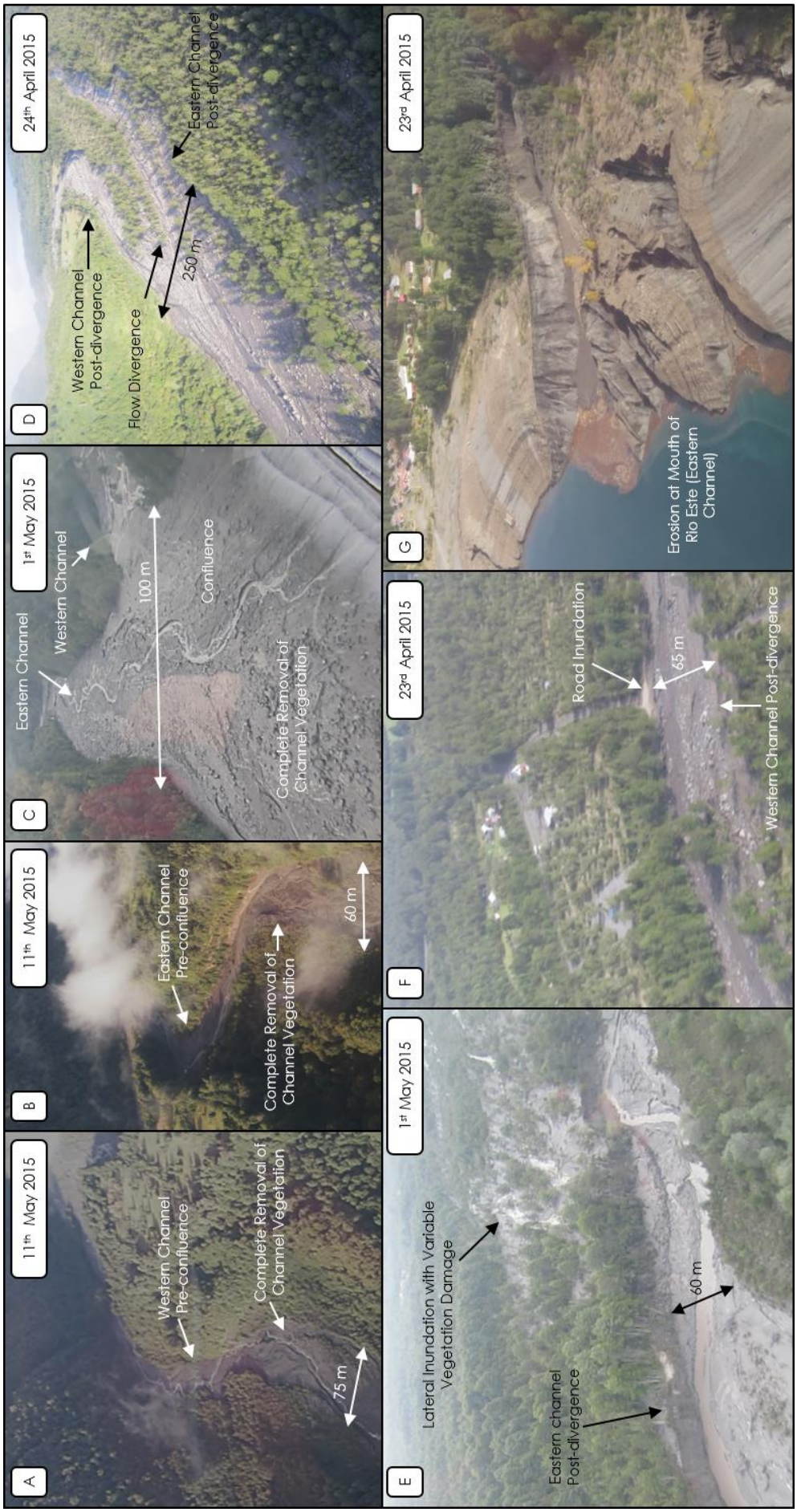

Figure 2.42: Aerial images displaying the post-eruption conditions in the Rio Este catchment between 23rd April 2015 and 11th May 2015 (SERNAGEOMIN, 2015). A: Western Channel Pre-Confluence. B: Eastern Channel Pre-Confluence. C: Confluence of Western and Eastern Channels. D: Bifurcation of Single Channel. E: Eastern Channel Post-Bifurcation. F: Mouth of Eastern Channel at Lago Chapo.

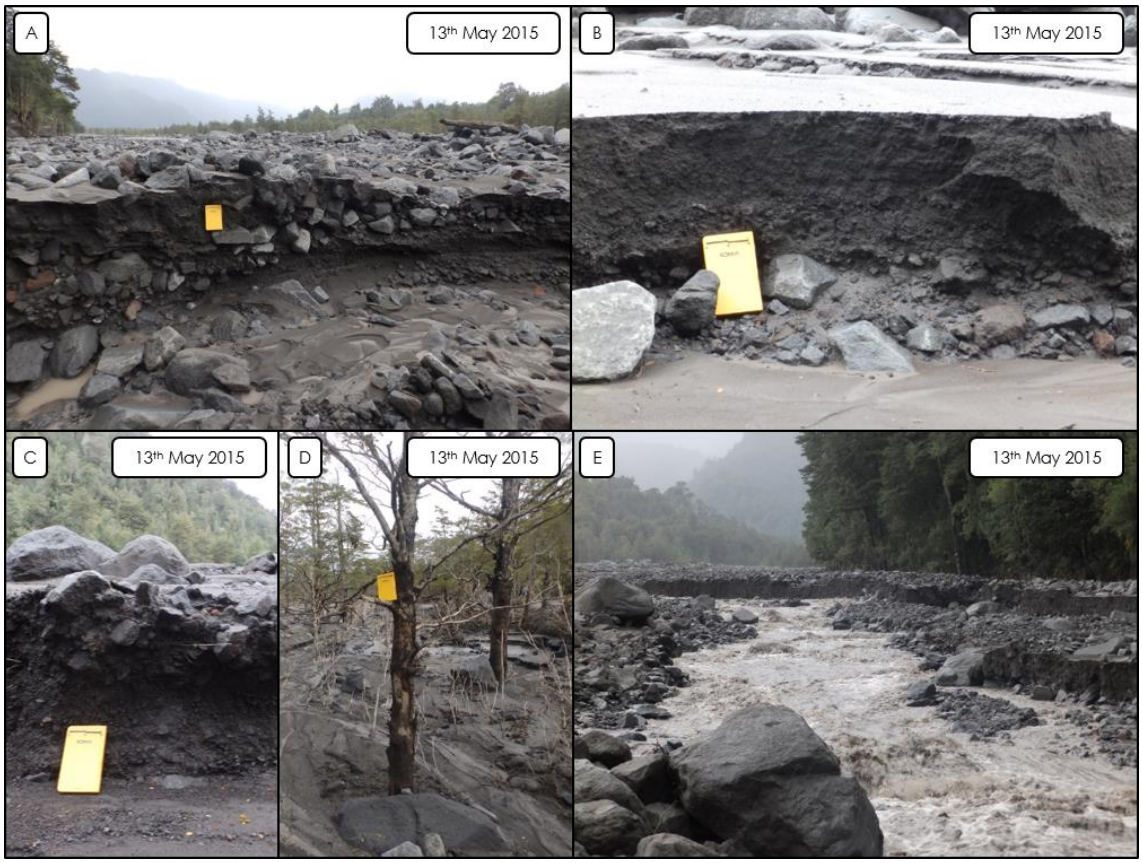

Figure 2.43: Field photos taken in the single channel region of the Rio Este on 13th May 2015 (SERNAGEOMIN, 2015). A: Debris Flow Deposits. B: Fluvial and hyperconcentrated flow Deposits. C: Hyperconcentrated flow and debris flow deposits. D: Mud marks on still-standing vegetation. E: Post-eruption condition of the river.

After several hundred metres as a single channel the Rio Este diverges into two channels (Fig. 2.27). As the flow diverges into these two channels there is significant boulder deposition in the centre of the respective channels and spatially variable vegetation removal (Fig. 2.42D). The two post-divergence channels independently flow into Lago Chapo, and with distance downstream the percentage of surviving vegetation in inundated areas increases. This is especially evident in Figure 2.42E which features a vegetation-stripped Eastern central channel but also surrounding surviving inundated forest. There was also disruption to the road network caused by primary lahar activity in the Rio Este (Fig. 2.42F), which as in the Rio Blanco Sur (e.g. Fig. 2.34A) functions to destroy the

road link between some Northern Lago Chapo communities and the rest of Chile. Deposits in the lower course of the Western channel of the Rio Este indicate a largely channel-confined flow featuring widespread but not total vegetation removal across the inundated region and deposition of boulders in the central channel (Fig. 2.42F). Figure 2.42G displays erosion of the banks of Lago Chapo at the Mouth of the Western channel, indicating that primary lahars in the Rio Este reached the lake.

2.3.10. Southern Flanks of Volcán Osorno

The primarily north-easterly dispersal of tephra from the April 2015 eruption of Calbuco resulted in the deposition of tephra across the southern and eastern flanks of Volcán Osorno. These flanks consist of numerous drainage channels associated with streamflow generated by annual snowmelt (Fig. 2.44). The addition of tephra deposits on the flanks of Osorno destabilised the system and in combination with post-eruption rainfall produced a rain-triggered lahar hazard. At site O1 (Fig. 2.44) tephra deposits mantled the topography of one of the aforementioned drainage channels, and these tephra deposits remained undisturbed nearly two months after deposition (Fig. 2.45), despite significant regional rainfall (Fig. 2.11). Evidence of the occurrence of seasonal snow-melt triggered flows at this location was present in the form of less developed vegetation within the primary channels relative to the terrace vegetation (Fig. 2.45). However, no rain-triggered flows resulting in the remobilisation of Calbuco tephra had impacted site O1 before June 14th 2015.

Figure 2.44: Location map of the southern flanks of Osorno Volcano. Highlighted are the various drainage networks, field site locations and notable local infrastructure (GoogleEarth, 2016).

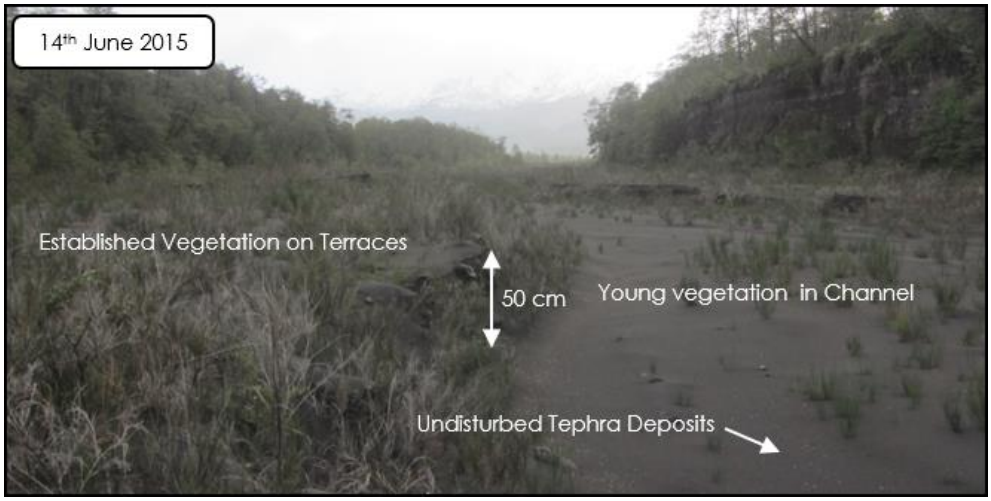

Figure 2.45: Image of field site O1 taken 14th June 2015 displaying undisturbed Calbuco tephra deposits and established vegetation on channel terraces.

Site O2 is located several hundred metres east of O1 and displayed evidence of numerous rain-triggered flows involving the remobilisation of Calbuco tephra deposits prior to June 14th 2015. Immediately downstream of the road bridge at this location there was a central channel with terraces of up to 1.2 m in height (Fig. 2.46B). These terraces were topped with either undisturbed Calbuco tephra deposits or re-mobilised material depending on whether the location had been inundated since tephra deposition. At site O2 undisturbed surface tephra deposits from the Calbuco eruption were 12 cm thick and consisted of a 4 cm thick lower unit of coarsening upwards light brown pumice-rich lapilli (Fig. 2.46A). Above this unit was a further 8 cm of tephra, which transitioned from light-brown pumice-rich tephra at the base to darker, denser tephra at the surface. The thickness of deposits overlying Calbuco tephra deposits at locations that have been inundated by post-eruption flows is highly spatially variable. At one location within site O2 (Fig. 2.46B) 0.7 m of re-mobilised material has been deposited above the Calbuco tephra deposits and within this 0.7 m unit were thin (≈1 cm) layers of distinct light-brown pumice-rich tephra from the Calbuco eruption with an accompanying fine matrix. In addition to this were layers of largely fine-grained re-mobilised material with no significant sorting containing dark red lithics indicative of material produced by previous eruptions of Osorno (Moreno, 1999). The upper 0.2 m (Fig. 2.46B) of this unit contained the largest clasts of the remobilised material, suggesting a potentially higher sediment concentration and more energetic flow than those producing the underlying deposits.

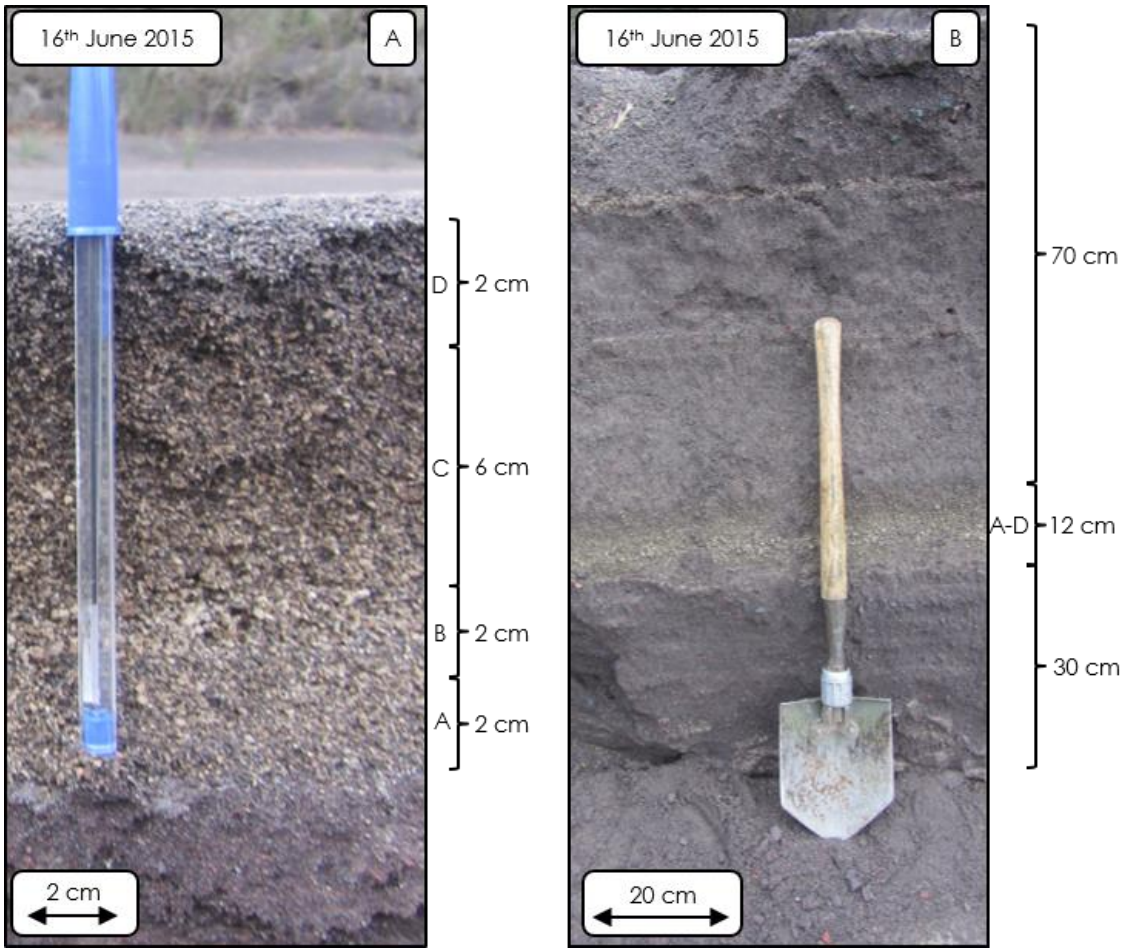

Figure 2.46: Images displaying the stratigraphy of two exposed channel terraces (channel created by post-eruption rain-triggered flows) at field site O2 taken on 16th June 2015. A: Undisturbed Calbuco tephra deposits. B: Calbuco Tephra deposits topped with remobilised material containing both the April 2015 eruptive products of Calbuco as well as Osorno eruptive products.

On the northern edge of the approximately 20 m wide channel at site O2 (Fig. 2.47A) were largely non-inundated terraces topped with Calbuco tephra (e.g. Fig. 2.46A) and to the southern edge were predominantly inundated terraces topped with re-mobilised volcaniclastic material (e.g. Fig. 2.46B). At specific locations there were examples of the transition from undisturbed surface tephra deposits to inundated tephra deposits due to rain-triggered flow activity (e.g. 2.47B). 200 m downstream of the road bridge at O2 the channel narrowed as the drainage neared the Rio Petrohué. This narrowing resulted in the undercutting of banks and the resultant addition of large boulders into the

channel although there was no evidence of the flows being energetic enough to re-mobilise these boulders.

Figure 2.47: Images displaying the conditions at field site O2 taken on 14th June 2015. A: Downstream view from the road bridge at site O2 displaying a post-eruption eroded central channel as well as undisturbed Calbuco tephra on the left channel terrace and remobilised deposits on the right channel terrace. B: Channel terrace stratigraphy displaying the transition from undisturbed Calbuco tephra deposits to inundated Calbuco tephra deposits topped with post-eruption remobilised material.

Sites O3 and O4 also displayed evidence of post-eruption flows but these were smaller in magnitude than those at location O2. At site O3 there was undercutting of banks and fluvial re-mobilisation of material immediately downstream of the inundated road crossing (Fig. 2.48A). Undisturbed tephra deposits and living vegetation on top of 0.5 m high terraces within the main channel indicate flow depths of below 0.5 m. Approximately 100 m upstream of the road crossing at O3 there was a central channel approximately 0.7 m in width featuring no vegetation (Fig. Fig. 2.48B). This channel featured 5-10 cm high channel terraces which feature damaged and bent vegetation which transitions

to living unaffected vegetation as distance from the central channel increases (Fig. 2.48B). Such discrete channelization of flows is not ever-present at this location, with some regions displaying passive flow margins with surface deposits transitioning from fine-grained re-mobilised material to unaffected Calbuco tephra deposits (Fig. 2.48C).

Figure 2.48: Images displaying the conditions at field site O3 taken on 14th June 2015. A: Undisturbed Calbuco tephra on top of terraces as low as 50 cm above the base of the central channel. B: Channelised flow evidence at site O3 with a lack of channel vegetation, vegetation damage at channel margins and healthy vegetation away from the channel. C: Passive flow margins at unconfined locations of O3.

Site O4 (Fig. 2.49) featured a straighter, wider and less vegetated channel than that at O3 (Fig. 2.48), suggesting more frequent and/or larger seasonal snow-melt triggered flows. This wide, straight channel displayed visible surface fluvial re-mobilisation features created after the deposition of Calbuco tephra (Fig. 2.49A). This location immediately upstream of the road crossing features undisturbed tephra-mantled channel terraces at its lateral margins (Figs. 2.49C &

2.49E). Downstream of the previously inundated road crossing there were 0.1 m high undisturbed tephra terraces in the central channel indicating very shallow flows (Figs. 2.49B & 2.49D).

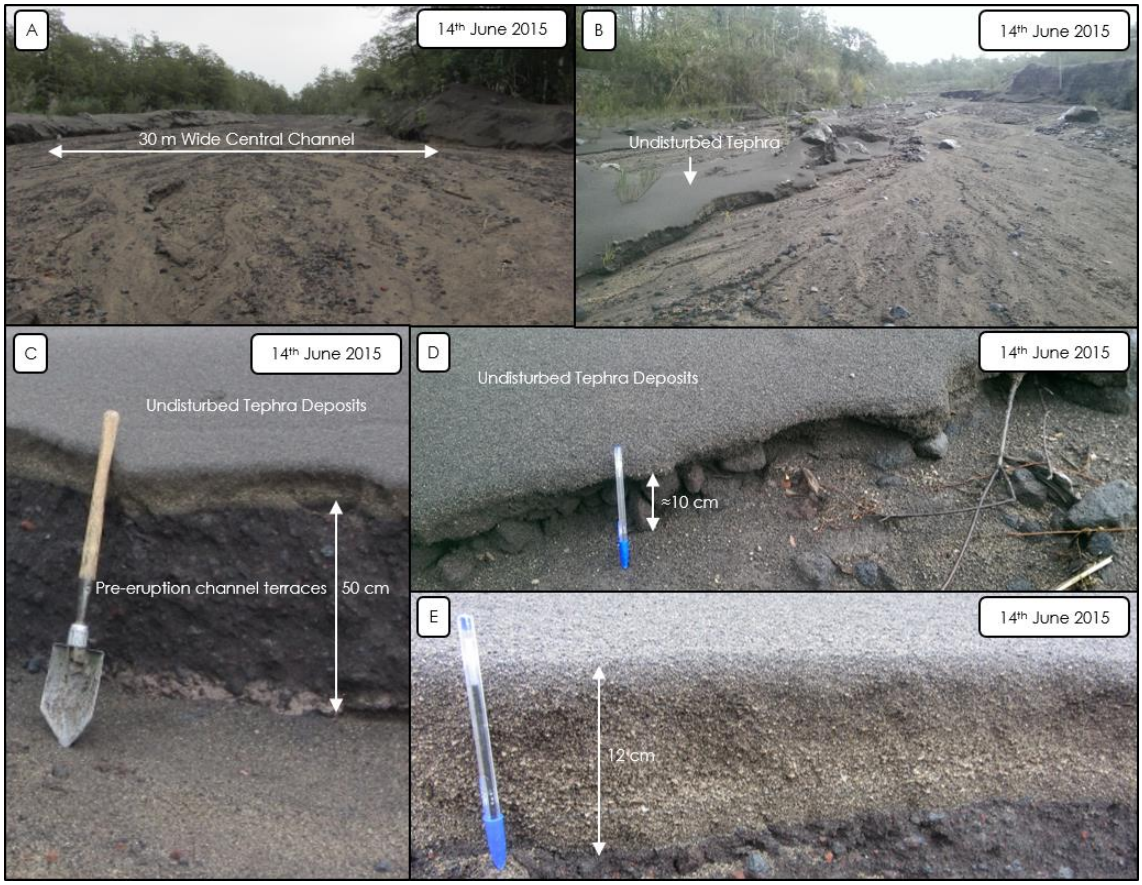

Figure 2.49: Images displaying the conditions at field site O4 taken on 14th June 2015. A+B: Characteristics of the wide, un-vegetated central channel at site O4. C-E: Undisturbed Calbuco tephra deposits at site O4.

Between the Petrohué waterfalls and Petrohué Village locations (Fig. 2.44) there are further sites (O5-O8) located adjacent to channels which all drain the south-eastern flanks of Osorno. As with the southern flank locations O1-O4, these drainages are ephemeral and are affected by seasonal snow-melt triggered flows. Post-eruption re-mobilisation of Calbuco tephra has resulted in largely fluvial activity with occasional hyperconcentrated flows at each of sites O5-O8. The surface of undisturbed tephra deposits on channel terraces at site O7 (Fig. 2.50C) was approximately 20 cm above the channel bed, indicating shallow

flows immediately prior to the confluence with the Rio Petrohué. Undisturbed tephra deposits of a total depth of approximately 6 cm were present at site O8 (Fig. 2.50D) and display an eastward reduction in tephra depth as well as grain size distribution relative to sites O2 (Fig. 2.46A) and BE1 (Fig. 2.5).

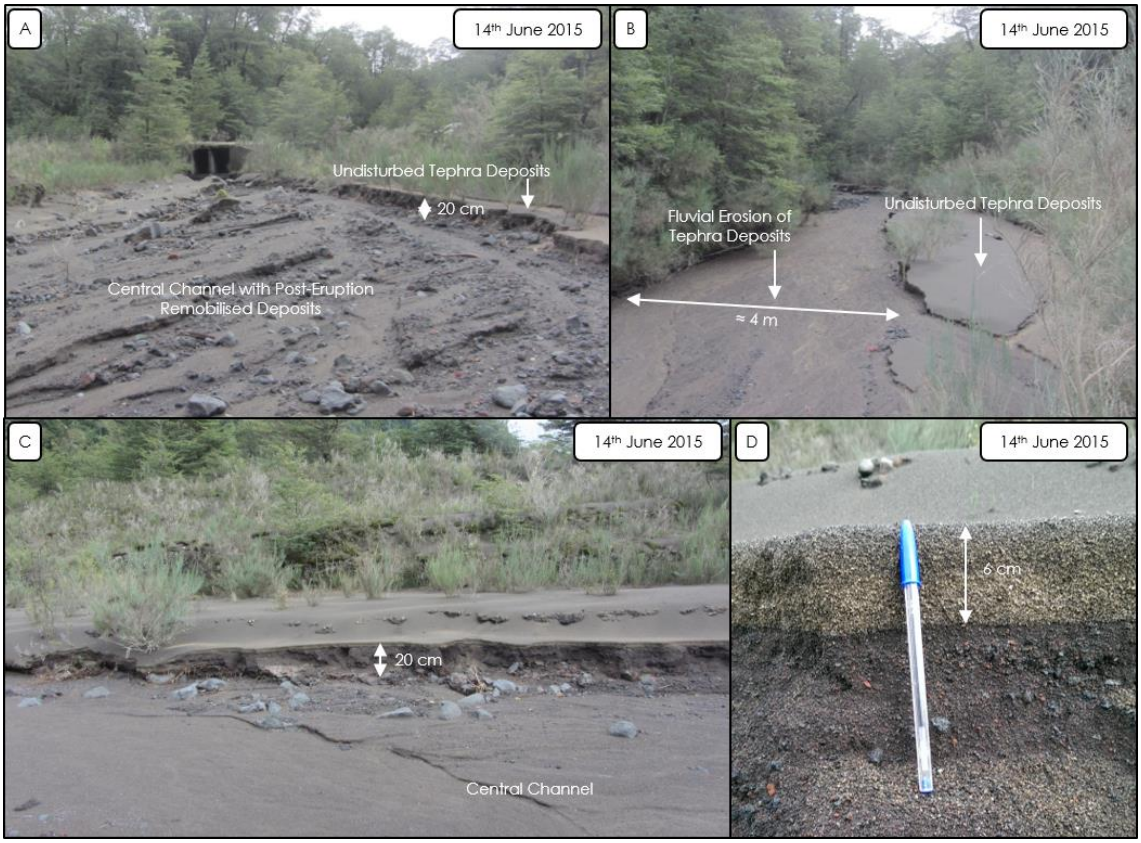

Figure 2.50: Images displaying the post-eruption characteristics of small drainage channels near Petrohué Falls taken on 14th June 2015. A-C: Evidence of shallow, fluvial-hyperconcentrated post-eruption flow with undisturbed Calbuco tephra atop 20 cm channel terraces at site O7. D: Calbuco tephra deposits at site O8.

The eastern drainages of Osorno which flow directly into Lago Todos Los Santos were not visited during the field visit in June 2015 but also experience ephemeral seasonal snow-melt triggered flows. Upstream of Petrohué Village there was a wide debris fan with minimal vegetation coverage and a mantling of Calbuco tephra deposits (Fig. 2.51E). Man-made levees are visible in the foreground and were constructed in an attempt to divert future flows into the lake without inundating the village.

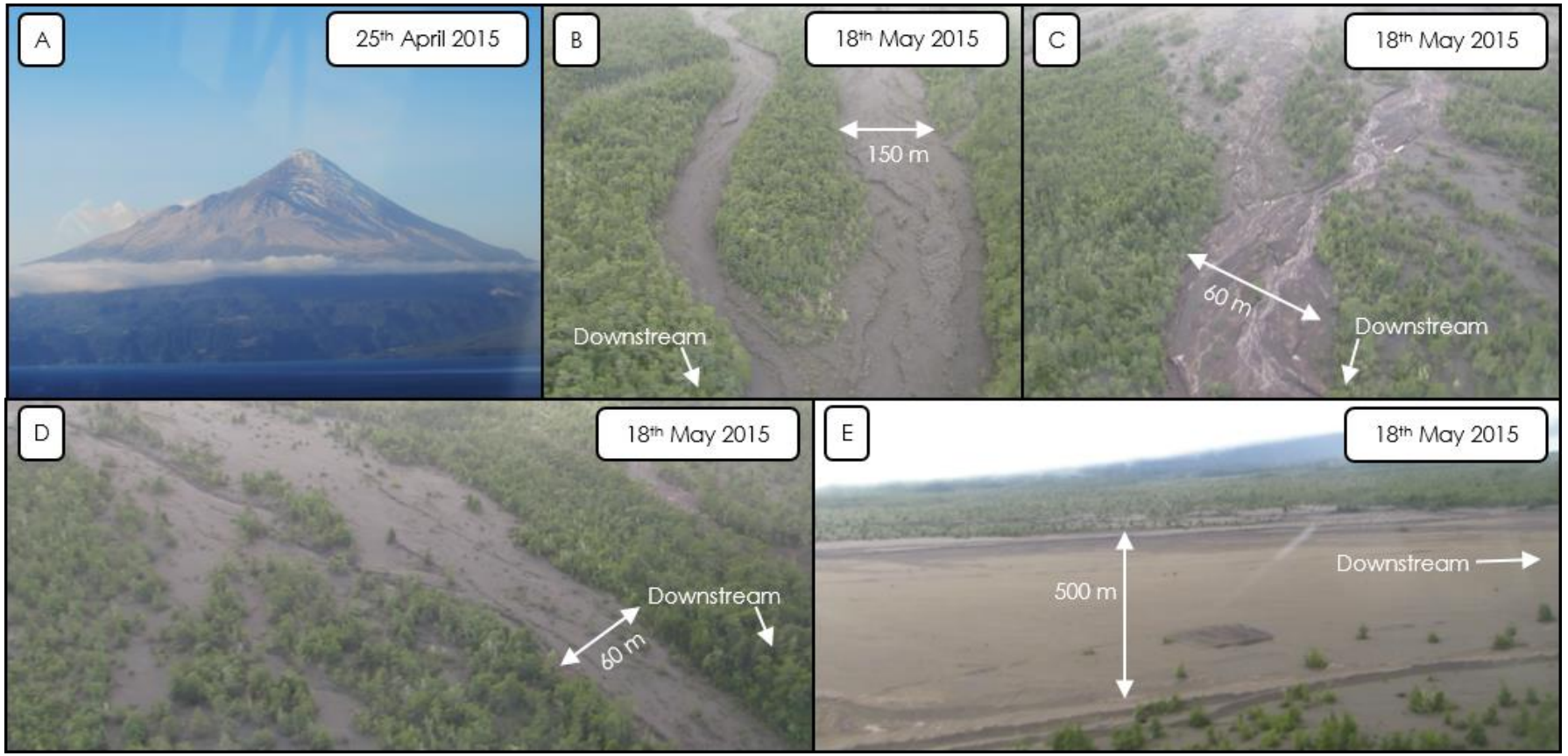

Figure 2.51: Aerial perspectives of Osorno Volcano after the eruption of Calbuco taken between 25th April 2015 and 18th May 2015 (SERNAGEOMIN, 2015). A: Illustration of the covering of Osorno by Calbuco tephra deposits and the lack of exposed snow cover. B: The condition of the channel upstream of field site O1. C: The erosion of tephra deposits and remobilisation of material upstream of site O2. D: Erosion of tephra deposits and remobilisation of material upstream of sites O3 and O4. E: Conditions upstream of Petrohué Village.

2.4. Snow and Ice Cover

The location and extent of Calbuco's glaciers and seasonal snow pack at the time of the eruption influenced the primary lahar hazard during the April 2015 eruption. A satellite image taken on 20th March 2013 at a time with negligible snow cover shows the main summit ice cap (A) and smaller glaciers located above the south-western (B) and north-western (C) flanks (Fig. 2.52A). As illustrated by the arrows in Figure 2.52A the summit ice cap (A) drains into the Rio Este, Rio Colorado and Rio Blanco Sur, the south-western glacier (B) drains exclusively into the Rio Blanco Sur and the north-western glacier (C) drains into the northern and southern contributing channels of the Rio Sur. Figure 2.52B displays Calbuco with increased seasonal snow-pack cover relative to Figure 2.52A and demonstrates a more even spatial distribution of snow around the edifice relative to the location of the glaciers. The April 2015 eruption of Calbuco occurred in autumn, therefore coinciding with a period of relatively low snow cover prior to the onset of the southern hemisphere winter. A reduction in snow cover results in decreased moisture storage on the upper slopes of the volcano, potentially lessening the likelihood of large snow and ice melt-triggered lahars in some drainages (Pierson, 1985).

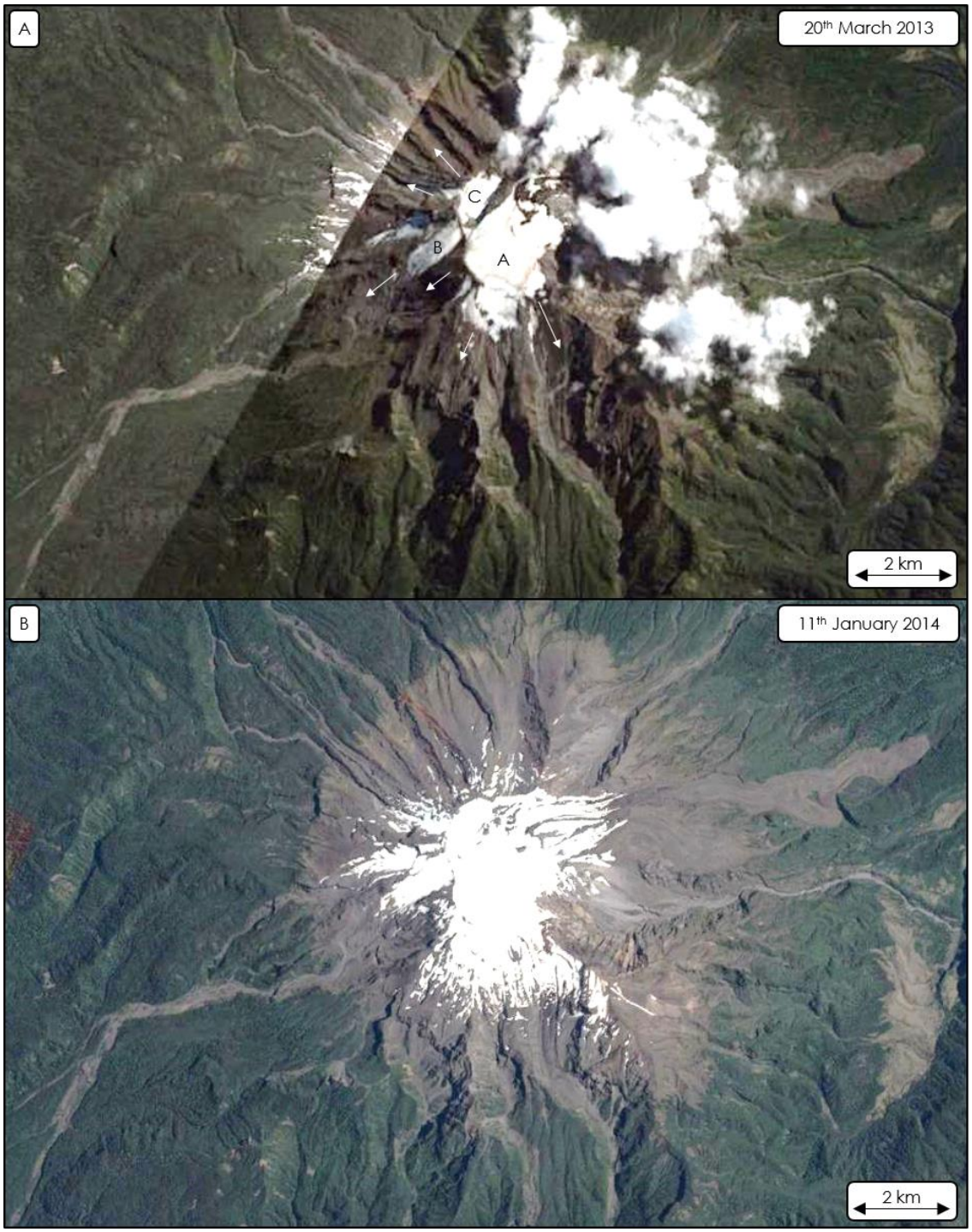

Figure 2.52: Google Earth images illustrating two examples of snow and ice cover on Calbuco. A: 20th March 2013 image displaying the location of permanent ice cover near the summit of Calbuco with minimal seasonal snow cover. B: 11th January 2014 image displaying more widely distributed snow cover (GoogleEarth, 2016).

2.5. Discussion

Through a combination of fieldwork and the analysis of aerial photography it has been established that there was significant spatial variation in the post-eruption rain-triggered lahar hazard at Calbuco Volcano following the April 2015 eruption (Fig. 2.53). The spatial distribution of tephra deposits (along with its grain size distribution), PDCs and pre-eruption glaciers has driven this variation. Assessment of the eruption chronology enhances the understanding of the post-eruption conditions and this eruption chronology was well exposed in the Blanco Este catchment at field site BE1 (approximately 6 km from the crater at a heading of 46°) (Fig. 2.5). Tephra layers A and B (Fig. 2.5) are attributed to phase 1 of the eruption, which began at approximately 18:00 local time on 22nd April 2015 and lasted 1.5 hours, with the coarsest tephra of these two layers in layer B representing the paroxysm of pulse 1 (Romero et al., 2016). There is no evidence of PDC emplacement during phase 1 of the eruption in the Blanco Este catchment. Layer C represents the onset of phase 2 of the eruption, which began at 04:10 local time on 23rd April 2015 and lasted approximately 6 hours with a column height of >15 km. At field site BE1 layer C is divided into a lower 15 cm (C_1) and upper 7 cm (C_2) by the emplacement of PDC deposits of approximately 9 m in thickness. These PDCs were a product of partial column collapse, with the deposits at BE1 a result of PDC transit down the Rio Frio channel (Fig. 2.4). Above layer C_2 at site BE1 is 8 cm of denser, less vesicular, coarse, dark grey lapilli (D). This layer represents the final stages of phase 2 of the eruption and at site BE1 is overlain by 10 cm of post-eruption fine-grained fluvial deposits as a result of initial non-erosive surface flow at site BE1 after the eruption. During the field study in June 2015 there was no preservation of the fine-grained light grey co-PDC fall deposit evident in post-eruption aerial images.

The complete tephra stratigraphy was also exposed in the drainage channels of the Southern flanks of Osorno Volcano due to their location to the northeast of Calbuco (Figs. 2.46 & 2.50). Deposits on the southern flanks of Osorno also illustrate the change in tephra colour from light brown (A) to dark grey (D) as a product of the reduction in vesicularity during the eruption (e.g. Fig. 2.50D). Tephra deposits decreased in thickness and median grain size with distance away from Calbuco (Fig. 2.53). Due to the north-easterly dispersal of the tephra the Blanco Este, Tepu and southern flanks of Osorno were the primary regions of proximal tephra deposition (Romero et al., 2016) (Fig. 2.53).

Evidence of column collapse PDCs is more radially distributed around the volcano compared to the primarily north-easterly distribution of the tephra deposits (Fig. 2.53). The Blanco Este (Fig. 2.7), Rio Tepu (Fig. 2.15), Rio Sur (Fig. 2.20) and Blanco Sur (Fig. 2.29) catchments all display visible post-eruption steaming of PDC deposits in the available aerial footage, whilst the Este and Colorado catchments are also likely to have experienced PDCs during the eruption given the nature of the post-eruption primary lahar deposits within these catchments. PDC plumes produced fine-grained fallout deposits which mantled the surface of the Rio Blanco Este and upper Rio Tepu catchments immediately after the eruption. These deposits were finer grained than the coarse underlying tephra deposits and therefore further reduced post-eruption infiltration rates. These surface co-PDC fall deposits were short-lived and had been removed by rainfall-driven remobilisation prior to the field study in June 2015.

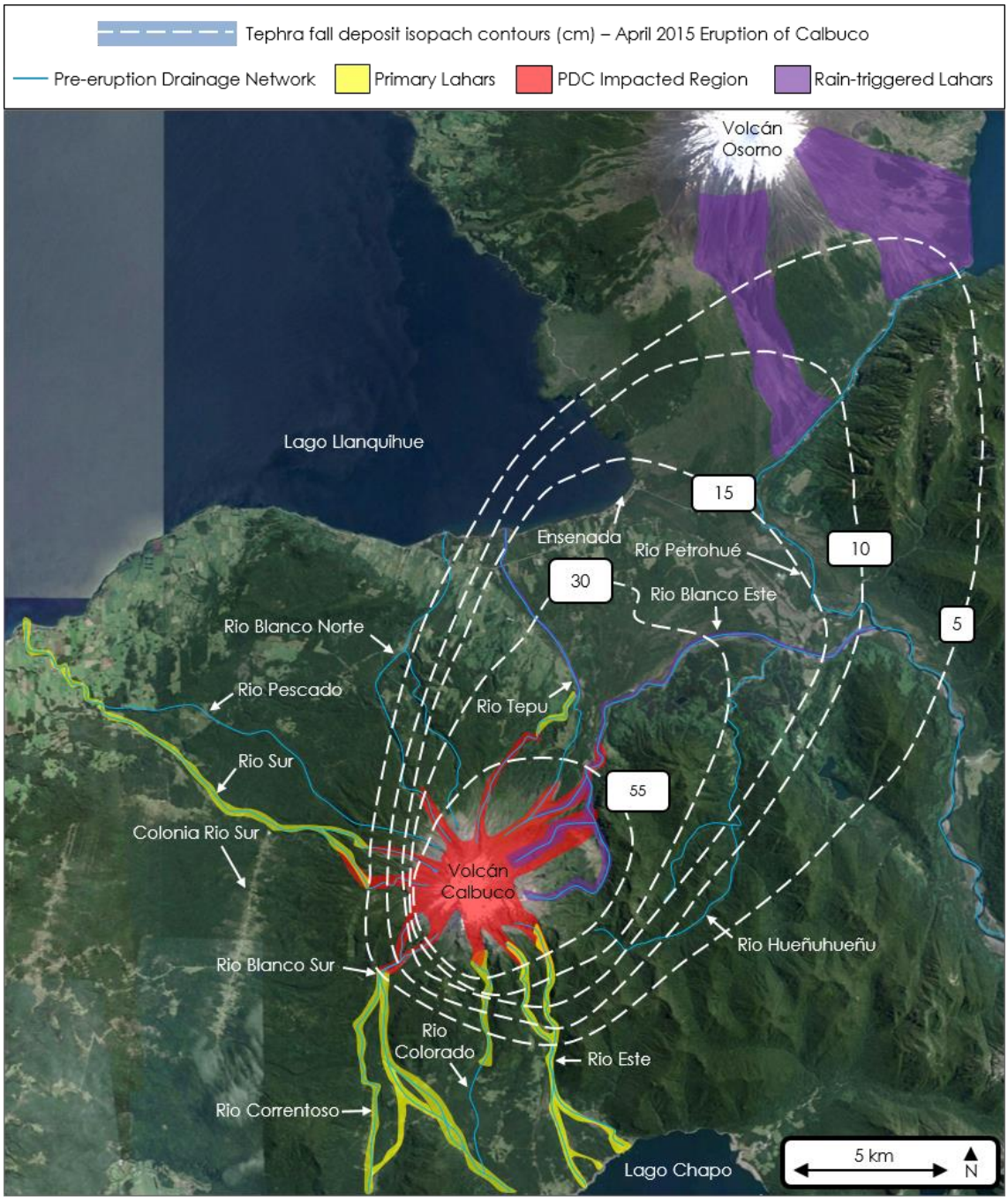

Figure 2.53: Map displaying the spatial catchment-by-catchment variation in post-eruption volcano-hydrologic response at Calbuco Volcano following the April 2015 eruption. Depicted are the pre-eruption drainage network, regions impacted by PDC inundation, locations of primary lahars, areas featuring evidence of post-eruption rain-triggered lahars and tephra isopach contours (cm).

The location of glaciers and permanent ice near the summit of Calbuco (Fig. 2.52) was a key factor, along with the location of PDC occurrence, in the initiation and spatial distribution of primary lahars during the April 2015 eruption. Primary lahars occurred in the Rio Este, Rio Colorado, Rio Blanco Sur, Rio Correntoso and Rio Sur due to the melting of snow and ice by PDCs (Fig. 2.53). This mechanism of primary lahar occurrence has been identified at many global locations including Mt. St. Helens (Pierson, 1985), Nevado Del Ruiz (Lowe et al., 1986; Pierson et al., 1990; Thouret, 1990), Redoubt (Waythomas et al., 2013) and Calbuco (Klohn, 1963). Such lahars are formed by the transfer of heat from the PDCs to ice and snow, creating meltwater which can entrain large volumes of pyroclastic material (Major and Newhall, 1989; Pierson et al., 1990). Primary lahars can have large runout distances (>100 km) and this presents significant potential risk to downstream communities as highlighted by the >23,000 fatalities caused by the primary lahars triggered during the 1985 eruption of Nevado del Ruiz (Lowe et al., 1986). Due to the potentially large volumes of water stored in ice and snow on the upper flanks of volcanic edifices large primary lahars can be created by relatively small eruptions (Pierson et al., 1990).

The largest primary lahars triggered during the April 2015 eruption of Calbuco occurred on the Southern Flanks, with the upper Blanco Sur featuring a heavily abraded lahar channel as identified at Nevado del Ruiz by Pierson et al. (1990). The maximum observed inundated width of primary lahar deposits within the Blanco Sur was approximately 150 m at field site BS1, which was also the location of the destruction and almost complete burial of a large fish farm facility. Primary highways were repeatedly inundated and bridges destroyed in the Rio Blanco Sur, Rio Correntoso and Rio Este with impacts as far as 14 km downstream (Fig. 2.36F). Avulsing primary lahars between the Blanco Sur and Correntoso also

caused damage to transport links, blocking road access to the rest of Chile for inhabitants of the northern Lago Chapo region. Despite significant rainfall in Late-May and during the field visit in June (Fig. 2.11), post-eruption rainfall produced insignificant variation in flow magnitude across the southern flanks of Calbuco in June 2015 relative to the size and impacts of the initial large primary lahars. This was because valley-confined late stage (post-primary lahar) PDC deposits covered a low percentage (<10%) of the upper catchments, resulting in the dominant rainfall-driven post-eruption remobilisation process being the re-working of primary lahar deposits.

Primary lahars in the Rio Sur were smaller than those in the Rio Blanco Sur and Rio Este, and featured rapid attenuation with distance downstream, but still destroyed several bridges including the Puente Zapatero (Fig. 2.24). Minimal rain-triggered lahar activity was identified in the Rio Sur in June 2015 with only minor variation in streamflow discharge during periods of rainfall (Fig. 2.23).

There was no evidence of large primary lahars in the Rio Tepu at field sites accessed during the field visit in June 2015, indicating that any flows rapidly attenuated downstream. The lack of glaciers draining into the catchment limited the magnitude of the moisture source upon PDC occurrence, prohibiting the initiation of large primary flows such as those which occurred on the Southern flanks. The catchment was widely mantled with coarse tephra deposits and the western contributing channel displays evidence of long-runout (7 km) valley-confined PDCs (Fig. 2.15); although these flows and the resultant deposits were less voluminous than those in the Blanco Este catchment. Preservation of undisturbed tephra terraces adjacent to the Rio Tepu 50 cm above the river level at sites T1 and T2 in June 2015 along with undamaged bridges indicates that only

small rain-triggered lahars had been initiated in the Rio Tepu following the eruption despite the PDC deposits (Fig. 2.16). Fine-grained co-PDC fall deposits proved insignificant to trigger large lahars in the catchment, and once exposed, underlying coarse tephra deposits did not sufficiently reduce infiltration rates to initiate large flows. Despite this, the long-runout valley-confined PDC deposits indicate the potential for long-term remobilisation. There was ponding of water and flooding in the lower reaches of the catchment due to rainfall saturation of tephra deposits in flat regions, whilst gradual channel aggradation near the mouth of the river illustrates the cumulative effects of small rain-triggered lahars.

The two areas featuring significant rain-driven remobilisation of pyroclastic material following the eruption of Calbuco were the Blanco Este and the Southern Flanks of Osorno Volcano (Fig. 2.53). The Blanco Este lies on the axis of tephra dispersal during the eruption and also experienced PDCs which were not channel confined in the upper catchment, thus mantling the entire upper catchment in fine-grained PDC and fine-grained co-PDC fall deposits. Once channel confined, PDCs during phase 2 of the eruption travelled down both the Rio Caliente and Rio Frio tributaries, destroying hydroelectric infrastructure near the confluence of these two channels and resulting in maximum PDC runout distances of approximately 7 km. The widespread PDC deposits and finer-grained surface PDC fallout deposits decreased surface roughness, eliminated rainfall-intercepting vegetation and added a supply of easily erodible pyroclastic material within the catchment; all factors which act to enhance surface runoff generation during rainfall. Post-eruption rain-triggered remobilisation of the PDC and tephra deposits in the Blanco Este resulted in approximately 14.5 m of vertical erosion at site BE1 between April 23rd and June 15th 2015, whilst 13.5 m of post-eruption aggradation occurred at the Ensenada

Hydroelectric Powerhouse location by March 2016. Flow variation of the nature shown in the Blanco Este (Figs. 2.8 & 2.9) was not identified across the southern drainages of Calbuco, the Rio Sur or the Rio Tepu.

Due to their location on the axis of tephra dispersal (Fig. 2.51A), the southern catchments of Osorno also displayed evidence of post-eruption rain-triggered lahar initiation. Unlike the Blanco Este these catchments were not affected by PDCs, so remobilisation is exclusively of 2015 Calbuco tephra and the underlying eruptive products of previous Osorno and Calbuco eruptions (Fig. 2.46). The grain-size and thickness of tephra deposits decreased with distance from the active crater, resulting in more fine-grained and thinner deposits at site O1 relative to the Blanco Este and Tepu catchments (Fig. 2.46) as well as a further gradual reduction in these parameters between sites O1-O8 (Fig. 2.50D). As a result of the reduction in tephra grain size, Infiltration rates were reduced at tephra mantled locations on the southern flanks of Osorno compared to tephra mantled locations in the Rio Tepu and Blanco Este catchments. This promoted rain-triggered lahar occurrence at sites O1-O8 even without the fine-grained surface co-PDC fall deposits in the Blanco Este. Rain-triggered remobilisation was not consistent across all of the southern drainages of Osorno, with site O1 displaying no evidence of post-eruption fluvial activity (Fig. 2.45), site O2 exhibiting the largest, most frequent flows (Fig. 2.47) and sites O3-O8 featuring smaller magnitude post-eruption flows (Fig. 2.50). Rain-triggered lahar deposits at O2 (Fig. 2.46B) contained a mixture of source material including layers of distinctive light brown pumice-rich tephra from the 2015 eruption of Calbuco. As a single, discrete eruption the sediment yield due to rain-triggered remobilisation of pyroclastic material in the Blanco Este, Rio Tepu and on the Southern Flanks of Osorno following the April 2015 eruption of Calbuco would be expected to

decline exponentially with time as identified at other global locations (e.g. Schumm and Rea, 1995; Major et al., 2000).

Pre-eruption conditions, namely the location of summit glaciers, and the spatio-temporal variation and nature of eruptive products dictated the catchment-by-catchment variation of the volcano-hydrologic response to the 2015 eruption of Calbuco. PDCs triggered primary lahars via the melting of ice and snow in all of the catchments in to which the summit glaciers drained prior to the eruption. These primary lahars destroyed infrastructure, scoured upper channels, stripped vegetation from valleys and inundated areas as wide as 150 m. In three areas (the Blanco Este catchment, Rio Tepu and the Southern flanks of the adjacent Osorno Volcano) featuring no upstream glaciers an immediate post-eruption rain-triggered lahar hazard was generated. However, the magnitude of this hazard varied in these three locations, and was enhanced in the Blanco Este due to the large volume of unconfined fine-grained PDC deposits emplaced in the upper catchment. Short-lived fine-grained PDC fallout deposits mantled topography to the northeast of the volcano after the eruption and were an important factor in the initial rain-triggered remobilisation of material in the Blanco Este. The post-eruption rain-triggered hazard in the catchments featuring large primary lahars was minimal, with rainfall-driven variation in streamflow magnitude insignificant relative to the size of the primary lahars as remobilisation was reliant on the re-working of primary lahar deposits.

Catchment-by-catchment variation in the volcano-hydrologic response to landscape disturbances as identified at Calbuco has been observed globally after both discrete and intermittent eruptive activity. At Tungurahua, tephra, lahar, PDC and lava flow hazards are primarily distributed in an arc from the West

to the North of the volcano due to the topographical impacts of a debris avalanche amphitheatre and the prevalent wind direction (Hall et al., 1999; Jones et al., 2015). Similarly, at Semeru the rain-triggered lahar hazard driven by persistent eruptive activity is primarily located to the south and east of the volcano (Thouret et al., 2007), whilst at Merapi the hazard is predominantly directed to the South and West (de Bélizal et al., 2013). The magnitude and longevity of the volcano-hydrologic response within the different catchments of Mt. St. Helens following the 1980 eruption was heavily dependent on the nature of the experienced hazards; with catchments impacted by the debris avalanche and directed volcanic blast displaying the most extreme and long-lived response (Major and Mark, 2006). Similarly, at Pinatubo following the 1991 eruption the percentage of the catchment inundated with PDC deposits, catchment gradient and the degree of PDC deposit confinement influenced the timing and magnitude of the peak sediment yield as well as the rate of catchment recovery (Janda et al., 1996; Gran and Montgomery, 2005). Relatively low volume PDC deposits within the steep-walled valleys of the eastern catchments of Pinatubo triggered an early peak sediment yield followed by a rapid decline (Janda et al., 1996). Contrastingly, large volume PDC deposits across the broad, gently-sloping, unconfined pyroclastic apron to the west of Pinatubo produced a later peak sediment yield followed by a slower recovery (Janda et al., 1996).

In addition to the deposit mechanism and volume of pyroclastic material, hydrologic and geomorphic recovery rates are heavily influenced by the rate of vegetation recovery (e.g. Yamakoshi and Suwa, 2000; Major and Yamakoshi, 2005). This can be rapid in regions of high precipitation, particularly if regrowth from pre-eruption root systems is viable (Swanson et al., 2013). Contrastingly, volcaniclastic deposits can remain without vegetation coverage for decades in

arid climates, a factor enhanced at locations where plant tissues are completely destroyed during the initial catchment disturbance (Pierson and Major, 2014). Contrasting vegetation recovery rates were identified in the western and eastern catchments of Pinatubo between 1991 and 1993, with relatively rapid recovery in the eastern catchments a product of lower PDC deposit volume and steeper gradients (Janda et al., 1996).

Rapid, post-eruption identification of the spatial variation and magnitude of secondary volcanic hazards is vital for effective hazard mitigation. Such evaluation facilitates the appropriate distribution of resources including observers and monitoring equipment as well as the effective assessment of rain-triggered lahar related exclusion zones. This study of the April 2015 eruption of Calbuco highlights the importance of factors including the grain-size, spatial distribution, thickness and emplacement mechanism of the various pyroclastic deposits; the spatial distribution and magnitude of syn-eruptive primary lahars; local and regional topography; degree of vegetation damage; and the magnitude and distribution of pre-eruption snow and ice cover upon the variability of the volcano-hydrologic response to the eruption and the resultant rain-triggered lahar hazard. Specifically, infiltration-inhibiting fine-grained pyroclastic deposits were observed to be a vital component in generating a post-eruption rain-triggered lahar hazard and the volume of such deposits dictated the magnitude of this hazard. The extent of pre-eruption ice and snow cover was also identified as indirectly affecting the generation of this secondary hazard, as snow and ice-melt triggered primary lahars scoured upper drainages and reduced the volume of available source material.

2.6. Conclusions

Analysis of post-eruption aerial footage and field investigations seven weeks after the April 2015 eruption of Calbuco have revealed significant catchment-by-catchment variation in the volcano-hydrologic response to the discrete eruption. The pre-eruption location of glaciers and the distribution of PDCs dictated the location and magnitude of ice-melt driven primary lahars. These flows were largest on the southern Flanks of Calbuco where the majority of the pre-eruption ice volume was located. These flows produced widespread damage to infrastructure including the destruction of fish farm facilities, inundation of transport links and severe damage to settlements. There was minimal post-eruption rain-triggered lahar activity in the primary lahar effected catchments, which featured scoured channels in their upper reaches.

Significant post-eruption rain-triggered lahar activity in the Rio Blanco Este was driven by voluminous, largely unconfined fine-grained PDC deposits in the upper part of the catchment in addition to tephra deposits. On the Southern flanks of the adjacent Osorno Volcano, the rain-triggered lahar hazard was driven by the mantling of the region in finer-grained tephra deposits due to the increased distance from Calbuco. The input of Calbuco tephra deposits destabilised the Osorno drainages, triggering rainfall-driven remobilisation of both Calbuco and Osorno eruptive products. Only small magnitude rain-triggered lahars were present in the Rio Tepu despite evidence of valley-confined PDC deposits and significant tephra deposits in the catchment. Rain-triggered lahars in the Rio Tepu were smaller than those in the Blanco Este due to the confined nature of the PDC deposits, and associated low infiltration rates, and

the high infiltration rates of the coarse tephra deposits emplaced throughout the rest of the catchment.

The single, discrete eruption of Calbuco in April 2015 produced significant catchment-by-catchment variation in the post-eruption volcano-hydrologic response. This study observes and identifies key factors which acted to enhance or inhibit the generation of a post-eruption rain-triggered lahar hazard in the various drainages proximal to the volcano. This illustrates the importance of identifying the volume and location of pre-eruption ice and snow cover; the primary syn-eruptive lahar impacts; and the grain-size, spatial distribution, thickness and emplacement mechanism of pyroclastic deposits when assessing post-eruption rain-triggered lahar hazards.

Chapter 3: Rainfall-runoff properties of tephra: Simulated effects of grain-size and antecedent rainfall

Summary

Rain-triggered lahars are a significant and often persistent secondary volcanic hazard at many volcanoes around the world. Rainfall on unconsolidated volcaniclastic material is the primary initiation mechanism of rain-triggered lahars: the resultant flows have the potential for large runout distances (>100 km) and present a substantial hazard to downstream infrastructure and communities. Rain-triggered lahars are frequently anticipated in the aftermath of eruptions, but the pattern, timing and scale of lahars varies on an eruption-by-eruption and even catchment-by-catchment basis. This variability is driven by a set of local factors including the grain size distribution, thickness, stratigraphy and spatial distribution of source material in addition to topography, vegetation coverage and rainfall conditions. These factors are often qualitatively discussed in rain-triggered lahar studies based on post-eruption lahar observations or instrumental detections. Conversely, this study aims to move towards a quantitative assessment of rain-triggered lahar hazard in order to facilitate rain-triggered lahar predictions and forecasts based on constrained rainfall, grain size distribution and isopach data. Calibrated simulated rainfall and laboratory-constructed tephra beds are used within a repeatable experimental set-up to isolate the effects of individual parameters and to examine runoff and infiltration processes from analogous rain-triggered lahar source conditions.

Laboratory experiments show that increased antecedent rainfall and finer-grained surface tephra individually increase runoff rates and decrease runoff lag times, while a combination of these factors produces a compound effect. These impacts are driven by increased residual moisture content and decreased permeability due to surface sealing, and have previously been inferred from downstream observations of lahars but not identified at source in the field. Water and sediment transport mechanisms differ based on surface grain size distribution: a fine-grained surface layer displayed airborne remobilisation, accretionary pellet formation, rapid surface sealing and infiltration-excess overland flow generation whilst a coarse surface layer demonstrated exclusively rainsplash-driven particle detachment throughout the rainfall simulations. This experimental protocol has the potential to quantitatively examine the effects of a variety of individual parameters in rain-triggered lahar initiation under controlled conditions.

3.1. Introduction

Rainfall on unconsolidated volcaniclastic material, typically pyroclastic density current (PDC) and/or ash-fall deposits, is the primary initiation mechanism of secondary, rain-triggered lahars. These flows pose a significant hazard to downstream infrastructure, with impacts ranging from damage to building contents via flow inundation, to complete destruction and burial of structures (Jenkins et al., 2015a). Rain-triggered lahars often pose a long-lived secondary hazard, with discrete large eruptions resulting in significant catchment disturbance for many decades (Major et al., 2000; Gran and Montgomery, 2005; Major and Yamakoshi, 2005; Van Westen and Daag, 2005; Major and Mark,

2006). The combination of intense rainfall and a source of volcaniclastic material required for rain-triggered lahar initiation is particularly common throughout the tropics and sub-tropics, and has been documented at volcanoes including Mayon (Arguden and Rodolfo, 1990; Rodolfo and Arguden, 1991; Orense and Ikeda, 2007; Paguican et al., 2009), Pinatubo (Arboleda and Martinez, 1996; Martinez et al., 1996; Rodolfo et al., 1996; Tungol and Regalado, 1996; Van Westen and Daag, 2005), Merapi (Lavigne et al., 2000ab; Lavigne and Thouret, 2003; de Bélizal et al., 2013), Semeru (Lavigne and Suwa, 2004; Doyle et al., 2010; Dumaisnil et al., 2010; Thouret et al., 2014), Soufrière Hills (Barclay et al., 2007), Colima (Davila et al., 2007; Capra et al., 2010) and Tungurahua (Jones et al., 2015), illustrating the global extent of locations with significant documented histories of rain-triggered lahar activity.

The initiation of rain-triggered lahars typically occurs via either particle detachment by rainsplash erosion and subsequent transport by overland flow (Segerstrom, 1950; Waldron, 1967), rill erosion caused by surface runoff (Nammah et al., 1986; Leavesley et al., 1989; Yamakoshi and Suwa, 2000; Lavigne and Thouret, 2003; Major and Yamakoshi, 2005; Barclay et al., 2007) or by shallow landsliding of saturated tephra layers above basal décollement surfaces (Rodolfo and Arguden, 1991; Hodgson and Manville, 1999; Manville et al., 2000b; Jensen et al., 2013) (Fig. 3.1). Numerous temporally and spatially variable factors contribute towards these lahar initiation processes including grain size distribution (Pierson et al., 2013), thickness (Janda et al., 1996; Scott et al., 1996a; Manville et al., 2000b) extent of compaction (Manville et al., 2000b) and volatile content (Waldron, 1967) of pyroclastic material; vegetation cover (Yamakoshi and Suwa, 2000; Barclay et al., 2007; Ogawa et al., 2007; Alexander et al., 2010) and type (Capra et al., 2010); rainfall intensity and duration (Rodolfo and Arguden, 1991;

Lavigne et al., 2000b; Van Westen and Daag, 2005; Hikida et al., 2007; Okano et al., 2012); slope angle (Pierson et al., 2013) and antecedent rainfall (Lavigne et al., 2000b; Barclay et al., 2007; Okano et al., 2012; Jones et al., 2015) (Fig. 3.2).

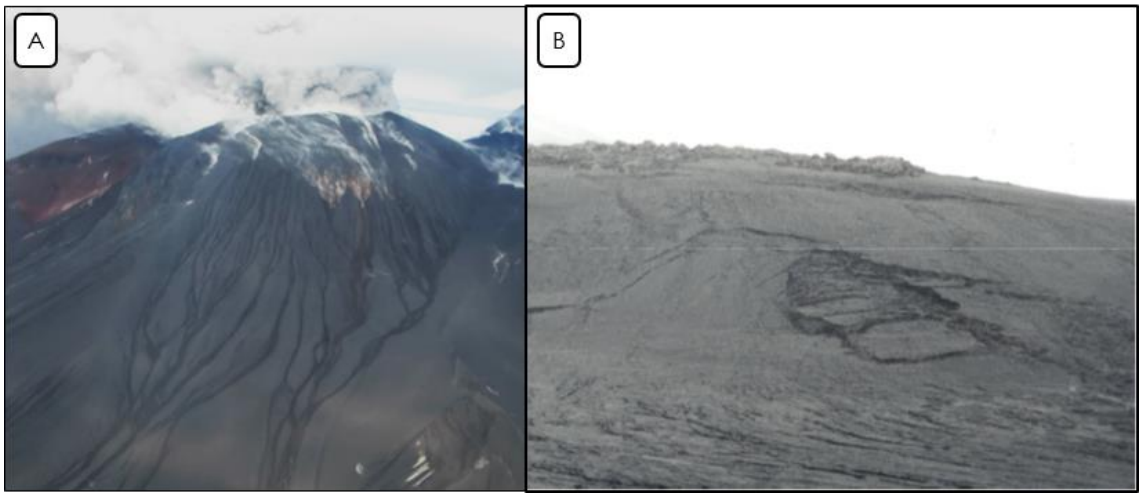

Figure 3.1: Photographs illustrating erosion mechanisms of pyroclastic deposits. A: Rill network and channel development on the upper edifice of Calbuco Volcano, Chile (April 2015). B: Shallow landsliding of the tephra blanket in the Mangatoetoenui catchment of Ruapehu, New Zealand (October 1995). The 0.20 m thick tephra layer was sliding on a thin (sub-cm) layer of fine-grained phreatomagmatic ash that was frozen to the underlying snow and ice.

The deposition mechanism of the volcaniclastic material, usually either PDC or ash-fall deposits, plays an important role in controlling spatio-temporal variability of rain-triggered lahar initiation. PDC deposits typically contain more fines as a result of a lack of aerodynamic sorting, are generally valley confined, and usually eroded by headward migration of knickpoints and channel widening/bank collapse (Manville et al., 2009b; Pierson and Major, 2014). Ash-fall deposits mantle the topography, are thinner, more widely distributed, better sorted, and easily eroded by rilling, uniform sheetwash or shallow landsliding (Pierson and Major, 2014). They typically display an exponential decrease in particle size and deposit thickness with increased distance from the vent but dispersal patterns can be more complex (e.g. Brazier et al., 1983).

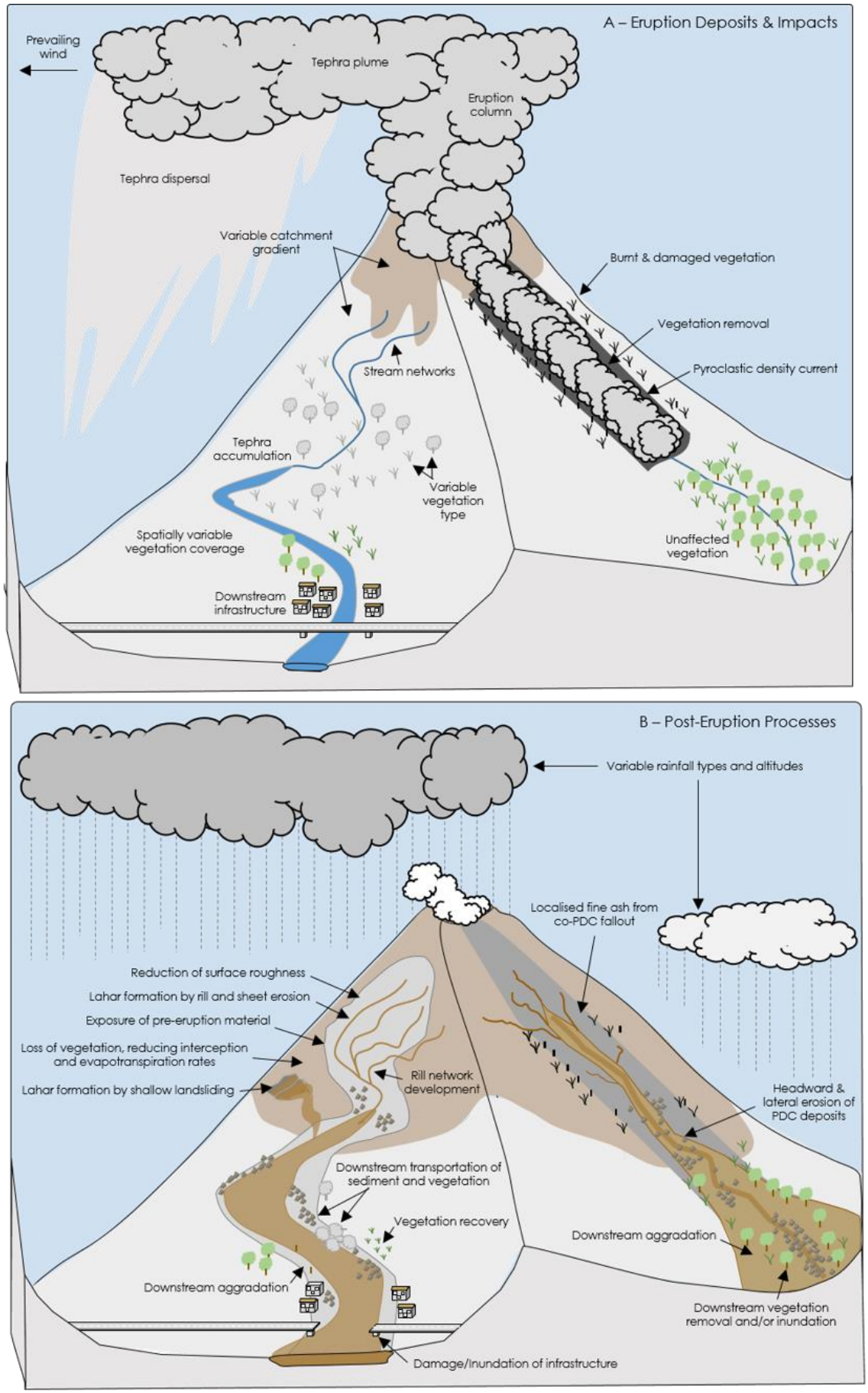
A – Eruption Deposits & Impacts
Prevailing wind
Tephra plume
Eruption column
Tephra dispersal
Variable catchment gradient
Burnt & damaged vegetation
Vegetation removal
Pyroclastic density current
Stream networks
Tephra accumulation
Variable vegetation type
Spatially variable vegetation coverage
Unaffected vegetation
Downstream infrastructure
B – Post-Eruption Processes
Variable rainfall types and altitudes
Localised fine ash from co-PDC fallout
Reduction of surface roughness
Lahar formation by rill and sheet erosion
Exposure of pre-eruption material
Loss of vegetation, reducing interception and evapotranspiration rates
Lahar formation by shallow landsliding
Rill network development
Headward & lateral erosion of PDC deposits
Downstream transportation of sediment and vegetation
Vegetation recovery
Downstream aggradation
Downstream aggradation
Downstream vegetation removal and/or inundation
Damage/Inundation of infrastructure

Figure 3.2: Schematic diagram illustrating the important factors in rain-triggered lahar initiation. A: Eruption deposits and impacts within proximal catchments. B: Post-eruption volcano-hydrologic processes within eruption-impacted catchments.

The surface of ash-fall deposits often undergoes post-deposition surface sealing and crusting as a result of raindrop impact and/or chemical precipitation, a process which increases surface resistance to erosion but also increases runoff (Waldron, 1967). Once the surface crust has been disturbed, runoff can remobilise underlying material, potentially resulting in rain-triggered lahar initiation (Waldron, 1967). PDC deposits are described by Pierson and Major (2014) as loose and highly erodible by rainfall and streamflow; although large, hot PDCs can produce deposits featuring welded zones which are more resistant to erosion. Ash-fall can damage vegetation via abrasion, weight-induced failure, burial, chemical damage or interference with leaf surface metabolic activity (Alexander et al., 2010; Swanson et al., 2013; Pierson and Major, 2014). PDCs can sand blast, burn, fell and in some examples strip and remove all vegetation within a valley (Pierson, 1985; Pierson and Major, 2014; Stinton et al., 2014).

Rainfall intensity/duration relationships have been a frequently utilised method of post-eruption rain-triggered lahar analysis. Studies at volcanoes including Pinatubo (Arboleda and Martinez, 1996; Tungol and Regalado, 1996; Van Westen and Daag, 2005), Mayon (Rodolfo and Arguden, 1991), Tungurahua (Jones et al., 2015), Merapi (Lavigne et al., 2000b) and Colima (Capra et al., 2010) have used this method, which typically displays a power-law relationship that suggests that lahar initiation occurs along a continuum from short duration, high intensity rainfall events to long duration, low-intensity events. Intensity/duration analysis compiles datasets of identified and/or instrumentally-detected lahars and identifies the range of rainfall conditions under which lahars

can potentially occur. Probabilistic analysis and forecasting of lahars has been undertaken at Tungurahua (Jones et al., 2015) using peak rainfall intensity and antecedent rainfall data. Probabilistic analysis of this nature uses the lahar and rainfall databases to examine the likelihood of lahars under different rainfall conditions and then applies it to real-time rainfall data to make lahar forecasts. Probabilistic lahar forecasting acknowledges the uncertainty present in the lahar triggering rainfall range identified during intensity/duration analysis. Such uncertainty is difficult to constrain during field-based studies due to the challenges of observing lahar initiation zones, given their typical proximity to the active vents of frequently eruptive volcanoes. This access issue, in combination with the complex nature of rain-triggered lahar initiation processes, makes it difficult to isolate the impacts of individual parameters upon rain-triggered lahar initiation. Rainfall simulation experiments are one method of approaching this issue, and have previously been utilised to study rainfall-runoff relationships in other disturbed earth systems such as wildfire-affected areas. Such simulations have typically been either field-based (e.g. Pierson et al., 2008; Woods and Balfour, 2010; Huang et al., 2013; Zhao et al., 2014) or lab-based (e.g. Bradford et al., 1987a; Singh et al., 2000; Jomaa et al., 2013; Wang et al., 2014) and have focused on a variety of parameters using different slope angles, rainfall regimes and bed compositions (Römkens et al., 2002; Liu et al., 2011; Huang et al., 2013).

Previous rainfall simulation studies have indicated that enhanced vegetation cover, and thus the process of vegetation recovery, increases infiltration and decreases runoff and erosion rates. This is a result of heightened permeability due to surface seal and crust disruption as well as increased soil stability and rainfall interception (Morgan et al., 1997; Major and Yamakoshi, 2005; Cerda and Doerr, 2008; Huang et al., 2013; Zhao et al., 2014). Elevated

slope angle and rainfall intensity increase runoff rates due to heightened occurrence of infiltration-excess overland flow (Horton, 1933; Luk, 1985; Liu et al., 2011; Huang et al., 2013; Jomaa et al., 2013). High surface moisture content and thus surface water potential, often induced by significant antecedent rainfall or long-duration rainfall events, acts to increase rainsplash-driven particle detachment in inter-rill regions via a reduction in surface shear strength (Luk, 1985; Bryan, 2000). In addition, increased surface roughness was shown by Römkens et al. (2002) to increase sediment yield under pre-defined rainfall conditions and rill development is heightened on steeper slopes (Gómez et al., 2003). Zhao et al. (2014) described runoff mechanisms on grassland plots under rainfall simulation conditions as infiltration-excess overland flow-dominant regardless of antecedent conditions, with saturation-excess flow occurring simultaneously after rainfall of sufficient duration. Despite such examples, quantitative studies of the relationship between rainfall intensity, antecedent conditions and surface sealing (important factors in rain-triggered lahar initiation) are limited (Jomaa et al., 2013), and while the systems studied to date have some parallels with elements of rain-triggered lahar initiation environments, none have focused specifically on rain-triggered lahars. This study aims to use calibrated rainfall simulations to identify the impact of grain size distribution and antecedent rainfall upon the rainfall-runoff properties of fresh tephra deposits in conditions analogous to those present in rain-triggered lahar initiation zones.

3.2. Methods

3.2.1. Ash Bed

Two airfall tephra samples were used during this study. The first was produced by the plinian andesitic eruption of Mt. Kelud, Indonesia on 13th February 2014. The second sample was a product of the plinian rhyolitic eruption of Chaitén, Chile in 2008. Both of these eruptions generated a rain-triggered lahar hazard due to the widespread deposition of pyroclastic sediments (Pierson et al., 2013; Umazano et al., 2014; Dibyosaputro et al., 2015; Major et al., 2016) The Chaitén sample was finer (D_{50} = 54.3 µm) than the Kelud sample (D_{50} = 525.8 µm) (Fig. 3.3; Table 3.1), offering a contrast in simulated lahar initiation conditions.

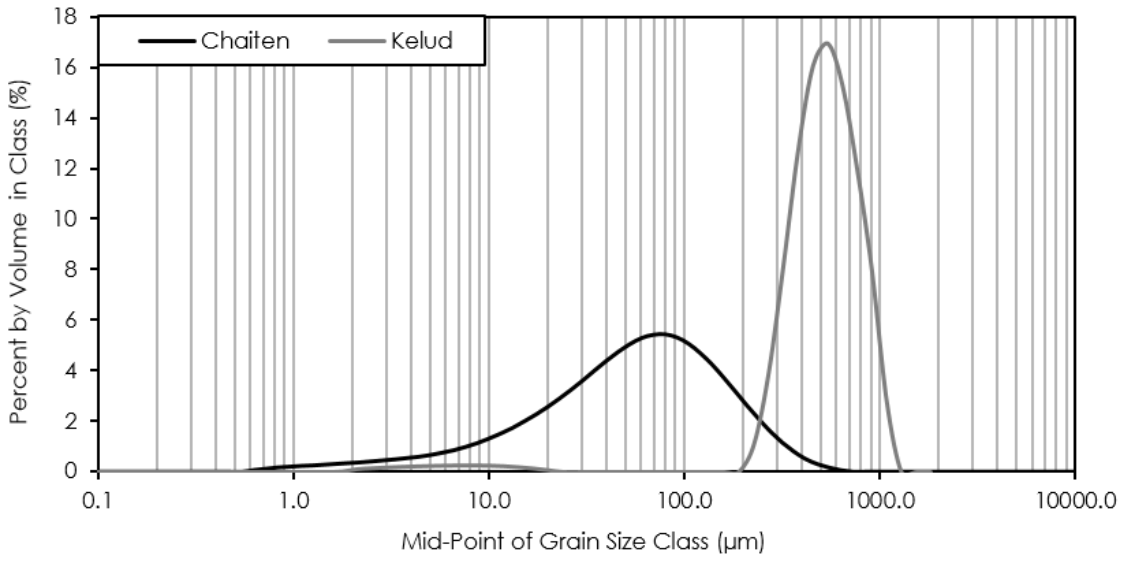

Figure 3.3: Grain size distributions of Kelud and Chaitén ash samples as measured using a Malvern Mastersizer 2000E laser diffractometer.

	d_{10}	d_{20}	d_{50}	d_{80}	d_{90}
Chaitén (µm)	9.4	19.2	54.3	120.5	173.9
Kelud (µm)	313.8	374.7	525.8	732.5	852.2

Table 3.1: Grain size distribution characteristics of Kelud and Chaitén ash samples as measured using a Malvern Mastersizer 2000E laser diffractometer.

Ash bed construction was dictated by the requirement to constrain the bulk density of the tephra while maintaining an experimental set-up which replicated natural conditions. To achieve this, ash beds were constructed within a 0.3 m × 0.3 m × 0.1 m stainless steel insert inside a rigid 0.3 m × 0.3 m shear box. Ash beds were lightly compacted using a 0.3 m ×x 0.3 m 10 kg mass, which was applied under gravity for 1800 s. The use of a shear box in this manner ensured that all samples were compacted under consistent normal and lateral stresses and rates of strain, while preventing the application of any shear. This approach also ensured no deformation of the walls of the ash bed during construction, thus allowing accurate capture of the mass and volume of tephra.

Samples were air dried, resulting in initial moisture contents by weight of 0.05% (Kelud) and 0.11% (Chaitén). Two types of ash bed were constructed: Ash Bed 1 (AB1), which consisted purely of the coarse Kelud ash (0.1 m depth) and Ash Bed 2 (AB2), which comprised 0.095 m depth of Kelud ash topped with 5 mm of finer Chaitén ash. These proportions were driven primarily by the availability of the different samples. The beds were each constructed in three uniform layers, with light raking of the surface of lower layers to minimise discontinuities (Huang et al., 2013). The surface was finally smoothed, levelled and lightly compacted, resulting in similar bulk densities of 1468 kgm^{-3} (AB1) and 1467 kgm^{-3} (AB2). These bulk tephra densities are within the range of 1200-1600 kgm^{-3} reported by Spence et al. (2005) from the eruption of Mt. Pinatubo in 1991 and close to the 1400 kgm^{-3} and 1450 kgm^{-3} values described at Eyjafjallajökull (Gudmundsson et al., 2012) and Pillate, Tungurahua (Bernard, 2013) respectively. When completed, the ash beds and steel insert were removed from the shear box and placed in a 75 mm-deep plastic tray on top of a micro-porous steel mesh. The base of the tray was free-draining to allow water to pass through the bottom of the ash bed.

3.2.2. Rainfall Simulator

A rainfall simulator was designed and constructed to replicate lahar-triggering rainfall under laboratory conditions. The experimental configuration (Fig. 3.4) consisted of a water tank, pulse-free gear pump, flow meter and nozzle-holding frame. The nozzles (Fulljet-1/2HH-30WSQ and Fulljet-1/2HH-40WSQ) were held by the frame at a height of 2.3 m above the ground, the maximum possible ground clearance.

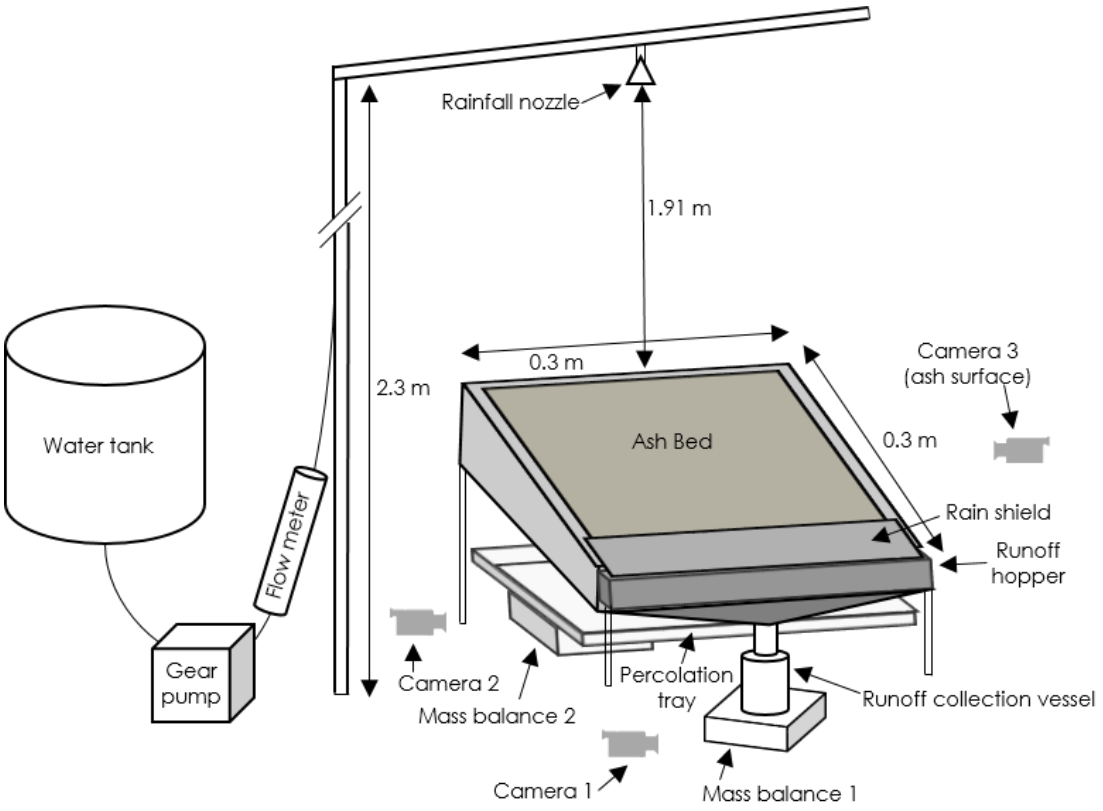

Figure 3.4: Schematic illustration of the experimental configuration utilised in this study.

In order to determine the optimal configuration for the production of analogous rainfall, and to identify the optimal sub-area within the 1 m^2 calibration area in which to locate the 0.3 m × 0.3 m ash bed, calibration of the rainfall rate was performed across a surface area of 1 m^2 using 65 spatially-distributed rainfall collection vessels, each with a diameter of 30 mm (Loch et al.,

2001). During each calibration experiment, the rainfall simulator was run for a period of 60 s and then the mass of water was measured in each container. Different pump settings (and therefore flow rates) were tested, with each nozzle separately tested for each pump setting and each pump setting/nozzle combination repeated three times. Simulator performance was assessed both in terms of rainfall intensity and uniformity. Uniformity was quantified using Christiansen's uniformity coefficient (C_U) (Christiansen, 1942). This coefficient takes as parameters the mean value ($\bar{x}$), the number of observations (n) and the sum of the deviations from the mean $\sum_1^n(x-\bar{x})$. It is expressed as a percentage; a higher percentage indicating more uniform rainfall, with values over 80% considered sufficient for successful rainfall simulations (Loch et al., 2001).

$$C_u = 100\left(1 - \frac{\sum_1^n(x-\bar{x})}{n\bar{x}}\right)$$

The selected configuration produced a flow rate of 8 × 10^{-4} m^3 s^{-1}. The spatial distribution of rainfall intensity produced by this configuration across both the entire 1 m^2 rainfall calibration area and the optimal 0.3 m × 0.3 m ash bed location is shown in Figure 3.5. The mean rainfall intensity for the entire rainfall calibration area under the rainfall conditions shown in Figure 3.5 was 2.5 mm min^{-1} with a C_U of 79.1%, but this value was improved in the optimal 0.3 m × 0.3 m sub-plot to 1.7 mm min^{-1} with a C_U of 91.9%. This rainfall intensity represents intense lahar-triggering rainfall; for example, it would be expected to trigger a lahar 100% of the time if sustained for >600 s at Tungurahua using the forecasting approach of Jones et al. (2015). Similar sustained rainfall intensity values are documented in many tropical rainfall datasets including Larsen and Simon (1993), Van Westen and Daag (2005) and Thouret et al. (2014).

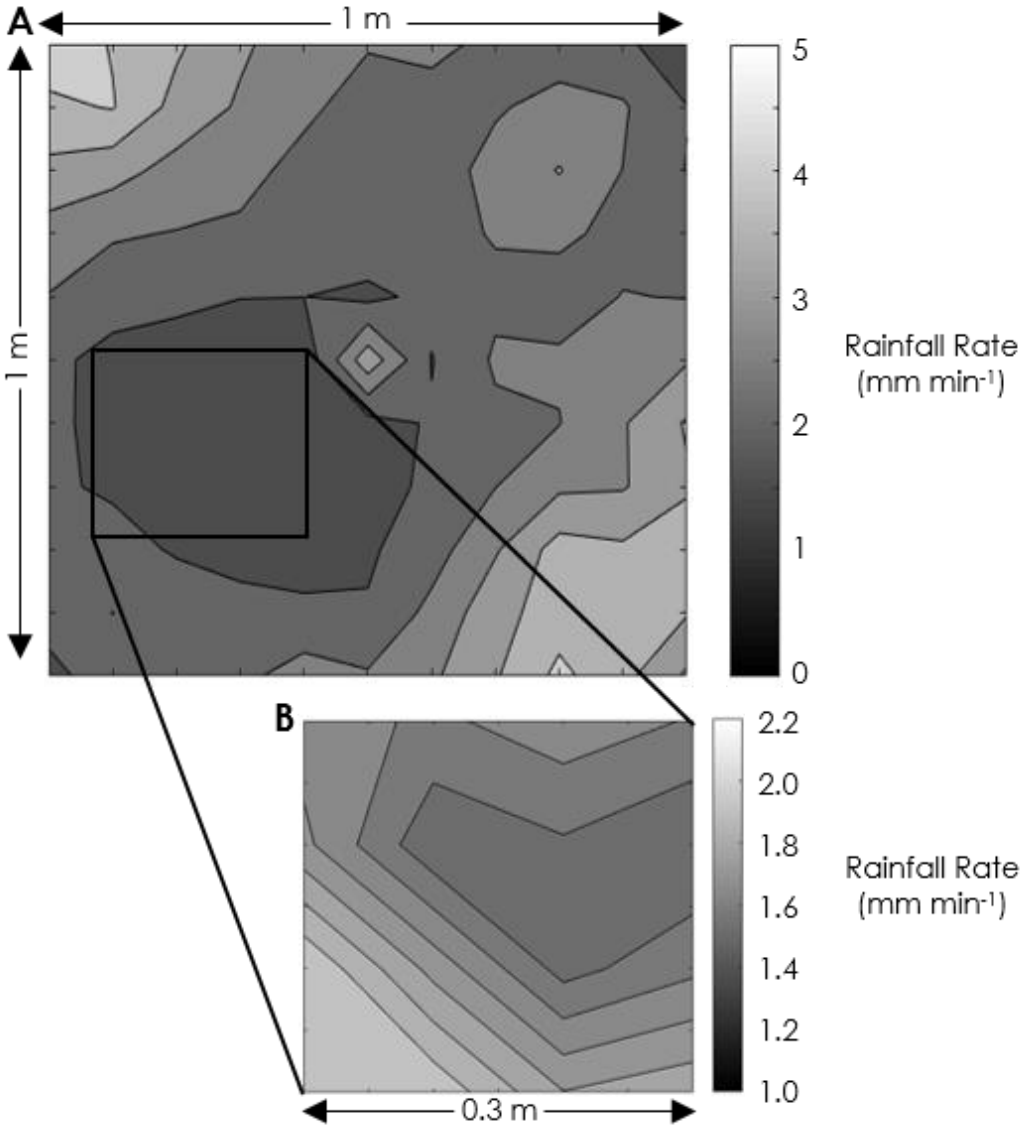

Figure 3.5: Spatial distribution of simulated rainfall using selected settings. A: Entire 1 m² rainfall calibration area. B: Optimal 0.3 m × 0.3 m sub-plot used for subsequent rainfall simulation experiments.

3.2.3. Experiment Configuration

Figure 3.4 illustrates the experimental configuration, featuring both the ash bed and rainfall simulator components. The ash bed was fitted onto a frame providing an angle of 28.2°, which was kept constant during this study. The use of this frame provided a minimum nozzle height of 1.91 m above the upslope extremity of the ash bed surface. A gutter hopper was fitted at the downslope

edge of the ash bed in order to funnel surface runoff into a beaker atop a mass balance (Ohaus NV4101; 0.2 g resolution), generating a continuous time series of runoff volume. Underneath the ash bed, a tray of identical dimensions sat atop a second mass balance, generating a continuous time series of infiltrated rainfall as it passed through the base of the 0.1 m-thick ash bed. A skirt around the sides of the frame waterproofed the infiltration tray and runoff beaker while a shield was in place to prevent rainfall directly entering the runoff gutter. High definition video cameras capturing 30 frames per second recorded continuous video of both the mass balance screens and the surface of the ash bed (Fig. 3.4).

Rainfall simulations were 1200 s in duration and were predominantly separated by consecutive "dry" periods of 24 hours. AB1 was used for four simulations (1.1-1.4), each separated by 24 hours. AB2 featured five simulations, the first four also separated by 24 hours (2.1-2.4) and the last (2.5) after an extended "dry" period of 120 hours. This method generated a range of pre-simulation antecedent conditions (Table 3.2), with the magnitude of 72-hour antecedent rainfall ranging from a minimum of 0 mm (Sims. 1.1, 2.1 & 2.5) to a maximum of 102 mm (Sims. 1.4 & 2.4). Time series of both runoff and infiltration through the base of the ash bed were recorded, as was footage of surface processes during the simulation.

Simulation:	1.1	1.2	1.3	1.4	2.1	2.2	2.3	2.4	2.5
Antecedent Rainfall - 24 HR - (mm):	0	34	34	34	0	34	34	34	0
Antecedent Rainfall - 48 HR - (mm):	0	34	68	68	0	34	68	68	0
Antecedent Rainfall - 72 HR - (mm):	0	34	68	102	0	34	68	102	0
Antecedent Rainfall - 96 HR - (mm):	0	34	68	102	0	34	68	102	0
Antecedent Rainfall - 120 HR - (mm):	0	34	68	102	0	34	68	102	0
Antecedent Rainfall - 144 HR - (mm):	0	34	68	102	0	34	68	102	34
Antecedent Rainfall - 168 HR - (mm):	0	34	68	102	0	34	68	102	68
Antecedent Rainfall - 192 HR - (mm):	0	34	68	102	0	34	68	102	102

Table 3.2: Antecedent rainfall amounts (in mm) applied to the tephra beds at timescales ranging from 24 hours to 192 hours prior to the commencement of each rainfall simulation.

Moisture content was analysed by oven drying samples before the first and immediately after the last simulation of each ash bed. The former used tephra samples from which the ash beds were constructed, while the latter was achieved by taking cores from the ash beds immediately after the final simulations. Samples were subsequently oven dried at 50°C until intermittent recordings of mass ceased to decrease. Moisture content could not be calculated after each individual simulation as disturbance of the ash bed surface would impact runoff and erosion in subsequent rainfall simulations.

3.3. Analysis

3.3.1. Surface Processes

The first rainfall simulations of each ash bed (1.1 & 2.1) demonstrate the behaviour of dry tephra deposits when initially exposed to rainfall. Video footage of the surfaces of AB1 and AB2 illustrates contrasting processes under such conditions, driven by the difference in grain size distribution at the surface (Fig. 3.6). The development of AB1 during simulation 1.1 is shown in Figs. 3.6A-C. The behaviour of this coarse ash bed was characterised by a darkening in colour

once rainfall was applied, an absence of visible surface runoff generation and a lack of surface texture variation. Particle movement was dominated by rain-splash driven detachment of individual coarse tephra grains, with no obvious rill formation or overland flow. As can be seen in Figs. 3.6A-C there was little visual change in the surface texture of AB1 during the first 870 s of simulation 1.1. Individual coarse particles reached the AB1 runoff collection vessel via particle detachment, but at low frequency. AB1 displayed little visual change during simulations 1.2-1.4, with rainsplash particle detachment remaining the dominant re-mobilisation mechanism. In contrast, the fine-grained surface layer of AB2 underwent significant visual change during the course of simulation 2.1 (Figs. 3.6D-I). With the onset of rainfall, the initial smooth, off-white surface immediately changed due to a combination of particle detachment and ash pellet formation. Particle detachment produced visible "puffs" of airborne ash upon raindrop impact as opposed to the visible parabolic movement of individual particles during simulation 1.1. Pellets of ash also formed as raindrops impacted the dry surface ash, with some ash pellets subsequently rolling downslope (Fig. 3.6E). These processes continued throughout the first 60 s of simulation 2.1, with visible particle detachment and pellet formation decreasing with time as the entire surface wetted up. Pellets of ash led to a rough, undulating surface across AB2 (Fig. 3.6F), similar to the "curd texture" identified at Mt. Ruapehu by Manville et al. (2000b). The first signs of surface runoff as Hortonian infiltration-excess overland flow, a product of surface sealing due to raindrop impact, occurred after 95 s and this soon became the dominant process of tephra re-mobilisation. Figs. 3.6G-H illustrate the inundation of the entire rough surface of AB2 with Hortonian overland flow within 240 s of the start of the simulation. Over the remaining 960 s, overland flow was the dominant mechanism driving sediment

transport and, together with physical raindrop impact, smoothed the surface of AB2 (Fig. 3.6l). Overland flow continued to be the dominant mechanism of sediment transport throughout simulations 2.2-2.4, resulting in the deposition of entrained fine-grained material in the runoff collection vessel. Nevertheless, it was noted that the erosion of AB2 during simulations 2.1-2.5 was not sufficient to visually expose the underlying coarse, more permeable tephra.

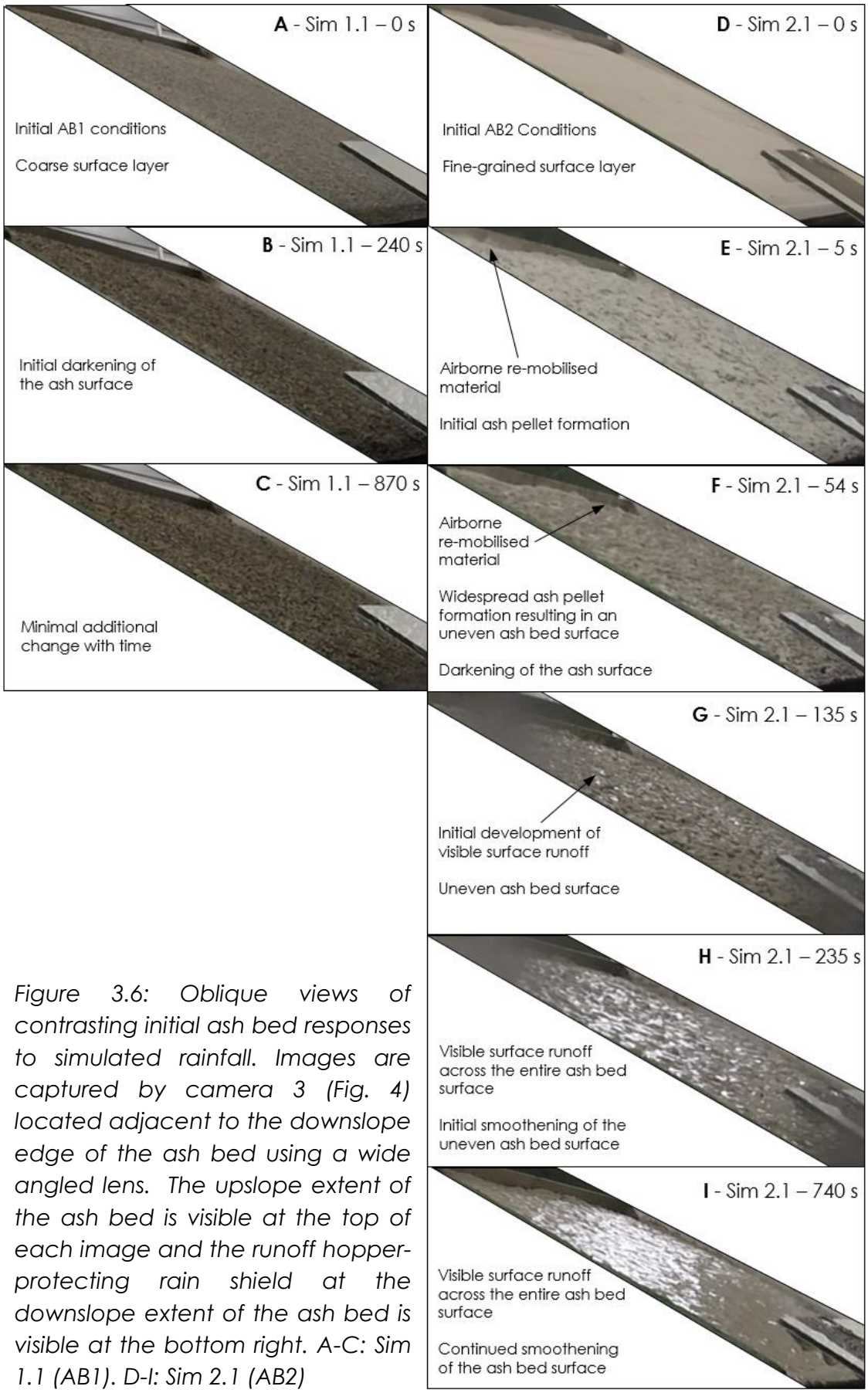

Figure 3.6: Oblique views of contrasting initial ash bed responses to simulated rainfall. Images are captured by camera 3 (Fig. 4) located adjacent to the downslope edge of the ash bed using a wide angled lens. The upslope extent of the ash bed is visible at the top of each image and the runoff hopper-protecting rain shield at the downslope extent of the ash bed is visible at the bottom right. A-C: Sim 1.1 (AB1). D-I: Sim 2.1 (AB2)

3.3.2. Rainfall-Runoff

Both total runoff volumes and runoff-rates (Fig. 3.7) increased from simulation 1.1-1.4 and 2.1-2.4; i.e. with increased antecedent rainfall (Table 3.2). Runoff rates from AB1 were lower than AB2, with simulations 2.3 and 2.4 producing runoff rates over an order of magnitude higher than simulations 1.3 and 1.4 under identical antecedent conditions. Initial impacts of an extended dry period (120 hours) can be seen in the total runoff values produced during simulation 2.5, which were 80% lower than the preceding simulation (2.4) and less than those produced during simulation 2.1 (Fig. 3.7). Runoff sediment concentration was negligible for AB1 simulations, with isolated coarse grains re-mobilised by rainsplash-driven particle detachment the only sediment to reach the runoff beaker. The sediment concentration of AB2 runoff was higher due to surface runoff entrainment but still low due to the lack of rill erosion within the rainfall simulations as a result of the limited slope length of the ash bed. AB2 mean runoff sediment concentrations (by weight) increased from 0.42% (2.1) to 0.60% (2.2) and reached a peak sediment concentration of 1.16% (2.3). Subsequent simulations (2.4 & 2.5) produced mean sediment concentrations of approximately 1% and 1.05%, respectively. The recorded runoff sediment mass from each AB2 simulation indicates that cumulative erosion resulted in the removal of at least 5.2% of the fine-grained surface layer of AB2 at the end of simulation 2.5. Maximum erosion from an individual simulation occurred during simulation 2.4 (2.1%).

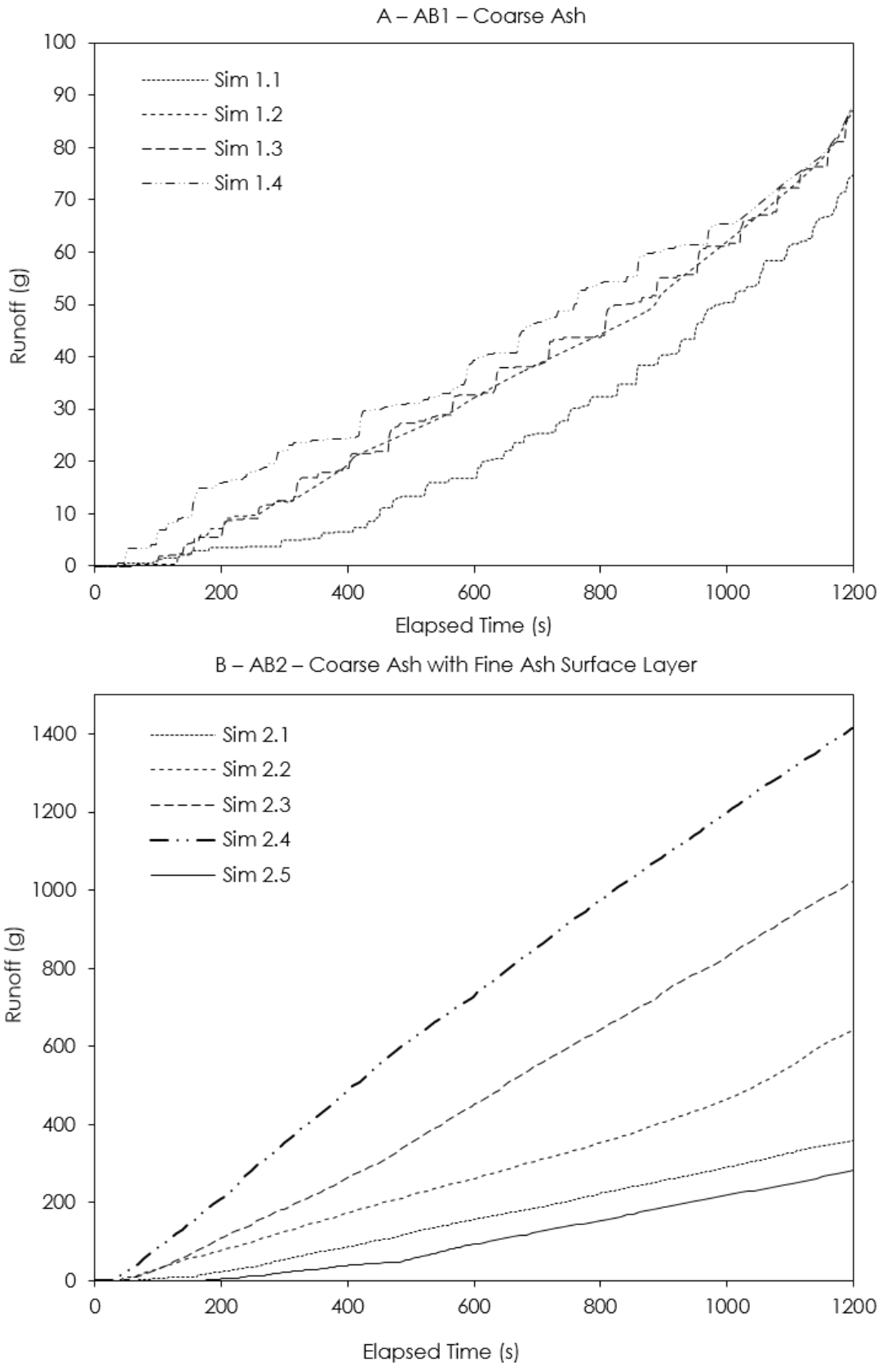

Figure 3.7: Time series of total runoff during all rainfall simulations. A: AB1 (coarse ash) B: AB2 (coarse ash with fine ash surface layer). Note differences in vertical scale.

In addition to the absolute increase in AB2 runoff rate compared with AB1 (Fig. 3.7), the impact of antecedent rainfall upon runoff relative to the initial simulations was enhanced for AB2 (Fig. 3.8). This is further emphasised in Figure 3.9, which isolates the final runoff totals at the end of AB1 and AB2 simulations and displays both the higher total runoff from AB2 compared to AB1 and the greater rate of AB2 runoff increase with heightened antecedent rainfall. When considering the total 1200 s runoff, both AB1 and AB2 exhibited increased runoff with increased antecedent rainfall. However, runoff increased by 292% for simulation 2.4 relative to 2.1 while this increase was only 18% for 1.4 relative to 1.1 (Fig. 3.8). Individual simulation-by-simulation increases in total runoff for AB2 simulations were 79% (2.1-2.2), 60% (2.2-2.3) and 38% (2.3-2.4). When the simulations are divided into four sub-periods of 300 s, it can be seen that the most marked impact of increased antecedent rainfall on runoff occurred during the first 300 s (Figs. 3.8 & 3.10). Runoff during this initial 300 s sub-period increased by 553% for simulation 2.4 relative to 2.1 and 334% for simulation 1.4 relative to 1.1 (Fig. 3.8B). Comparing simulation 2.4 to simulation 2.1, runoff increased by >200% in each of the four 300 s duration sub-periods (Fig. 3.8B). Conversely, comparing simulation 1.4 to simulation 1.1, runoff increased by only 44% for the 300-600 s sub period and decreased by approximately 20% during each of the last two 300 s duration sub-periods (Fig. 3.8A).

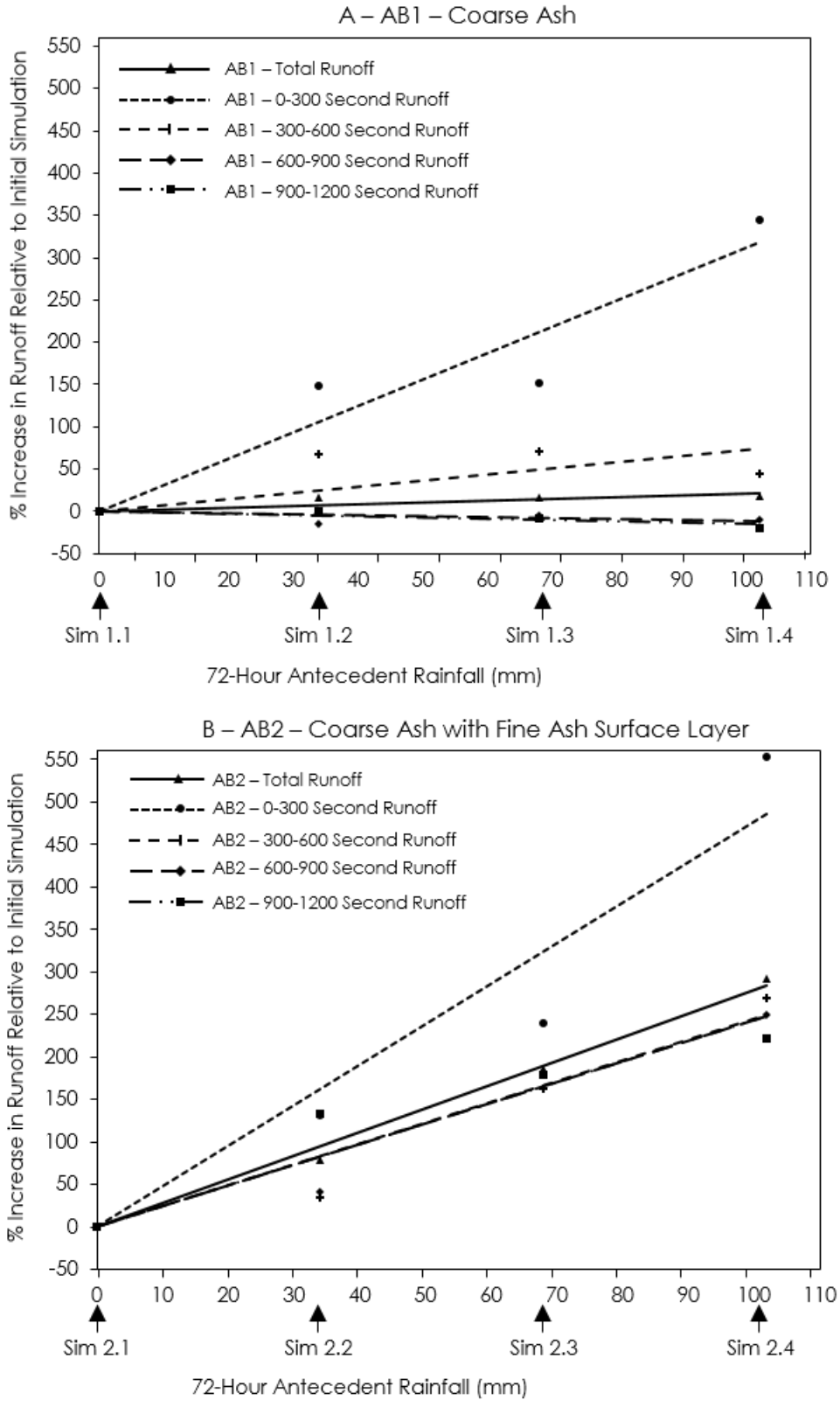

Figure 3.8: Percentage increase of both total and 300 s sub-period runoff relative to the runoff generated during the initial rainfall simulations (simulation 1.1 and 2.1, respectively) of A: AB1 (coarse ash) and B: AB2 (coarse ash with fine ash surface layer) simulations as antecedent rainfall was increased. Best fit least-squares linear regression lines are displayed for simulations 1.1 and 2.1.

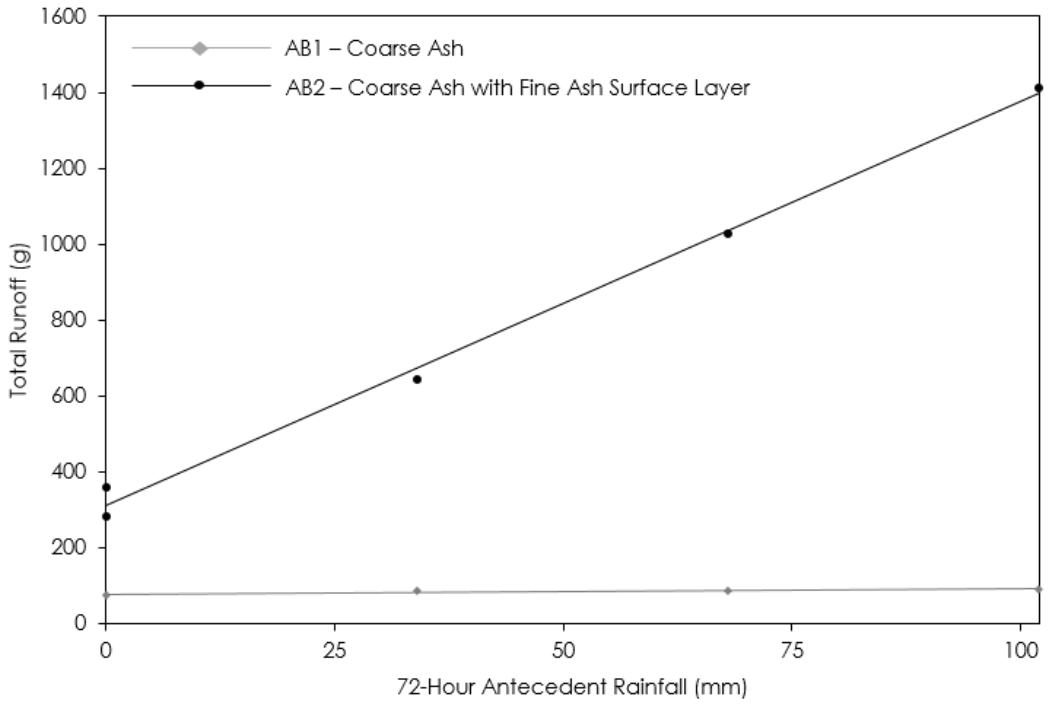

Figure 3.9: Total runoff mass at the conclusion of 1200 s duration rainfall simulations for AB1 (coarse ash) and AB2 (coarse ash with fine surface layer) under variable antecedent rainfall conditions. Best fit least-squares linear regression lines are displayed for both AB1 and AB2.

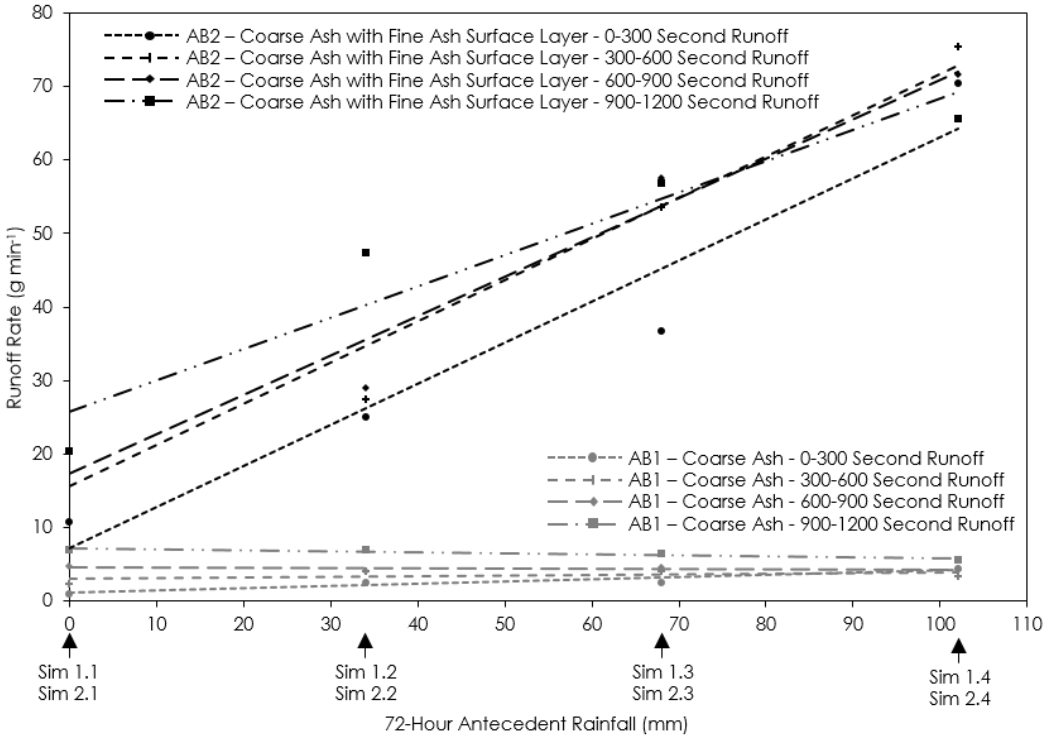

Figure 3.10: Runoff rates for the four 300 s sub-periods of both AB1 (coarse ash) and AB2 (coarse ash with fine ash surface layer) during rainfall simulations featuring variable antecedent conditions. Best fit least-squares linear regression lines are displayed for each 300 s sub-period of both AB1 and AB2.

Despite the biggest antecedent rainfall-driven impact on runoff rates occurring in the first 300 s of a rainfall simulation, runoff rates predominantly increase with time during simulations (Fig. 3.10). This increase during the simulation is largest and most consistent under conditions of low antecedent rainfall. As antecedent rainfall increased, runoff rates for the 300 s sub-periods converged, resulting in less extreme runoff rate increases during the simulations.

Variations in runoff rates between AB1 and AB2 impacts runoff lag time, which in this study is defined as the time period between the beginning of the rainfall simulation and the recording of 10 g of surface runoff. In both simulations, lag times declined as antecedent rainfall was increased (Fig. 3.11). Lag times were higher for AB1 than AB2 because of the coarse nature of the ash bed and the dominant mechanism of downslope transport: rainsplash and particle detachment.

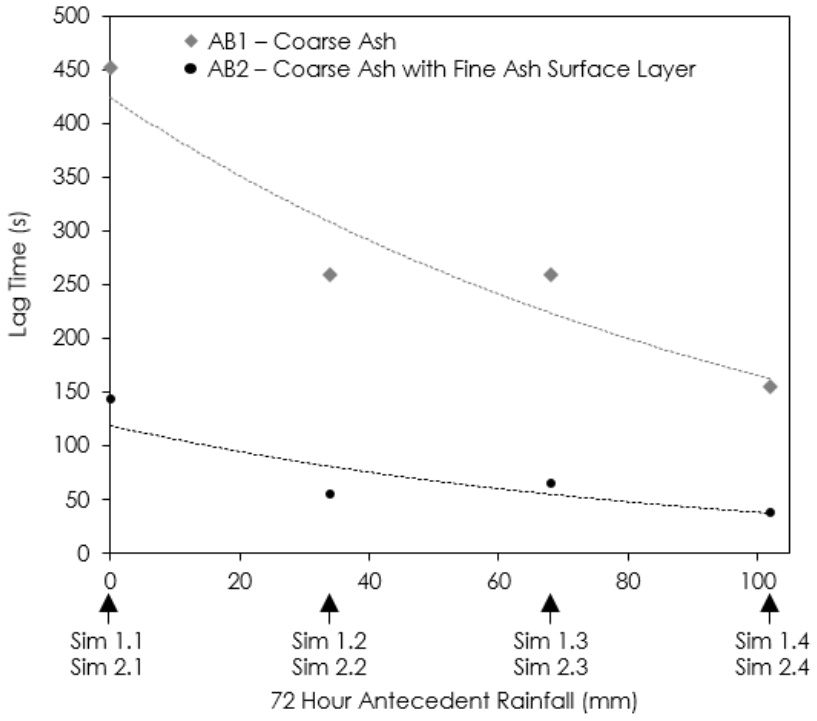

Figure 3.11: Runoff lag times of AB1 (coarse ash) and AB2 (coarse ash with fine ash surface layer) under variable antecedent conditions. Best fit least-squares linear regression lines are displayed for both AB1 and AB2.

Examining the temporal change in the relationship between runoff and infiltration during each rainfall simulation provides insight into the destination of applied rainfall under different conditions. Apparent infiltration rates (f') (Hawkins and Cundy, 1987; Dunne et al., 1991; Yu et al., 1997) during each of the rainfall simulations are derived using the average plot-scale rainfall rate (I) and recorded runoff rate (q).

$$f' = I - q$$

Previous studies have identified that apparent infiltration rates measured both in the field and in laboratory-based rainfall simulation experiments vary with slope angle and rainfall intensity (Hawkins and Cundy, 1987; Dunne et al., 1991; Major and Yamakoshi, 2005). In the present study, rainfall intensity and slope angle are constant, facilitating the inter-simulation comparison of apparent infiltration rates across all AB1 and AB2 simulations (Fig. 3.12). AB1 simulations displayed consistently high rates of apparent infiltration, with a small linear decrease in apparent infiltration rates with time during the simulations (Fig. 3.12). All AB2 simulations displayed decreased apparent infiltration rates relative to AB1 simulations (Fig. 3.12), with apparent infiltration rates during AB2 demonstrating exponential decay during the rainfall simulations (Fig. 3.12). Apparent infiltration rates progressively decreased during simulations 2.1-2.4, but simulation 2.5 displayed the highest apparent infiltration rates of all AB2 simulations, illustrating the impact of an extended dry period of 120 hours. Moisture content ($mass_{water}/mass_{ash+water}$) was calculated for tephra samples (Kelud and Chaitén) prior to ash bed construction and for both AB1 and AB2 immediately after the last simulations (1.4 and 2.5 respectively). Moisture content for the "dry" Kelud sample was 0.05%, while the moisture content for the "dry" Chaitén sample was

0.11%. The moisture content of the AB1 ash bed was 17.39% immediately after simulation 1.4, while the moisture content of AB2 was 17.11% immediately after simulation 2.5.

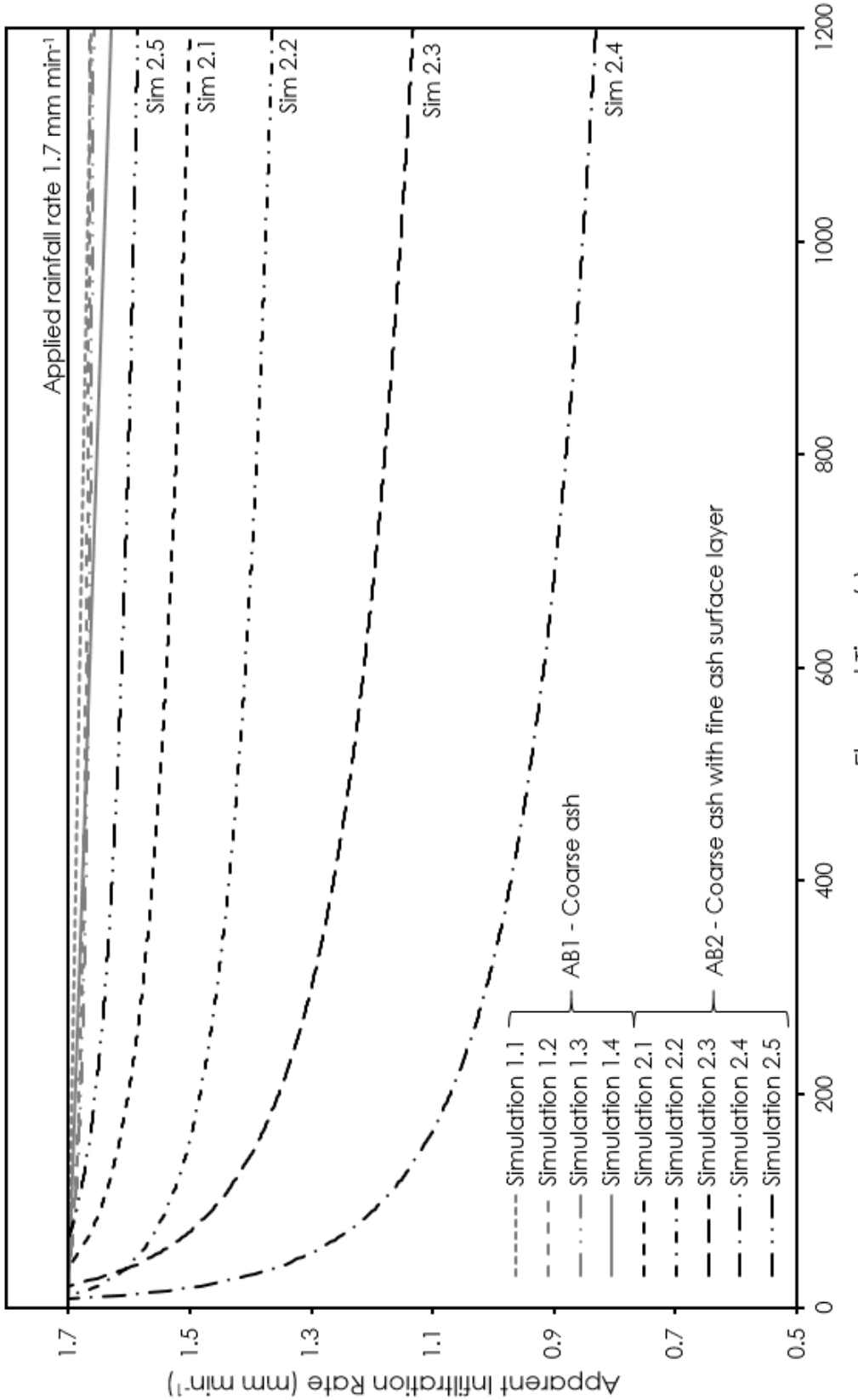

Figure 3.12: Apparent infiltration rate (f') curves for all AB1 and AB2 rainfall simulations derived from rainfall and runoff rate information. Best fit least-squares linear regression lines are displayed for AB1 simulations, and least-squares power regression lines are displayed for AB2 simulations.

3.4. Discussion

3.4.1. Grain Size Distribution

Variation in the grain size distribution of pyroclastic material is one of the primary factors impacting the frequency and mechanism of rain-triggered lahar initiation (e.g. Manville et al., 2000b; Pierson et al., 2013). Runoff increased by up to 1500% for AB2 compared to AB1 under identical antecedent conditions (Fig. 3.9), a product of the reduced permeability of the fine-grained surface layer of AB2. Runoff rates were further enhanced by surface sealing in AB2, which occurs as a product of aggregate breakdown, rearrangement of disrupted fragments, compaction and flattening (Slattery and Bryan, 1992). This surface sealing resulted in decreased infiltration rates and increased resistance to raindrop impact (Bradford et al., 1987a). Surface seal development during simulation 2.1, after initial rainsplash-driven particle detachment and the formation of ash pellets, is evident in Fig. 3.6, with gradual development resulting in widespread overland flow 740 s (Fig. 3.6l) after the onset of rainfall. Increasing runoff rates from simulations 2.1-2.4 indicate that no reduction in surface seal efficiency occurred until the extended dry period prior to simulation 2.5. Owing to the coarse nature of the tephra, such surface sealing did not occur during AB1 simulations; infiltration rates were sufficiently high that infiltration-excess overland flow did not occur and raindrop impact resulted in rainsplash-driven particle detachment throughout the simulations. As a result of these surface grain size distribution-driven impacts, apparent infiltration rates (Fig. 3.12) were lower for all AB2 simulations than AB1 simulations. This highlights the increased potential for lahar initiation as a result of enhanced runoff due to surface sealing of fine-grained surface layers.

The fine-grained surface layer of AB2 also acted to reduce the runoff lag time at the start of the simulations relative to AB1 (in the present study runoff lag time is defined as the time taken to record 10 g of runoff). This reduction in lag time was caused by the generation of infiltration-excess overland flow. Due to the limited slope length within the experimental set up, overland flow did not reach sufficient depths or velocities to induce rill erosion. Rills form following the exceedance of the threshold critical fluid shear stress or unit stream power for surface sediment entrainment (Nearing et al., 1989; Gilley et al., 1993). Fluid shear stress is a function of the flow depth and slope angle, while unit stream power is a function of flow depth, velocity and slope angle; for non-cohesive substrata, particle size, shape and mass density control the threshold value required to initiate rilling for a given slope angle (Gilley et al., 1993). Flow rates were not sufficient to induce rill erosion within the present study, but enhanced overland flow in AB2 simulations indicates the potential for rill network development if slope length was increased. Overland flow was minimal during AB1 simulations, which instead relied on rainsplash as the primary mechanism of downslope transport and runoff collection as a result of high infiltration rates (Figs. 3.11 & 3.12). The infiltration-dominated regime of AB1 indicates that rain-triggered lahar would require either extreme rainfall intensities or landsliding of the tephra layer above a basal décollement surface when saturated (Manville et al., 2000b; Jensen et al., 2013), particularly if emplaced above a less permeable substrate and on a steep slope.

3.4.2. Antecedent Rainfall

Increased antecedent rainfall and thus increased moisture content has been shown to enhance surface runoff in a variety of environments (e.g. Tisdall, 1951; Luk, 1985; Le Bissonnais et al., 1995; Castillo et al., 2003). With respect to volcanoes, increased antecedent rainfall has been shown to increase lahar frequency under specific rainfall conditions at locations including Soufrière Hills (Barclay et al., 2007) and Tungurahua (Jones et al., 2015). Rainfall simulations confirm that increased antecedent rainfall (Table 3.2) acts to increase runoff (Fig. 3.9), but AB2 displayed a much greater antecedent rainfall-driven impact than AB1. Total runoff from AB1 increased by 18% from simulation 1.1 to 1.4, while this increase was 292% for AB2 from simulation 2.1 to 2.4. The heightened runoff increase seen in AB2 relative to AB1 illustrates the compound impact of a reduction in pore space between ash particles, an increase in residual tephra moisture content due to prior simulations and enhanced surface sealing of the fine-grained surface layer of AB2. In the absence of surface sealing or infiltration-excess overland flow, the increase in runoff from AB1 is singularly a product of heightened rainsplash as a result of increased surface water content. Demonstrated antecedent rainfall-induced increases in runoff indicate that the peak rainfall intensity required for lahar initiation can be reduced under high antecedent rainfall conditions, an effect that is enhanced when fine-grained surface seal-forming layers are present.

Increased antecedent rainfall also acts to decrease runoff lag times from both AB1 and AB2 (Fig. 3.11). For AB1, this was a product of enhanced initial rainsplash due to increased residual surface water content. For AB2, this was driven by a reduction of infiltration rates as a product of both increased surface sealing and heightened initial tephra moisture content. Antecedent rainfall-

induced lag time reduction suggests that shorter duration rainfall events can still trigger lahars when residual moisture content is high, particularly if fine-grained surface layers featuring effective surface seals are present.

The extended dry period between simulations 2.4 and 2.5 (120 hours) replicated the recovery of an ash bed after an initial period of sustained rainfall. After the dry period, both total and 300 s sub-period runoff rates reduced; total runoff for simulation 2.5 was 80% lower than that of simulation 2.4. Total runoff for simulation 2.5 fell to below the values produced during simulation 2.1 (Fig. 3.12), while apparent infiltration rates for simulation 2.5 were the lowest of all AB2 simulations. No bed-wide infiltration-excess overland flow occurred during the entire 1200 s-duration simulation period of 2.5, a process that was visible after approximately 240 s of simulation 2.1 and during the entirety of simulations 2.2-2.4. This emphasises both the efficiency of surface sealing (of previously dry ash) throughout simulations 2.1-2.4, and the substantial increase in infiltration rates as a result of the 120-hour dry period before simulation 2.5. This is because extended dry periods (such as prior to simulation 2.5) impact the structure of surface seals (Assouline, 2004), with increased infiltration rates a product of reduced moisture content as well as inter-storm desiccation microcracking producing a more granular seal structure that acts to increase the permeability of the ash bed (Kuhn and Bryan, 2004). The absence of ash pellets or easily remobilised surface particles immediately prior to simulation 2.5 prevents the filling of pores with tephra upon the commencement of rainfall and therefore surface sealing to the extent identified in simulations 2.1-2.4 could not take place within simulation 2.5.

3.4.3. Simulation Duration

Changes in rainfall-runoff relationships during the course of individual simulations are intrinsically linked to both initial moisture content (and thus antecedent rainfall) and the total rainfall applied during the simulation. The rate of runoff increased during simulations for both AB1 and AB2, with this effect enhanced under low antecedent rainfall conditions (Fig. 3.10). Under low antecedent rainfall conditions, runoff rates increase gradually with time for both AB1 and AB2, caused by rising surface water content, and enhanced surface sealing induced by rain-beat compaction, respectively. As initial moisture content was increased through increased antecedent rainfall, runoff rates converged for all 300 s sub-periods, indicating more consistent runoff rates during the course of the simulations (Fig. 3.10).

3.4.4. Implications for Rain-Triggered Lahar Research

Using a new, inexpensive experimental set up, the present study has investigated and isolated some of the key factors previously identified in both field-based studies of rain-triggered lahars and statistical analysis of rain-triggered lahar initiation thresholds. Antecedent impacts on lahar frequency have been highlighted previously at Soufrière Hills (Barclay et al., 2007), Tungurahua (Jones et al., 2015), Merapi (Lavigne et al., 2000a), Yakedake (Okano et al., 2012), Colima (Capra et al., 2010) and Semeru (Lavigne and Suwa, 2004). The present study demonstrates that when residual ash moisture content is high, antecedent rainfall-driven runoff is increased and lag time is decreased, enhancing the potential for both lower intensity and shorter duration storm events to trigger lahars. This indicates that both lahar frequency and lahar

volume can be expected to increase with heightened antecedent rainfall (e.g., as identified at Tungurahua by Jones et al., 2015). The impact of extended dry spells is also demonstrated, with a 120 hour-long dry spell reducing total runoff to below that produced by the initial dry ash bed but not affecting erosion rates. Wetting and drying cycles thus play an important role in surface seal development, destruction and potential re-development, highlighting the importance of the post-eruption rainfall and drying history upon rainfall-runoff relationships and thus lahar-triggering thresholds.

Surface sealing of fine-grained tephra has been reported to cause increased lahar frequencies at Unzen (Yamakoshi and Suwa, 2000), while coarse, permeable deposits have been reported to cause reduced lahar frequencies at Merapi (Lavigne et al., 2000a) and Mayon (Rodolfo and Arguden, 1991). The development of surface seals (as observed in AB2 simulations) may act to delay peak post-eruption rain-triggered lahar probability as early rainfall that is insufficient to remobilise the ash may instead prime it for later major lahars by creating an effective surface seal. This study emphasises the compound impacts of both a fining of the grain-size distribution and increased antecedent rainfall, displaying a 1790% increase in runoff and a 92% decrease in lag time for an ash bed with a fine-grained surface layer that had received 102 mm of 72-hour antecedent rainfall relative to a coarse dry ash bed.

Primarily due to a limited ash supply, the present study focused on grain size distribution and antecedent rainfall as independent variables. However, a similar experimental configuration could be utilised to isolate and study the impact of factors including gradient, rainfall intensity, rainfall duration, vegetation coverage and deposit thickness on rain-triggered lahar generation

under controlled conditions. The extension of the length of the ash bed would also facilitate the further investigation of the role of rill formation in RTL initiation.

3.5. Conclusions

A new and repeatable rainfall simulation-based experimental configuration has been used to study conditions analogous to those present during the initiation of rain-triggered lahars. Calibrated rainfall simulations have illustrated that both finer-grained surface material and increased antecedent rainfall increase runoff rates and decrease runoff lag time from laboratory-constructed tephra beds. Surface sealing occurred within minutes of rainfall on dry fine-grained surface tephra after initial airborne remobilisation and ash pellet formation but was not evident on coarser material. This surface seal reduced infiltration rates and generated downslope sediment transport via entrainment within infiltration-excess overland flow, illustrating the potential for enhanced lahar initiation after initial surface seal-inducing rainfall. Additionally, an antecedent rainfall-driven increase in runoff and a reduction in runoff lag time highlights the potential for lahar formation from both lower intensity and shorter duration storm events when tephra residual moisture content is high. Conversely, extended dry periods reduced the effectiveness of the surface seal and increased infiltration rates, highlighting the importance of wetting and drying cycles upon lahar initiation thresholds. Rainsplash-driven particle detachment was the primary transport mechanism of sediment from simulations featuring coarser surface tephra due to consistently high infiltration rates irrespective of antecedent rainfall. Rainfall simulations of the nature designed and developed in this study could be utilised to investigate a range of features related to lahar

initiation under controlled conditions. Expanding the range of studied ash samples, rainfall parameters, antecedent conditions and slope angles would give further insight into lahar-triggering processes that are often difficult to directly examine in the field due to access issues associated with the location of lahar initiation zones.

Chapter 4: Probabilistic Analysis of Rain-Triggered Lahar Initiation at Tungurahua Volcano

Summary

Semi-continuous production of pyroclastic material by intermittent strombolian, vulcanian and sub-plinian eruptions at Volcán Tungurahua, Ecuador has created a persistent rain-triggered lahar hazard during the 1999-present eruptive episode. Lahars threaten the city of Baños, which lies approximately 8 km from the crater, as well as other villages and vital infrastructure situated in close proximity to the dense radial drainage network of the volcano. This study analyses the initiation of rain-triggered lahars and the influence of antecedent rainfall on this process in two northern instrumented drainages, La Pampa and the Vazcun. Analysis of lahar-triggering rainfall intensity and duration between March 2012 and June 2013 yields a power-law relationship, while Receiver Operating Characteristic (ROC) analysis indicates that peak rainfall intensity (10 minute, 30 minute and 60 minute) is the most effective single predictor of lahar occurrence. The probability of a lahar exceeding a pre-defined magnitude increases with peak rainfall intensity. Incorporation of antecedent rainfall (24 hour, 3 day, 5 day and 7 day) as a secondary variable significantly impacts lahar probabilities, particularly during moderate-high intensity rainfall events. The resultant two and three-dimensional lahar probability matrices are applied to rainfall data between 1st July and 31st December 2013 with the aim of predicting lahar occurrence. Composite lahar indicators compiled from the mean lahar probability estimates of individual matrices are shown to perform this task most effectively. ROC analysis indicates

a probability >80% that these composite indicators will generate a higher estimated lahar probability for a randomly selected lahar event than a randomly selected non-lahar event. This method provides an average of 24 minutes of additional warning time compared with the current Acoustic Flow Monitors (AFMs) used for lahar detection, effectively doubling warning times for key downstream infrastructure in the two drainages. Ultimately, this method of lahar analysis could be used to construct real-time probabilistic rain-triggered lahar forecasts as an aid to current lahar hazard mitigation techniques at any location with a significant rain-triggered lahar hazard and a basic instrumental set-up.

4.1 Introduction

Volcán Tungurahua (Lat. 01°28'S; long. 78°27'W) is a 5,023 m high stratovolcano located in the Eastern Cordillera of the Ecuadorian Andes (Fig. 4.1), lying approximately 120 km south of Quito and 33 km Southeast of Ambato, the capital of Tungurahua Province (Hall et al., 2013). The steep-sided edifice features a radial drainage pattern, whilst the Puela, Chambo and Pastaza rivers surround the volcano to the South, West and North respectively. The Pastaza river flows eastwards, past the city of Baños (pop. 18,000), which lies c. 8 km North of the summit of the volcano at an altitude of 1,800 metres above sea level (Williams et al., 2008; Eychenne et al., 2012; Hall et al., 2013). Baños is a popular tourist destination and its population increases to as much as 50,000 during holiday periods (Hall et al., 2013). Due to its location, the city (along with surrounding smaller villages) is threatened by numerous hazards from Tungurahua including lahars, pyroclastic density currents (PDCs) and ashfall (Williams et al., 2008). This issue is further exacerbated by recent increases in population, infrastructure and

economic activity in the region (Biggs et al., 2010). The primary road linking Baños with the Pan-American Highway and other provincial cities crosses several of the lahar-prone northern drainages of Tungurahua; whilst smaller roads which reduce travel times to the large city of Riobamba cross many of the western drainages (Sorenson et al., 2003).

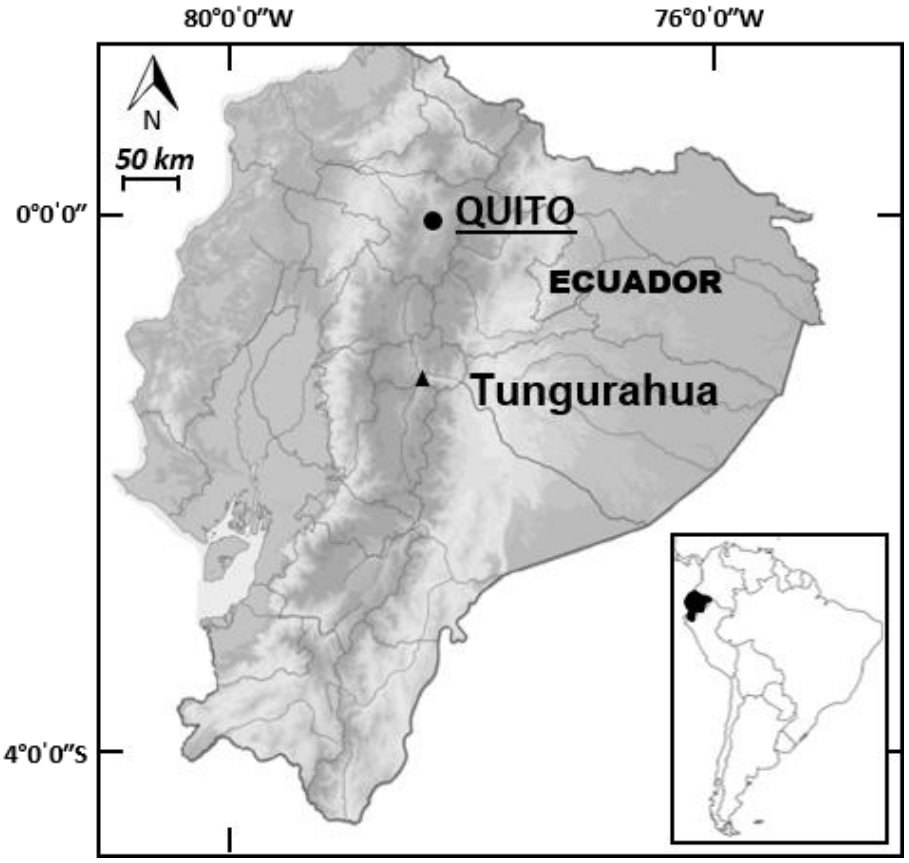

Figure 4.1: Location Map of Tungurahua Volcano.

Previous lahar-centric studies at Tungurahua have focused on the modelling of single flow events (Williams et al., 2008). This contrasts with studies of lahar initiation thresholds over a significant time period such as those undertaken at Mt. Pinatubo (Arboleda and Martinez, 1996; Martinez et al., 1996; Rodolfo et al., 1996; Tungol and Regalado, 1996; Van Westen and Daag, 2005); Mt. Mayon (Rodolfo and Arguden, 1991); Mt. Merapi (Lavigne et al., 2000a; Lavigne et al., 2000b); Mt. Semeru (Lavigne and Suwa, 2004); Soufrière Hills (Barclay et al., 2007);

Volcán de Colima (Capra et al., 2010); Sakurajima (Hikida et al., 2007) and Yakedake (Okano et al., 2012). This study presents an evaluation of the lahar activity within two lahar-prone Northern drainages of Tungurahua between March 2012 and December 2013; with a primary focus on the impacts of antecedent rainfall on the probability of lahar occurrence.

4.2 Eruptive Activity at Volcán Tungurahua

Since Spanish colonial records began in 1532 AD, Tungurahua has displayed frequent eruptive activity (Hall et al., 1999). There are 17 known distinct eruptions during this timespan, and an average of one major eruptive episode per century. Such major eruptions have occurred in 1640-1641, 1773-1777, 1886-1888, 1916-1918 and 1999-Present and range in composition from basaltic andesite to dacite (Hall et al., 1999; Le Pennec et al., 2008; Biggs et al., 2010).

The current period of eruptive activity began in October 1999 after approximately 80 years of dormancy and has featured intermittent strombolian, vulcanian and sub-plinian eruptions (Eychenne et al., 2012; Hall et al., 2013). Eruptive products have been predominantly andesitic (58-59% SiO_2) with rare dacitic outbreaks (Samaniego et al., 2011; Eychenne et al., 2012; Hall et al., 2013). This activity (VEI 1-3) has been characterised by lava emissions, tephra falls, PDCs and lahars; with one explosive phase in August 2006 producing PDCs with runout distances of 7.5-8.6 km. These flows reached the base of Tungurahua's edifice and caused six fatalities (Eychenne et al., 2012; Douillet et al., 2013a; Douillet et al., 2013b; Hall et al., 2013; Bernard et al., 2014). May 2010 included another explosive eruptive phase featuring PDCs with runout distances of 1-3 km (Eychenne et al., 2012; Myers et al., 2014); more recently eruptive activity in July

2013 and February, April and August 2014 has produced PDCs and ashfall deposits.

4.3 Lahar Background

A lahar is commonly defined as "a rapidly flowing mixture of rock debris and water (other than normal stream flow) from a volcano" (Smith and Fritz, 1989). Therefore, the term lahar describes a continuum of flow types, often categorised in scientific literature into sub-divisions such as debris flows (>60% sediment by volume), hyperconcentrated flows (20-60% sediment by volume) and streamflows (<20% sediment by volume) (Fagents and Baloga, 2006; Doyle et al., 2010). Liquid-solid interactions within a lahar can be highly variable on both a spatial and temporal scale due to erosional and depositional processes including bulking (the increase in flow volume by erosion), de-bulking (volume loss by selective deposition), dilution (the increase in flow volume via the interaction with a water source) and infiltration (the loss of liquid into permeable substrates) (Fagents and Baloga, 2006).

Lahar initiation requires a supply of volcaniclastic material, a source of water, adequate relief and a trigger mechanism. The latter can include crater lake ejection (Kilgour et al., 2010); crater lake breaching (Manville and Cronin, 2007; Massey et al., 2009); syn-eruptive melting of ice and snow by PDCs and surges (Lowe et al., 1986; Major and Newhall, 1989; Pierson et al., 1990; Waythomas et al., 2013); debris avalanche de-watering (Cummans, 1980) and rainfall initiation (Waldron, 1967; Rodolfo and Arguden, 1991; Major et al., 1996; Rodolfo et al., 1996; Hodgson and Manville, 1999; Lavigne and Thouret, 2003; Barclay et al., 2007; Capra et al., 2010; Dumaisnil et al., 2010; de Bélizal et al.,

2013). The primary initiation mechanism at Tungurahua is that of rainfall on fresh pyroclastic deposits.

Rain-triggered lahars occur due to a variety of specific mechanisms. These mechanisms include rilling and erosion due to heightened Hortonian overland flow as a result of deposit saturation (Horton, 1945; Collins et al., 1983; Collins and Dunne, 1986; Kean et al., 2011); as well as shallow landslides (often above an internal detachment surface such as a contact between ash layers) via buoyant support provided by heightened sub-surface water pressure within saturated deposits (Iverson and Lahusen, 1989; Hodgson and Manville, 1999; Manville et al., 2000b; Crosta and Dal Negro, 2003; Zanchetta et al., 2004). Additional competing processes involved in rain-triggered lahar initiation are those of surface crust formation and rain splash erosion (Fiksdal, 1982; Collins et al., 1983; Collins and Dunne, 1986; Folsom, 1986; Bradford et al., 1987a; Leavesley et al., 1989; Manville et al., 2000b). Below a rainfall kinetic energy threshold, rain beat compaction forms a runoff-enhancing surface crust on pyroclastic deposits that enhances Hortonian overland flow and encourages potential lahar formation via sheetwash. Once this rainfall kinetic energy threshold is exceeded the detachment of surface particles by splash erosion becomes the dominant process rather than crust formation (Wang et al., 2014). Rain splash erosion of this nature has high erosional potential and whilst it does not decrease deposit infiltration rates like surface crust formation, it does increase the amount of available material that can be easily transported (Bradford et al., 1987a; Wang et al., 2014). Other factors which have been identified as impacting the nature of the rain-triggered lahar hazard include pyroclastic deposit thickness (Rodolfo and Arguden, 1991; Janda et al., 1996; Scott et al., 1996a), the grain size distribution of the pyroclastic material (Yamakoshi and Suwa, 2000; Ogawa et al.,

2007; Craddock et al., 2012), deposit volatile content (Waldron, 1967), slope angle (Gómez et al., 2003), vegetation coverage (Yamakoshi and Suwa, 2000; Major and Yamakoshi, 2005; Alexander et al., 2010), vegetation type (Capra et al., 2010), climate (Lavigne et al., 2007; Okano et al., 2012; de Bélizal et al., 2013), the presence of volatile salts and/or hydro-repellent compounds (Murata et al., 1966; Waldron, 1967; Capra et al., 2010), and the post-deposition age and experiences of the deposit (Fiksdal, 1982; Major and Yamakoshi, 2005).

Lahars are a high-frequency hazard at Tungurahua due to high annual rainfall and the frequent eruptive activity which regularly replenishes supplies of loose unconsolidated pyroclastic material on the volcano. This hazard is further enhanced by the steep upper slopes of Tungurahua, which have an average gradient of c. 28° (Hall et al., 2013). Tungurahua lies in the Intertropical Convergence Zone (ITCZ) and this results in warm, moist air from the Amazon lowlands condensing as it meets the Eastern Cordillera of Ecuador, giving rise to an estimated 3,000 mm of annual rainfall. However, sharp topographic irregularities and high relief in the region produce significant spatial variability and numerous local microclimates (Garreaud, 2009; Le Pennec et al., 2012; Hunink et al., 2014) so that some high altitude locations receive >6,000 mm yr^{-1} due to enhanced orographic rainfall (Garreaud, 2009). Summer precipitation in the region is typically characterised by intermittent *aguaceros* (deluges) between dry periods whilst winter precipitation usually occurs in the form of more sustained *lovizna* (drizzle) that gives larger total rainfall (Le Pennec et al., 2012).

4.4. Methods

4.4.1. Study Region

The Vazcun (Figs. 4.2A & 4.2B) and La Pampa (Fig. 4.2C) catchments located on the northern slopes of Volcán Tungurahua are the focus of this study (Fig. 4.3). The La Pampa catchment (5.07 km^2) covers twice the area of the Vazcun catchment (2.23 km^2). The Vazcun is generally steeper (mean slope 40.4° versus 31.8°), but both catchments have a similar maximum gradient (77.0° and 77.6° respectively). These two drainages were selected for analysis due to the high frequency of rain-triggered lahars within them, their proximity to human activity and vital infrastructure, and the fact that they are instrumented (Fig. 4.3).

Figure 4.2: Images of lahars and lahar impacts in the Vazcun and La Pampa catchments. A: Early Stages of the 12th February 2005 Vazcun Valley lahar. Flow front is visible at the upstream end of the El Salado Baths. B: Peak stage height of the 12th February 2005 Vazcun Valley lahar. C: Efforts to clear the Baños to Pan-American Highway link in October 2007 after a lahar in the La Pampa drainage inundated the road. All photos courtesy of IGEPN.

Following the onset of new eruptive activity in October 1999, the majority of lahars in the La Pampa drainage partially or totally blocked the road between Baños and the Pan-American Highway for hours or even days (Fig. 4.2C). No injuries or fatalities occurred as a result but several cars have been buried by lahar deposits after failed attempts to cross the La Pampa during the early-stages of flow inundation. In 2008 this issue was alleviated by the construction of a bridge; however large lahars still pose a risk to this vital piece of infrastructure. One of the largest known lahars in the La Pampa catchment occurred on the 10th May 2000, with an estimated peak discharge of 110 $m^3 s^{-1}$ and a flow volume of at least $1x10^5$ m^3.

The El Salado Baths are a popular visitor attraction within the Vazcun Valley located approximately 1 km upstream of Baños. These baths host around 300 visitors per day in peak season and on the 12th February 2005 the outer walls were partially destroyed by a large lahar (Fig. 2) (Williams et al., 2008). This flow came within tens of centimetres of inundating the baths, had a peak discharge of approximately 100 $m^3 s^{-1}$ and an estimated total volume of $5.4\text{-}7x10^4$ m^3 (Williams et al., 2008). The El Salado Baths remain a location at risk from lahars in the Vazcun Valley, along with the primary road bridge approximately 1 km further downstream and other structures proximal to the drainage in western parts of Baños.

Acoustic Flow Monitors (AFMs) perform simple signal processing on the ground vibration signals picked up by cheap and robust geophones to detect the passage of lahars [e.g. Pinatubo (Tungol and Regalado, 1996); Merapi (Lavigne et al., 2000b); Ruapehu (Cole et al., 2009)]. There is a network of c. 14 active AFMs around Tungurahua located in 6 different drainages. The Vazcun

(VAZ-01) and La Pampa (JUI-01) AFMs utilised in this study (visible in Fig. 4.3) are located at altitudes of 2,455 m and 2,390 m respectively. The Vazcun AFM lies c. 4 km upstream of the primary road crossing (alt. 1,850 m) and 2.9 km upstream of the El Salado Baths (alt. 1,950 m). The La Pampa AFM lies c. 1.9 km upstream of the primary road crossing (alt. 2,000 m). These AFMs register the average amplitude recorded at five minute intervals on a continuous basis. The single telemetered rain gauge on the slopes of Tungurahua is located at an altitude of 2,725 m in the Pondoa region on the Northern slopes of the volcano (Fig. 4.3) and provides rainfall data every 5 minutes at a sensitivity of 0.5 mm.

Tungurahua is monitored from the Tungurahua Volcano Observatory (OVT), operated by the Instituto Geofísico, Escuala Politécnica Nacional (IGEPN) and located approximately 12 km NNW of the crater. In addition to the monitoring at OVT, a community-based monitoring system consisting of a network of volunteers known as vigias has existed at Tungurahua since 2000 (Stone et al., 2014). This network currently consists of approximately 35 vigias and fulfils multiple risk reduction roles by working collaboratively with both local communities and the scientists at OVT (Stone et al., 2014).

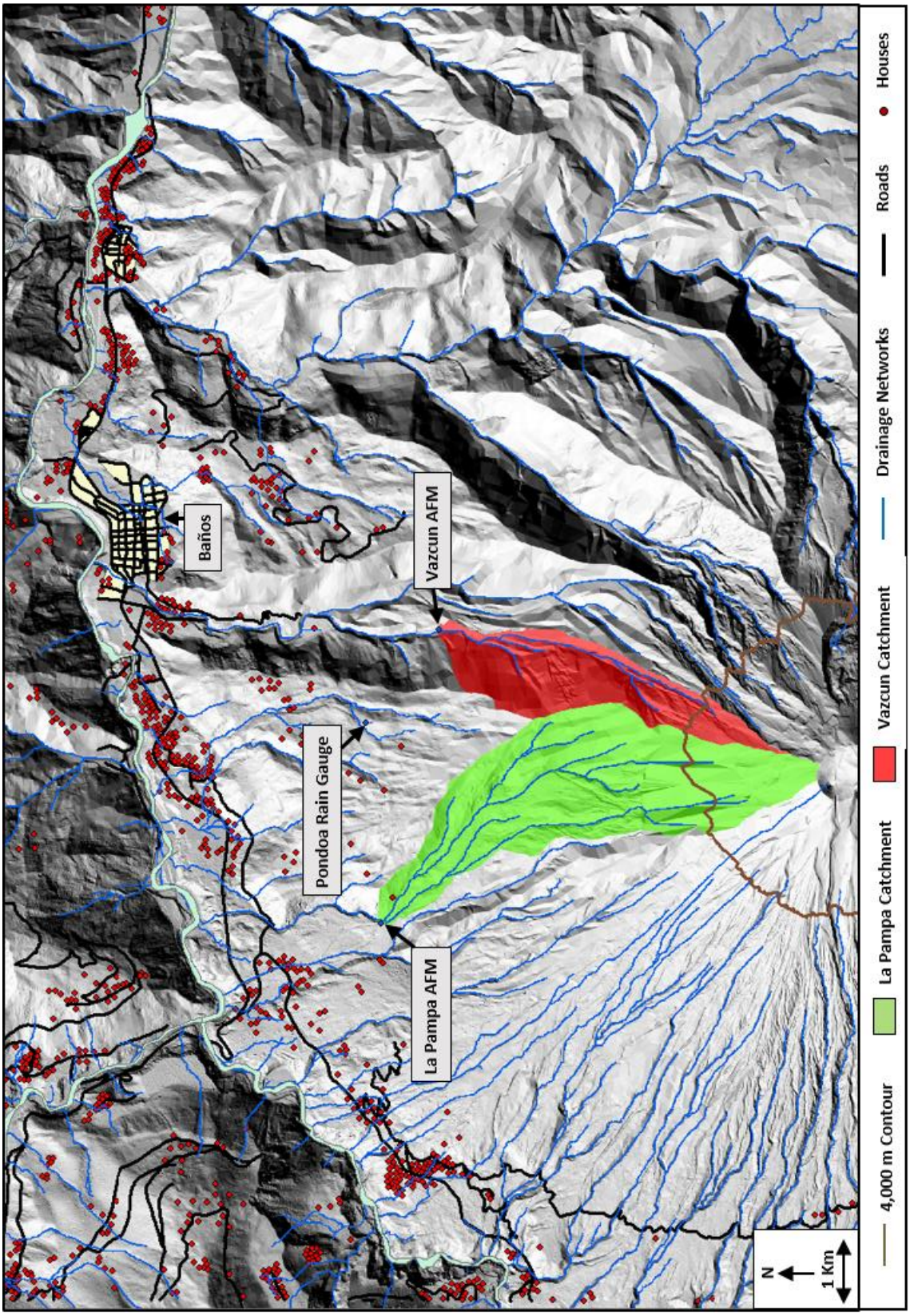

Figure 4.3: Shaded relief DEM map of the northern slopes of Tungurahua Volcano. The catchment upstream of the La Pampa AFM is displayed in green and the catchment upstream of the Vazcun AFM is displayed in red.

4.4.2. Datasets

AFMs can yield information regarding flow magnitude via the calibration of output data with visual observations of active flows and their velocity and stage height, assuming that sediment concentration and grain-size distribution are constant. Sequential AFMs along the same channel can indicate the frontal propagation velocity of flows (Lavigne et al., 2000b; Marchi et al., 2002; Cole et al., 2009). The sediment concentration and grain-size distribution of flows can also be inferred if broadband seismometers are utilised in conjunction with AFMs (Burtin et al., 2008; Cole et al., 2009; Kumagai et al., 2009; Zobin et al., 2009; Schneider et al., 2010). Debris flows typically peak in the low band (<100 Hz) of AFMs whilst hyperconcentrated flows and streamflows typically peak at higher frequencies (Marcial et al., 1996; Huang et al., 2004; Cole et al., 2009; Doyle et al., 2009). The AFMs installed at Tungurahua use L10AR digital exploration geophones with a maximum dynamic range of $3.8x10^{-3}$ cm s^{-1} vertical ground velocity: signal processing produces amplitude measures in low frequency (10-100 Hz), high frequency (100-300 Hz) and full frequency (10-300 Hz) bands.

AFM data at Tungurahua are in daily spreadsheets containing timestamp, average low band amplitude, average high band amplitude, average full band amplitude and battery functionality at a resolution of five minutes. Rainfall data are also in daily spreadsheets; containing 5-minute resolution information regarding measured rainfall to a sensitivity of 0.5 mm. Initial data processing involves compilation and synchronisation of Vazcun AFM, La Pampa AFM and Pondoa rain gauge data to enable the initial identification of lahar activity and rainfall events.

4.4.3. Event Selection

Two primary criteria have been employed to select events for further study. First, if at least 10 mm of rainfall is recorded in a single event at the Pondoa rain gauge then the event will be analysed. A rainfall event is defined in this instance as a period of recorded rainfall between two dry spells of six hours or longer. This minimum inter-event time of six hours is selected due to its frequent use in soil erosion studies (Wischmeier and Smith 1978; Todisco, 2014) Second, events on the AFM records that feature sustained low band amplitudes of >100 counts for >10 minutes will also be analysed.

A lahar "alert" event occurs when the pre-defined "alert" threshold in the low band signal is exceeded for consecutive recordings (i.e. > 10 minutes). This binary alert system detects lahars with discharges that could pose a potential risk to people and/or infrastructure. During this study period, the threshold values were set by the OVT at 530 for the Vazcun AFM and 500 for the La Pampa AFM, corresponding to currently estimated flow discharges in excess of c. 10-15 $m^3 s^{-1}$. This study thus provides a detailed analysis of all rainfall events of ≥10 mm recorded at the Pondoa rain gauge between March 2012 and December 2013; as well as detailed analysis of all significant lahar activity in the Vazcun and La Pampa drainages over the same duration.

4.5. Intensity/Duration (I/D) Analysis

Lahar-triggering rainfall is here defined as "rainfall that includes no pauses longer than 30 minutes and results in a flow that exceeds a pre-defined AFM amplitude" (Tungol and Regalado, 1996); in this case the pre-defined AFM amplitudes are the lahar alert thresholds described above. Analysis of lahar-

triggering rainfall duration and lahar-triggering rainfall intensity has been frequently utilised as a means of examining lahar initiation thresholds at many volcanoes; e.g. in the Philippines (Rodolfo and Arguden, 1991; Arboleda and Martinez, 1996; Martinez et al., 1996; Rodolfo et al., 1996; Tungol and Regalado, 1996; Van Westen and Daag, 2005), Indonesia (Lavigne et al., 2000a; Lavigne et al., 2000b; Lavigne and Suwa, 2004), Mexico (Capra et al., 2010), Montserrat (Barclay et al., 2007) and Japan (Hikida et al., 2007; Okano et al., 2012). This analysis typically produces a power-law relationship suggesting lahar initiation occurs along a continuum from short duration, high intensity rainfall events to long duration, low intensity events.

Figure 4.4 illustrates this relationship for 23 of 29 lahar alert events within the Vazcun and La Pampa drainages of Tungurahua between March 2012 and June 2013 associated with triggering rainfall recorded at the Pondoa rain gauge. Six lahar alerts (20.7%) occurred with no detected triggering rainfall at the Pondoa rain gauge and were omitted from the analysis. These six lahar alerts highlight the spatial variability of rainfall around Tungurahua and the potential limitations of the single telemetered rain gauge. Of the remaining lahar alerts, 82.6% plot between a lower boundary curve of $I=1.1D^{-0.75}$ and an upper boundary curve of $I=5D^{-0.75}$. The eruptive activity, lahar and rainfall record for the time period used to construct Figure 4.4 is displayed in Figure 4.5. This timeline includes the elapsed time since PDC activity and the number of recorded daily explosions as proxies for eruptive activity, total daily rainfall (mm) to display precipitation and recorded lahar alerts to indicate lahar frequency.

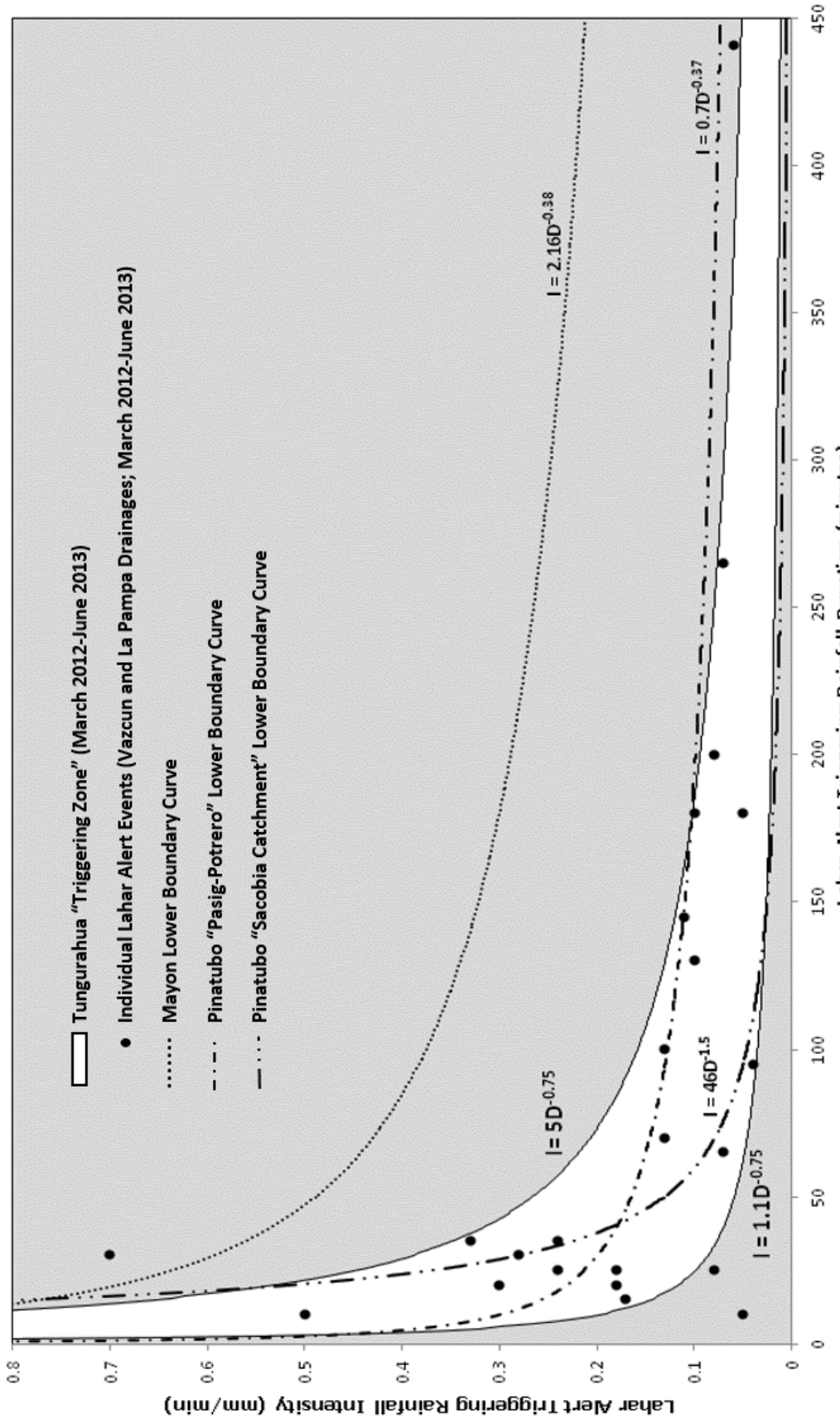

Figure 4.4: Lahar alert triggering rainfall intensity vs duration plot for Vazcun and La Pampa lahar alerts between March 2012 and June 2013. Upper and lower power-law best fit curves illustrate the boundaries of the estimated lahar alert triggering zone. Lower boundary curves for Mayon volcano debris flows between 1986 and 1989 (Rodolfo and Arguden, 1991); Pinatubo Pasig-Potrero lahars in 1992 (Arboleda and Martinez, 1996) and Pinatubo Sacobia lahars in 1992 (Tungol and Regalado, 1996) are also displayed for comparison.

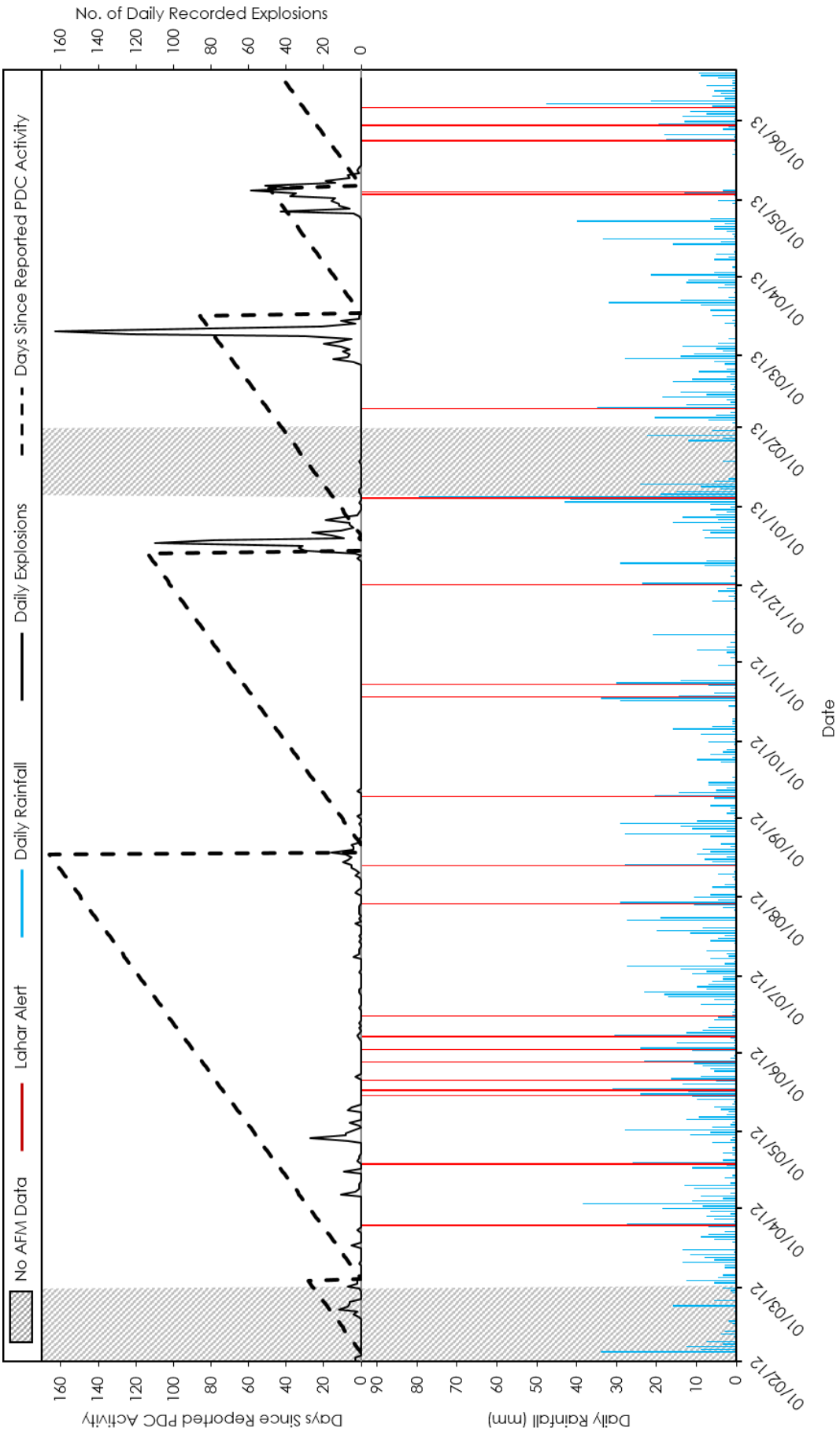

Figure 4.5: Timeline displaying the elapsed time since the last reported PDC activity at Tungurahua (dashed line), the number of daily recorded daily explosions (green) and the daily rainfall (blue) between 1st February 2012 and 20th June 2013. The occurrence of lahar alert signals (red) is also depicted.

4.6. Receiver Operating Characteristic (ROC) Analysis

The I/D analysis method (Fig. 4.4) does not take into account factors such as antecedent rainfall magnitude and eruptive activity that could impact both rainfall-runoff relationships and sediment availability, potentially affecting the rainfall thresholds required to initiate lahars of a given magnitude. Here, the influence of these factors is investigated using Receiver Operating Characteristic (ROC) analysis within the IBM SPSS statistics software package.

ROC analysis is a statistical method used to assess the performance of a binary classifier system as a discrimination threshold is varied (Fawcett, 2006). Binary classification is the task of classifying the elements of a given set into two groups, in this case identifying which rainfall events trigger lahars and which do not. The method was first utilised during World War Two to assess the ability of radar systems to differentiate between noise and signals associated with enemy planes (Swets et al., 1988). Within this thesis the exceedance (positive) or non-exceedance (negative) of lahar magnitude thresholds is established as the specific binary outcome. A range of test variables are utilised as binary classifier systems, including both individual rainfall parameters and derived probabilistic lahar forecasts. ROC analysis evaluates the ability of all possible thresholds within these test variables to discriminate between lahar and non-lahar events. When examining the performance of a system which predicts either positive or negative outcomes, there are four possible eventualities (Fig. 4.6):

I. If the outcome and the prediction are positive, this is a true positive.

II. If the outcome is negative and the prediction is positive, this is a false positive.

III. If the outcome and the prediction are negative, this is a true negative.

IV. If the outcome is positive and the prediction is negative, this is a false negative.

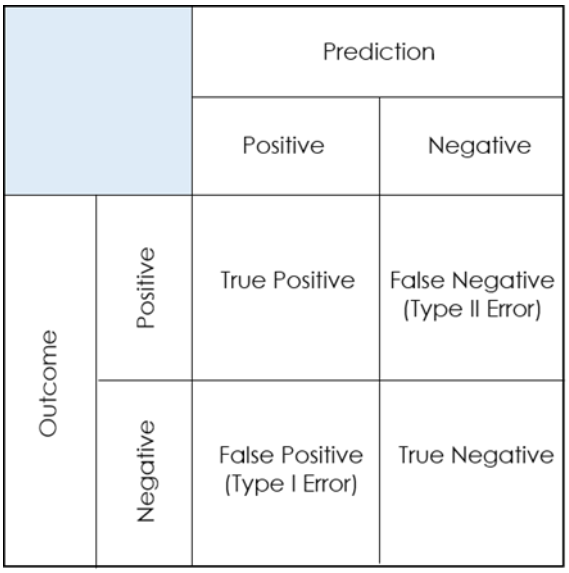

Figure 4.6: A confusion matrix Illustrating the four potential eventualities when attempting to predict a binary outcome.

A confusion matrix (Fig. 4.6) is a two-dimensional contingency table used to indicate the performance of a diagnostic test at predicting positive or negative outcomes within a dataset where the actual outcomes of the dataset are known. Visible in Figure 4.6 are the two types of potential error within a confusion matrix. A "Type I Error" or "False Positive" is the incorrect rejection of a null hypothesis, or with respect to this thesis the incorrect prediction of a lahar resulting in a "false alarm". A "Type II Error" or "False Negative" is the incorrect retention of a false null hypothesis, or with respect to this thesis the failure to predict a lahar. In short, a Type I Error is predicting an event which does not occur, and a Type II Error is failing to predict an event which does occur.

A ROC curve (Fig. 4.7) is a graphical method of illustrating the performance of a binary classifier system as a discrimination threshold is varied. It is thus an effective way of utilising confusion matrix information to visually assess and compare diagnostic tests. A ROC curve is constructed by plotting the True Positive Rate (true positives/all positives) against the False Positive Rate (false positives/all positives). The true positive rate or "hit rate" is equal to the sensitivity

of the diagnostic test, indicating how effectively it predicts positive outcomes, and the false positive rate or "false alarm rate" is equal to 1-specificity, indicating how effectively it predicts negative outcomes. Selection of the optimal diagnostic threshold value of a binary classifier system involves the evaluation of the trade-off between false positives and false negatives. The examples displayed in Fig. 4.7 display the optimal discrimination threshold if false positives and false negatives are valued equally, but this is often not the case in real-life scenarios.

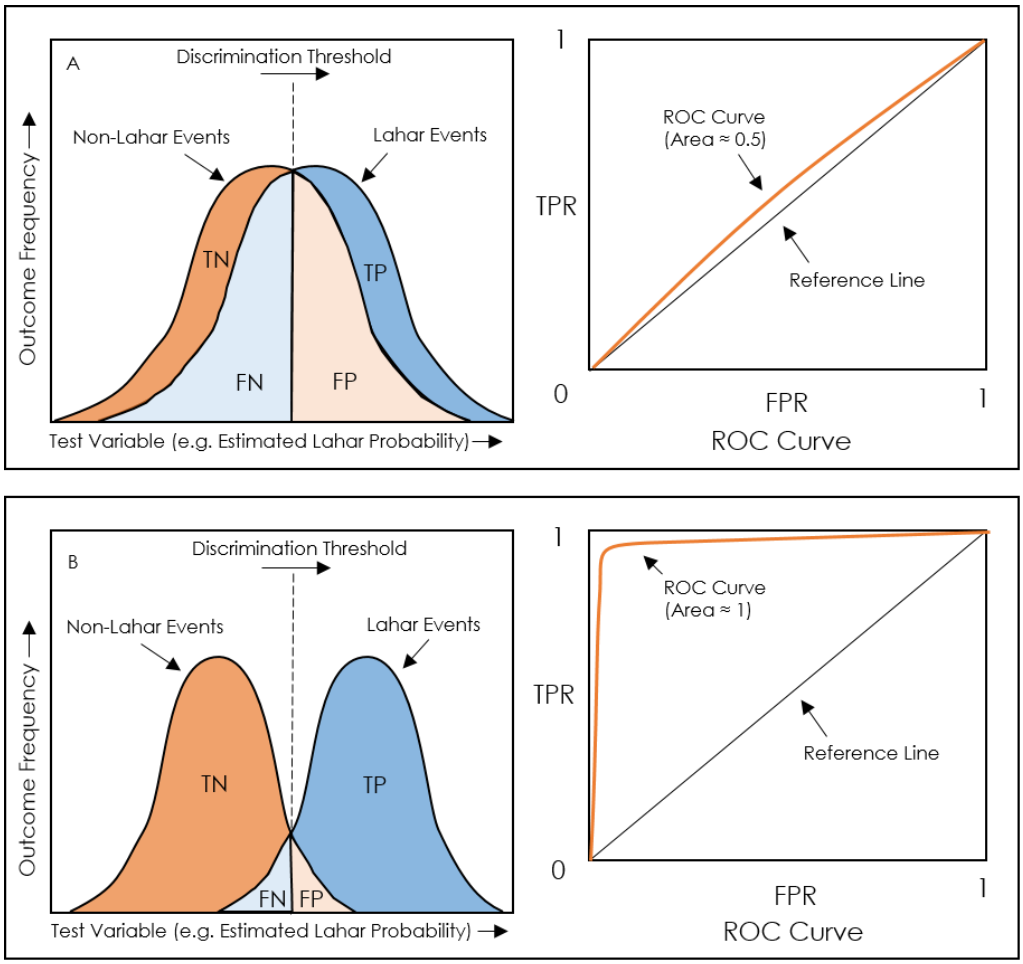

Figure 4.7: Illustration of ROC curves and their derivation by the variation of discrimination thresholds based on selected test variables. True Positives (TP), False Positives (FP) True Negatives (TN) and False Negatives (FN) are annotated for a given discrimination threshold (dashed line) in each example. A: An ineffective test variable which fails to distinguish between positive (blue) and negative (pink) outcomes. The resultant ROC curve plots close to the diagonal reference line and thus has an area under the curve close to 0.5. B: A test variable

which effectively distinguishes between positive (blue) and negative (pink) outcomes. The resultant ROC curve plots close to the top left corner of ROC space and thus has an area under the curve close to 1.

The area under a ROC curve is a quantitative measure of the effectiveness of a diagnostic test, with a random relationship producing an area of 0.5 and a perfect test producing an area of 1 (Fawcett, 2006). A test which fails to effectively differentiate between positive and negative outcomes (e.g. Fig. 4.7A) plots close to the diagonal reference line (which represents a chance relationship), as hit rates and false alarm rates are similar regardless of the discrimination threshold. Conversely, an effective diagnostic test will produce hit rates that exceed false alarm rates, resulting in a ROC curve that plots closer to the top left corner of ROC space and an increased area under the curve (e.g. Fig 4.7B). The area under a ROC curve is a valuable parameter when attempting to compare and evaluate the performance of binary classifier systems.

ROC analysis is used within this study to investigate the sensitivity of lahar alert occurrence in the Vazcun and La Pampa drainages to potential contributing variables between March 2012 and June 2013. The tested variables are total event rainfall, peak rainfall intensity, antecedent rainfall, number of recorded explosions and elapsed time since last reported PDC activity. In order to apply this analysis technique to lahars at Tungurahua the test variables need to be defined and quantified.

Total Event Rainfall is defined as the rainfall recorded between two dry periods of ≥6 hours. Rainfall events featuring ≥10 mm of total rainfall are utilised in the ROC analysis; with total rainfall recorded at a resolution of 0.5 mm.

Peak Rainfall Intensity (mm/min) is defined as the maximum rainfall intensity value recorded by the Pondoa rain gauge during the same rainfall event that produced the relevant lahar alert. *Peak Rainfall Intensity* is analysed during all

rainfall events ≥10 mm and is recorded at a time resolution of five minutes for three rainfall intensity time scales; 60 minutes, 30 minutes and 10 minutes.

Antecedent rainfall is calculated for each analysed rainfall event at a resolution of 0.5 mm. Four antecedent rainfall timescales are recorded; 24 hours, and 3, 5 and 7 days. In the case of a lahar alert event the antecedent rainfall is calculated for the period preceding the onset of the relevant rainfall event.

In order to analyse the relationship between renewed sediment supply and lahar occurrence an eruptive activity timeline for the data period was created from the daily activity reports published by IGEPN. These reports contain information on long-period, volcanic-tectonic and tremor seismicity, number of explosions, visibility level, evidence of ash fall, observed plume height, wind direction, evidence of PDC activity and runout distance/direction of PDCs. *Explosion frequency* over 5 different timescales (24 hours, 3 days, 7 days, 30 days and 60 days) and time since last reported PDC activity were selected for use in the ROC analysis as proxies for sediment supply in an attempt to statistically analyse the temporal impacts of persistent vulcanian activity at Tungurahua upon lahar initiation.

4.6.1. ROC Curves

Figure 4.8A displays lahar alert centric ROC curves for the three peak rainfall intensity timescales (10, 30 and 60 minutes) and total event rainfall, Figure 4.8B displays lahar alert centric ROC curves for four antecedent rainfall periods (24 hour, 3, 5 and 7 days) and time since last PDC activity, whilst Figure 4.8C displays lahar alert centric ROC curves for reported explosion frequency over the 5 timescales ranging from 24 hours to 60 days. The three peak rainfall intensity timescales (ROC areas >0.8), and to a lesser extent total event rainfall (ROC area

>0.76), are the most effective independent predictors of lahar alert occurrence (Fig. 4.8A). All four of these variables achieve statistical significance at a level >99%. Conversely, antecedent rainfall, explosion frequency and time since last PDC activity show no relationship with lahar alert occurrence (i.e. they plot close to the diagonal reference line representing a random relationship) *(Fig. 4.8B & 4.8C)*.

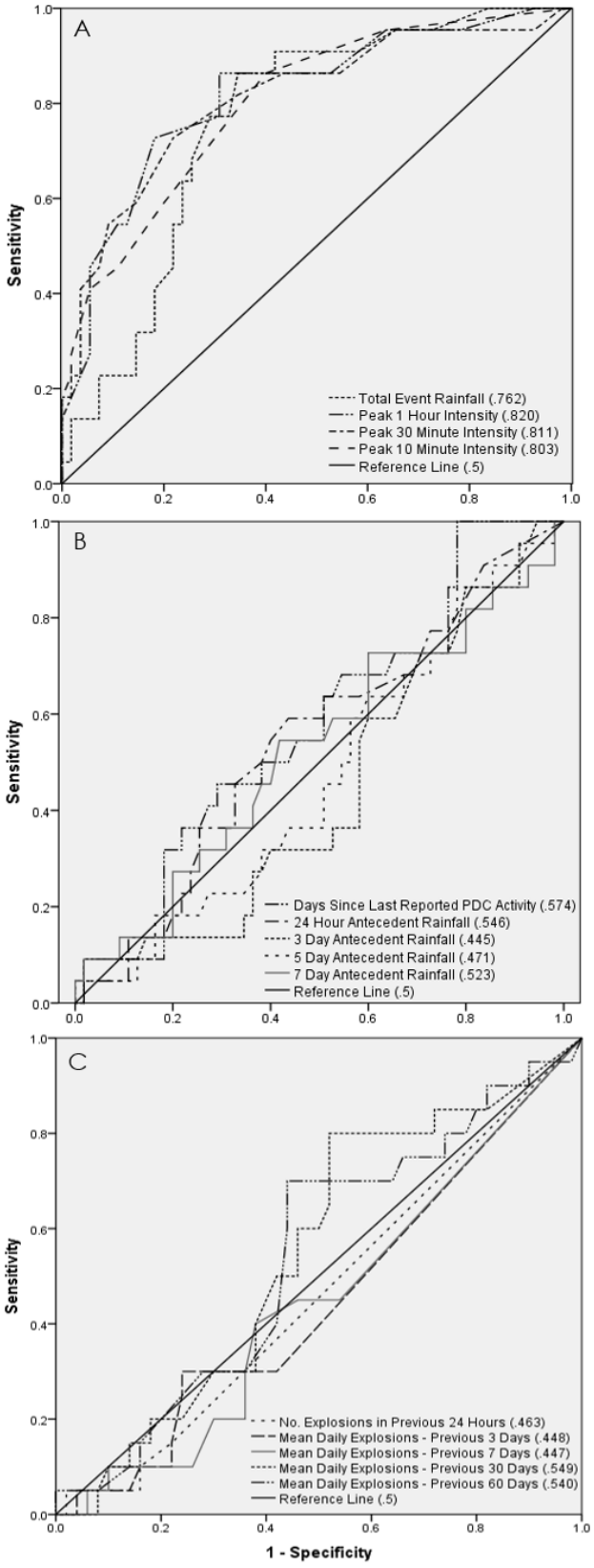

D Area Under the Curve Statistics

Test Result Variable(s)	Area	Standard Error[a]	P-Value[b]
Total Event Rainfall	.762	.056	.000
Peak 1 Hour Rainfall Intensity	.820	.055	.000
Peak 30 Minute Rainfall Intensity	.811	.058	.000
Peak 10 Minute Rainfall Intensity	.803	.055	.000
Time Since Last PDC Activity	.574	.070	.316
24 Hour Antecedent Rainfall	.546	.072	.531
3 Day Antecedent Rainfall	.445	.071	.450
5 Day Antecedent Rainfall	.471	.071	.689
7 Day Antecedent Rainfall	.523	.075	.752
Mean Daily Explosions – Previous 24 Hours	.463	.075	.631
Mean Daily Explosions – Previous 3 Days	.448	.076	.495
Mean Daily Explosions – Previous 7 Days	.447	.075	.487
Mean Daily Explosions – Previous 30 Days	.549	.073	.528
Mean Daily Explosions – Previous 60 Days	.540	.075	.603

a. Under the nonparametric assumption

b. Null hypothesis: true area = 0.5.

Figure 4.8: Receiver Operating Characteristic (ROC) curves displaying the ability of several variables to predict the occurrence of lahar alerts. The diagonal reference lines are an example of an idealised random relationship. The accompanying table (D) describes the output statistics relating to the lahar alert centric ROC curves.

4.7. Probabilistic Analysis

Probabilistic analysis of lahar alert occurrence is a potentially useful tool for lahar hazard mitigation. ROC analysis indicates that the best individual indicator of lahar alert occurrence is peak rainfall intensity (Fig. 4.8) and therefore this variable is utilised to investigate lahar alert probability. Figure 4.9 displays the variation in lahar alert probability as peak rainfall intensity increases for rainfall events ≥10 mm (n = 99, of which 30 were associated with 44 separate periods of lahar alert). The 10 mm rainfall event analysis criterion excludes 2 lahar alert-producing rainfall events: i.e. 6.25% of rainfall events that produced a lahar alert signal did not exceed the rainfall event threshold (≥10 mm of rain) in the Vazcun and La Pampa drainages between March 2012 and December 2013.

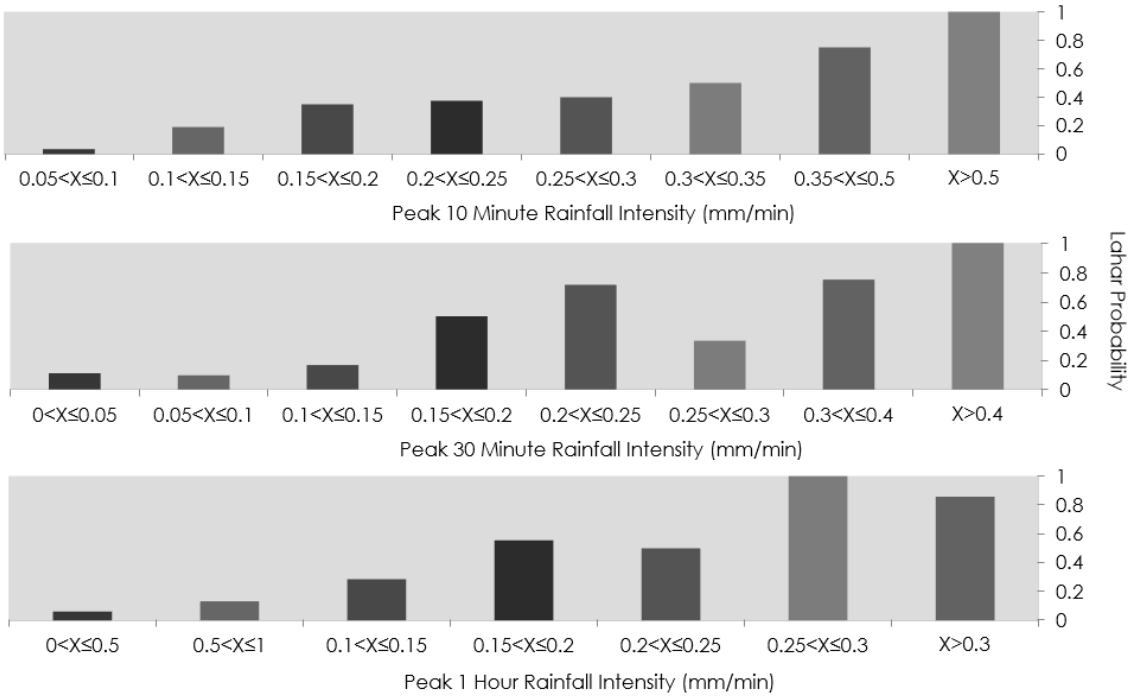

Figure 4.9: Two-Dimensional probability plots displaying the variation in lahar alert probability as peak rainfall intensity increases. 10 minute peak rainfall intensity (top); 30 minute peak rainfall intensity (middle); 1 hour peak rainfall intensity (bottom). March 2012-December 2013 data.

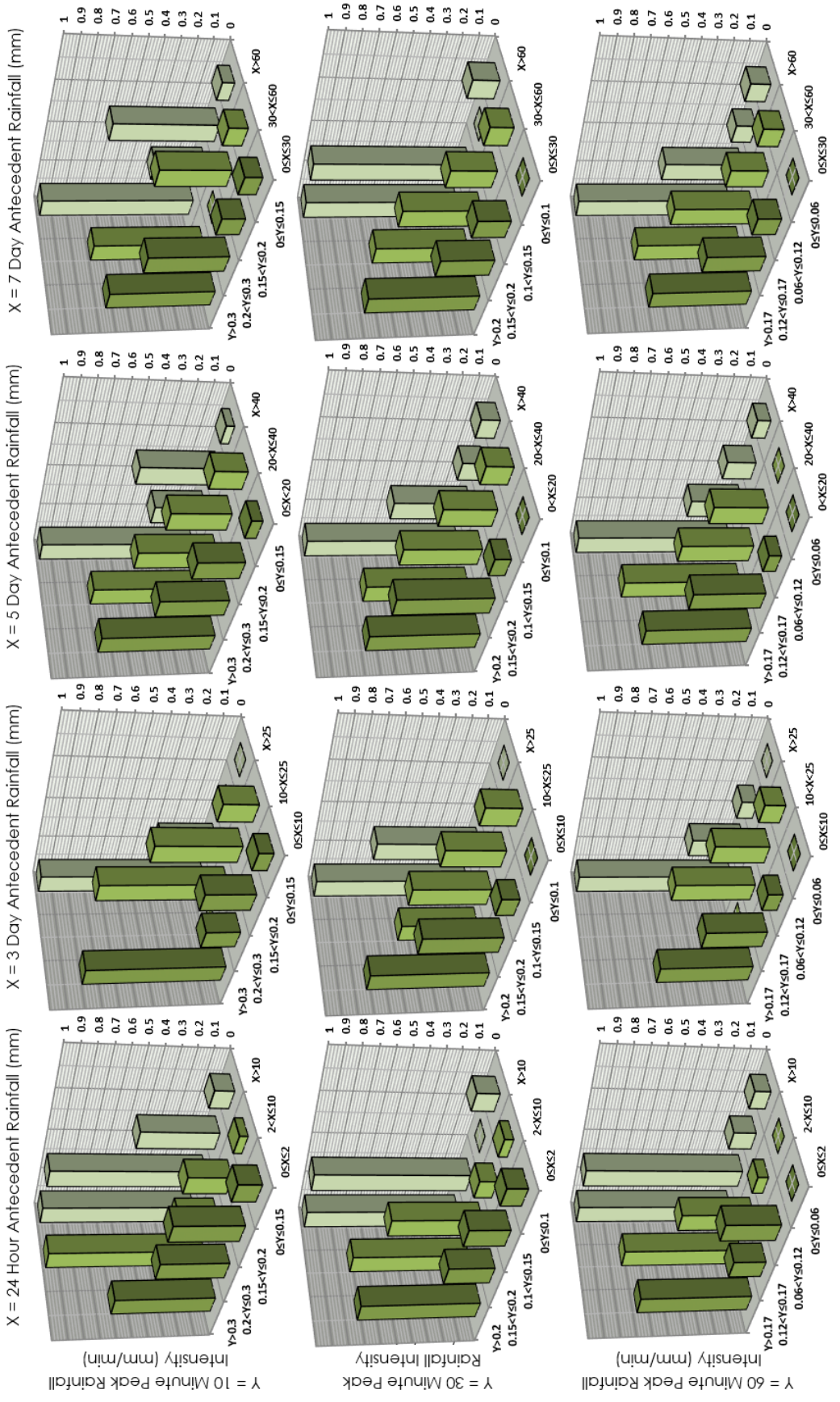

Figure 4.10: Three dimensional probability plots depicting the probability of a lahar alert (scale on vertical axis) in the Vazcun and La Pampa drainages based on various peak rainfall intensities and antecedent rainfall conditions. March 2012-December 2013.

Several previous studies have suggested that high levels of antecedent rainfall functions to saturate deposits, increase runoff and thus lower the rainfall required to trigger lahars (Lavigne et al., 2000a; Barclay et al., 2007; Okano et al., 2012). Therefore, high antecedent rainfall would be expected to increase lahar probability across a whole spectrum of rainfall conditions. Despite displaying little correlation with lahar alert occurrence when utilised as a single variable during ROC analysis (Fig. 4.8), antecedent rainfall has a significant impact when used as a secondary variable in combination with peak rainfall intensity at Tungurahua (Fig. 4.10). In the three-dimensional probability plots in Figure 4.10, lahar alert probability increases when antecedent rainfall is increased, but only during mod-high peak rainfall intensity events. At low peak rainfall intensities, the lahar probability is relatively unaffected by antecedent rainfall impacts. This pattern could be explained by two mechanisms. Firstly, the infiltration rates of Tungurahua eruptive deposits may remain sufficiently high, even after significant antecedent rainfall, to prevent lahar triggering runoff during low intensity rainfall, but not during moderate and high rainfall intensity events. Secondly, antecedent rainfall could increase the bulking efficiency of lahars due to higher water content in channel floor deposits: low-intensity rainfall fails to trigger lahars regardless of channel saturation, but moderate-high intensity rainfall-triggered lahars more readily grow to a level where they trigger an alert. Increased bulking efficiency under high antecedent rainfall conditions is attributed to the development of positive pore pressures in saturated channel floor sediments as the flows pass over them (Iverson et al., 2010; Reid et al., 2011), promoting progressive bed scour, introducing additional fluid to the lahar, and preventing fluid loss from the flow into the channel floor (Kean et al., 2011). In summary, I infer in this specific case that increased antecedent rainfall does not reduce lahar

initiation thresholds; instead it acts only to increase lahar alert probability at high rainfall intensities.

4.8. Predicting Events – "Real-time" Lahar Forecasting

As a test of the utility of using the two and three-dimensional probability matrices displayed in Figures 4.9 & 4.10 as a tool to predict lahar alert probability using "real-time" rainfall data, the rainfall record was examined between 1st July and 31st December 2013. As this time period is included in the construction of Figures 4.9 & 4.10 (comprised of 99 ≥10 mm rainfall events between 1st March 2012 and 31st December 2013) each rainfall event is analysed using probability matrices constructed from the other 98 rainfall events in order to minimise bias. The optimal method for this testing would use probability matrices constructed from all events that had occurred prior to the test-event; however due to the limited size of the dataset and considering the relatively constant lahar hazard at Tungurahua, all 98 other rainfall events are used to construct the probability matrices in order to maximise the amount of information in the subsets of each matrix (Druzdzel and van der Gaag, 2000). All ≥10 mm rainfall events in the test period were analysed to estimate the associated lahar alert probability and then the predicted lahar alert catalogue (Table 4.1) was compared with the actual lahar alert record.

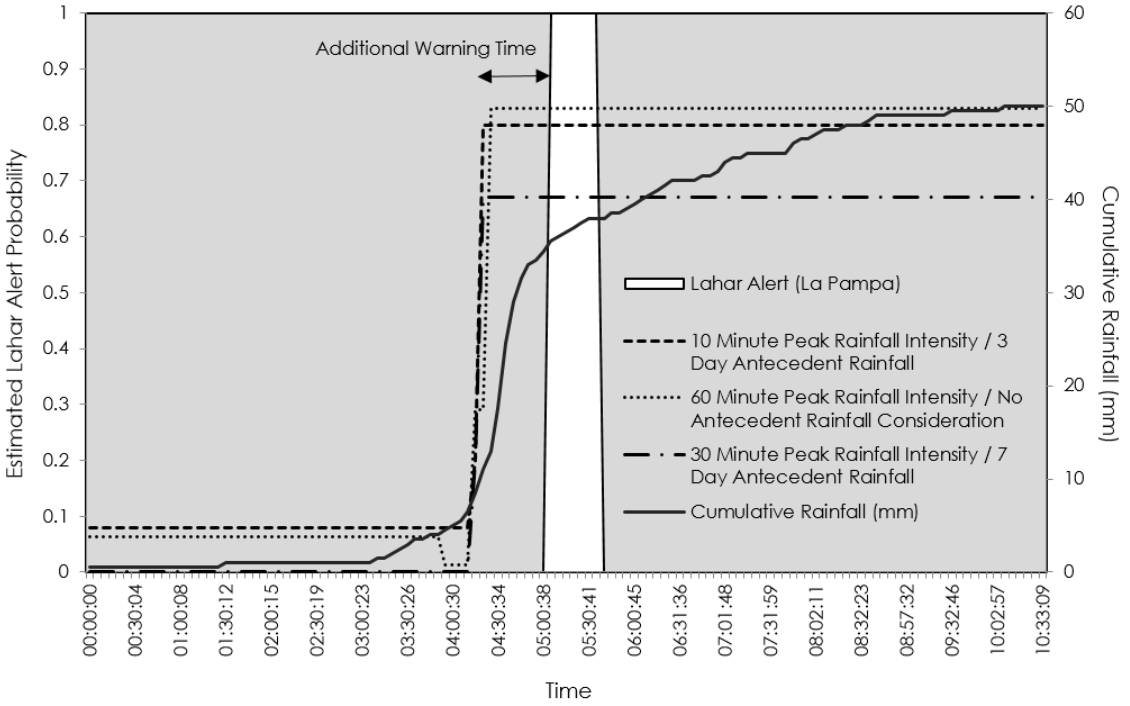

Figure 4.11: Lahar Alert event which occurred on December 20th 2013. 3 of the 12 lahar alert probability matrices shown in Figure 4.10 are utilised in conjunction with "real-time" rainfall data to produce dynamic lahar alert occurrence probabilities throughout the rainfall event.

For example, a single rainfall event on 20th December 2013 produced a lahar alert signal in the La Pampa drainage (Fig. 4.11). Calculated lahar alert probability goes up as peak rainfall intensity increases with time during the rainfall event (Fig. 4.11). Significantly, peak estimated lahar alert probability for each of the three displayed matrices occurs prior to triggering of the (AFM-derived) lahar alert signal by the flow itself. Calculated peak lahar alert probability estimates for all ≥10 mm rainfall events between 1st July and 31st December 2013 are displayed in Table 4.1. Comparison with the actual lahar alert record enables the performance of the two and three-dimensional probability matrices to be assessed using ROC analysis.

	A	B	C	D	E	F	G	H	I	J	K	L	M	N	O	P	Q	R	S	T	U	V	W	X	Y		
	No Antecedent Rainfall Consideration			24 Hour Antecedent Rainfall Consideration			3 Day Antecedent Rainfall Consideration			5 Day Antecedent Rainfall Consideration			7 Day Antecedent Rainfall Consideration														
Rainfall Event Start Date	10 Minute Peak Rainfall Intensity	30 Minute Peak Rainfall Intensity	60 Minute Peak Rainfall Intensity	10 Minute Peak Rainfall Intensity	30 Minute Peak Rainfall Intensity	60 Minute Peak Rainfall Intensity	10 Minute Peak Rainfall Intensity	30 Minute Peak Rainfall Intensity	60 Minute Peak Rainfall Intensity	10 Minute Peak Rainfall Intensity	30 Minute Peak Rainfall Intensity	60 Minute Peak Rainfall Intensity	10 Minute Peak Rainfall Intensity	30 Minute Peak Rainfall Intensity	60 Minute Peak Rainfall Intensity	Overall Mean	"No Antecedent Rainfall" Mean	Antecedent Rainfall Mean (All Timescales)	24 Hour Antecedent Rainfall Mean	3 Day Antecedent Rainfall Mean	5 Day Antecedent Rainfall Mean	7 Day Antecedent Rainfall Mean	10 Minute Peak Rainfall Intensity Mean	30 Minute Peak Rainfall Intensity Mean	60 Minute Peak Rainfall Intensity Mean	Alert	Alert Extent
07/07/13	*0.35*	*0.17*	*0.29*	*0.43*	*0.25*	*0.20*	*0.29*	*0.11*	*0.38*	*0.29*	*0.10*	*0.44*	*NA*	*NA*	*NA*	*0.28*	*0.27*	*0.28*	*0.29*	*0.26*	*0.28*	*NA*	*0.34*	*0.16*	*0.26*	*NA*	*NA*
09/07/13	**0.67**	**0.47**	**0.26**	**0.60**	**0.17**	**0.29**	**1.00**	**0.50**	**0.00**	**0.67**	**0.43**	**0.27**	**0.67**	**0.43**	**0.17**	**0.44**	**0.46**	**0.43**	**0.35**	**0.50**	**0.46**	**0.42**	**0.72**	**0.40**	**0.16**	**Yes**	**LP**
12/07/13	0.04	0.10	0.14	0.06	0.06	0.00	0.21	0.24	0.14	0.06	0.13	0.09	0.13	0.15	0.14	0.11	0.09	0.12	0.04	0.20	0.09	0.14	0.10	0.14	0.08	No	NA
15/07/13	**0.15**	**0.08**	**0.10**	**0.00**	**0.00**	**0.00**	**0.16**	**0.18**	**0.29**	**0.14**	**0.09**	**0.27**	**0.06**	**0.08**	**0.17**	**0.12**	**0.11**	**0.12**	**0.00**	**0.21**	**0.17**	**0.10**	**0.10**	**0.09**	**0.14**	**Yes**	**LP&V**
24/07/13	*0.19*	*0.17*	*0.29*	*0.05*	*0.11*	*0.07*	*0.08*	*0.11*	*0.09*	*0.07*	*0.10*	*0.08*	*0.11*	*0.20*	*0.14*	*0.12*	*0.22*	*0.10*	*0.08*	*0.09*	*0.08*	*0.15*	*0.10*	*0.14*	*0.11*	*NA*	*NA*
29/07/13	*0.19*	*0.10*	*0.13*	*0.05*	*0.06*	*0.07*	*0.08*	*0.00*	*0.09*	*0.05*	*0.12*	*0.18*	*0.12*	*0.14*	*0.23*	*0.11*	*0.14*	*0.10*	*0.06*	*0.06*	*0.12*	*0.16*	*0.10*	*0.08*	*0.12*	*NA*	*NA*
02/08/13	*0.40*	*0.71*	*0.56*	*0.25*	*0.75*	*0.75*	*0.33*	*1.00*	*1.00*	*0.33*	*1.00*	*1.00*	*0.33*	*1.00*	*1.00*	*0.69*	*0.56*	*0.73*	*0.58*	*0.78*	*0.78*	*0.78*	*0.33*	*0.89*	*0.72*	*NA*	*NA*
06/08/13	*0.19*	*0.10*	*0.13*	*0.05*	*0.06*	*0.07*	*0.00*	*0.00*	*0.10*	*0.05*	*0.12*	*0.18*	*0.08*	*0.17*	*0.13*	*0.10*	*0.14*	*0.08*	*0.06*	*0.03*	*0.12*	*0.12*	*0.07*	*0.09*	*0.10*	*NA*	*NA*
13/08/13	*0.19*	*0.17*	*0.13*	*0.05*	*0.11*	*0.07*	*0.08*	*0.11*	*0.09*	*0.07*	*0.10*	*0.08*	*0.11*	*0.20*	*0.14*	*0.11*	*0.16*	*0.10*	*0.08*	*0.09*	*0.08*	*0.15*	*0.10*	*0.14*	*0.08*	*NA*	*NA*
14/08/13	*0.04*	*0.10*	*0.13*	*0.13*	*0.14*	*0.10*	*0.20*	*0.22*	*0.13*	*0.20*	*0.17*	*0.00*	*0.12*	*0.14*	*0.13*	*0.13*	*0.09*	*0.14*	*0.12*	*0.18*	*0.12*	*0.13*	*0.14*	*0.15*	*0.08*	*NA*	*NA*
16/08/13	*0.19*	*0.17*	*0.13*	*0.14*	*0.25*	*0.33*	*0.20*	*0.38*	*0.33*	*0.20*	*0.33*	*0.33*	*0.12*	*0.29*	*0.23*	*0.24*	*0.16*	*0.26*	*0.24*	*0.30*	*0.29*	*0.21*	*0.17*	*0.28*	*0.23*	*NA*	*NA*
26/08/13	0.04	0.10	0.07	0.15	0.14	0.00	0.09	0.00	0.00	0.07	0.00	0.00	0.11	0.00	0.00	0.05	0.07	0.05	0.10	0.03	0.02	0.04	0.09	0.05	0.01	No	NA
28/08/13	0.04	0.10	0.07	0.15	0.14	0.00	0.21	0.24	0.14	0.07	0.00	0.00	0.11	0.00	0.00	0.08	0.07	0.09	0.10	0.20	0.02	0.04	0.12	0.10	0.03	No	NA
31/08/13	**0.15**	**0.13**	**0.10**	**0.08**	**0.18**	**0.29**	**0.00**	**0.00**	**0.00**	**0.14**	**0.20**	**0.27**	**0.06**	**0.11**	**0.08**	**0.12**	**0.13**	**0.12**	**0.18**	**0.00**	**0.20**	**0.08**	**0.08**	**0.12**	**0.12**	**Yes**	**LP**
09/09/13	0.20	0.10	0.14	0.06	0.06	0.07	0.21	0.24	0.36	0.07	0.00	0.08	0.11	0.00	0.15	0.12	0.15	0.12	0.06	0.27	0.05	0.09	0.13	0.08	0.13	No	NA
15/09/13	0.20	0.10	0.14	0.15	0.14	0.36	0.09	0.00	0.10	0.07	0.00	0.08	0.11	0.00	0.15	0.11	0.15	0.10	0.22	0.06	0.05	0.09	0.12	0.05	0.14	No	NA
17/09/13	**0.25**	**0.67**	**0.50**	**0.33**	**0.72**	**0.11**	**0.67**	**0.33**	**0.45**	**0.00**	**0.60**	**0.40**	**0.43**	**0.67**	**0.30**	**0.43**	**0.47**	**0.42**	**0.39**	**0.48**	**0.33**	**0.47**	**0.34**	**0.60**	**0.29**	**Yes**	**LP**
29/09/13	**0.32**	**0.47**	**0.26**	**0.33**	**0.17**	**0.11**	**0.17**	**0.40**	**0.29**	**0.17**	**0.50**	**0.38**	**0.00**	**0.20**	**0.30**	**0.27**	**0.35**	**0.25**	**0.20**	**0.29**	**0.35**	**0.17**	**0.20**	**0.35**	**0.22**	**Yes**	**LP**
04/10/13	0.20	0.10	0.14	0.05	0.06	0.07	0.21	0.24	0.36	0.07	0.00	0.08	0.13	0.15	0.25	0.14	0.15	0.14	0.06	0.27	0.05	0.18	0.13	0.11	0.15	No	NA
08/10/13	0.10	0.04	0.10	0.07	0.15	0.14	0.00	0.21	0.24	0.14	0.21	0.18	0.00	0.13	0.15	0.12	0.08	0.13	0.12	0.15	0.18	0.09	0.06	0.15	0.14	No	NA
14/10/13	0.37	0.17	0.30	0.30	0.13	0.07	0.56	0.43	0.36	0.33	0.11	0.08	0.50	0.33	0.25	0.29	0.28	0.29	0.17	0.45	0.17	0.36	0.41	0.23	0.18	No	NA
16/10/13	0.04	0.10	0.14	0.15	0.14	0.36	0.21	0.24	0.36	0.21	0.18	0.36	0.11	0.00	0.15	0.18	0.09	0.21	0.22	0.27	0.25	0.09	0.14	0.13	0.23	No	NA
22/10/13	0.04	0.10	0.14	0.15	0.14	0.36	0.09	0.00	0.10	0.07	0.00	0.08	0.11	0.00	0.15	0.10	0.09	0.10	0.22	0.06	0.05	0.09	0.09	0.05	0.14	No	NA
13/11/13	0.37	0.17	0.30	0.30	0.13	0.07	NA	NA	NA	NA	NA	NA	NA	NA	NA	0.22	0.28	0.17	0.17	NA	NA	NA	0.34	0.15	0.12	No	NA
17/11/13	**1.00**	**0.67**	**1.00**	**0.60**	**0.73**	**0.67**	**0.80**	**0.73**	**0.55**	**0.67**	**0.60**	**0.67**	**NA**	**NA**	**NA**	**0.72**	**0.89**	**0.67**	**0.67**	**0.69**	**0.65**	**NA**	**0.77**	**0.68**	**0.58**	**Yes**	**LP&V**
26/11/13	**1.00**	**1.00**	**0.83**	**0.60**	**0.73**	**0.67**	**0.80**	**0.73**	**0.55**	**0.67**	**0.67**	**0.63**	**0.60**	**0.67**	**0.57**	**0.71**	**0.94**	**0.66**	**0.67**	**0.69**	**0.66**	**0.61**	**0.73**	**0.76**	**0.54**	**Yes**	**LP**
30/11/13	0.60	0.50	0.63	0.70	0.82	0.78	0.90	0.82	0.64	0.83	0.80	1.00	0.83	0.75	1.00	0.77	0.58	0.82	0.77	0.79	0.88	0.86	0.77	0.74	0.68	No	NA
20/12/13	**1.00**	**1.00**	**0.83**	**0.60**	**0.73**	**0.67**	**0.80**	**0.73**	**0.55**	**0.67**	**0.67**	**0.63**	**0.60**	**0.67**	**0.57**	**0.71**	**0.94**	**0.66**	**0.67**	**0.69**	**0.66**	**0.61**	**0.73**	**0.76**	**0.54**	**Yes**	**LP**
27/12/13	0.20	0.10	0.14	0.06	0.06	0.07	0.09	0.00	0.10	0.07	0.00	0.08	0.11	0.00	0.15	0.08	0.15	0.07	0.06	0.06	0.05	0.09	0.11	0.03	0.09	No	NA
28/12/13	0.04	0.10	0.07	0.13	0.15	0.11	0.00	0.00	0.00	0.21	0.18	0.00	0.11	0.00	0.00	0.07	0.07	0.07	0.13	0.00	0.13	0.04	0.10	0.09	0.03	No	NA

Table 4.1: Peak estimated lahar alert probabilities during all ≥10 mm rainfall events occurring between July 1st and December 31st 2013; as predicted by all probability matrices displayed in Figure 4.10. In addition to the outputs of the individual probability matrices (columns A-O), categorised mean probabilities are also displayed (columns P-Y). Black rows depict lahar alert producing events. Grey rows represent events which did not trigger a lahar alert signal. White rows display events which did not feature available AFM data.

Each column in Table 4.1 is analysed relative to the real-life occurrence or non-occurrence of lahar alert signals during the 30 featured rainfall events between 1st July and 31st December 2013. ROC curves and associated statistics (Table 4.2) describing the performance of each set of peak estimated lahar alert probabilities are generated and a selection of these curves are displayed in Figure 4.12. Results show mixed performance by the individual probability matrices shown in columns A-P of Table 4.1. Several matrices achieved ROC curve areas >0.8 and statistical significance at a level of 95% (p-value ≤0.05), displaying effective lahar prediction, whereas other individual matrices performed less effectively over the test period. The performance of the "composite" lahar indicators (composed of the mean probability outputs of multiple individual probability matrices) displayed in columns P-Y of Table 4.1 was more consistently effective. 90% of these composite indicators achieved statistical significance at a level of 95% and they produced ROC curve areas ranging from 0.71 to 0.89 with a mean value of 0.80.

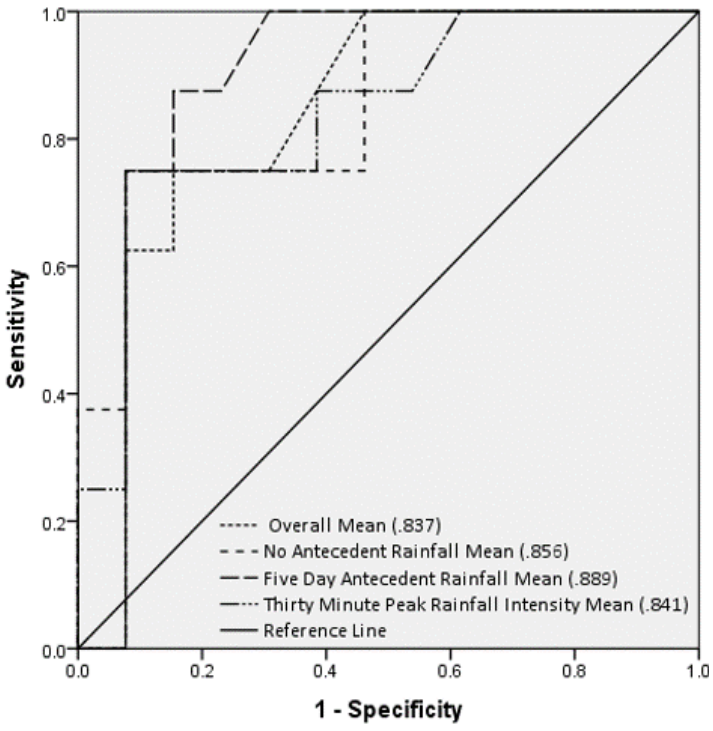

Figure 4.12: Receiver Operating Characteristic (ROC) curves describing the ability of several of the probability matrices shown in Table 4.1 to predict the generation of lahar alert signals between July and December 2013. Corresponding ROC curve areas are displayed in the figure legend. The diagonal reference line depicts an example of a random relationship.

Area Under the Curve Statistics				
Test Result Variable(s)		Area	Standard Error[a]	P-Value[b]
No Antecedent Rainfall Consideration	10 Minute Peak Rainfall Intensity	0.82	0.09	0.01
	30 Minute Peak Rainfall Intensity	0.84	0.11	0.01
	60 Minute Peak Rainfall Intensity	0.75	0.12	0.06
24 Hour Antecedent Rainfall Consideration	10 Minute Peak Rainfall Intensity	0.74	0.13	0.07
	30 Minute Peak Rainfall Intensity	0.81	0.12	0.02
	60 Minute Peak Rainfall Intensity	0.69	0.12	0.14
3 Day Antecedent Rainfall Consideration	10 Minute Peak Rainfall Intensity	0.71	0.13	0.11
	30 Minute Peak Rainfall Intensity	0.75	0.12	0.07
	60 Minute Peak Rainfall Intensity	0.64	0.14	0.31
5 Day Antecedent Rainfall Consideration	10 Minute Peak Rainfall Intensity	0.71	0.13	0.11
	30 Minute Peak Rainfall Intensity	0.87	0.09	0.01
	60 Minute Peak Rainfall Intensity	0.89	0.08	0.00
7 Day Antecedent Rainfall Consideration	10 Minute Peak Rainfall Intensity	0.54	0.17	0.75
	30 Minute Peak Rainfall Intensity	0.82	0.10	0.02
	60 Minute Peak Rainfall Intensity	0.78	0.12	0.04
Overall Mean		0.83	0.09	0.01
"No Antecedent Rainfall" Mean		0.85	0.09	0.01
Antecedent Rainfall Mean (All Timescales)		0.81	0.10	0.02
24 Hour Antecedent Rainfall Mean		0.76	0.12	0.05
3 Day Antecedent Rainfall Mean		0.76	0.12	0.05
5 Day Antecedent Rainfall Mean		0.89	0.08	0.00
7 Day Antecedent Rainfall Mean		0.77	0.12	0.05
10 Minute Peak Rainfall Intensity Mean		0.71	0.13	0.10
30 Minute Peak Rainfall Intensity Mean		0.83	0.09	0.01
60 Minute Peak Rainfall Intensity Mean		0.79	0.10	0.02
a. Under the nonparametric assumption b. Null hypothesis: true area = 0.5.				

Table 4.2: Summary statistics relating to the Receiver Operating Characteristic (ROC) analysis of the probability estimates shown in Table 4.1, with respect to their ability to effectively predict lahar alert signals between 1st July and 31st December 2013. Grey rows indicate the matrices shown in Figure 4.11.

The timing of the calculated peak lahar alert probabilities is also important, in addition to the performance of the probability matrices in predicting lahar alerts. This method of probabilistic analysis only provides a significant advance over the real-time AFM outputs if it consistently predicts potential lahars before such flows are detected by AFMs. Table 4.3 considers the 8 known lahar alert signal events that took place between 1st July and 31st December 2013 and assesses the time of peak estimated probability relative to the initial generation of the lahar alert signal. The mean additional warning time per matrix type ranges from 17 minutes to 36 minutes with a mean value of 24.5 minutes, whilst 75% of the tested lahar alert events featured a mean additional warning time of >20 minutes (Table 4.3). Lahar transit times between the La Pampa AFM and the primary road bridge crossing the drainage are currently estimated at 14±2 minutes, whereas in the Vazcun this value is estimated at 19±2 minutes.

Lahar Alert Signal Date	Lahar Alert Signal Start Time	Time of Max 10 Minute Peak Rainfall Intensity Based Probability With No Antecedent Rainfall Consideration	Net Time	Time of Max 30 Minute Peak Rainfall Intensity Based Probability With No Antecedent Rainfall Consideration	Net Time	Time of Max 60 Minute Peak Rainfall Intensity Based Probability with No Antecedent Rainfall Consideration	Net Time	Time of Max Antecedent Rainfall & 10 Minute Peak Rainfall Intensity Based Probability	Net Time	Time of Max Antecedent Rainfall & 30 Minute Peak Rainfall Intensity Based Probability	Net Time	Time of Max Antecedent Rainfall & 60 Minute Peak Rainfall Intensity Based Probability	Net Time	Mean Warning Time Per Event
09/07/13	14:15	13:23	00:52	13:33	00:42	14:05	00:10	13:23	00:52	13:33	00:42	13:23	00:52	00:41
15/07/13	23:50	22:52	00:58	23:50	00:00	23:12	00:38	23:50	00:00	23:50	00:00	23:17	00:33	00:21
31/08/13	15:35	15:26	00:09	15:35	00:00	15:35	00:00	15:35	00:00	15:35	00:00	15:35	00:00	00:01
17/09/13	01:25	00:05	01:20	01:15	00:10	01:10	00:15	00:05	01:20	01:15	00:10	00:50	00:35	00:38
29/09/13	10:25	09:51	00:34	09:56	00:29	09:51	00:34	09:51	00:34	09:56	00:29	10:01	00:24	00:30
17/11/13	18:35	18:35	00:00	18:35	00:00	18:35	00:00	18:35	00:00	18:35	00:00	18:35	00:00	00:00
26/11/13	22:10	21:50	00:20	21:50	00:20	21:50	00:20	21:35	00:35	21:35	00:35	21:40	00:30	00:26
20/12/13	05:05	04:30	00:35	04:30	00:35	04:35	00:30	04:20	00:45	04:20	00:45	04:25	00:40	00:38
Mean Warning Time Provided Per Matrix Type			00:36		00:17		00:18		00:30		00:20		00:26	

Table 4.3: Analysis of the additional warning time that is provided by the various probability matrices when applied to the eight lahar alert signal producing events between 1st July and 31st December 2013. The time-scale of the antecedent rainfall consideration is not considered in this table as it only impacts the magnitude of the peak probability and has no effect upon its timing.

4.9. Discussion

4.9.1. Rainfall I/D Analysis

Initial analysis of lahar alert triggering rainfall in the Vazcun and La Pampa drainages of Tungurahua indicated a power-law relationship between lahar-triggering rainfall intensity and duration. This is in common with previous studies of rain-triggered mass-flow events in disturbed earth systems, such as other active volcanoes (Rodolfo and Arguden, 1991; Arboleda and Martinez, 1996; Tungol and Regalado, 1996). The majority of lahar alerts analysed at Tungurahua between March 2012 and June 2013 plotted within a region bounded by the curves $I=1.1D^{-0.75}$ (lower boundary) and $I=5D^{-0.75}$ (upper boundary) (Fig. 4.4). The coefficients of the power-law relationship vary from volcano to volcano, likely as a function of a range of factors including the grain-size distribution of the pyroclastic material covering the flanks of the volcano. The relatively high position of the Mayon curve in Figure 4.4 is induced by relatively high infiltration rates as a result of the comparatively coarse, granular and porous volcaniclastic surface materials present on the slopes of the volcano (Rodolfo and Arguden, 1991). The three lower boundary curves at Pinatubo (Sacobia & Pasig-Potrero) and Tungurahua display relatively similar, overlapping thresholds, possibly due to finer ash, lower surface infiltration rates, and thus heightened surface runoff. Furthermore, the definitions of 'triggering rainfall' in Tungol and Regalado (1996), Rodolfo and Arguden (1991), Arboleda and Martinez (1996), and this study differ. The definition of a "lahar event" also varies; Rodolfo and Arguden (1991) pick events subjectively judged to have reached debris flow status; Arboleda and Martinez (1996) and Tungol and Regalado (1996) use events which exceed a low band AFM value of 100 (estimated at 25 $m^3 s^{-1}$); and this study uses events that

trigger a lahar alert signal (estimated at >10-15 $m^3 s^{-1}$ in the Vazcun drainage and >20-25 $m^3 s^{-1}$ in the La Pampa). All of these factors preclude I/D relationships derived at one volcano from being applied at another. Furthermore, in addition to the lack of standardisation within the process, the intensity/duration method is of limited use for real-time lahar prediction due to an inability to predict the likelihood of a lahar under any given set of rainfall parameters (Fig. 4.4). Incorporating "non-lahar" events into analytical methods in order to generate lahar alert probabilities is potentially a more valuable method from a lahar forecasting perspective.

4.9.2. ROC Analysis

The initial aim of the probabilistic lahar alert analysis was to identify the key indicators of lahar alert occurrence. The ROC curves displayed in Figure 4.8 indicate that peak rainfall intensity is the most accurate independent indicator of lahar alert occurrence. Conversely, antecedent rainfall, explosion frequency and time since last PDC activity are shown to be ineffective when used as independent indicators of lahar alert occurrence.

Rainfall event magnitude (ROC curve area of 0.76) also displays statistically significant (>99%) correlation with lahar alert occurrence, but to a lesser degree than peak rainfall intensity. This indicates that peak rainfall intensity is more effective than total volume of rainfall in predicting lahars large enough to trigger lahar alerts. From a physical viewpoint, short timescale, high-intensity rainfall may be more likely to overwhelm deposit infiltration capacity and generate lahar-forming surface run-off. Rainfall event magnitude (i.e. total rainfall) fails to make a distinction between low intensity rainfall events which may not overcome such

an infiltration rate threshold and higher intensity rainfall events which have the potential to do so.

The importance of short term peak rainfall intensity relative to total rainfall in predicting lahar alerts highlights several potentially important competing processes. As discussed in the introduction, surface crust formation due to rain beat compaction of fine eruptive material has been well documented at a number of volcanoes (Leavesley et al., 1989; Pierson et al., 1996; Manville et al., 2000b; Yamakoshi and Suwa, 2000). This crust is often initially formed during post-deposition periods of high intensity rainfall, reducing infiltration rates and increasing surface runoff, thus heightening the potential for rain-triggered lahars (Yamakoshi and Suwa, 2000). This process competes with rain splash erosion, which disrupts surface crusting once a rainfall kinetic energy threshold is exceeded, increasing the amount of material available for transport by Hortonian overland flow but also exposing more permeable substrates (Bradford et al., 1987b; Wang et al., 2014). Rill formation similarly exposes more permeable substrates to subsequent rainfall events, but also yields additional sediment (Leavesley et al., 1989). This dynamic between surface crusting of deposits, rain splash erosion and rill network formation plays an important role in lahar initiation (Leavesley et al., 1989; Yamakoshi and Suwa, 2000). Despite the potential of this cyclical process to create temporal and spatial variation in surface infiltration rates, peak rainfall intensity is shown by the ROC analysis to perform consistently well as an independent indicator of lahar alert occurrence in the Vazcun and La Pampa drainages at Tungurahua.

4.9.3. Probabilistic Analysis & Real-Time Forecasting

The probabilistic analysis of lahar alert occurrence displays the increasing probability of a lahar alert as peak rainfall intensity (10 minute, 30 minute and 60 minute) increases (Fig. 4.9), as well as the impacts of antecedent rainfall upon these probabilities (Fig. 4.10). This probabilistic analysis enables the calculation of an evolving lahar alert probability if the database is updated in real-time. It also enables the analysis of different time periods within the overall database; aiding assessment of temporal changes in lahar initiation thresholds and thus lahar occurrence probabilities. Such temporal changes can be due to catchment disturbances as a result of eruptive activity or landslides, fluctuations in sediment availability and seasonal meteorological variations impacting rainfall type and frequency.

The method also acknowledges the uncertainty associated with rain gauge location and meteorological variability. The telemetered Pondoa rain gauge at 2,725 m on the Northern slopes of Tungurahua lies c. 1,300 m below the estimated "lahar initiation region". As such there is likely to be significant spatial and temporal variation in rainfall between the two locations: i.e. 6 lahar alerts between March 2012 and December 2013 were not associated with any recorded triggering rainfall at the Pondoa gauge. A denser network of rain gauges at a variety of altitudes would aid the identification and reduction of uncertainty between actual and recorded rainfall. This rainfall variation is prevalent at Tungurahua due to the steep slopes, high relief and topographic irregularities. Orographic rainfall in particular could be more effectively captured if high altitude (>4000 m) rain gauges were installed; however, this would not be a cost effective measure given the likely lifespan of such instruments.

A probabilistic approach acknowledges the possibility of lahar occurrence when low rainfall intensities are recorded at the rain gauge as well as the potential for lahar absence when high rainfall intensities are recorded. This emphasises the potential benefit of simultaneously using multiple techniques for lahar hazard mitigation, with probabilistic lahar forecasting offering heightened warning times and the AFM network acting as a failsafe whilst also yielding additional information regarding specific lahar magnitudes and timing. With such an approach there is the potential for the occurrence of false alarms. Volcanology frequently exhibits the complexity of managing potentially high-impact hazards with variable probabilities and therefore the balance between issuing warnings and being concerned about false alarms is challenging (Donovan et al., 2014). At Tungurahua this balance would rely upon the effective performance of the lahar probability matrices, the AFM network and the community-based volcano monitoring of the Vigía network. Vigías living near major lahar-prone valleys have previously been given motorbikes by Civil Defence so that they can check for lahars during rainfall whilst as a network they also act as a communication channel for increasing community awareness (Stone et al., 2014). Therefore, they would act as a key component in both the early identification of any potential false alarms and in enhancing understanding within the communities as to why such false alarms could occur.

In order to test the lahar alert probability matrices in real-time, two and three-dimensional probability matrices were applied to the rainfall record between 1st July and 31st December 2013. Assessment of the performance of the lahar alert probability matrices was achieved via ROC analysis of the peak output probabilities of each matrix relative to the actual lahar alert record during this time span (Table 4.1). The results of this forecasting exercise show that

dynamic lahar alert probability matrices based on peak rainfall intensity and antecedent rainfall have the potential to effectively predict lahar alert occurrence in conjunction with real-time rainfall data at Tungurahua. Effectiveness is improved when the output peak lahar probability estimates of different probability matrices (based on various timescales of peak rainfall intensity and antecedent rainfall) are combined and averaged to form a composite indicator of potential lahar occurrence. In addition to the effective prediction of lahar occurrence, only one significant false alarm (30/11/13) occurred during this 6-month test period.

The timing of the peak lahar probability estimated from rainfall data relative to the generation of an AFM lahar alert signal is also important for assessing the potential applications of the method (Table 4.3). Lahar prediction from rainfall data effectively doubles warning times based on AFM lahar alert signals alone in the Vazcun and La Pampa drainages. Automation of probabilistic analysis of real-time telemetered rainfall data at Tungurahua could act as an accurate first-stage lahar warning system at *OVT* for IGEPN, backed up by second-stage AFM alerts (event confirmation or failsafe), in addition to the community-based monitoring of the vigía network.

4.10. Conclusions

Investigation of rain-triggered lahars in two northern drainages of Tungurahua showed a power-law relationship between rainfall intensity (I) and duration (D), in common with previous studies at other active volcanoes and wild-fire impacted watersheds. 82.6 % of lahar events occur between a lower boundary of $I=1.1D^{-0.75}$ and an upper boundary of $I=5D^{-0.75}$.

ROC analysis has demonstrated that peak rainfall intensity (10 minute, 30 minute and 60 minute) is the most effective predictor of lahar alert occurrence, whereas antecedent rainfall magnitude, explosion frequency and time since last known PDC activity have no value as independent indicators of lahar alert occurrence. Probabilistic analysis of all rainfall events of ≥10 mm confirmed this relationship for multiple peak rainfall intensity timescales, with escalating 10 minute, 30 minute and 60 minute peak rainfall intensities demonstrating an increase in lahar alert probability.

Antecedent rainfall was shown to have significant impacts upon lahar alert probability when used as a secondary variable in conjunction with peak rainfall intensity, increasing lahar alert probabilities at moderate-high peak rainfall intensities but not during low intensity rainfall events. Increased antecedent rainfall does not appear to reduce lahar initiation thresholds, due to relatively high saturated infiltration rates on the upper edifice of Tungurahua, but rather increases lahar alert probability during moderate- high intensity rainfall events by increasing flow bulking efficiency through entrainment of saturated channel deposits. Tungurahua does not appear to be sediment-limited with respect to lahar initiation, with flows occurring consistently during the study period of March 2012-December 2013 irrespective of the cycle of eruptive activity.

Application of two and three dimensional probability matrices to real-time rainfall data between 1st July and 31st December 2013 displayed the potential to predict lahar alert occurrence at a high level of confidence. Furthermore, lahar prediction based on composite indicators created from the mean values of multiple probability matrices yielded more reliable lahar warnings than the individual matrices. The matrix derived peak lahar probabilities yielded

significantly earlier warnings than the AFM-based lahar alert signals, producing average additional warning times of over 24 minutes per event. Lahar transit times between the La Pampa and Vazcun AFMs and the primary road crossing of each drainage are estimated at 14±2 minutes and 19±2 minutes respectively. As such, this method displays the potential to significantly increase effective lahar warning times.

This study illustrates a probabilistic method of lahar analysis that could be used as a tool in lahar hazard mitigation at any location where rain-triggered lahars present a hazard. Currently, lahar warning systems typically depend on the exceedance of a single pre-defined AFM amplitude. Calibration of AFM records with visual observations of flow volumes, discharges, velocities and sediment concentrations can refine lahar detection to produce multiple AFM thresholds correlated with different peak discharges and/or flow properties. The addition of multiple flow magnitude thresholds into this probabilistic method could assist in the effective modelling of potential flow inundation and arrival times. Despite the low false alarm generation rate during the 6-month test period uncertainty remains regarding the disparity between recorded rainfall at the Pondoa rain gauge and actual rainfall in the lahar initiation region. Further work on the spatial variation of rainfall at the volcano would test the strength of the Pondoa rain gauge as a single data source from which to make effective lahar predictions.

Chapter 5: Real-time prediction of rain-triggered lahars: incorporating seasonality and catchment recovery

Summary

Rain-triggered lahars are a significant secondary hazard at volcanoes where unconsolidated pyroclastic material is exposed to intense rainfall, often occurring for years to decades after the initial eruptive activity affects proximal areas or primary hazard zones. Previous studies have shown that secondary lahar initiation is a function of rainfall parameters, source material characteristics and time since eruptive activity. However, many volcanoes are located in regions with dramatic variations in seasonal rainfall; such seasonality may be a key factor affecting the predictability of lahar generation.

In this study the influence of rainfall seasonality and catchment evolution on rain-triggered lahars in the Belham River Valley at Soufrière Hills Volcano, Montserrat between April 2010 and April 2012 is examined. Lahar probability increases with peak one-hour rainfall intensity throughout the two-year dataset, and is higher under given rainfall conditions in year one than year two. The probability of lahars is also enhanced during the wet season, when large-scale synoptic weather systems (including tropical cyclones) are more common and antecedent rainfall and thus levels of deposit saturation are typically increased. The incorporation of antecedent conditions and catchment evolution into logistic regression-based lahar probability estimation models displays the

potential for successful real-time prediction of lahars, even in areas featuring strongly seasonal climates and temporal catchment recovery.

5.1. Introduction

Lahars are rapidly flowing mixtures of rock debris and water (other than normal streamflow) from a volcano and represent a significant hazard due to their energetic nature and mobility (Smith and Fritz, 1989). Globally, 17% of historical volcano-related fatalities have occurred due to lahars (Auker et al., 2013); with decadal-scale lahar hazards being created by some large eruptions (Major et al., 2000; Gran and Montgomery, 2005; Van Westen and Daag, 2005). Secondary, post-eruption lahars are dominantly the result of rainfall on unconsolidated pyroclastic deposits, which are typically remobilised by rainsplash-driven particle detachment followed by transport via surface runoff (Segerstrom, 1950; Waldron, 1967), rill erosion due to Hortonian overland flow (Leavesley et al., 1989; Yamakoshi and Suwa, 2000; Lavigne and Thouret, 2003; Major and Yamakoshi, 2005) or by shallow landsliding of saturated tephra layers above basal décollement surfaces (Iverson, 2000; Manville et al., 2000b).

Previous studies at a range of volcanoes have displayed a power-law relationship indicating that lahar initiation occurs along a continuum from short duration, high intensity rainfall events to long duration, low-intensity events (e.g. Rodolfo and Arguden, 1991; Arboleda and Martinez, 1996; Tungol and Regalado, 1996; Van Westen and Daag, 2005). At present, rain-triggered lahar hazard identification is predominantly based on ground-based flow detection systems such as Acoustic Flow Monitors (AFMs) or trip-wires at locations where such resources are available (e.g. Lavigne et al., 2000b; Van Westen and Daag, 2005;

Jones et al., 2015). Maximising the use of local telemetered rainfall gauge networks within lahar hazard monitoring has the potential to increase the number of available mitigation tools whilst negating the lag-time between flow initiation and flow detection inherent in ground-based detection and observation. Globally, such pre-emptive prediction and forecasting of rain-triggered lahars based on telemetered rainfall data is lacking, although the use of real-time rainfall data has demonstrated increased lahar warning times compared with ground-based flow detection (Jones et al., 2015).

Regions of high rainfall seasonality are predominantly distributed in the tropics and sub-tropics either side of the equator (Wang et al., 2010); whereas approximately 46% of active volcanoes are identified as being located in the humid tropics (Rodolfo and Arguden, 1991). Despite this geographic coincidence and the importance of climatic rainfall regimes on storm intensities, durations and antecedent conditions (all important factors in lahar initiation), the impacts of seasonal rainfall on rain-triggered lahar initiation has not previously been incorporated into any lahar forecasting models.

Catchment recovery also impacts lahar frequency and magnitude. Following a discrete volcanic eruption, sediment yields in impacted fluvial systems decline exponentially (Major et al., 2000; Hayes et al., 2002; Gran and Montgomery, 2005; Major and Mark, 2006), which is consistent with other examples of disturbed earth systems (Graf, 1977). Mechanisms include a reduction in available particulate material, vegetation recovery, fragmentation of runoff-enhancing surface crusts, exposure of more permeable substrates and the stabilisation of rill networks (Collins et al., 1983; Collins and Dunne, 1986; Schumm and Rea, 1995; Major et al., 2000). Conversely, at locations featuring

recurrent or persistent volcanic activity, the magnitude of the lahar occurrence remains relatively constant with time due to the regular supply of new material (Thouret et al., 2014).

This study uses probabilistic and diagnostic methods, including binary logistic regression and Receiver Operating Characteristic (ROC) analysis, to develop real-time rainfall-based lahar forecasting tools which account for the impacts of seasonal rainfall and catchment recovery on lahar occurrence in the Belham Valley, Montserrat. Such hazard assessment tools have the potential to be utilised both where ground-based detection equipment is unavailable, and in conjunction with the latter in instrumented catchments to increase lahar warning times.

5.2. Soufrière Hills Volcano, Montserrat

Soufrière Hills Volcano (SHV, Montserrat, Lesser Antilles, 16.72°N, 62.18°W) lies on the northern edge of the Inter-Tropical Convergence Zone and has a strongly seasonal climate. Rainfall-producing weather systems affecting the island fall into two broad categories; large-scale synoptic (>100 km across) systems and local mesoscale (<100 km across) systems (Froude, 2015). Both can produce high intensity precipitation, but large-scale events can potentially be forecast days in advance whereas this timescale reduces to hours for local weather systems (Barclay et al., 2006).

The andesitic dome-forming eruption of SHV began in July 1995 and has featured several phases of activity consisting of dome growth, dome collapse and vulcanian explosions as well as pauses in magma extrusion (Bonadonna et al., 2002; Cole et al., 2002; Sparks et al., 2002; Edmonds et al., 2006; Komorowski

et al., 2010; Stinton et al., 2014). This intermittent eruptive activity has triggered a complex sedimentological response in drainages surrounding the volcano since 1995 (Barclay et al., 2006, 2007; Alexander et al., 2010; Froude, 2015).

5.3. The Belham Catchment

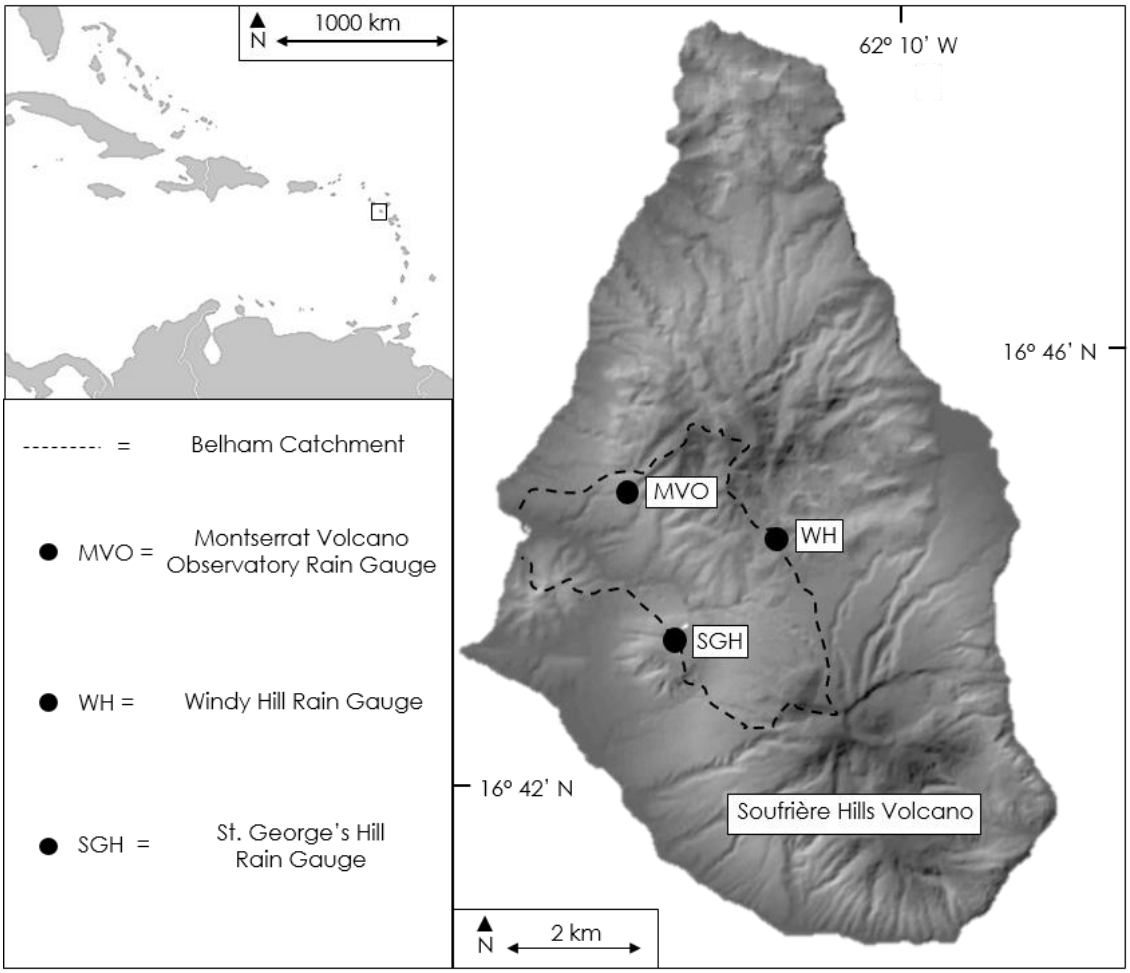

Figure 5.1: Location map of Montserrat and Soufrière Hills Volcano.

Data from the Belham Valley, Montserrat (Fig. 5.1) was used to examine the influence of rainfall seasonality and catchment evolution on the occurrence of rain-triggered lahars between April 2010 and April 2012 (Fig. 5.2). Lahars have persisted in the valley since the onset of eruptive activity in 1995 and have damaged infrastructure, including burying the Belham Bridge (1998), resulting in

the river bed being used as the primary transportation link between the "Safe Zone" and the "Daytime Entry Zone" (Barclay et al., 2007).

The Belham Catchment had a pre-1995 surface area of c. 13.7 km^2, increasing to c. 14.8 km^2 early in the eruptive episode (Froude, 2015). During eruptive episodes tephra fall and Pyroclastic Density Current (PDC) deposits accumulate in the upper catchment. The destruction and burial of vegetation reduces the infiltration and interception of precipitation (Yamakoshi and Suwa, 2000; Major and Yamakoshi, 2005; Ogawa et al., 2007; Pierson et al., 2013), and in combination with a reduction in surface roughness enhances run-off and erosion rates and promotes rain-triggered lahar generation (Barclay et al., 2007; Alexander et al., 2010). Aggradation and sedimentation in the upper catchment during periods of eruptive activity is counter-balanced during periods of quiescence by channel development and stabilisation, exposure of more permeable substrates, vegetation recovery and a reduction in available sediment (Froude, 2015). The data period used here coincides with a lack of substantial eruptive activity at SHV and thus a period of channel development and stabilisation within the upper catchment following the 11 February 2010 dome collapse at the end of Phase 5, which deposited stacked lobes of pumiceous PDC deposits up to 5.7 km from source in the Belham Valley (Stinton et al., 2014).

5.4. Rainfall and Lahar Record

The record used in this study (Fig. 5.2) comprises 0.1 mm resolution hourly precipitation data recorded at the Montserrat Volcano Observatory (MVO) Helipad Gauge between February 2010 and February 2011, the St George's Hill

gauge between March 2011 and May 2011, and the maximum of the St Georges Hill and Windy Hill gauges (Fig. 5.1) between May 2011 and February 2012. The use of multiple rain gauges during the two-year study period is due to rain gauge malfunction and intermittent data availability. Within this study a rainfall event is defined as any recorded rainfall in between two dry periods of at least six hours (Wischmeier and Smith 1978; Todisco, 2014; Jones et al., 2015) The lahar database (Fig. 5.2) is compiled from inspection of seismic records and visual observations. Lahar size (small, medium, large) is estimated based on seismic amplitude and occupied valley width alongside flow start time, end time and duration.

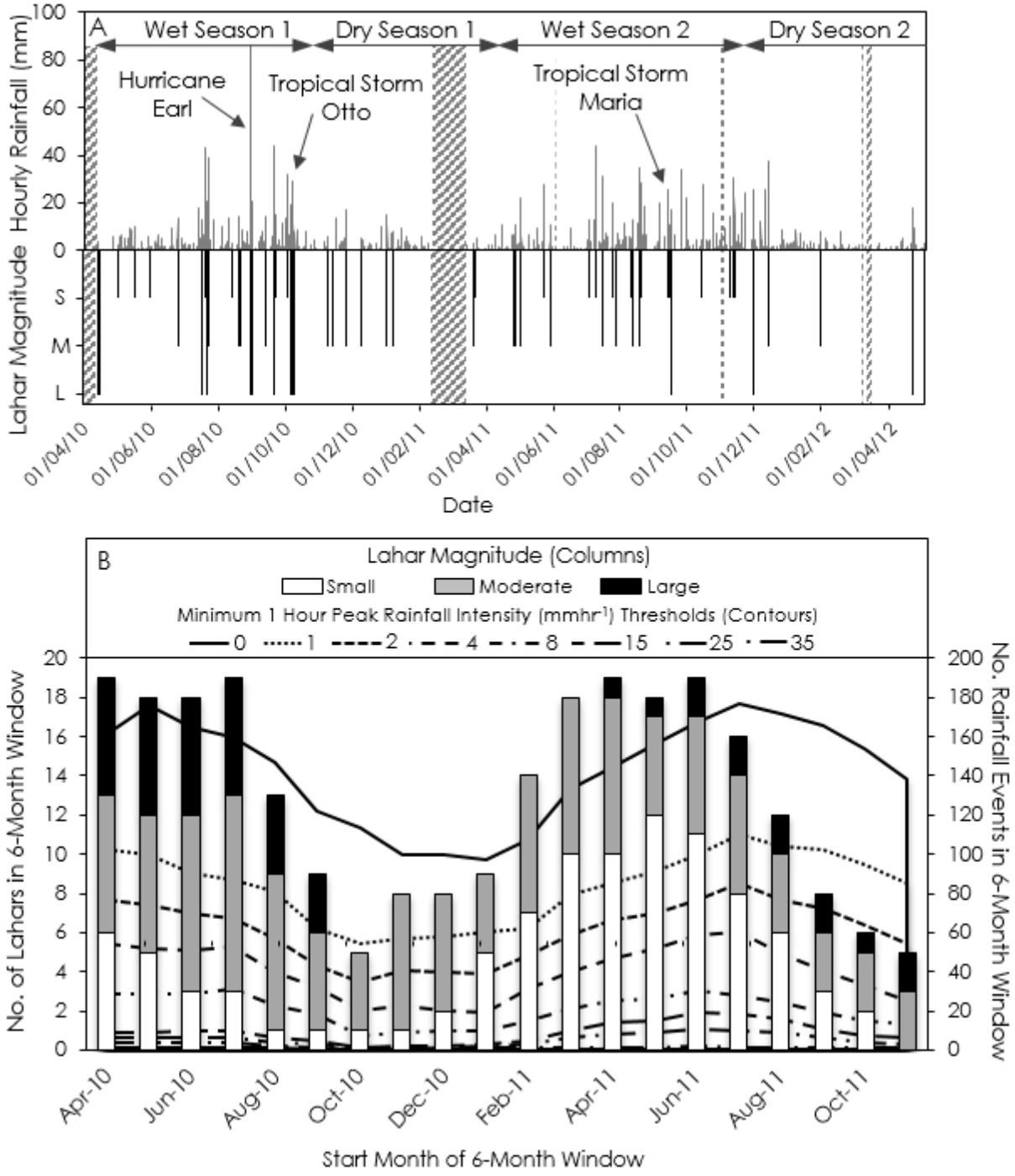

Figure 5.2: Timelines illustrating the occurrence of rainfall events and rain-triggered lahars. A: Hourly rainfall data (above) and lahar activity (below) in the Belham Valley, Montserrat between April 2010 and April 2012 (with minor gaps due to equipment failures). B: Seasonal fluctuations in lahar occurrence displayed using 6-month data windows with 1-month staggered start dates. Vertical bars indicate the number of lahar events, categorised by magnitude, in each 6-month period. Background contours display the number of rainfall events exceeding specified Peak One Hour Rainfall Intensity (1hrPRI) thresholds.

Division of the dataset into six-month moving windows, with staggered one-month start dates, illustrates the seasonal variation in both the number of rainfall events exceeding various One Hour Peak Rainfall Intensity (1hrPRI: the highest resolution available) thresholds and the occurrence (and assessed magnitude) of lahars (Fig. 5.2B). The assessed magnitudes of lahars are subjectively categorised, as no calibration between recorded seismic amplitudes and quantitative lahar magnitude is available. Dividing the dataset up into six-month moving windows, with staggered one-month start dates both generates optimal sample sizes and allows high resolution examination of lahar and rainfall variation, which would not be evident from four discrete six-month datasets.

The six-month window between April and October is classified as the peak wet season in this study, with ≈1700 mm of recorded rainfall in the 2010 peak wet season (WS1) and ≈1500 mm in the 2011 peak wet season (WS2). The 2010/11 peak dry season (DS1) featured ≈750 mm of rainfall, whilst ≈1100 mm of rainfall was recorded in the 2011/12 peak dry season (DS2). Mean WS1 and WS2 1hrPRIs are 5.2 $mmhr^{-1}$ and 5.0 $mmhr^{-1}$ respectively, whilst mean dry season 1hrPRIs are 2.2 $mmhr^{-1}$ (DS1) and 3.3 $mmhr^{-1}$ (DS2).

Receiver Operating Characteristic (ROC) analysis (Appendix 1.1) was used to analyse the statistical relationship between the rainfall and lahar records. As described in Chapter 4, ROC analysis plots the true positive rate (sensitivity) against the false positive rate (1-specificity) as the threshold of a test parameter is varied in order to assess its ability to discriminate between a binary outcome (Fawcett, 2006). In this study the binary outcome refers to whether a rainfall event did or did not trigger a lahar and the test parameters are predominantly based

on rainfall characteristics, an approach also utilised by Jones et al. (2015). The area under the ROC curve (AUC) is a measure of the ability of a parameter to distinguish between the two outcomes, and varies between 0.5 (no predictive ability) and 1.0 (perfect predictive ability). There was significant ($p < 0.01$) correlation between recorded rainfall on timescales of 1-168 hours when used as test parameters and the occurrence of lahars in the Belham Valley, with optimal timescales (AUCs > 0.85) of between 4 and 24 hours. Peak AUC was achieved when the 1hrPRI of a rainfall event was utilised as the test parameter, producing an AUC of 0.93 when applied to the entire two-year dataset. When lahars are categorised by estimated magnitude, large lahars are strongly correlated with longer term (>24 hours) rainfall, produced by the passage of synoptic weather systems. Between April 2010 and April 2012 large flows were directly attributed to several named tropical cyclones (Fig. 5.2A). In contrast, smaller lahars display increased correlation with high levels of short-term (<24 hours) rainfall, more commonly associated with mesoscale weather systems.

5.5. Probabilistic Rain-Triggered Lahar Analysis

The displayed ability of 1hrPRI (AUC = 0.93) to distinguish between lahar-triggering and non lahar-triggering rainfall events in the Belham Valley (April 2010-April 2012) provided the platform for probabilistic analysis of lahar occurrence based on the 1hrPRI of a rainfall event. Results show that lahar probability increases with greater 1hrPRI in both years of the dataset, with higher lahar probabilities in *Year 1* than *Year 2* for a given 1hrPRI (Fig. 5.3).

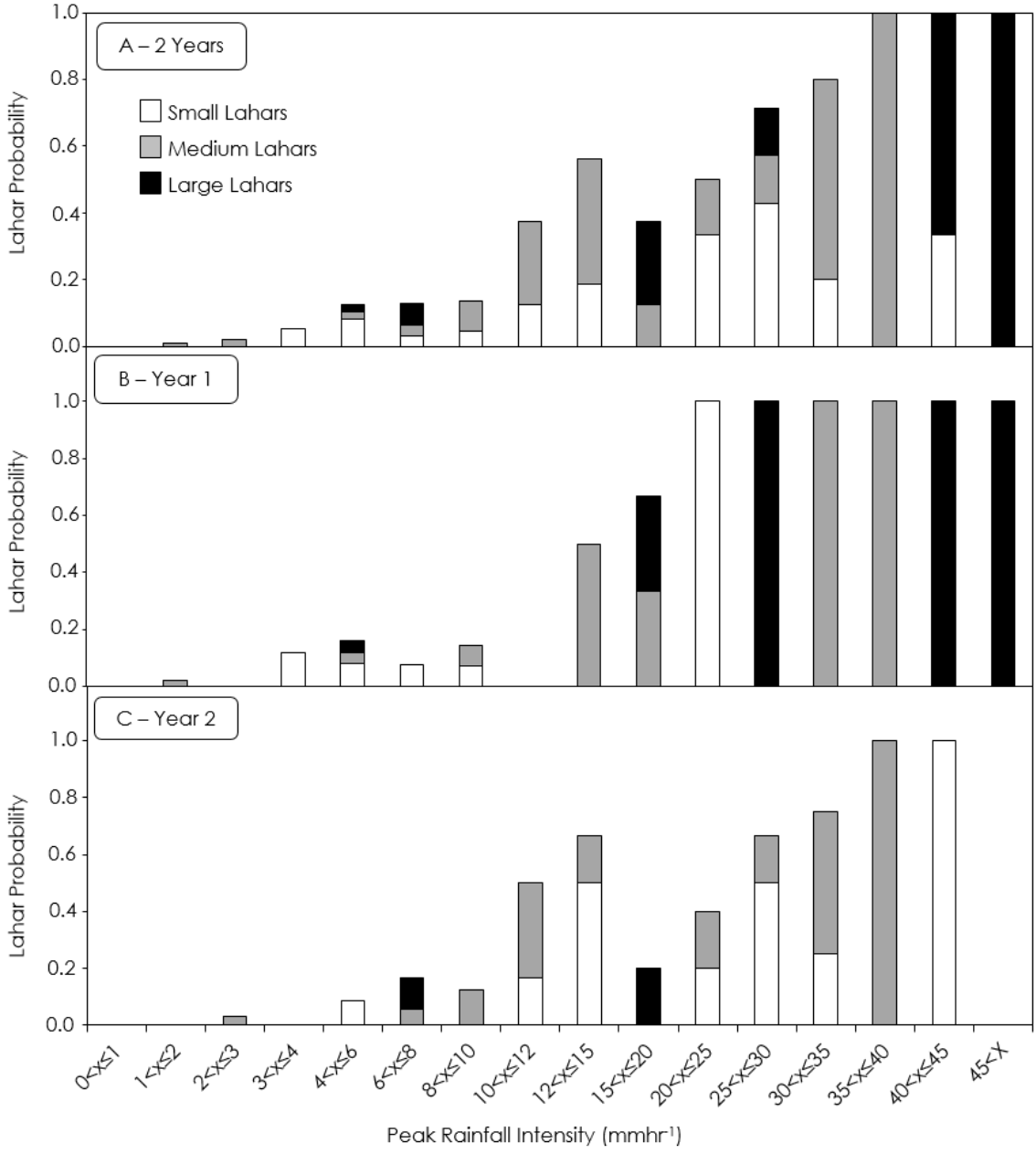

Figure 5.3: Lahar probability, classified by assessed flow magnitude, as categorised One Hour Peak Rainfall Intensity (1hrPRI) increases. A: April 2010-April 2012 B: April 2010-April 2011 C: April 2011-April 2012.

Lahar probability for a given 1hrPRI fluctuates during the study period as a function of seasonality (Fig. 5.4A). The empirically-derived 1hrPRI exceedance-based lahar probability contours in Figure 5.4A display the probability of a lahar of any magnitude being triggered in the Belham Valley when the 1hrPRI of a rainfall event exceeds a threshold value. These probabilities are initially stable during the 6-month windows focused on WS1 before decreasing during DS1, increasing during WS2 and once again decreasing into DS2. Throughout the two-year study period increased 1hrPRI correlates with increased lahar probability; displaying its effectiveness as a first-order lahar forecasting parameter.

In addition to seasonal fluctuations in relative lahar probability driven by differing antecedent conditions (Fig. 5.4A), there is an overall decline in relative lahar probabilities with time (Figs. 5.3 & 5.4). Following the empirically-derived 4 $mmhr^{-1}$ PRI contour on Figure 5.4A, there is a 20% probability of a lahar if this threshold is exceeded at ① (6-month start date of 13/10/2010). This probability increases to 38% at ② (13/04/2011); and declines to 18% at ③ (13/10/2011). Alternatively, reading horizontally across the graph for a lahar probability of 38% the associated PRI threshold increases from 4 $mmhr^{-1}$ at ② (13/04/2011) to approximately 15 $mmhr^{-1}$ at ④ (13/10/2011).

The combination of seasonal fluctuation and temporal decline in lahar probability displayed in Figure 5.4A is examined further using binary logistic regression, a statistical method which estimates the probability of a dichotomous outcome using one or more independent explanatory variables (Hosmer Jr et al., 2013). In this study lahar occurrence or non-occurrence is the dichotomous outcome and initially 1hrPRI is the singular independent explanatory variable. Figure 5.4B displays logistic regression-based lahar probability estimation models

produced by four datasets; *Year 1*, *Year 2*, *Wet Seasons* and *Dry Seasons*. Within each of these four models the model chi-square test indicated statistically significant lahar prediction ability ($p < 0.01$). Figure 5.4B displays higher estimated lahar probabilities at identical 1hrPRI values for *Year 1* relative to *Year 2* and *Wet Seasons* relative to *Dry Seasons*.

The potential benefit of incorporating seasonal and temporal effects within lahar forecasting models was further investigated using additional binary logistic regression. Proxies for seasonal effects (antecedent rainfall on timescales ranging from 1-90 days) and catchment recovery (long-term cumulative rainfall since the start of the dataset and days since significant eruptive activity) were tested in combination with 1hrPRI to examine their impacts upon model performance. A minimum total rainfall threshold of 8 mm per rainfall event (a threshold under which only two lahars occurred during the two-year dataset) was implemented for the initial binary logistic regression and model composition as well as the subsequent assessment of the lahar forecasting performance of the model. This minimum total rainfall threshold was implemented in order to increase the balance between lahar and non-lahar outcomes and thus reduce skewed predicted probability during the binary logistic regression. Alternate chronological rainfall events of ≥8 mm are selected for use in the binary logistic regression, creating a dataset of 74 rainfall events of which 25 produced lahars. The remaining 73 events, of which 20 produced lahars, are retained for lahar forecasting assessment.

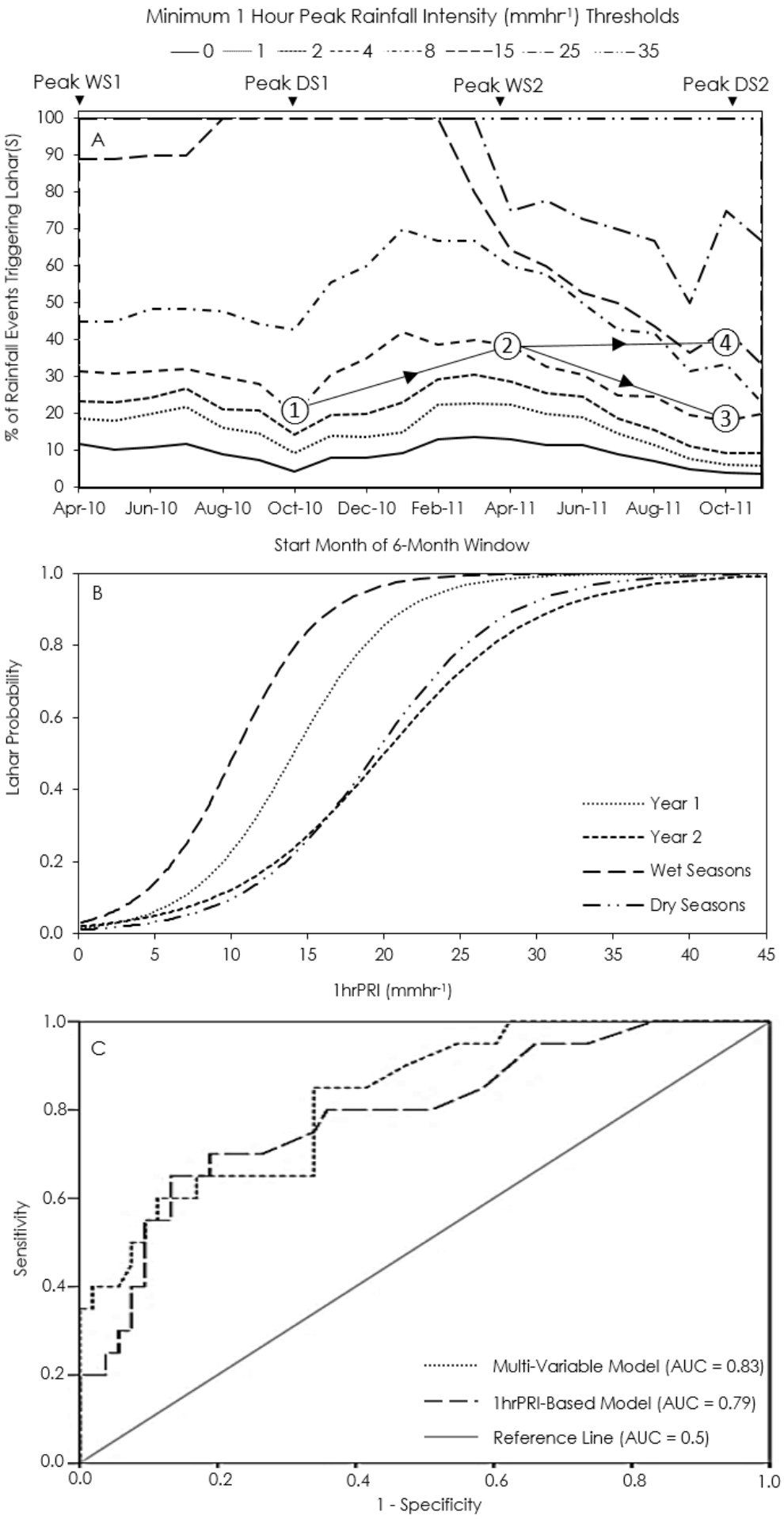
Minimum 1 Hour Peak Rainfall Intensity (mmhr-1) Thresholds
0
1
2
4
8
15
25
35
Peak WS1
Peak DS1
Peak WS2
Peak DS2
A
% of Rainfall Events Triggering Lahar(S)
Apr-10
Jun-10
Aug-10
Oct-10
Dec-10
Feb-11
Apr-11
Jun-11
Aug-11
Oct-11
Start Month of 6-Month Window
B
Lahar Probability
1hrPRI (mmhr-1)
Year 1
Year 2
Wet Seasons
Dry Seasons
C
Sensitivity
1 - Specificity
Multi-Variable Model (AUC = 0.83)
1hrPRI-Based Model (AUC = 0.79)
Reference Line (AUC = 0.5)

Figure 5.4: Seasonal and temporal effects on lahar probability. A: Contour graph of empirically-derived lahar probability relative to the exceedance of One Hour Peak Rainfall Intensity (1hrPRI) thresholds in 6-month moving data windows with 1-month staggered start dates. White numbers and dashed lines show temporal trends, see text for details. B: Four binary logistic regression-based lahar probability estimation models created from Year 1, Year 2, Wet Season and Dry Season data. C: ROC curves assessing the lahar forecasting performance of an exclusively 1hrPRI-centric logistic regression-based lahar probability estimation model and a multi-variable (1hrPRI, antecedent rainfall and long-term cumulative rainfall) model.

Three-day antecedent rainfall displayed the biggest influence of tested antecedent timescales over lahar occurrence and is utilised in the binary logistic regression alongside 1hrPRI and total cumulative rainfall since the start of the dataset, which best captured temporal catchment recovery. The reverse stepwise logistic regression method retained these three independent variables (Hosmer Jr et al., 2013), increasing correct classification of rainfall event outcomes from a null model value of 66% (when all events in the database are predicted to not trigger lahars) to 80% when using the selected explanatory variables, with model chi-square tests again indicating significant prediction ability ($p<0.01$). Model variables (x_i) and output regression coefficients (β_i) are used to construct lahar probability estimation equations by conversion of the logistic regression logit model (Eq. 1) in terms of probability.

$$(1) \qquad logit(p) = \beta_0 + \beta_1 X_1 + \beta_2 X_2 + \cdots + \beta_n X_n$$

Eq. 2 displays the application of this to the multi-variable model, featuring the probability of lahar occurrence *(p)*, 1hrPRI *(R_i)*, three-day antecedent rainfall (A_3) and cumulative rainfall since significant eruptive activity (*C*).

$$(2) \qquad p = \frac{1}{1 + e^{-(-2.10 + 0.133R_i + 0.018A_3 - 0.215C)}}$$

Eq.3 displays the lahar probability estimation model produced by the same dataset of 74 rainfall events using only 1hrPRI as a sole independent variable.

$$p = \frac{1}{1 + e^{-(-2.33+0.133R_i)}} \quad (3)$$

Application of Eqs. 2 & 3 to the 73 rainfall events in the forecasting assessment dataset produces two sets of model-derived lahar probability estimates which can be compared with the actual outcomes (lahar or no-lahar) using ROC analysis (Fawcett, 2006). The multiple-variable lahar probability estimation model shown in Eq. 2 produced an AUC of 0.83 ($p<0.01$), whilst the single variable model shown in Eq. 3 produced an AUC of 0.79 ($p<0.01$) (Fig. 5.4C). The AUC produced by Eq. 2 increases to 0.93 if the 8 mm event threshold is removed and the multi-variable model is applied to all 508 rainfall events between April 2010 and April 2012 that were not used in the initial binary logistic regression-based model development.

5.6. Discussion

Analysis of the Belham Valley lahar and rainfall record over a two-year period indicates that lahar occurrence probability and magnitude is a function of: (i) temporal catchment evolution towards more stable conditions – lahars are harder to trigger with time; and (ii) seasonal variations in rainfall – lahars are more common in the wet season both in terms of frequency and probability relative to 1hrPRI.

The multi-year temporal trend is attributed to a declining supply of easily erodible pyroclastic material in the upper catchment, coupled with stabilisation of channel networks, vegetation re-growth, and increased infiltration rates and

capacity (Collins et al., 1983; Collins and Dunne, 1986; Leavesley et al., 1989; Schumm and Rea, 1995; Scott et al., 1996a; Major et al., 2000; Hayes et al., 2002; Gran and Montgomery, 2005; Major and Yamakoshi, 2005; Van Westen and Daag, 2005). Probabilistic analysis shows increased absolute numbers of lahars, and easier triggering of lahars in the wet seasons. Seasonality in the nature and frequency of rainfall-generating weather systems controls this pattern. Large lahars are often associated with the passage of synoptic weather systems, which typically produce long-duration catchment-wide rainfall. Increased rainfall in the wet season also enhances antecedent effects such as reduced infiltration rates due to deposit saturation (Barclay et al., 2007), and effective surface sealing and increased bulking efficiency during lahar transit due to high water contents in channel floor deposits (Iverson et al., 2010; Reid et al., 2011). These effects increase the likelihood of small lahars in the wet season due to flash-flood type responses to rainfall. The absence of large lahars in the dry season is also attributed to antecedent effects (low antecedent rainfall inhibits bulking efficiency in the dry season) as well as the occurrence of fewer sustained catchment-wide synoptic weather systems.

Incorporation of proxies for temporal catchment recovery (long-term cumulative rainfall) and rainfall seasonality (three-day antecedent rainfall) into logistic regression-based lahar probability estimation models alongside 1hrPRI increases rain-triggered lahar forecasting performance. Antecedent rainfall has been previously identified as an important factor in rain-triggered lahar initiation at several other locations including Tungurahua (Jones et al., 2015), Semeru (Lavigne and Suwa, 2004), Merapi (Lavigne et al., 2000a) and Yakedake (Okano et al., 2012). The incorporation of antecedent rainfall into lahar forecasting models within this study effectively modulates lahar probability estimates to

account for variations in the initial deposit moisture content at the onset of rainfall. At Soufrière Hills, the seasonal rainfall regime induces a seasonal pattern in the dominant antecedent conditions, and the incorporation of antecedent rainfall data into lahar forecasting models over a two-year period effectively accounts for this seasonal variation. Incorporation of long-term cumulative rainfall into lahar forecasting models as a proxy for gradual catchment recovery during a period of eruptive quiescence effectively modulated lahar forecasts to account for gradually increasing lahar initiation thresholds. Integration of further information such as sediment yield data, upper edifice infiltration rates and knowledge of vegetation recovery into proxies for catchment recovery would be preferable, but such data is very rarely available at rain-triggered lahar prone locations.

ROC analysis indicates that the multi-variable model clearly differentiates between lahar and non-lahar outcomes (AUC = 0.83) when considering only larger rainfall events resulting in ≥8 mm of total rainfall, and this ability improves even further (AUC = 0.93) when the 8 mm threshold is removed. The readily available model inputs of 1hrPRI, three-day antecedent rainfall and cumulative rainfall since significant eruptive activity used within this study can be easily assimilated into functional real-time lahar probability estimation models and produces real benefits. Application of the methods described in this study to other locations and for longer time periods would help to further develop the understanding of the impacts of differing climate regimes and volcano-hydrologic responses upon lahar forecasting model performance.

Within this study multiple rain gauges were utilised due to gauge malfunction and intermittent data availability. Optimal rainfall gauge networks

would provide dense radial and vertical coverage around the studied volcanic edifice, with gauges recording data from high-altitude lahar initiation zones providing particular potential benefits. Such rainfall gauge networks would facilitate the accurate real-time capture of spatial variation in recorded precipitation, reducing uncertainty regarding the difference between recorded rainfall and actual lahar-triggering rainfall (e.g. Rodolfo and Arguden, 1991). Extensive rainfall data of this nature is not readily available at rain-triggered lahar prone locations, primarily due to high installation costs, maintenance access issues and the relatively short expected lifespans of the instruments. Despite limited spatial rain gauge coverage, both this study and Jones et al. (2015) demonstrate effective methods of lahar forecasting using real-time telemetered rainfall data, increasing rainfall gauge coverage would further enhance the performance of these methods.

Calibration of AFM and seismic networks with flow measurements and observations can facilitate quantitative assessments of lahar discharges and volumes (Lavigne, 2004). At Soufrière Hills, lahar magnitude was subjectively categorised based on observations, seismic records and inundated valley width, and therefore this study focused upon the prediction of the occurrence of lahars of any magnitude. Future quantitative calibration of flow magnitudes and integration of this information within the forecasting methods developed in this study could facilitate the generation of a series of probabilities under given rainfall conditions, each describing the probability of a lahar exceeding a different flow magnitude.

Lahar forecasting using real-time telemetered rainfall data of the manner developed within this study has the potential to both effectively predict lahars

and increase lahar warning times, even in areas where AFMs, proximal seismometers and trip wires are unavailable. When used in conjunction with ground-based detectors in instrumented catchments, lahar warning times can still be significantly increased by lahar forecasting models (Jones et al., 2015).

5.7. Conclusions

This study demonstrates that rainfall seasonality and catchment recovery are important controlling factors in the severity of the rain-triggered lahar hazard at Soufrière Hills Volcano, Montserrat, and by extension similar volcanoes worldwide. Seasonal influences increase both the absolute number of lahars and the probability of lahar occurrence under pre-defined rainfall conditions during the wet season due to antecedent effects. Lahar probability is also shown to decline with time as a product of catchment evolution. This study develops one-hour peak rainfall intensity-driven binary logistic regression-based lahar probability estimation models, which are shown to effectively forecast lahars using real-time rainfall data. The lahar forecasting performance of the model is enhanced when proxies for initial deposit moisture content and temporal catchment recovery are incorporated into the model. These results demonstrate the potential for successful real-time prediction of secondary lahars, even in areas featuring strongly seasonal climates and periods of eruptive quiescence.

Chapter 6: Discussion

A combination of fieldwork, laboratory-based experiments and the analysis of monitoring network data has been used to examine the initiation of rain-triggered lahars and the manifestation of the rain-triggered lahar hazard at Calbuco, Tungurahua and Soufrière Hills volcanoes. The nature of post-eruption rain-triggered lahar hazards varies on a volcano-by-volcano and catchment-by-catchment basis, as highlighted by the contrasting intensity/duration curves derived at Tungurahua, Pinatubo (Arboleda and Martinez, 1996; Tungol and Regalado, 1996) and Mayon (Rodolfo and Arguden, 1991) in Figure 4.4. Field-based research at Calbuco after the April 2015 eruption revealed severe catchment-by-catchment variation in the post-eruption volcano-hydrologic response to a sub-plinian eruption.

This variation at Calbuco was identified as being driven by numerous factors including the volume and grain-size of PDC and tephra deposits; the extent of vegetation damage; the magnitude and location of primary lahars; and the pre-eruption ice and snow cover. Each of these factors has been identified as directly impacting the physical processes underlying rain-triggered lahar initiation. The grain-size of deposited pyroclastic material affects infiltration rates and therefore rainfall:runoff relationships (e.g. Pierson et al., 2013), whereas the volume of deposits dictates the amount of available source material (e.g. Major et al., 2000) and the extent of vegetation damage (e.g. Major et al., 2013). Vegetation burial and damage reduces interception, infiltration and evapotranspiration rates as well as surface roughness and deposit stability (e.g. Ogawa et al., 2007), all factors which act to increase runoff. The distribution and

volume of pre-eruption snow and ice cover dictates the nature of primary lahars and these flows can extensively scour upper catchments (Pierson, 1995), reducing the post-eruption availability of rain-triggered lahar source material.

Such primary syn-eruptive lahars were triggered during the 2015 eruption of Calbuco by the interaction of column-collapse PDCs with snow and ice (Fig. 2.52). These lahars occurred in several drainages (Fig. 2.53), scouring the upper catchments of sediment and vegetation, and causing significant damage to downstream infrastructure (e.g. Fig. 2.31). Scouring of valleys by snow and ice melt-triggered primary lahars has been identified at other volcanoes including Nevado del Ruiz and Mt. St. Helens, with the downstream extent of channel scouring driven by the size of the lahar and the channel gradient (Pierson, 1995). Upstream erosion by primary lahars at Calbuco, specifically in the Rio Blanco Este, Rio Este and Rio Sur, limited the source of easily-erodible post-eruption pyroclastic material in the upper catchments to late-stage (post-primary lahar) PDC and tephra deposits. Therefore, the occurrence of primary lahars at Calbuco impacted the potential for post-eruption rain-triggered lahars in affected catchments. The extent to which post-eruption rain-triggered lahar hazard is reduced as a result of the erosion of pyroclastic deposits by primary lahars is dependent on the chronology of primary lahars and PDCs.

The emplacement of PDC deposits and surface mantling co-PDC fall deposits (e.g. Fig. 2.3) was an essential component in generating a post-eruption rain-triggered lahar hazard in proximal drainages of Calbuco. The fine-grained nature of these deposits, in addition to the associated reduction in surface roughness and widespread vegetation damage, reduced infiltration rates relative to the coarse proximal tephra deposits and induced surface runoff and

rill formation. Conversely, within the radial drainage network of Calbuco, tephra deposits alone failed to induce a significant post-eruption rain-triggered lahar hazard due to the high infiltration rates of the coarse deposits. This contrasting response identified at Calbuco between areas of PDC and tephra deposition has also been identified by Pierson and Major (2014), who assert that the magnitude and longevity of sedimentary response after the emplacement of valley-fill PDC deposits is typically increased compared to the erosion of topography mantling tephra deposits. The longevity of the response is dictated by the volume of deposits and degree of catchment disturbance, with large eruptions potentially generating decadal-scale lahar hazards (e.g. Major et al., 2000; Torres et al., 2004; Major and Yamakoshi, 2005; Van Westen and Daag, 2005). However, the nature of the immediate post-eruption response, as identified in Chapter 2 at Calbuco and after the 2008 eruption of Chaitén (Pierson et al., 2013), is largely a product of the grain-size of surface deposits. The only locations featuring purely tephra-driven rain-triggered lahars after the eruption of Calbuco were the southern slopes of the adjacent Volcán Osorno (Fig. 2.46). This was a product of the decreased grain-size of tephra deposited on Osorno due to the increased distance from Calbuco, resulting in reduced infiltration rates compared to the coarse proximal tephra deposits.

The effects of surface grain-size variability upon rainfall-runoff processes were quantitatively investigated using a new experimental configuration featuring a calibrated rainfall simulator and an inclined tephra bed (Fig. 3.5). This research demonstrated increased runoff (Fig. 3.7) and decreased runoff lag times (Fig. 3.11) when the tephra bed featured a finer-grained surface layer. Surface runoff from a dry tephra bed with a fine-grained surface layer (d_{50} = 54.3 μm) was increased by 481% compared to a dry ash bed with a coarse surface

layer (d_{50} = 525.8 μm). This runoff increase as a product of a reduction in surface grain size is identified as inducing acute volcano-hydrologic responses after eruptions producing fine-grained pyroclastic material (e.g. Pierson et al., 2013), as well as providing the basis for catchment-by-catchment variation in the magnitude of immediate post-eruption rain-triggered lahar hazards such as identified at Calbuco. Sediment and water transport mechanisms were also affected by the presence of a fine-grained surface layer, with surface seal formation reducing infiltration rates and inducing infiltration-excess overland flow (Fig. 3.6). Surface seals and crust formation have been highlighted as important processes in rain-triggered lahar initiation at various locations including Mt. St. Helens, Pinatubo, Unzen and Chaitén (e.g. Leavesley et al., 1989; Pierson et al., 1996; Yamakoshi and Suwa, 2000; Watt et al., 2009), but are difficult to directly identify in the aftermath of eruptions due to restrictions in gaining access to lahar initiation zones. Video footage of the rainfall simulation experiments described in Chapter 3 illustrates the processes of pellet formation, aggregate breakdown, rearrangement of disrupted fragments, compaction and flattening during surface seal formation on previously dry tephra, processes often inferred in the aftermath of eruptions but not observed (e.g. Pierson et al., 1996; Major and Mark, 2006; Umazano et al., 2014). This indicates that if initial post-eruption rainfall on fine-grained deposits is not sufficient to trigger lahars, it may instead act to prime the deposits for future major lahars via the creation of an effective runoff-enhancing surface seal.

Exclusively coarse tephra beds did not form surface seals during rainfall simulations and downslope water and sediment transport was exclusively a product of rainsplash and particle detachment. These findings mirrored the assessment of post-eruption rainfall-runoff relationships at Calbuco, where only

areas featuring supplies of fine-grained pyroclastic material generated a significant rain-triggered lahar response. The behaviour of coarse tephra under simulated rainfall was also similar to the post-eruption behaviour of coarse proximal tephra deposits at Calbuco, such as those mantling the catchment of the Rio Tepu. These deposits displayed little post-eruption response to rainfall as a result of high infiltration rates, with the coarse nature of the tephra resulting in very high lahar initiation thresholds, behaviour also identified at Mt. Mayon (Rodolfo and Arguden, 1991).

The contrasting response to rainfall from tephra beds featuring fine-grained and coarse-grained surface layers was further enhanced by increased antecedent rainfall, a factor frequently cited as important in rain-triggered lahar initiation both in the previously published literature (e.g. Barclay et al., 2007; Lavigne et al., 2007; Okano et al., 2012) and within this thesis. Rainfall simulation experiments were used to quantitatively study this parameter, which has been identified as contributing towards increased lahar frequency late in the wet season due to deposit saturation (Barclay et al., 2007), influencing the hydraulic magnitude and rheology of flows (Okano et al., 2012) and reducing lahar initiation thresholds (Lavigne et al., 2000a). 102 mm of 72-hour antecedent rainfall increased runoff from the coarse tephra bed by 18% and from the tephra bed featuring the fine-grained surface layer by 293% relative to their initial "dry" simulations. Conversely, infiltration rates of fine-grained surface layers featuring effective surface seals increased substantially after extended dry periods, with subsequent rainfall failing to produce surface seals as effective as those present prior to the extended dry period; thus reducing subsequent runoff and erosion rates. This highlights the significance of wetting and drying cycles upon rain-triggered lahar initiation thresholds as well as the importance of specifically

considering initial post-eruption rainfall, due to its potential to create highly effective surface seals, when assessing rain-triggered lahar hazards.

The relatively minor impact of antecedent rainfall upon the runoff from coarse tephra beds emphasises why proximal Calbuco tephra deposits displayed minor post-eruption response to rainfall, even during periods of sustained precipitation. This behaviour was identified previously at Mayon, where antecedent rainfall was assessed as having negligible impacts upon lahar initiation at locations featuring coarse tephra deposits (Rodolfo and Arguden, 1991; Paguican et al., 2009). The disparity between the runoff from the coarse tephra bed and the tephra bed with a fine-grained surface layer increased from 481% under dry conditions to 1602% with 102 mm of 72-hour antecedent rainfall. Rainfall simulations have thus quantitatively demonstrated a compound increase in surface runoff under given rainfall conditions due to reduced surface grain size and increased antecedent rainfall. This emphasises the importance of incorporating considerations for antecedent rainfall into any lahar hazard and risk assessment tools, such as the probabilistic lahar forecasting methods described in Chapters 4 & 5. Assessment of the grain-size distribution of emplaced pyroclastic material is also of particular importance when attempting to rapidly assess the magnitude and spatial distribution of lahar hazards after discrete eruptions, particularly at locations featuring no established pre-eruption lahar hazard. The April 2015 eruption of Calbuco is an example of this, as it featured high levels of catchment recovery since the previous eruption in 1961 and the locations of post-eruption secondary lahar hazards were primarily driven by the spatial distribution of fine-grained pyroclastic deposits. Antecedent rainfall has previously been incorporated as a parameter within the estimation of 60 minute rainfall-based lahar initiation thresholds (e.g. Lavigne et al., 2000a), however such

methods do not acknowledge the uncertainty inherent in predicting lahar occurrence (i.e. there is never a perfect threshold between rain-triggered lahar occurrence and non-occurrence).

Within this research real-time telemetered rainfall and AFM data from both Tungurahua and Soufrière Hills volcanoes has been utilised to develop location-specific real-time probabilistic lahar forecasts which take into account antecedent rainfall, peak rainfall intensity and catchment recovery. This approach aimed to enhance the practical use of telemetered rainfall and AFM networks within lahar hazard and risk assessment by developing real-time rain-triggered lahar prediction tools, a method not previously utilised at rain-triggered lahar-prone volcanoes. The rain gauge and AFM networks which form the basis of this approach are often installed in lahar-prone regions but not utilised to their potential in terms of rain-triggered lahar risk mitigation. At both Tungurahua and Soufrière Hills volcanoes diagnostic testing revealed peak rainfall intensity to be the optimal real-time indicator of potential lahar occurrence (Fig. 4.8), with increased peak rainfall intensity resulting in increased lahar probability.

The effectiveness of peak rainfall intensity as a lahar forecasting parameter is a product of its relationship with rainfall kinetic energy (Salles et al., 2002; Brodie and Rosewell, 2007; Petan et al., 2010). Increased rainfall kinetic energy results in increased erosivity (van Dijk et al., 2002), and therefore peak rainfall intensity acts as a proxy for peak erosivity within the lahar forecasting methods developed in Chapters 4 & 5. The replacement of rainfall kinetic energy with peak rainfall intensity is not limited to the work within this thesis, as the technology required to accurately capture rainfall drop size distribution and thus kinetic energy is rarely practical outside of a laboratory environment (Sanchez-

Moreno et al., 2012). The background importance of rainfall kinetic energy upon rain-triggered lahar initiation raises multiple topics of importance for future work. Firstly, higher rainfall intensity doesn't always equal higher rainfall kinetic energy due to changing drop size distributions, indicating that variation in "storm types" is likely to impact peak rainfall intensity-based lahar initiation thresholds (Fornis et al., 2005; Wang et al., 2014). Additionally, rainfall kinetic energy increases 1% per 100 m increase in altitude, a potentially important factor to consider when assessing lahar initiation due to the predominantly mountainous topography (van Dijk et al., 2002).

Parameters such as peak rainfall intensity that can be easily monitored and adjusted in real-time during rainfall events are advantageous compared to parameters that are difficult to measure such as rainfall kinetic energy and parameters which can only be assessed after the event such as average rainfall intensity and storm duration. The timescales of studied peak rainfall intensity within this research were dependent on the available resolution of the telemetered rainfall data. This facilitated the examination of 10, 30 and 60 minute peak rainfall intensity at Tungurahua and exclusively 60 minute peak rainfall intensity at Soufrière Hills. Regardless of timescale, increased peak rainfall intensity increased the probability of rain-triggered lahars (Figs. 4.9 & 5.3). In Chapter 4, lahar occurrence at Tungurahua was assessed based on the exceedance of a pre-defined AFM amplitude, above which lahars were identified as posing a risk to downstream infrastructure. Such AFM amplitude-based thresholds are highly location specific as factors including instrument distance from the channel impact the relationship between AFM recordings and flow parameters. At Soufrière Hills (Chapter 5) the lahar record was compiled

from visual observations and seismic records as no integrated AFM network existed in the Belham River Valley.

Soufrière Hills and Tungurahua feature contrasting meteorological and volcaniclastic characteristics which impacts the driving factors behind lahar initiation. At Soufrière Hills the two-year study period featured no significant eruptive activity, indicating a period of gradual catchment recovery, whilst rainfall is strongly seasonal and this seasonality has been identified as influencing lahar frequency (Barclay et al., 2007). Conversely, at Tungurahua there is frequent vulcanian activity during the study period and there is little rainfall seasonality. The regular supply of new pyroclastic material at Tungurahua resulted in a consistent rain-triggered lahar hazard, as identified at other locations featuring persistent eruptive activity such as Semeru (Thouret et al., 2014) and Colima (Capra et al., 2010).

Initial research at Tungurahua used probability matrices (Fig. 4.10) with various peak rainfall intensity (10, 30 and 60 minute) and antecedent rainfall (1, 3, 5 and 7 day) timescales to estimate real-time continuous probabilities of lahar occurrence during all rainfall events featuring ≥10 mm of total rainfall. Selection of the optimal antecedent rainfall timescale for use within rain-triggered lahar research is typically climate-dependant, with shorter optimal timescales (3 days) previously selected at Colima where there is lower monthly rainfall and higher evaporation rates (Capra et al., 2010) than at Merapi (7 days) (Lavigne et al., 2000a). At Tungurahua high levels of antecedent rainfall on all studied timescales increased lahar probabilities for a given rainfall intensity. This was especially prevalent during moderate-high intensity rainfall events, potentially as a product of increased bulking efficiency as a result of saturated channel floor deposits; a

factor which has been identified in large scale debris flow flume experiments (Iverson et al., 2010; Reid et al., 2011). Diagnostic analysis illustrated the effectiveness of this method of real-time lahar forecasting at Tungurahua (Fig. 4.12), with "composite" lahar indicators (composed of the mean probability outputs of multiple individual probability matrices) proving particularly effective (Table 4.2). Even if effective at predicting lahars, the real-time lahar forecasting methods developed within this thesis only add value over traditional ground-based lahar detection if warning time is increased. Peak estimated lahar probability at Tungurahua was reached on average 24 minutes before ground-based detection, doubling effective warning times before lahars reach downstream infrastructure.

This approach was developed further at Soufrière Hills from matrix based probability estimates (Chapter 4) to binary logistic regression-based probability estimation models (Chapter 5). Additionally, the catchment recovery within the Belham Valley and the seasonality of rainfall were two factors which needed to be considered when applying probabilistic lahar forecasting methods to the Belham Valley. Catchment recovery has been previously demonstrated to influence year-on-year lahar initiation thresholds (e.g. Van Westen and Daag, 2005), but has not been incorporated into any lahar risk mitigation tools. The lahar and rainfall record of the Belham valley once again illustrated the effectiveness of peak rainfall intensity when selecting an individual rainfall parameter to predict lahar occurrence (Fig. 5.3), with binary logistic regression-based lahar probability estimation models based purely on peak rainfall intensity data performing well when tested (Fig. 5.4). However, lahar probabilities are shown to fluctuate seasonally under given rainfall conditions, with lahar probability heightened in the wet season, whilst year 1 lahar probabilities are higher than

those in year 2 of the dataset (Fig. 5.4). These findings confirmed both the importance and feasibility of accounting for rainfall seasonality, and catchment recovery within lahar forecasting methods in the Belham Valley. Multiple timescales of antecedent rainfall were investigated in an attempt to account for the seasonal fluctuations in the dominant degree of deposit saturation, and "cumulative rainfall since significant eruptive activity" was utilised as a proxy for catchment recovery effects. The incorporation of three-day antecedent rainfall, the optimum timescale tested at Soufrière Hills, and "cumulative rainfall since significant eruptive activity" into binary logistic regression-based lahar probability estimation models alongside the base variable of peak-rainfall intensity increased model performance compared to single-variable models (Fig. 5.4). These lahar probability estimation models can be constructed using a custom (and potentially continuously updating) timescale of rainfall and lahar occurrence data and generate continuous lahar probability estimates as real-time rainfall data is received.

The lahar probability estimation models based on real-time rainfall data developed in this study could be implemented both alongside existing lahar detection systems or as a standalone method of lahar risk mitigation at locations where AFM networks are unavailable due to a lack of resources, equipment malfunction or damage. As demonstrated at Tungurahua, lahar probability estimation models can increase warning time over ground-based detection/observation, with ground-based detection networks and flow observations acting as a failsafe in the event of rain-gauge malfunction or lahar initiation by low levels of recorded rainfall. Conversely, at Montserrat no lahar-specific AFM network was established so the rain-gauge network could be utilised to facilitate real-time probabilistic lahar forecasting alongside flow

observations. At locations featuring eruptions following long-periods of quiescence, such as at Calbuco (Chapter 2), local telemetered rain-gauge networks are more likely to be pre-installed than AFM networks, making probabilistic forecasting of lahars using rainfall data a potentially easily and rapidly implemented tool for lahar risk mitigation.

A future challenge regarding the implementation of real-time rainfall-based lahar forecasting models is how to approach immediate post-eruption lahar predictions after significant catchment disturbance. Under this scenario, the described method of developing lahar forecasting models from previous site-specific lahar and rainfall records would not be possible. Extensive development of the rainfall simulation experiments described in Chapter 3 to investigate a wide variety of grain size distributions, slope angles and rainfall conditions would assist with this challenge. Knowledge of rainfall-runoff relationships gained from these experiments could be combined with methods such as conditional scenario-based probabilistic assessment of potential tephra and PDC inputs into catchments surrounding volcanoes (e.g. Jenkins et al., 2015b) to assess potential rain-triggered lahar hazards. These scenario-based probabilistic assessments often include stochastic tephra fallout models (e.g. TEPHRA2) and shallow-layer continuum models for PDCs (e.g. Titan2D) to evaluate the potential distribution and characteristics of pyroclastic deposits following various potential eruption scenarios and wind conditions (Jenkins et al., 2012a; Jenkins et al., 2012b). Observations of lahar frequency and magnitude at other locations, such as identified at Tungurahua and Soufrière Hills within this thesis, can then be combined with knowledge of parameters driving rainfall-runoff relationships to estimate real-time rainfall-driven lahar forecasting models for the various potential eruption scenarios. In the event of an eruption, the most appropriate

estimated lahar forecasting model could then be calibrated and adjusted in the time period after the eruption using the methods described in this thesis.

Within this research a rainfall event was defined as any recorded rainfall between two dry spells of 6 hours or longer. This definition was used in this research due to its frequent use in soil erosion studies (Wischmeier and Smith 1978; Todisco, 2014) as no standard definition exists within previous rain-triggered lahar initiation research. A similar issue was addressed in terms of defining lahar events within this research, with the minimum magnitude of studied lahars being a location specific consideration throughout previous lahar research. At Tungurahua the selection of the minimum AFM threshold which triggers a "lahar alert" signal was driven by the assessment of risk to downstream infrastructure. At Soufrière Hills lahars were identified from seismic records and visual observations and subjectively categorised as small, medium or large. Quantitative calibration of AFM networks with lahar magnitudes in order to generate knowledge of peak lahar discharges and flow volumes is an important area of future research, and would facilitate the enhancement of the real-time lahar forecasting methods developed within this thesis. Isolated examples of AFM calibration have been demonstrated at locations including Merapi (Lavigne, 2004), but are lacking globally. This current lack of widespread AFM calibration is attributed to a combination of factors including the intensive nature of calibrating each individual AFM to account for local site effects and limitations regarding financial resources. However, such calibration could facilitate the generation of multiple real-time estimated lahar probabilities relating to the exceedance of various quantitative lahar magnitude thresholds.

A practical illustration of the calibration of peak AFM amplitude values and peak lahar discharges is demonstrated in Figure 6.1 using research focused upon the La Pampa channel at Tungurahua. These data were collected between January 2012 and December 2014 and consisted of the visual observation (and magnitude quantification) of lahars and the analysis of a proximal AFM (Jui-01) within the drainage. The resultant analysis displays an exponential relationship between recorded AFM amplitude and estimated lahar discharge (Fig. 6.1). The potential practical applications of such AFM calibration methods are displayed in the lahar probability curves featured in Figures 6.2-6.5. These curves highlight the potential development from the subjective lahar occurrence-based curves described in Chapter 5 towards quantitative lahar magnitude exceedance probability curves. Within Figures 6.2-6.5 the equation of the trendline in Figure 6.1 is used to transform the AFM amplitude based methods of probabilistic lahar analysis discussed in Chapters 4 & 5 into lahar peak discharge exceedance probability curves. The initial examples displayed in Figures 6.1-6.5 highlight an important potential development, as quantitative estimates of lahar hydrograph parameters can be used within probabilistic lahar hazard assessment models to identify potential inundation zones (Mead et al., 2016). This would facilitate the identification of important lahar magnitude thresholds for risk mitigation at each relevant location. The conversion of AFM records into peak lahar discharge estimates and other lahar hydrograph characteristics (e.g. flow volume) also allows improved inter-location comparison of lahar initiation thresholds (Mead et al., 2016).

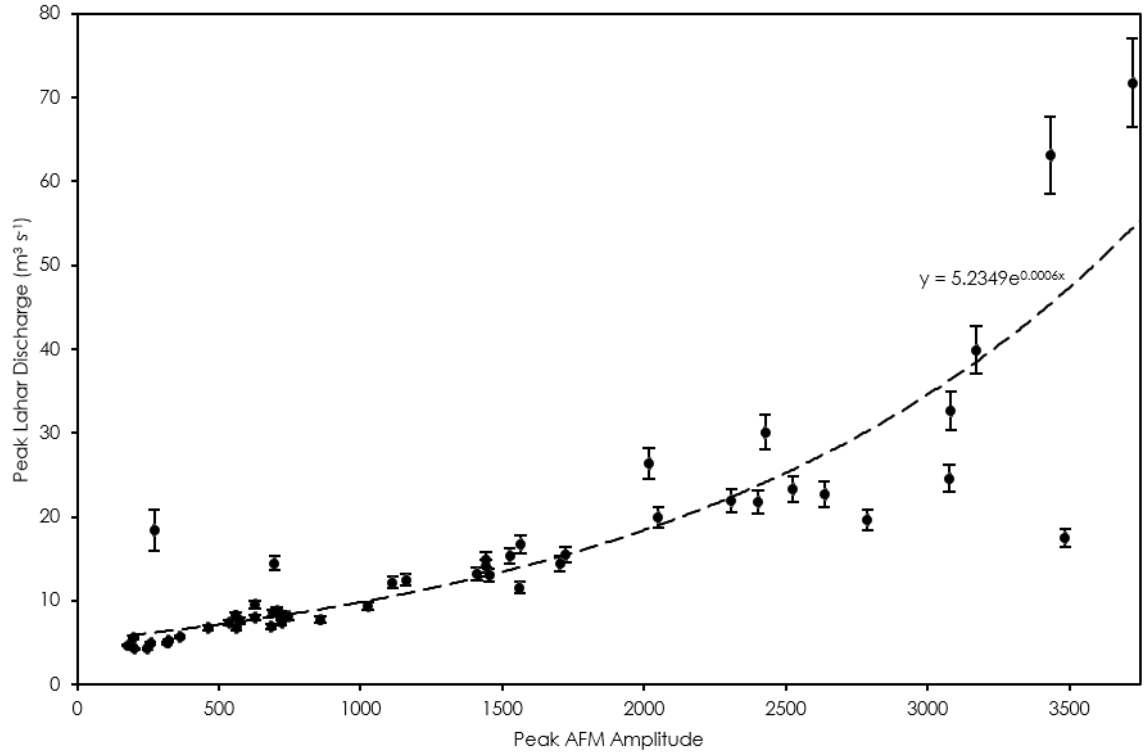

Figure 6.1: A plot of the relationship between observed peak lahar discharge and recorded peak AFM amplitude in the La Pampa drainage of Tungurahua between 2012 and 2014. The exponential dashed trendline estimates the best-fit relationship between the two parameters. Observed peak lahar discharges and rainfall data courtesy of IGEPN (2015).

The nature of lahars as a continuum of flow types and magnitudes as well as site-specific requirements in terms of lahar hazard and risk mitigation strategies means that variable definitions of "significant" lahars will continue to be used globally. The methods described within Chapters 4 & 5 can be adjusted to estimate the probability of the exceedance of location-specific lahar magnitude thresholds, as displayed at the two contrasting locations of Soufrière Hills and Tungurahua. Increased utilisation of peak lahar discharge exceedance thresholds (Figs. 6.2-6.5) would enhance location-specific adjustments as it is a directly comparable flow parameter, unlike peak AFM amplitude. Application of the methods described within this thesis to more locations would also generate additional knowledge regarding the parameters affecting the frequency and magnitude of lahars under given rainfall conditions. Evidence from controlled

laboratory experiments (Chapter 3) and field-based assessments of the volcano-hydrologic response to widespread catchment disturbance (Chapter 2) can also assist in the calibration of such real-time lahar forecasting methods to new locations. Previously, lahar risk mitigation techniques such as intensity/duration curves (e.g. Rodolfo and Arguden, 1991; Tungol and Regalado, 1996) have had to be constructed by the observation and/or detection of rain-triggered lahars in the weeks and months following eruptions, resulting in a limited availability of lahar risk mitigation tools during the period of peak lahar hazard magnitude. The lahar forecasting methods developed in this thesis have the potential to be rapidly implemented post-eruption using an initial base set of parameters and then site-specifically calibrated as more empirical data becomes available.

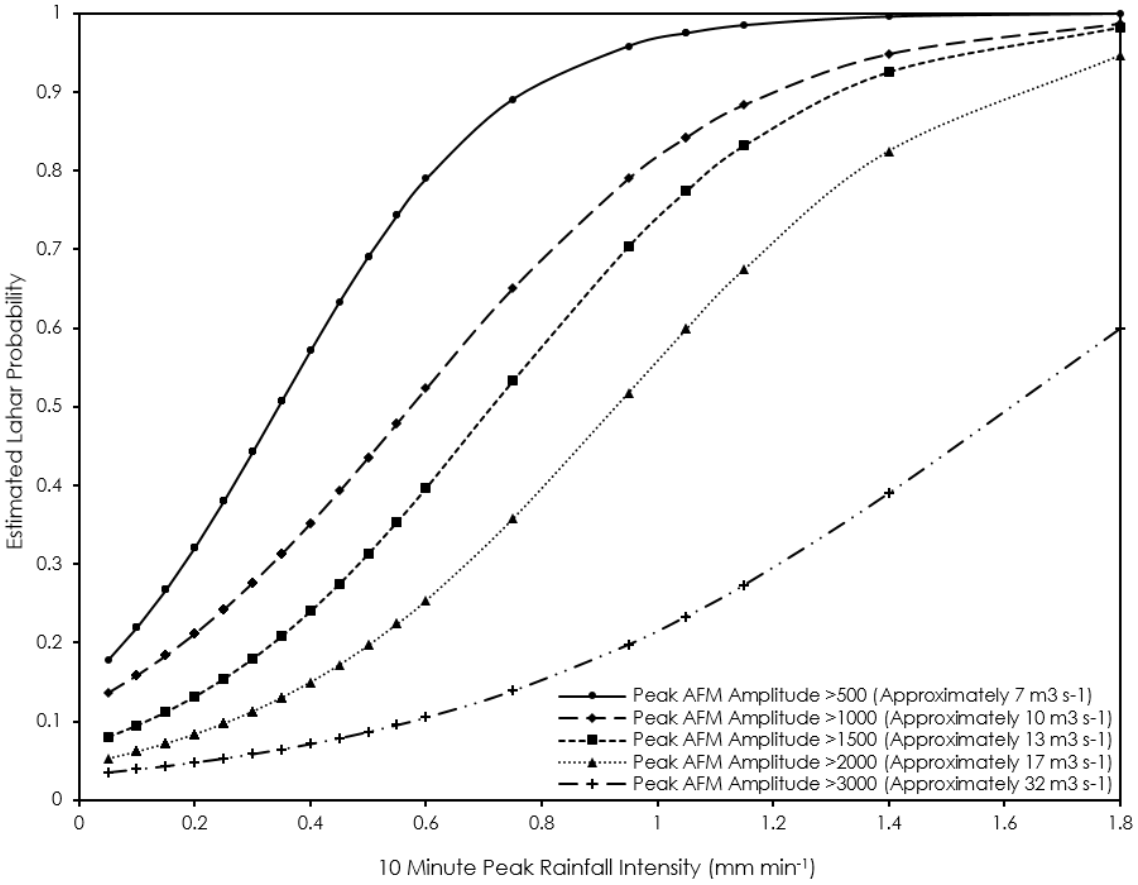

Figure 6.2: Lahar probability curves displaying the probability of lahars exceeding various peak discharge thresholds in the La Pampa drainage of Tungurahua as 10 minute peak rainfall intensity is varied. Based on lahar observation and detection between January 2012 and December 2014.

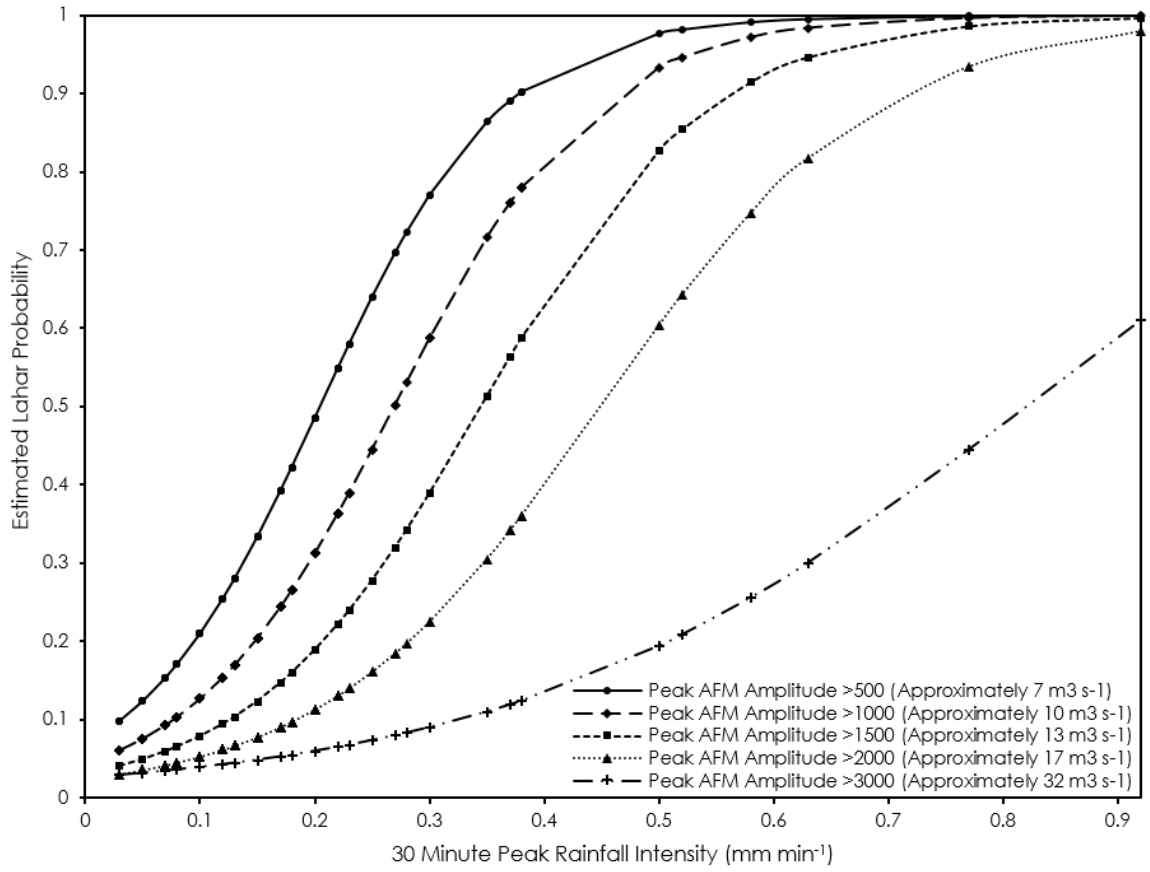

Figure 6.3: Lahar probability curves displaying the probability of lahars exceeding various peak discharge thresholds in the La Pampa drainage of Tungurahua as 30 minute peak rainfall intensity is varied. Based on lahar observation and detection between January 2012 and December 2014.

Figures 6.2-6.4 illustrate increased lahar probability with increased peak rainfall intensity, as demonstrated in Chapters 4 & 5. In addition, lahar magnitude increases with both increased peak rainfall intensity (Figs. 6.2-6.4) and total event rainfall (Fig. 6.5). The curves displayed in Figures 6.2-6.5 are based on single rainfall parameters as this facilitates the graphical illustration of the potential development of the method for the purposes of this discussion. However, as described in Chapter 5, multiple parameters could be incorporated into real-time probabilistic lahar peak discharge exceedance forecasts to improve performance. The importance of parameters including antecedent rainfall (Chapters 3, 4 & 5), surface grain size distribution (Chapters 2 & 3), vegetation destruction (Chapter 2), catchment topography (Chapter 2) and the volume

and emplacement mechanism of pyroclastic material (Chapters 2 & 5) upon the magnitude and frequency of rain-triggered lahars has been demonstrated within this thesis. Such parameters could be amongst those implemented within probabilistic lahar forecasting models via the use of either proxies or direct measurements depending on the key characteristics and available infrastructure at the respective location.

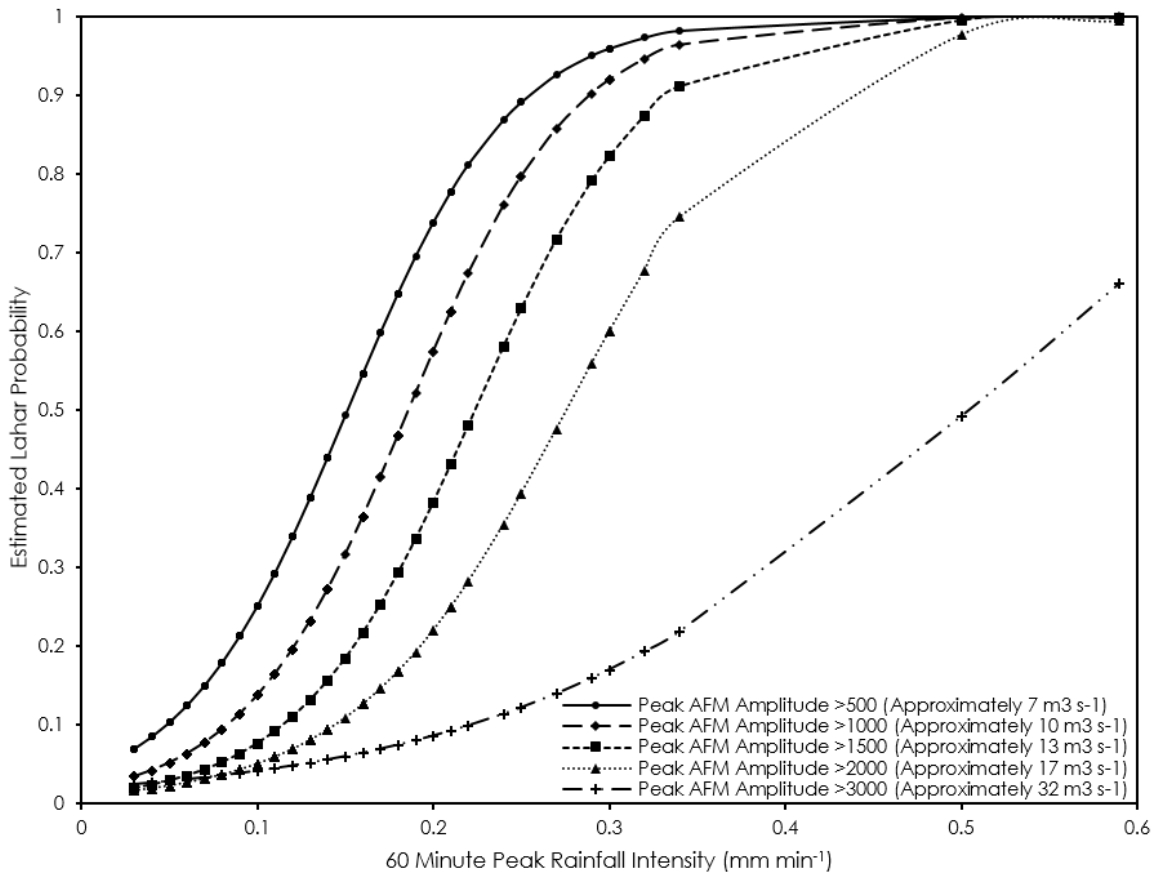

Figure 6.4: Lahar probability curves displaying the probability of lahars exceeding various peak discharge thresholds in the La Pampa drainage of Tungurahua as 60 minute peak rainfall intensity is varied. Based on lahar observation and detection between January 2012 and December 2014.

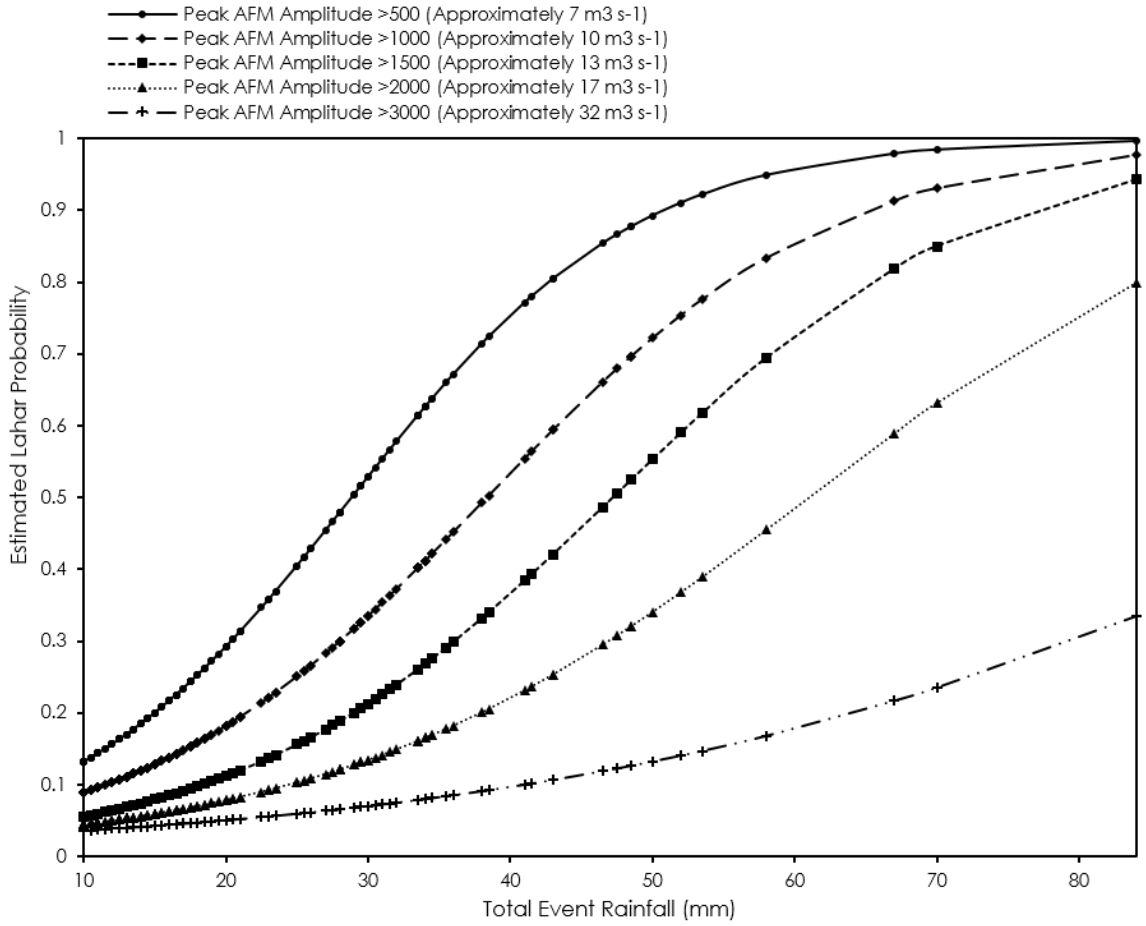

Figure 6.5: Lahar probability curves displaying the probability of lahars exceeding various peak discharge thresholds in the La Pampa drainage of Tungurahua as total event rainfall is varied. Based on lahar observation and detection between January 2012 and December 2014.

The discrepancy between rainfall recorded by local rainfall gauge networks and "actual" rainfall in the lahar initiation zones is a source of uncertainty within rain gauge-based approaches to rain-triggered lahar research and another topic requiring future research (Rodolfo and Arguden, 1991; Major et al., 1996; Scott et al., 2005; Pierson et al., 2013). The nature of the typical topography of volcanic edifices induces high levels of both orographic and rain-shadow effects upon the spatial distribution of precipitation (Lin et al., 2001; Buytaert et al., 2006). These effects can induce severe spatial rainfall variability around volcanic edifices, emphasising the value of radial and vertical rain-gauge coverage around rain-triggered lahar prone volcanoes. At both

Tungurahua and Soufrière Hills, utilised rain gauges were situated within the catchments of focus but at a lower altitude than that where lahar initiation took place. Despite this vertical disparity between lahar initiation zones and recorded rainfall, probabilistic lahar forecasting methods performed excellently at both Tungurahua and Soufrière Hills. The incorporation of more extensive rain gauge networks within probabilistic lahar forecasting would further enhance performance.

Chapter 7: Conclusions

Within this thesis the initiation of rain-triggered lahars and the mitigation of risk associated with these flows has been studied using a combination of field-, laboratory- and data-based techniques as outlined in the introduction. The aims of this research were to increase insight into the processes driving the initiation of rain-triggered lahars and how these processes impact resultant lahar hazard. The following section details the specific aims outlined in the introduction, how these aims were addressed, the key contributions to knowledge presented within this thesis and recommendations for future work.

(1) What does eruption-driven catchment disturbance and post-eruption catchment recovery reveal about the initiation of rain-triggered lahars and the magnitude and spatio-temporal variation of the rain-triggered lahar hazard generated by an eruption?

Field-based research described in Chapter 2 at Calbuco Volcano in Chile following the April 2015 eruption observed significant local catchment-by-catchment variation in the nature of the post-eruption rain-triggered lahar hazards and volcano-hydrologic response to the eruption. A combination of fieldwork and the analysis of aerial photography was used to observe and identify the key factors driving the spatial variation in the secondary lahar hazard.

At Calbuco, the presence of fine-grained surface tephra was observed to be a vital component in generating a post-eruption rain-triggered lahar hazard. This was attributed to reduced Infiltration rates and thus increased runoff

generation as a result of the reduced grain-size. Additionally, increased vegetation damage, larger volumes of available pyroclastic source material and steeper topography were all observed to enhance the potential for rain-triggered lahars. Both vegetation loss and increased gradient also decrease infiltration rates, whilst heightened vegetation damage decreases interception and evapotranspiration rates as well as surface roughness. The generation of the rain-triggered lahar hazard at Calbuco was also indirectly linked to the volume and spatial distribution of pre-eruption snow and ice cover as this influenced the magnitude and distribution of primary lahars. Such primary lahars resulted in widespread inundation of the southern catchments of Calbuco, causing extensive damage, but also stripping the upper drainages of pyroclastic source material, reducing the subsequent rain-triggered lahar hazard.

Chapter 2 identified that the volume and grain-size of pyroclastic material, extent of vegetation coverage, local topography and pre-eruption snow and ice cover were key factors in dictating the magnitude and spatio-temporal variation of the post-eruption volcano-hydrologic response at Calbuco. These factors accounted for the catchment-by-catchment variation in this response as a result of their influence over the physical processes involved in the initiation of rain-triggered lahars. This research particularly highlights the importance of infiltration rates in rain-triggered lahar source regions in determining rainfall thresholds required to trigger lahars, a concept further investigated in Chapter 3.

(2) Experimental Research – What can laboratory-based experiments reveal about the key physical factors involved in rain-triggered lahar initiation and how does this relate to practical lahar hazard and risk assessment?

Chapter 3 describes the development of a new experimental design which facilitated the study of the behaviour of man-made tephra beds under rainfall produced by a calibrated rainfall simulator. This experimental set-up was used to examine the influence of contrasting surface grain-size distributions, a factor identified as important in dictating the rain-triggered lahar hazard at Calbuco in Chapter 2, and antecedent rainfall conditions upon rainfall:runoff relationships and rain-triggered lahar initiation mechanisms under controlled conditions. This experimental research quantitatively demonstrated runoff increases due to reduced surface grain size distribution and increased antecedent rainfall, with a compound increase in runoff demonstrated when both of these factors are present. Runoff-enhancing crust formation was visually demonstrated using video footage when rainfall was applied to dry fine-grained surface tephra. Crust formation of this nature is often inferred after eruptions but rarely visually identified. The identification of this type of crust formation under experimental conditions highlights the potential for initial post-eruption rainfall to prime potential lahar initiation regions for future lahars, if rainfall intensity is insufficient to immediately trigger lahars. Surface crusts did not reform effectively after extended dry periods, illustrating the importance of wetting and drying cycles upon lahar initiation thresholds.

Chapter 3 described the development of a novel and repeatable experimental design, which quantitatively described the runoff-enhancing effects of both reduced surface tephra grain-size and increased antecedent

rainfall. The experimental research presented in Chapter 3 focused upon variable antecedent conditions and two contrasting surface tephra grain size distributions. However, this method could be utilised to examine many other important lahar-related parameters including rainfall intensity, total rainfall, vegetation coverage, slope gradient and tephra depth as well as expanding the range of currently studied antecedent conditions and surface tephra. Quantitative experimental research such as that developed in Chapter 3 can provide important information regarding the relative effects of various parameters when attempting to rapidly assess post-eruption lahar hazard, particularly at locations lacking long-term lahar records due to long periods of eruptive quiescence.

(3) Analysis of Lahar Monitoring Data – Can the use of real-time telemetered lahar monitoring information including rainfall and AFM data be enhanced within a lahar risk mitigation framework?

Research within Chapters 4 and 5 of this thesis has demonstrated the development of methods designed to enhance the use of currently underutilised resources, namely AFM and telemetered rain gauge networks, for lahar risk mitigation. Real-time telemetered rainfall data have been shown to perform well as a basis for predicitve lahar forecasting models, a new approach to rain-triggered lahar risk mitigation. Specifically, peak rainfall intensity has been identified as an effective first-order lahar forecasting parameter at multiple locations, with increased peak rainfall intensity consistently resulting in increased lahar probability. Initial development of this method at Tungurahua (Chapter 4) using peak rainfall intensity and antecedent rainfall-based probability matrices

demonstrated a consistent effective warning time increase of >100% relative to traditional ground-based detection, which still acts as a valuable failsafe.

At Soufrière Hills (Chapter 5) the probability matrix method was developed into binary logistic regression-based lahar forecasting models, which were shown to be effective at predicting lahars in the Belham River Valley. These models were also based on peak rainfall intensity, whilst the effects of seasonal rainfall and catchment recovery were effectively captured within the models using proxies in the form of antecedent rainfall and long-term cumulative rainfall respectively. Real-time rainfall based lahar forecasting models such as those developed within this thesis at Tungurahua and Montserrat have the potential to enhance lahar risk mitigation both at locations featuring exisiting lahar detection systems and at locations where only rainfall networks, which are more common, are available. The increased warning times provided by such forecasting models as indicated at Tungurahua demonstrates the additional value which could be provided at locations with existing AFM networks. At locations without AFMs or other lahar detection methods, in combination with the methods derived in this thesis, real-time telemetered rainfall data can be used provide a viable lahar risk mitigation tool.

The future development of the methods described in Chapters 4 and 5 from subjective binary 'lahar occurrence' thresholds towards quantitative lahar magnitude thresholds would enhance the practical use of such mitigation tools and facilitate enhanced inter-location comparisons. The potential of such methods is displayed within Chapter 6 of this thesis using peak lahar discharge calibrations in the La Pampa channel at Tungurahua, and this example highlights the importance of such methods as a future area of research. The rapid

assessment of lahar hazard in the aftermath of eruptions at locations featuring long periods of eruptive quiesence, and thus no long-term lahar records from which to calibrate lahar prediction models, is also an important area of future research. Such studies could potentially be enhanced by the incorporation of information from quantitative rainfall simulation experiments, such as those developed within Chapter 3, alongside rapid field-based assessments of eruptive products, vegetation coverage and topography as identified in Chapter 2.

The research presented within this thesis investigated the initiation of rain-triggered lahars through a combination of field-based observations (Chapter 2), experimental research (Chapter 3) and the analysis of rainfall and lahar records (Chapters 4 & 5). Key factors controlling the post-eruption spatio-temporal variation of the rain-triggered lahar hazard at Calbuco were identified in Chapter 2, investigated further and quantified in Chapter 3 and used as the basis for assumptions when developing new and innovative tools for lahar risk mitigation in Chapters 4 and 5. As summarised above, this combined approach addressed the research aims outlined in Chapter 1 of increasing insight into the initiation mechanisms of rain-triggered lahars, quantitatively investigating the parameters involved in lahar initiation and enhancing the use of available monitoring data.

References

1. Aguilera, E., Pareschi, M.T., Rosi, M., Zanchetta, G., 2004. Risk from Lahars in the northern valleys of Cotopaxi Volcano (Ecuador). *Natural hazards*, **33**(2), 161-189. 10.1023/b:nhaz.0000037037.03155.23.

2. Alexander, J., Barclay, J., Susnik, J., Loughlin, S.C., Herd, R.A., Darnell, A., Crosweller, S., 2010. Sediment-charged flash floods on Montserrat: The influence of synchronous tephra fall and varying extent of vegetation damage. *Journal of Volcanology and Geothermal Research*, **194**(4), 127-138. 10.1016/j.jvolgeores.2010.05.002.

3. Arboleda, R., Martinez, M., 1996. *1992 Lahars in the Pasig-Potrero River System*. In: C. Newhall, R. Punongbayan (Eds.), Fire and Mud, Eruptions and Lahars of Mt Pinatubo, Philippines. PHIVOLCS/University of Washington Press, Quezon City/Seattle, pp. 1045-1055.

4. Arguden, A., Rodolfo, K., 1990. Sedimentologic and dynamic differences between hot and cold laharic debris flows of Mayon Volcano, Philippines. *Geological Society of America Bulletin*, **102**(7), 865-876. 10.1130/0016-7606(1990)102<0865:saddbh>2.3.co;2.

5. Assouline, S., 2004. Rainfall-Induced Soil Surface Sealing: A Critical Review of Observations, Conceptual Models, and Solutions. *Vadose Zone Journal*, **3**(2), 570-591. 10.2113/3.2.570.

6. Auker, M.R., Sparks, R.S.J., Siebert, L., Crosweller, H.S., Ewert, J., 2013. A statistical analysis of the global historical volcanic fatalities record. *Journal of Applied Volcanology*, **2**(1). 10.1186/2191-5040-2-2.

7. Ayris, P.M., Delmelle, P., 2012. The immediate environmental effects of tephra emission. *Bulletin of Volcanology*, **74**(9), 1905-1936. 10.1007/s00445-012-0654-5.

8. Barclay, J., Johnstone, J.E., Matthews, A.J., 2006. Meteorological monitoring of an active volcano: Implications for eruption prediction. *Journal of Volcanology and Geothermal Research*, **150**(4), 339-358. 10.1016/j.jvolgeores.2005.07.020.

9. Barclay, J., Alexander, J., Susnik, J., 2007. Rainfall-induced lahars in the Belham Valley, Montserrat, West Indies. *Journal of the Geological Society*, **164**(4), 815-827. 10.1144/0016-76492006-078.

10. Bernard, B., 2013. Homemade ashmeter: a low-cost, high-efficiency solution to improve tephra field-data collection for contemporary explosive eruptions. *Journal of Applied Volcanology*, **2**(1), 1-9. 10.1186/2191-5040-2-1.

11. Bernard, J., Kelfoun, K., Le Pennec, J.L., Vargas, S.V., 2014. Pyroclastic flow erosion and bulking processes: comparing field-based vs. modeling results at Tungurahua volcano, Ecuador. *Bulletin of Volcanology*, **76**(9). 10.1007/s00445-014-0858-y.

12. Biggs, J., Mothes, P., Ruiz, M., Amelung, F., Dixon, T.H., Baker, S., Hong, S.H., 2010. Stratovolcano growth by co-eruptive intrusion: The 2008 eruption of Tungurahua Ecuador. *Geophysical Research Letters*, **37**(21). 10.1029/2010gl044942.

13. Bonadonna, C., Mayberry, G.C., Calder, E.S., Sparks, R.S.J., Choux, C., Jackson, P., Lejeune, A.M., Loughlin, S.C., Norton, G.E., Rose, W.I., Ryan, G., Young, S.R., 2002. Tephra fallout in the eruption of Soufriere Hills Volcano, Montserrat. *Geological Society, London, Memoirs*, **21**(1), 483-516. 10.1144/gsl.mem.2002.021.01.22.

14. Bradford, J.M., Ferris, J.E., Remley, P.A., 1987a. Interrill soil erosion processes: I. Effect of surface sealing on infiltration, runoff, and soil splash detachment. *Soil Science Society of America Journal*, **51**(6), 1566-1571. 10.2136/sssaj1987.03615995005100060029x.

15. Bradford, J.M., Ferris, J.E., Remley, P.A., 1987b. Interrill Soil Erosion Processes: II. Relationship of Splash Detachment to Soil Properties. *Soil Science Society of America Journal*, **51**(6), 1571-1575. 10.2136/sssaj1987.03615995005100060030x.

16. Brazier, S., Sparks, R.S.J., Carey, S.N., Sigurdsson, H., Westgate, J.A., 1983. Bimodal grain size distribution and secondary thickening in air-fall ash layers. *Nature*, **301**(5896), 115-119. 10.1038/301115a0.

17. Brodie, I., Rosewell, C., 2007. Theoretical relationships between rainfall intensity and kinetic energy variants associated with stormwater particle washoff. *Journal of Hydrology*, **340**(1-2), 40-47. 10.1016/j.jhydrol.2007.03.019.

18. Bryan, R.B., 2000. Soil erodibility and processes of water erosion on hillslope. *Geomorphology*, **32**(3-4), 385-415. 10.1016/s0169-555x(99)00105-1.

19. Burtin, A., Bollinger, L., Vergne, J., Cattin, R., Nabelek, J.L., 2008. Spectral analysis of seismic noise induced by rivers: A new tool to monitor spatiotemporal changes in stream hydrodynamics. *Journal of Geophysical Research-Solid Earth*, **113**(B5). 10.1029/2007jb005034.

20. Buytaert, W., Celleri, R., Willems, P., De Bievre, B., Wyseure, G., 2006. Spatial and temporal rainfall variability in mountainous areas: A case study from the south Ecuadorian Andes. *Journal of Hydrology*, **329**(3-4), 413-421. 10.1016/j.jhydrol.2006.02.031.

21. Capra, L., Macı□as, J.L., Scott, K.M., Abrams, M., Garduño-Monroy, V.H., 2002. Debris avalanches and debris flows transformed from collapses in the Trans-Mexican Volcanic Belt, Mexico – behavior, and implications for hazard assessment. *Journal of Volcanology and Geothermal Research*, **113**(1-2), 81-110. 10.1016/s0377-0273(01)00252-9.

22. Capra, L., Borselli, L., Varley, N., Gavilanes-Ruiz, J.C., Norini, G., Sarocchi, D., Caballero, L., Cortes, A., 2010. Rainfall-triggered lahars at Volcán de Colima, Mexico: Surface hydro-repellency as initiation process. *Journal of Volcanology and Geothermal Research*, **189**(1-2), 105-117. 10.1016/j.jvolgeores.2009.10.014.

23. Carrivick, J.L., Manville, V., Graettinger, A., Cronin, S.J., 2010. Coupled fluid dynamics-sediment transport modelling of a Crater Lake break-out lahar: Mt. Ruapehu, New Zealand. *Journal of Hydrology*, **388**(3-4), 399-413. 10.1016/j.jhydrol.2010.05.023.

24. Caruso, P., Pareschi, M.T., 1993. Estimation of Lahar and Lahar-Runout Flow Hydrograph on Natural Beds. *Environmental Geology*, **22**(2), 141-152. 10.1007/BF00789326.

25. Castillo, V.M., Gómez-Plaza, A., Martinez-Mena, M., 2003. The role of antecedent soil water content in the runoff response of semiarid catchments: a simulation approach. *Journal of Hydrology,* **284**(1–4), 114-130. 10.1016/S0022-1694(03)00264-6.

26. Castruccio, A., Clavero, J., 2015. Lahar simulation at active volcanoes of the Southern Andes: implications for hazard assessment. *Natural hazards*, **77**(2), 693-716. 10.1007/s11069-015-1617-x.

27. Castruccio, A., Clavero, J., Rivera, A., 2010. Comparative study of lahars generated by the 1961 and 1971 eruptions of Calbuco and Villarrica volcanoes, Southern Andes of Chile. *Journal of Volcanology and Geothermal Research*, **190**(3-4), 297-311. 10.1016/j.jvolgeores.2009.12.005.

28. Cerda, A., Doerr, S.H., 2008. The effect of ash and needle cover on surface runoff and erosion in the immediate post-fire period. *CATENA*, **74**(3), 256-263. 10.1016/j.catena.2008.03.010.

29. Christiansen, J., 1942. Irrigation by Sprinkling *University of California Agricultural Experimental Station Bulletin*, **670**, 110-116.

30. Cole, P.D., Calder, E.S., Sparks, R.S.J., Clarke, A.B., Druitt, T.H., Young, S.R., Herd, R.A., Harford, C.L., Norton, G.E., 2002. Deposits from dome-collapse and fountain-collapse pyroclastic flows at Soufriere Hills Volcano, Montserrat. *Geological Society, London, Memoirs*, **21**(1), 231-262. 10.1144/gsl.mem.2002.021.01.11.

31. Cole, S.E., Cronin, S.J., Sherburn, S., Manville, V., 2009. Seismic signals of snow-slurry lahars in motion: 25 September 2007, Mt Ruapehu, New Zealand. *Geophysical Research Letters*, **36**(9). 10.1029/2009gl038030.

32. Collins, B., Dunne, T., Lehre, A., 1983. Erosion of tephra-covered hillslopes North of Mount St. Helens, Washington: May 1980-May 1981 *Zeitschrift für Geomorphologische Naturwissenschaftliche Forschung*, **16**, 103-121.

33. Collins, B.D., Dunne, T., 1986. Erosion of Tephra from the 1980 Eruption of Mount St Helens. *Geological Society of America Bulletin*, **97**(7), 896-905. 10.1130/0016-7606(1986)97<896:eotfte>2.0.co;2.

34. Córdoba, G., Villarosa, G., Sheridan, M.F., Viramonte, J.G., Beigt, D., Salmuni, G., 2015. Secondary lahar hazard assessment for Villa la Angostura, Argentina, using Two-Phase-Titan modelling code during 2011 Cordón Caulle eruption. *Natural Hazards and Earth System Science*, **15**(4), 757-766. 10.5194/nhess-15-757-2015.

35. Craddock, R.A., Howard, A.D., Irwin, R.P., Tooth, S., Williams, R.M.E., Chu, P.-S., 2012. Drainage network development in the Keanakāko'i tephra, Kīlauea Volcano, Hawai'i: Implications for fluvial erosion and valley network formation on early Mars. *Journal of Geophysical Research*, **117**. 10.1029/2012je004074.

36. Cronin, S.J., Neall, V.E., Lecointre, J.A., Palmer, A.S., 1997. Changes in Whangaehu river lahar characteristics during the 1995 eruption sequence, Ruapehu volcano, New Zealand. *Journal of Volcanology and Geothermal Research*, **76**(1-2), 47-61. 10.1016/s0377-0273(96)00064-9.

37. Cronin, S.J., Neall, V.E., Lecointre, J.A., Palmer, A.S., 1999. Dynamic interactions between lahars and stream flow: A case study from Ruapehu volcano, New Zealand. *Geological Society of America Bulletin*, **111**(1), 28-38. 10.1130/0016-7606(1999)111<0028:diblas>2.3.co;2.

38. Crosta, G.B., Dal Negro, P., 2003. Observations and modelling of soil slip-debris flow initiation processes in pyroclastic deposits: the Sarno 1998 event. *NAtural Hazards and Earth System Sciences*, **3**(1-2), 53-69. 10.5194/nhess-3-53-2003.

39. Cummans, J., 1980. Mudflows Resulting from the May 18, 1980, Eruption of Mount St. Helens, Washington. *Geological Survey Circular*, **850-B**.

40. Darnell, A.R., Phillips, J.C., Barclay, J., Herd, R.A., Lovett, A.A., Cole, P.D., 2013. Developing a simplified geographical information system approach to dilute lahar modelling for rapid hazard assessment. *Bulletin of Volcanology*, **75**(4). 10.1007/s00445-013-0713-6.

41. Davila, N., Capra, L., Gavilanes-Ruiz, J.C., Varley, N., Norini, G., Vazquez, A.G., 2007. Recent lahars at Volcán de Colima (Mexico): Drainage variation and spectral classification. *Journal of Volcanology and Geothermal Research*, **165**(3-4), 127-141. 10.1016/j.jvolgeores.2007.05.016.

42. de Bélizal, E., Lavigne, F., Hadmoko, D.S., Degeai, J.-P., Dipayana, G.A., Mutaqin, B.W., Marfai, M.A., Coquet, M., Mauff, B.L., Robin, A.-K., Vidal, C., Cholik, N., Aisyah, N., 2013. Rain-triggered lahars following the 2010 eruption of Merapi volcano, Indonesia: A major risk. *Journal of Volcanology and Geothermal Research*, **261**, 330-347. 10.1016/j.jvolgeores.2013.01.010.

43. Dibyosaputro, S., Dipayana, G., Nugraha, H., Pratiwi, K., Valeda, H., 2015. Lahar at Kali Konto after the 2014 Eruption of Kelud Volcano, East Java: Impacts and Risk. *Forum Geografi*, **29**(1), 59-72.

44. Donovan, A., Eiser, J., Sparks, R., 2014. Scientists' views about lay perceptions of volcanic hazard and risk. *Journal of Applied Volcanology*, **3**(1). 10.1186/s13617-014-0015-5.

45. Douillet, G.A., Pacheco, D.A., Kueppers, U., Letort, J., Tsang-Hin-Sun, E., Bustillos, J., Hall, M., Ramon, P., Dingwell, D.B., 2013a. Dune bedforms produced by dilute pyroclastic density currents from the August 2006 eruption of Tungurahua volcano, Ecuador. *Bulletin of Volcanology*, **75**(11). 10.1007/S00445-013-0762-X.

46. Douillet, G.A., Tsang-Hin-Sun, E., Kueppers, U., Letort, J., Pacheco, D.A., Goldstein, F., Von Aulock, F., Lavallee, Y., Hanson, J.B., Bustillos, J., Robin, C., Ramon, P., Hall, M., Dingwell, D.B., 2013b. Sedimentology and geomorphology of the deposits from the August 2006 pyroclastic density currents at Tungurahua volcano, Ecuador. *Bulletin of Volcanology*, **75**(11). 10.1007/S00445-013-0765-7.

47. Doyle, E., Cronin, S., Cole, S., Thouret, J., 2009. The Challenges of Incorperating Temporal and Spatial Changes into Numerical Models of Lahars. In: R.S. Anderssen, B. R.D., N. L.T.H. (Eds.), 18th World IMACS Congress and MODSIM09 International Congress on Modelling and Simulation. Modelling and Simulation Society of Australia and New Zealand and International Association for Mathematics and Computers in Simulation, pp. 2665-2671.

48. Doyle, E.E., Cronin, S.J., Cole, S.E., Thouret, J.C., 2010. The coalescence and organization of lahars at Semeru volcano, Indonesia. *Bulletin of Volcanology*, **72**(8), 961-970. 10.1007/s00445-010-0381-8.

49. Doyle, E.E., Cronin, S.J., Thouret, J.C., 2011. Defining conditions for bulking and debulking in lahars. *Geological Society of America Bulletin*, **123**(7-8), 1234-1246. 10.1130/B30227.1.

50. Druitt, T.H., 1992. Emplacement of the 18 May 1980 lateral blast deposit ENE of Mount St. Helens, Washington. *Bulletin of Volcanology*, **54**(7), 554-572. 10.1007/bf00569940.

51. Druzdzel, M.J., van der Gaag, L.C., 2000. Building probabilistic networks: "Where do the numbers come from?" guest editors' introduction. *IEEE Transactions on Knowledge and Data Engineering*, **12**(4), 481-486. 10.1109/tkde.2000.868901.

52. Dumaisnil, C., Thouret, J.C., Chambon, G., Doyle, E.E., Cronin, S.J., Surono, 2010. Hydraulic, physical and rheological characteristics of rain-triggered lahars at Semeru volcano, Indonesia. *Earth Surface Processes and landforms*, **35**(13), 1573-1590. 10.1002/Esp.2003.

53. Dunne, T., Zhang, W., Aubry, B.F., 1991. Effects of rainfall, vegetation, and microtopography on infiltration and runoff. *Water Resources Research,* **27**(9), 2271-2285. 10.1029/91WR01585.

54. Edmonds, M., Herd, R.A., Strutt, M.H., 2006. Tephra deposits associated with a large lava dome collapse, Soufrière Hills Volcano, Montserrat, 12–15 July 2003. *Journal of Volcanology and Geothermal Research*, **153**(3-4), 313-330. 10.1016/j.jvolgeores.2005.12.008.

55. Eychenne, J., Le Pennec, J.L., Troncoso, L., Gouhier, M., Nedelec, J.M., 2012. Causes and consequences of bimodal grain-size distribution of tephra fall deposited during the August 2006 Tungurahua eruption (Ecuador). *Bulletin of Volcanology*, **74**(1), 187-205. 10.1007/s00445-011-0517-5.

56. Fagents, S.A., Baloga, S.M., 2005. Calculation of lahar transit times using digital elevation data. *Journal of Volcanology and Geothermal Research*, **139**(1-2), 135-146. 10.1016/J.Jvolgeores.2004.06.013.

57. Fagents, S.A., Baloga, S.M., 2006. Toward a model for the bulking and debulking of lahars. *Journal of Geophysical Research-Solid Earth*, **111**(B10). 10.1029/2005jb003986.

58. Fawcett, T., 2006. An introduction to ROC analysis. *Pattern Recognition Letters*, **27**(8), 861-874. 10.1016/j.patrec.2005.10.010.

59. Fiksdal, A., 1982. Infiltration Rates of Undisturbed and Disturbed Mount St. Helens tephra deposits. Keller, S.A.C., ed. Mount St. Helens - One Year Later. Eastern Washington University Press, Cheney, WA.

60. Folsom, M., 1986. Mount St. Helens tephra on range and forest lands of Eastern Washington-local erosion and redeposition. In: Keller, S.A.C., ed. Mount St. Helens-Five Years Later. Eastern Washington University Press, Cheney, WA.

61. Fornis, R., Vermeulen, H., Nieuwenhuis, J., 2005. Kinetic energy-rainfall intensity relationship for Central Cebu, Philippines for soil erosion studies. *Journal of Hydrology*, **300**(1-4), 20-32. 10.1016/j.jhydrol.2004.04.027.

62. Froude, M.J., 2015. *Lahar Dynamics in the Belham River Valley, Montserrat: Application of Remote Camera-Based Monitoring for Improved Sedimentological Interpretation of Post-Event Deposits*. PhD Thesis, University of East Anglia.

63. Garreaud, R.D., 2009. The Andes climate and weather. *Advances in Geosciences*, **22**, 3-11. 10.5194/adgeo-22-3-2009.

64. Gilley, J.E., Elliot, W.J., Laflen, J.M., Simanton, J.R., 1993. Critical shear stress and critical flow rates for initiation of rilling. *Journal of Hydrology,* **142**(1), 251-271. 10.1016/0022-1694(93)90013-Y.

65. Gómez, J.A., Darboux, F., Nearing, M.A., 2003. Development and evolution of rill networks under simulated rainfall. *Water Resources Research*, **39**(6). 10.1029/2002wr001437.

66. Google Earth, 2016. *7.1.5.1557*

67. Graettinger, A.H., Manville, V., Briggs, R., 2009. Depositional record of historic lahars in the upper Whangaehu Valley, Mt. Ruapehu, New Zealand: implications for trigger mechanisms, flow dynamics and lahar hazards. *Bulletin of Volcanology*, **72**(3), 279-296. 10.1007/s00445-009-0318-2.

68. Graf, W., 1977. The Rate Law in Fluvial Geomorphology. *American Journal of Science*, **277**, 178-191.

69. Gran, K.B., Montgomery, D.R., 2005. Spatial and temporal patterns in fluvial recovery following volcanic eruptions: Channel response to basin-wide sediment loading at Mount Pinatubo, Philippines. *Geological Society of America Bulletin*, **117**(1-2), 195-211. 10.1130/B25528.1.

70. Gudmundsson, M.T., Thordarson, T., Hoskuldsson, A., Larsen, G., Bjornsson, H., Prata, F.J., Oddsson, B., Magnusson, E., Hognadottir, T., Petersen, G.N., Hayward, C.L., Stevenson, J.A., Jonsdottir, I., 2012. Ash generation and distribution from the April-May 2010 eruption of Eyjafjallajokull, Iceland. *Sci Rep*, **2**, 1-12. 10.1038/srep00572.

71. Hadley, K.C., LaHusen, R.G., 1995. Technical manual for the experimental Acoustic Flow Monitor. *US Geological Survey Open-File Report*.

72. Hall, M.L., Robin, C., Beate, B., Mothes, P., Monzier, M., 1999. Tungurahua Volcano, Ecuador: structure, eruptive history and hazards. *Journal of*

Volcanology and Geothermal Research, **91**(1), 1-21. 10.1016/S0377-0273(99)00047-5.

73. Hall, M.L., Steele, A.L., Mothes, P.A., Ruiz, M.C., 2013. Pyroclastic density currents (PDC) of the 16–17 August 2006 eruptions of Tungurahua volcano, Ecuador: Geophysical registry and characteristics. *Journal of Volcanology and Geothermal Research*, **265**, 78-93. 10.1016/j.jvolgeores.2013.08.011.

74. Harris, A.J.L., Vallance, J.W., Kimberly, P., Rose, W.I., Matias, O., Bunzendahl, E., Flynn, L.P., Garbeil, H., 2006. Downstream aggradation owing to lava dome extrusion and rainfall runoff at Volcan Santiaguito, Guatemala. *Volcanic Hazards in Central America*, **412**, 85-104. 10.1130/2006.2412(05).

75. Hawkins, R.H., Cundy, T.W., 1987. Steady-state analysis of infiltration and overland flow for spatially-varied hillslopes. *Journal of the American Water Resources Association,* **23**(2), 251-256. 10.1111/j.1752-1688.1987.tb00804.x.

76. Hayes, S., Montgomery, D., Newhall, C., 2002. Fluvial sediment transport and deposition following the 1991 eruption of Mount Pinatubo. *Geomorphology*, **45**(3-4), 211-224. 10.1016/S0169-555x(01)00155-6.

77. Hikida, M., Moriyama, M., Nagai, Y., 2007. *Warning system for debris flow hazards at Sakurajima Volcano, Japan*. In: C.L. Chen, J.J. Major (Eds.), Debris-Flow Hazards Mitigation: Mechanics, Prediction, and Assessment. Millpress Science Publishers, Rotterdam, pp. 593-602.

78. Hodgson, K.A., Manville, V.R., 1999. Sedimentology and flow behavior of a rain-triggered lahar, Mangatoetoenui Stream, Ruapehu volcano, New Zealand. *Geological Society of America Bulletin*, **111**(5), 743-754. 10.1130/0016-7606(1999)111<0743:safboa>2.3.co;2.

79. Horton, R.E., 1933. The role of infiltration in the hydrologic cycle. *Transactions, American Geophysical Union*, **14**(1), 446-460. 10.1029/TR014i001p00446.

80. Horton, R.E., 1945. Erosional Development of Streams and Their Drainage Basins; Hydrophysical Approach to Quantitative Morphology. *Geological Society of America Bulletin*, **56**(3). 10.1130/0016-7606(1945)56[275:edosat]2.0.co;2.

81. Hosmer Jr, D.W., Lemeshow, S., Sturdivant, R.X., 2013. Applied logistic regression, 398. John Wiley & Sons.

82. Huang, C.J., Shieh, C.L., Yin, H.Y., 2004. Laboratory study of the underground sound generated by debris flows. *Journal of Geophysical Research-Earth Surface*, **109**. 10.1029/2003jf000048.

83. Huang, J., Wu, P., Zhao, X., 2013. Effects of rainfall intensity, underlying surface and slope gradient on soil infiltration under simulated rainfall experiments. *CATENA*, **104**, 93-102. 10.1016/j.catena.2012.10.013.

84. Hunink, J.E., Immerzeel, W.W., Droogers, P., 2014. A High-resolution Precipitation 2-step mapping Procedure (HiP2P): Development and application to a tropical mountainous area. *Remote Sensing of Environment*, **140**, 179-188. 10.1016/j.rse.2013.08.036.

85. IGEPN, 2015. *www.igepn.edu.ec/*

86. Iverson, R.M., Lahusen, R.G., 1989. Dynamic pore-pressure fluctuations in rapidly shearing granular materials. *Science*, **246**(4931), 796-799. 10.1126/science.246.4931.796.

87. Iverson, R.M., Schilling, S.P., Vallance, J.W., 1998. Objective delineation of lahar-inundation hazard zones. *Geological Society of America Bulletin*, **110**(8), 972-984. 10.1130/0016-7606(1998)110<0972:Odolih>2.3.Co;2.

88. Iverson, R.M., 2000. Landslide triggering by rain infiltration. *Water Resources Research*, **36**(7), 1897-1910. 10.1029/2000wr900090.

89. Iverson, R.M., Reid, M.E., Logan, M., LaHusen, R.G., Godt, J.W., Griswold, J.P., 2010. Positive feedback and momentum growth during debris-flow entrainment of wet bed sediment. *Nature Geoscience*, **4**(2), 116-121. 10.1038/ngeo1040.

90. Jakob, M., Hungr, O., 2005. Debris-Flow hazards and Related Phenomena. Springer-Praxis, Heidleberg.

91. Janda, R., Daag, A., Delos Reyes, P., Newhall, C., Pierson, T., Punongbayan, R., Rodolfo, K., Solidum, R., Umbal, J., 1996. *Assessment and response to lahar hazard around Mt Pinatubo, 1991 to 1993*. In: C. Newhall, R. Punongbayan (Eds.), Fire and Mud, Eruptions and Lahars of Mt Pinatubo, Philippines. PHIVOLCS/University of Washington Press, Quezon City/Seattle, pp. 107-140.

92. Jenkins, S., Magill, C., McAneney, J., Blong, R., 2012a. Regional ash fall hazard I: a probabilistic assessment methodology. *Bulletin of Volcanology*, **74**(7), 1699-1712. 10.1007/s00445-012-0627-8.

93. Jenkins, S., McAneney, J., Magill, C., Blong, R., 2012b. Regional ash fall hazard II: Asia-Pacific modelling results and implications. *Bulletin of Volcanology*, **74**(7), 1713-1727. 10.1007/s00445-012-0628-7.

94. Jenkins, S.F., Phillips, J.C., Price, R., Feloy, K., Baxter, P.J., Hadmoko, D.S., de Bélizal, E., 2015a. Developing building-damage scales for lahars:

application to Merapi volcano, Indonesia. *Bulletin of Volcanology*, **77**(9), 10.1007/s00445-00015-00961-00448. 10.1007/s00445-015-0961-8.

95. Jenkins, S.F., Barsotti, S., Hincks, T.K., Neri, A., Phillips, J.C., Sparks, R.S.J., Sheldrake, T., Vougioukalakis, G., 2015b. Rapid emergency assessment of ash and gas hazard for future eruptions at Santorini Volcano, Greece. *Journal of Applied Volcanology*, **4**(1). 10.1186/s13617-015-0033-y.

96. Jensen, E.H., Helgason, J.K., Einarsson, S., Sverrisdottir, G., Höskuldsson, A., Oddsson, B., 2013. *Lahar, floods and debris Flows resulting from the 2010 eruption of Eyjafjallajökull: observations, mapping, and modelling*. In: C. Margottini, P. Canuti, K. Sassa (Eds.), Landslide Science and Practice: Volume 3: Spatial Analysis and Modelling. Springer Berlin, pp. 435-440.

97. Jomaa, S., Barry, D.A., Heng, B.C.P., Brovelli, A., Sander, G.C., Parlange, J.Y., 2013. Effect of antecedent conditions and fixed rock fragment coverage on soil erosion dynamics through multiple rainfall events. *Journal of Hydrology*, **484**, 115-127. 10.1016/j.jhydrol.2013.01.021.

98. Jones, R., Manville, V., Andrade, D., 2015. Probabilistic analysis of rain-triggered lahar initiation at Tungurahua volcano. *Bulletin of Volcanology*, **77**(8). 10.1007/s00445-015-0946-7.

99. Jónsson, S., Adam, N., Björnsson, H., 1998. Effects of subglacial geothermal activity observed by satellite radar interferometry. *Geophysical Research Letters*, **25**(7), 1059-1062. 10.1029/98gl50567.

100. Kean, J.W., Staley, D.M., Cannon, S.H., 2011. In situ measurements of post-fire debris flows in southern California: Comparisons of the timing and magnitude of 24 debris-flow events with rainfall and soil moisture conditions. *Journal of Geophysical Research-Earth Surface*, **116**. 10.1029/2011jf002005.

101. Kilgour, G., Manville, V., Della Pasqua, F., Graettinger, A., Hodgson, K.A., Jolly, G.E., 2010. The 25 September 2007 eruption of Mount Ruapehu, New Zealand: Directed ballistics, surtseyan jets, and ice-slurry lahars. *Journal of Volcanology and Geothermal Research*, **191**(1-2), 1-14. 10.1016/j.jvolgeores.2009.10.015.

102. Klohn, E., 1963. The February 1961 Eruption of Calbuco Volcano. *Bulletin of the Seismological Society of America*, **53**(6), 1435-1436.

103. Komorowski, J.C., Legendre, Y., Christopher, T., Bernstein, M., Stewart, R., Joseph, E., Fournier, N., Chardot, L., Finizola, A., Wadge, G., Syers, R., Williams, C., Bass, V., 2010. Insights into processes and deposits of hazardous vulcanian explosions at Soufrière Hills Volcano during 2008 and 2009 (Montserrat, West Indies). *Geophysical Research Letters*, **37**(19). 10.1029/2010gl042558.

104. Kuhn, N.J., Bryan, R.B., 2004. Drying, soil surface condition and interrill erosion on two Ontario soils. *CATENA*, **57**(2), 113-133. 10.1016/j.catena.2003.11.001.

105. Kumagai, H., Palacios, P., Maeda, T., Castillo, D.B., Nakano, M., 2009. Seismic tracking of lahars using tremor signals. *Journal of Volcanology and Geothermal Research*, **183**(1-2), 112-121. 10.1016/j.jvolgeores.2009.03.010.

106. Larsen, M.C., Simon, A., 1993. A rainfall intensity-duration threshold for landslides in a humid-tropical environment, Puerto Rico. *Geografiska Annaler. Series A, Physical Geography*, **75**, 13-23. 10.2307/521049.

107. Lavigne, F., 1999. Lahar Hazard micro-zonation and risk assessment in Yogyakarta City, Indonesia. *GeoJournal*, **49**, 173-183. 10.1023/A:1007035612681.

108. Lavigne, F., Thouret, J.C., Voight, B., Suwa, H., Sumaryono, A., 2000a. Lahars at Merapi volcano, Central Java: an overview. *Journal of Volcanology and Geothermal Research*, **100**(1-4), 423-456. 10.1016/S0377-0273(00)00150-5.

109. Lavigne, F., Thouret, J.C., Voight, B., Young, K., LaHusen, R., Marso, J., Suwa, H., Sumaryono, A., Sayudi, D.S., Dejean, M., 2000b. Instrumental lahar monitoring at Merapi Volcano, Central Java, Indonesia. *Journal of Volcanology and Geothermal Research*, **100**(1-4), 457-478. 10.1016/S0377-0273(00)00151-7.

110. Lavigne, F., Thouret, J.C., 2003. Sediment transportation and deposition by rain-triggered lahars at Merapi Volcano, Central Java, Indonesia. *Geomorphology*, **49**(1-2), 45-69. 10.1016/s0169-555x(02)00160-5.

111. Lavigne, F., 2004. Rate of sediment yield following small-scale volcanic eruptions: A quantitative assessment at the Merapi and Semeru stratovolcanoes, Java, Indonesia. *Earth Surface Processes and landforms*, **29**(8), 1045-1058. 10.1002/Esp.1092.

112. Lavigne, F., Suwa, H., 2004. Contrasts between debris flows, hyperconcentrated flows and stream flows at a channel of Mount Semeru, East Java, Indonesia. *Geomorphology*, **61**(1-2), 41-58. 10.1016/j.geomorph.2003.11.005.

113. Lavigne, F., Thouret, J.C., Hadmoko, D., Sukatja, B., 2007. Lahars in Java: Initiations, Dynamic, Hazard Assessment and Deposition Processes. *Forum Geografi*, **21**(1), 17-32.

114. Le Bissonnais, Y., Renaux, B., Delouche, H., 1995. Interactions between soil properties and moisture content in crust formation, runoff and interrill erosion from tilled loess soils. *CATENA,* **25**(1), 33-46. 10.1016/0341-8162(94)00040-L.

115. Le Pennec, J.L., Jaya, D., Samaniego, P., Ramón, P., Moreno Yánez, S., Egred, J., van der Plicht, J., 2008. The AD 1300–1700 eruptive periods at Tungurahua volcano, Ecuador, revealed by historical narratives, stratigraphy and radiocarbon dating. *Journal of Volcanology and Geothermal Research*, **176**(1), 70-81. 10.1016/j.jvolgeores.2008.05.019.

116. Le Pennec, J.-L., Ruiz, G.A., Ramón, P., Palacios, E., Mothes, P., Yepes, H., 2012. Impact of tephra falls on Andean communities: The influences of eruption size and weather conditions during the 1999–2001 activity of Tungurahua volcano, Ecuador. *Journal of Volcanology and Geothermal Research*, **217-218**, 91-103. 10.1016/j.jvolgeores.2011.06.011.

117. Leavesley, G., Lusby, G., Lichty, R., 1989. Infiltration and erosion characteristics of selected tephra deposits from the 1980 eruption of Mt St Helens, Washington, USA. *Hydrological Sciences*, **34**(3), 339-353.

118. Lee, S.-K., Lee, C.-W., Lee, S., 2015. A comparison of the Landsat image and LAHARZ-simulated lahar inundation hazard zone by the 2010 Merapi eruption. *Bulletin of Volcanology*, **77**(6). 10.1007/s00445-015-0920-4.

119. Lin, Y.-L., Chiao, S., Wang, T.-A., Kaplan, M.L., Weglarz, R.P., 2001. Some Common Ingredients for Heavy Orographic Rainfall. *Weather and Forecasting*, **16**(6), 633-660. 10.1175/1520-0434(2001)016<0633:scifho>2.0.co;2.

120. Liu, H., Lei, T.W., Zhao, J., Yuan, C.P., Fan, Y.T., Qu, L.Q., 2011. Effects of rainfall intensity and antecedent soil water content on soil infiltrability under rainfall conditions using the run off-on-out method. *Journal of Hydrology*, **396**(1-2), 24-32. 10.1016/j.jhydrol.2010.10.028.

121. Loch, R.J., Robotham, B.G., Zeller, L., Masterman, N., Orange, D.N., Bridge, B.J., Sheridan, G., Bourke, J.J., 2001. A multi-purpose rainfall simulator for field infiltration and erosion studies. *Australian Journal of Soil Research*, **39**(3), 599-610. 10.1071/Sr00039.

122. Lowe, D.R., Williams, S.N., Leigh, H., Connort, C.B., Gemmell, J.B., Stoiber, R.E., 1986. Lahars initiated by the 13 November 1985 eruption of Nevado del Ruiz, Colombia. *Nature*, **324**(6092), 51-53. 10.1038/324051a0.

123. Lube, G., Cronin, S.J., Manville, V., Procter, J.N., Cole, S.E., Freundt, A., 2012. Energy growth in laharic mass flows. *Geology*, **40**(5), 475-478. 10.1130/G32818.1.

124. Luk, S.-h., 1985. Effect of antecedent soil moisture content on rainwash erosion. *CATENA*, **12**(2-3), 129-139. 10.1016/0341-8162(85)90005-0.

125. Major, J.J., Newhall, C.G., 1989. Snow and ice perturbation during historical volcanic eruptions and the formation of lahars and floods. *Bulletin of Volcanology*, **52**(1), 1-27. 10.1007/bf00641384.

126. Major, J.J., Janda, R., Daag, A., 1996. *Watershed Disturbance and Lahars on the East Side of Mount Pinatubo during the Mid-June 1991 Eruptions*. In: C. Newhall, R. Punongbayan (Eds.), Fire and Mud, Eruptions and Lahars of Mt Pinatubo, Philippines. PHIVOLCS/University of Washington Press, Quezon City/Seattle, pp. 895-921.

127. Major, J.J., Iverson, R.M., 1999. Debris-flow deposition: Effects of pore-fluid pressure and friction concentrated at flow margins. *Geological Society of America Bulletin*, **111**(10), 1424-1434. 10.1130/0016-7606(1999)111<1424:dfdeop>2.3.co;2.

128. Major, J.J., Pierson, T.C., Dinehart, R.L., Costa, J.E., 2000. Sediment yield following severe volcanic disturbance - A two-decade perspective from Mount St. Helens. *Geology*, **28**(9), 819-822. 10.1130/0091-7613(2000)28<819:Syfsvd>2.0.Co;2.

129. Major, J.J., Yamakoshi, T., 2005. Decadal-scale change of infiltration characteristics of a tephra-mantled hillslope at Mount St Helens, Washington. *Hydrological Processes*, **19**(18), 3621-3630. 10.1002/Hyp.5863.

130. Major, J.J., Mark, L.E., 2006. Peak flow responses to landscape disturbances caused by the cataclysmic 1980 eruption of Mount St. Helens, Washington. *Geological Society of America Bulletin*, **118**(7-8), 938-958. 10.1130/b25914.1.

131. Major, J.J., Pierson, T.C., Hoblitt, R.P., Moreno, H., 2013. Pyroclastic density currents associated with the 2008-2009 eruption of Chaiten Volcano (Chile): Forest disturbances, deposits, and dynamics. *Andean Geology*, **40**(2), 324-358. 10.5027/andgeoV40n2-a09.

132. Major, J.J., Bertin, D., Pierson, T.C., Amigo, Á., Iroumé, A., Ulloa, H., Castro, J., 2016. Extraordinary sediment delivery and rapid geomorphic response following the 2008-2009 eruption of Chaitén Volcano, Chile. *Water Resources Research*, **52**(7), 5075-5094. 10.1002/2015wr018250.

133. Manville, V., White, J.D.L., Hodgson, K.A., 2000a. Dynamic interactions between lahars and stream flow: A case study from Ruapehu volcano, New Zealand: Discussion and reply: Discussion. *Geological Society of America Bulletin*, **112**(7), 1149-1151. 10.1130/0016-7606(2000)112<1149:diblas>2.0.co;2.

134. Manville, V., Hodgson, K., Houghton, B., Keys, J., White, J., 2000b. Tephra, snow and water: complex sedimentary responses at an active snow-

capped stratovolcano, Ruapehu, New Zealand. *Bulletin of Volcanology*, **62**(4-5), 278-293. 10.1007/s004450000096.

135. Manville, V., Cronin, S.J., 2007. Breakout Lahar From New Zealand's Crater Lake. *Eos, Transactions American Geophysical Union*, **88**(43). 10.1029/2007eo430001.

136. Manville, V., Nemeth, K., Kano, K., 2009a. Source to sink: A review of three decades of progress in the understanding of volcaniclastic processes, deposits, and hazards. *Sedimentary Geology*, **220**(3-4), 136-161. 10.1016/j.sedgeo.2009.04.022.

137. Manville, V., Segschneider, B., Newton, E., White, J.D.L., Houghton, B.F., Wilson, C.J.N., 2009b. Environmental impact of the 1.8 ka Taupo eruption, New Zealand: Landscape responses to a large-scale explosive rhyolite eruption. *Sedimentary Geology*, **220**(3-4), 318-336. 10.1016/j.sedgeo.2009.04.017.

138. Marchi, L., Arattano, M., Deganutti, A.M., 2002. Ten years of debris-flow monitoring in the Moscardo Torrent (Italian Alps). *Geomorphology*, **46**(1-2), 1-17. 10.1016/S0169-555x(01)00162-3.

139. Marcial, S., Melosantos, A., Hadley, K., LaHusen, R., Marso, J., 1996. *Instrumental Lahar Monitoring at Mount Pinatubo*. In: C. Newhall, R. Punongbayan (Eds.), Fire and Mud, Eruptions and Lahars of Mt Pinatubo, Philippines. PHIVOLCS/University of Washington Press, Quezon City/Seattle, pp. 1015-1023.

140. Martinez, M., Arboleda, R., Delos Reyes, P., Gabinete, E., Dolan, M., 1996. *Observations of 1992 Lahars along the Sacobia-Bamban River System*. In: C. Newhall, R. Punongbayan (Eds.), Fire and Mud, Eruptions and Lahars of Mt Pinatubo, Philippines. PHIVOLCS/University of Washington Press, Quezon City/Seattle, pp. 1033-1045.

141. Massey, C.I., Manville, V., Hancox, G.H., Keys, H.J., Lawrence, C., McSaveney, M., 2009. Out-burst flood (lahar) triggered by retrogressive landsliding, 18 March 2007 at Mt Ruapehu, New Zealand—a successful early warning. *Landslides*, **7**(3), 303-315. 10.1007/s10346-009-0180-5.

142. Mead, S., Magill, C., Hilton, J., 2016. Rain-triggered lahar susceptibility using a shallow landslide and surface erosion model. *Geomorphology*, **273**, 168-177. 10.1016/j.geomorph.2016.08.022

143. Moreno, H., 1999. Mapa de Peligros del Volcan Osorno, Region de los Lagos. In: S.N.d.G.y. Mineria (Ed.), Documentos de Trabajo, Santiago, pp. 1 mapa escale 1:75.000.

144. Morgan, R., McIntyre, K., Vickers, A., Quinton, J., Rickson, R., 1997. A rainfall simulation study of soil erosion on rangeland in Swaziland. *Soil Technology*, **11**(3), 291-299. 10.1016/S0933-3630(97)00013-5.

145. Muñoz-Salinas, E., Castillo-Rodríguez, M., Manea, V., Manea, M., Palacios, D., 2009. Lahar flow simulations using LAHARZ program: Application for the Popocatépetl volcano, Mexico. *Journal of Volcanology and Geothermal Research*, **182**(1-2), 13-22. 10.1016/j.jvolgeores.2009.01.030.

146. Murata, K.J., Dondoli, C., Saenz, R., 1966. The 1963–65 eruption of Irazú volcano, Costa Rica (the period of March 1963 to October 1964). *Bulletin Volcanologique*, **29**(1), 763-793. 10.1007/bf02597194.

147. Myers, M.L., Geist, D.J., Rowe, M.C., Harpp, K.S., Wallace, P.J., Dufek, J., 2014. Replenishment of volatile-rich mafic magma into a degassed chamber drives mixing and eruption of Tungurahua volcano. *Bulletin of Volcanology*, **76**(11). 10.1007/S00445-014-0872-0.

148. Nairn, I.A., Wood, C.P., Hewson, C.A.Y., 1979. Phreatic eruptions of Ruapehu: April 1975. *New Zealand Journal of Geology and Geophysics*, **22**(2), 155-170. 10.1080/00288306.1979.10424215.

149. Nammah, H., Larsen, F.E., McCool, D.K., Fritts, R., Molnau, M., 1986. Mt. St. Helens volcanic ash: Effect of incorporated and unincorporated ash of two particle sizes on runoff and erosion. *Agriculture, Ecosystems & Environment*, **15**(1), 63-72. 10.1016/0167-8809(86)90114-3.

150. Neall, V.E., 1976. Lahars as major geological hazards. *Bulletin of the International Association of Engineering Geology*, **13**(1), 233-240. 10.1007/bf02634799.

151. Nearing, M.A., Foster, G.R., Lane, L.J., Finkner, S.C., 1989. A process-based soil erosion model for USDA-Water Erosion Prediction Project technology. *Transactions of the American Society of Agricultural Engineers*, **32**(5), 1587-1593. 10.13031/2013.31195.

152. Ogawa, Y., Daimaru, H., Shimizu, A., 2007. Experimental study of post-eruption overland flow and sediment load from slopes overlain by pyroclastic-flow deposits, Unzen volcano, Japan. *Géomorphologie : relief, processus, environnement*, **13**(3), 237-246. 10.4000/geomorphologie.3962.

153. Okano, K., Suwa, H., Kanno, T., 2012. Characterization of debris flows by rainstorm condition at a torrent on the Mount Yakedake volcano, Japan. *Geomorphology*, **136**(1), 88-94. 10.1016/j.geomorph.2011.04.006.

154. Orense, R.P., Ikeda, M., 2007. Damage caused by typhoon-induced lahar flows from Mayon Volcano, Philippines. *Soils and Foundations*, **47**(6), 1123-1132. 10.3208/sandf.47.1123.

155. Paguican, E.M.R., Lagmay, A.M.F., Rodolfo, K.S., Rodolfo, R.S., Tengonciang, A.M.P., Lapus, M.R., Baliatan, E.G., Obille, E.C., 2009. Extreme rainfall-induced lahars and dike breaching, 30 November 2006, Mayon Volcano, Philippines. *Bulletin of Volcanology*, **71**(8), 845-857. 10.1007/s00445-009-0268-8.

156. Pareschi, M.T., Favalli, M., Giannini, F., Sulpizio, R., Zanchetta, G., Santacroce, R., 2000. May 5, 1998, debris flows in circum-Vesuvian areas (southern Italy): Insights for hazard assessment. *Geology*, **28**(7). 10.1130/0091-7613(2000)28<639:mdfica>2.0.co;2.

157. Petan, S., Rusjan, S., Vidmar, A., Mikos, M., 2010. The rainfall kinetic energy-intensity relationship for rainfall erosivity estimation in the mediterranean part of Slovenia. *Journal of Hydrology*, **391**(3-4), 314-321. 10.1016/j.jhydrol.2010.07.031.

158. Pierson, F.B., Robichaud, P.R., Moffet, C.A., Spaeth, K.E., Williams, C.J., Hardegree, S.P., Clark, P.E., 2008. Soil water repellency and infiltration in coarse-textured soils of burned and unburned sagebrush ecosystems. *CATENA*, **74**(2), 98-108. 10.1016/j.catena.2008.03.011.

159. Pierson, T.C., 1985. Initiation and flow behavior of the 1980 Pine Creek and Muddy River Lahars, Mount-St-Helens, Washington. *Geological Society of America Bulletin*, **96**(8), 1056-1069. 10.1130/0016-7606(1985)96<1056:lafbot>2.0.Co;2.

160. Pierson, T.C., Janda, R.J., Thouret, J.-C., Borrero, C.A., 1990. Perturbation and melting of snow and ice by the 13 November 1985 eruption of Nevado del Ruiz, Colombia, and consequent mobilization, flow and deposition of lahars. *Journal of Volcanology and Geothermal Research*, **41**(1-4), 17-66. 10.1016/0377-0273(90)90082-q.

161. Pierson, T.C., 1995. Flow Characteristics of Large Eruption-Triggered Debris Flows at Snow-Clad Volcanos - Constraints for Debris-Flow Models. *Journal of Volcanology and Geothermal Research*, **66**(1-4), 283-294. 10.1016/0377-0273(94)00070-W.

162. Pierson, T., Daag, A., Delos Reyes, P., TM, R., Solidum, R., Tubianosa, B., 1996. *Flow and Deposition of Posteruption Hot Lahars on the East Side of Mount Pinatubo, July-October 1991*. In: C. Newhall, R. Punongbayan (Eds.), Fire and Mud, Eruptions and Lahars of Mt Pinatubo, Philippines. PHIVOLCS/University of Washington Press, Quezon City/Seattle, pp. 921-951.

163. Pierson, T., 2005. Distinguishing between Debris Flows and Floods from Field Evidence in Small Watersheds. *USGS Fact Sheet*, **2004-3142**.

164. Pierson, T.C., Major, J.J., Amigo, A., Moreno, H., 2013. Acute sedimentation response to rainfall following the explosive phase of the 2008-2009 eruption of Chaiten volcano, Chile. *Bulletin of Volcanology*, **75**(5), 1-17. 10.1007/S00445-013-0723-4.

165. Pierson, T.C., Major, J.J., 2014. Hydrogeomorphic effects of explosive volcanic eruptions on drainage basins. *Annual Review of Earth and Planetary Sciences*, **42**(1), 469-507. 10.1146/annurev-earth-060313-054913.

166. Pierson, T.C., Wood, N.J., Driedger, C.L., 2014. Reducing risk from lahar hazards: concepts, case studies, and roles for scientists. *Journal of Applied Volcanology*, **3**(1). 10.1186/s13617-014-0016-4.

167. Pyle, D.M., 1989. The thickness, volume and grainsize of tephra fall deposits. *Bulletin of Volcanology*, **51**(1), 1-15. 10.1007/bf01086757.

168. Reid, M., Iverson, R., Logan, M., Lahusen, R.G., Godt, J., Griswold, J., 2011. Entrainment of Bed Sediment By Debris Flows: Results From Large Scale Experiments. In: R. Genevois, D.L. Hamilton, A. Prestinizi (Eds.), Fifth International Conference on Debris-flow Hazards Mitigation, Mechanics, Prediction and Assessment, Casa Editrice Universita La Sapienza, Rome, pp. 367-374.

169. Rodolfo, K., 1989. Origin and Early Evolution of Lahar Channel at Mabinit, Mayon Volcano, Philippines. *Geological Society of America Bulletin*, **101**(3), 414-426. 10.1130/0016-7606(1989)101<0414:Oaeeol>2.3.Co;2.

170. Rodolfo, K., Arguden, A., Solidum, R., Umbal, J., 1989. Anatomy and behaviour of a post-eruptive rain lahar triggered by a typhoon on Mayon volcano, Philippines. *Bulletin of the International Association of Engineering Geology*, **40**(1), 55-66. 10.1007/bf02590341.

171. Rodolfo, K., Arguden, A., 1991. *Rain-lahar generation and sediment-delivery systems at Mayon Volcano, Philippines*. In: R. Fisher, G. Smith (Eds.), Sedimentation in Volcanic Settings. SEPM, Special Publication 45, pp. 71-87.

172. Rodolfo, K., Umbal, J., Alonso, R., Remotigue, C., Paladio-Melosantos, L., Salvador, J., Evangelista, D., Miller, Y., 1996. *Two years of lahars on the Western flank of mount Pinatubo: Initiation, flow processes, deposits, and attendant geomorphic and hydraulic changes*. In: C. Newhall, R. Punongbayan (Eds.), Fire and Mud, Eruptions and Lahars of Mt Pinatubo, Philippines. PHIVOLCS/University of Washington Press, Quezon City/Seattle, pp. 989-1015.

173. Romero, J.E., Morgavi, D., Arzilli, F., Daga, R., Caselli, A., Reckziegel, F., Viramonte, J., Díaz-Alvarado, J., Polacci, M., Burton, M., Perugini, D., 2016. Eruption dynamics of the 22–23 April 2015 Calbuco Volcano (Southern Chile): Analyses of tephra fall deposits. *Journal of Volcanology and Geothermal Research*, **317**, 15-29. 10.1016/j.jvolgeores.2016.02.027.

174. Römkens, M.J.M., Helming, K., Prasad, S.N., 2002. Soil erosion under different rainfall intensities, surface roughness, and soil water regimes. *CATENA*, **46**(2-3), 103-123. 10.1016/s0341-8162(01)00161-8.

175. Salles, C., Poesen, J., Sempere-Torres, D., 2002. Kinetic energy of rain and its functional relationship with intensity. *Journal of Hydrology*, **257**(1-4), 256-270. 10.1016/S0022-1694(01)00555-8.

176. Samaniego, P., Le Pennec, J.L., Robin, C., Hidalgo, S., 2011. Petrological analysis of the pre-eruptive magmatic process prior to the 2006 explosive eruptions at Tungurahua volcano (Ecuador). *Journal of Volcanology and Geothermal Research*, **199**(1-2), 69-84. 10.1016/j.jvolgeores.2010.10.010.

177. Sanchez-Moreno, J.F., Mannaerts, C.M., Jetten, V., Loffler-Mang, M., 2012. Rainfall kinetic energy-intensity and rainfall momentum-intensity relationships for Cape Verde. *Journal of Hydrology*, **454**, 131-140. 10.1016/j.jhydrol.2012.06.007.

178. Schneider, D., Bartelt, P., Caplan-Auerbach, J., Christen, M., Huggel, C., McArdell, B.W., 2010. Insights into rock-ice avalanche dynamics by combined analysis of seismic recordings and a numerical avalanche model. *Journal of Geophysical Research-Earth Surface*, **115**(F4). 10.1029/2010jf001734.

179. Schumm, S.A., Rea, D.K., 1995. Sediment Yield from Disturbed Earth Systems. *Geology*, **23**(5), 391-394. 10.1130/0091-7613(1995)023<0391:Syfdes>2.3.Co;2.

180. Scott, K., Janda, R., De La Cruz, E., Gabinete, E., Eto, I., Isada, M., Sexon, M., Hadley, K., 1996a. *Channel and sedimentation responses to large volumes of 1991 volcanic deposits on the East flank of Mt Pinatubo*. In: C. Newhall, R. Punongbayan (Eds.), Fire and Mud, Eruptions and Lahars of Mt Pinatubo, Philippines. PHIVOLCS/University of Washington Press, Quezon City/Seattle, pp. 971-989.

181. Scott, K., Vallance, J., Kerle, N., Luis Macías, J., Strauch, W., Devoli, G., 2005. Catastrophic precipitation-triggered lahar at Casita volcano, Nicaragua: occurrence, bulking and transformation. *Earth Surface Processes and landforms*, **30**(1), 59-79. 10.1002/esp.1127.

182. Scott, W., Hoblitt, R., Torres, R., Self, S., Martinez, M., Nillos Jr, T., 1996b. *Pyroclastic Flows of the Jun 15th 1991, Climactic Eruption of Mt. Pinatubo*. In: C. Newhall, R. Punongbayan (Eds.), Fire and Mud, Eruptions and Lahars of Mt Pinatubo, Philippines. PHIVOLCS/University of Washington Press, Quezon City/Seattle, pp. 545-571.

183. Segerstrom, K., 1950. Erosion studies at Paricutin, State of Michoacan, Mexico. *USGS Bulletin*, **965-A**, 164 pp.

184. SERNAGEOMIN, 2015. *http://www.sernageomin.cl/*

185. Shea, T., Gurioli, L., Houghton, B.F., Cioni, R., Cashman, K.V., 2011. Column collapse and generation of pyroclastic density currents during the A.D. 79 eruption of Vesuvius: The role of pyroclast density. *Geology*, **39**(7), 695-698. 10.1130/g32092.1.

186. Shepherd, R., 1989. Correlations of Permeability and Grain-Size. *Ground Water*, **27**(5), 633-638. 10.1111/j.1745-6584.1989.tb00476.x.

187. Siebert, L., 1984. Large volcanic debris avalanches: Characteristics of source areas, deposits, and associated eruptions. *Journal of Volcanology and Geothermal Research*, **22**(3-4), 163-197. 10.1016/0377-0273(84)90002-7.

188. Singh, S., Tack, F., Gabriels, D., Verloo, M., 2000. Heavy metal transport from dredged sediment derived surface soils in a laboratory rainfall simulation experiment. *Water Air and Soil Pollution*, **118**(1-2), 73-86. 10.1023/A:1005140726372.

189. Slattery, M.C., Bryan, R.B., 1992. Laboratory experiments on surface seal development and its effect on interrill erosion processes. *Journal of Soil Science*, **43**(3), 517-529. 10.1111/j.1365-2389.1992.tb00157.x.

190. Smith, G.A., Fritz, W.J., 1989. Volcanic Influences on Terrestrial Sedimentation. *Geology*, **17**(4), 375-376.

191. Snorrason, Jnsson, P., Sigursson, O., Plsson, S., rnason, S., Vkingsson, S., Kaldal, I., 2002. November 1996 Jökulhlaup on Skeiðarársandur Outwash Plain, Iceland. 10.1002/9781444304299.ch4, 53-65. 10.1002/9781444304299.ch4.

192. Sorenson, O., Rose, W., Jaya, D., 2003. Lahar Hazard Modelling at Tungurahua, Ecuador., GS - AGU - EUG Joint Assembly, Nice, France.

193. Sparks, R.S.J., 1976. Grain size variations in ignimbrites and implications for the transport of pyroclastic flows. *Sedimentology*, **23**(2), 147-188. 10.1111/j.1365-3091.1976.tb00045.x.

194. Sparks, R.S.J., Barclay, J., Calder, E.S., Herd, R.A., Komorowski, J.C., Luckett, R., Norton, G.E., Ritchie, L.J., Voight, B., Woods, A.W., 2002. Generation of a debris avalanche and violent pyroclastic density current on 26 December (Boxing Day) 1997 at Soufriere Hills Volcano, Montserrat. *Geological Society, London, Memoirs*, **21**(1), 409-434. 10.1144/gsl.mem.2002.021.01.18.

195. Spence, R.J.S., Kelman, I., Baxter, P.J., Zuccaro, G., Petrazzuoli, S., 2005. Residential building and occupant vulnerability to tephra fall. *Natural Hazards and Earth System Science*, **5**(4), 477-494. 10.5194/nhess-5-477-2005.

196. Stinton, A.J., Cole, P.D., Stewart, R.C., Odbert, H.M., Smith, P., 2014. The 11 February 2010 partial dome collapse at Soufriere Hills Volcano, Montserrat. *Geological Society, London, Memoirs*, **39**(1), 133-152. 10.1144/m39.7.

197. Stone, J., Barclay, J., Simmons, P., Cole, P.D., Loughlin, S.C., Ramón, P., Mothes, P., 2014. Risk reduction through community-based monitoring: the vigías of Tungurahua, Ecuador. *Journal of Applied Volcanology*, **3**(1). 10.1186/s13617-014-0011-9.

198. Swanson, F.J., Jones, J.A., Crisafulli, C.M., Lara, A., 2013. Effects of volcanic and hydrologic processes on forest vegetation: Chaiten Volcano, Chile. *Andean Geology*, **40**(2), 359-391. 10.5027/andgeoV40n2-a10.

199. Swets, J., Dawes, R., Monahan, J., 1988. Better Decisions through Science. *Scientific American*, **240**, 1285-1293.

200. Takeshi, T., 2011. Evolution of Debris-flow Monitoring Methods on Sakurajima. *International Journal of Erosion Control Engineering*, **4**(1), 21-31. 10.13101/ijece.4.21.

201. Thouret, J.-C., 1990. Effects of the November 13, 1985 eruption on the snow pack and ice cap of Nevado del Ruiz volcano, Colombia. *Journal of Volcanology and Geothermal Research*, **41**(1-4), 177-201. 10.1016/0377-0273(90)90088-w.

202. Thouret, J.C., Abdurachman, K.E., Bourdier, J.L., Bronto, S., 1998. Origin, characteristics, and behaviour of lahars following the 1990 eruption of Kelud volcano, eastern Java (Indonesia). *Bulletin of Volcanology*, **59**(7), 460-480. 10.1007/s004450050204.

203. Thouret, J.C., Lavigne, F., Suwa, H., Sukatja, B., Surono, 2007. Volcanic hazards at mount semeru, east java (Indonesia), with emphasis on lahars. *Bulletin of Volcanology*, **70**(2), 221-244. 10.1007/s00445-007-0133-6.

204. Thouret, J.C., Oehler, J.F., Gupta, A., Solikhin, A., Procter, J.N., 2014. Erosion and aggradation on persistently active volcanoes-a case study from

Semeru Volcano, Indonesia. *Bulletin of Volcanology*, **76**(10). 10.1007/S00445-014-0857-Z.

205. Tisdall, A., 1951. Antecedent soil moisture and its relation to infiltration. *Australian Journal of Agricultural Research,* **2**(3). 342-348. 10.1071/AR9510342.

206. Todisco, F., 2014. The internal structure of erosive and non-erosive storm events for interpretation of erosive processes and rainfall simulation. *Journal of Hydrology*, **519**, 3651-3663. 10.1016/j.jhydrol.2014.11.002.

207. Torres, R., Self, S., Martinez, M., 1996. *Secondary Pyroclastic Flows from the June 15, 1991, Ignimbrite of Mount Pinatubo*, Fire and Mud: Eruptions and Lahars of Mount Pinatubo, Philippines. Philippine Institute of Volcanology and Seismology and University of Washington Press, pp. 665-678.

208. Torres, R., Mouginis-Mark, P., Self, S., Garbeil, H., Kallianpur, K., Quiambao, R., 2004. Monitoring the evolution of the Pasig-Potrero alluvial fan, Pinatubo Volcano, using a decade of remote sensing data. *Journal of Volcanology and Geothermal Research*, **138**(3-4), 371-392. 10.1016/j.jvolgeores.2004.08.005.

209. Tungol, N., Regalado, T., 1996. *Rainfall, acoustic flow monitor records, and observed lahars of the Sacobia River in 1992*. In: C. Newhall, R. Punongbayan (Eds.), Fire and Mud, Eruptions and Lahars of Mt Pinatubo, Philippines. PHIVOLCS/University of Washington Press, Quezon City/Seattle, pp. 1023-1033.

210. Umazano, A.M., Melchor, R.N., Bedatou, E., Bellosi, E.S., Krause, J.M., 2014. Fluvial response to sudden input of pyroclastic sediments during the 2008–2009 eruption of the Chaitén Volcano (Chile): The role of logjams. *Journal of South American Earth Sciences*, **54**, 140-157. 10.1016/j.jsames.2014.04.007.

211. Umbal, J., Rodolfo, K., 1996. *The 1991 Lahars of Southwestern Mount Pinatubo and Evolution of the Lahar-Dammed Mapanuepe Lake*. In: C. Newhall, R. Punongbayan (Eds.), Fire and Mud, Eruptions and Lahars of Mt Pinatubo, Philippines. PHIVOLCS/University of Washington Press, Quezon City/Seattle, pp. 951-971.

212. Vallance, J.W., Scott, K.M., 1997. The Osceola Mudflow from Mount Rainier: Sedimentology and hazard implications of a huge clay-rich debris flow. *Geological Society of America Bulletin*, **109**(2), 143-163. 10.1130/0016-7606(1997)109<0143:tomfmr>2.3.co;2.

213. Vallance, J.W., Iverson, R.M., 2015. *Lahars and their Deposits*. In: H. Sigurdsson, B. Houghton, H. Rymer, J. Stix, S. McNutt (Eds.), The Encyclopedia of Volcanoes Elsevier, Amsterdam, pp. 649-664.

214. Van Bemmelen, R., 1949. The Geology of Indonesia. *General Geology*, 1-732.

215. van Dijk, A.I.J.M., Bruijnzeel, L.A., Rosewell, C.J., 2002. Rainfall intensity–kinetic energy relationships: a critical literature appraisal. *Journal of Hydrology*, **261**(1-4), 1-23. 10.1016/s0022-1694(02)00020-3.

216. Van Westen, C., Daag, A., 2005. Analysing the relation between rainfall characteristics and lahar activity at Mt Pinatubo, Philippines. *Earth Surface Processes and landforms*, **30**, 1663-1674.

217. Waldron, H., 1967. Debris Flow and Erosion Control problems caused by the Ash eruptions of Irazu. *USGS Bulletin*, **1241-1**, 37 pp.

218. Wang, B., Kim, H.-J., Kikuchi, K., Kitoh, A., 2010. Diagnostic metrics for evaluation of annual and diurnal cycles. *Climate Dynamics*, **37**(5-6), 941-955. 10.1007/s00382-010-0877-0.

219. Wang, L., Shi, Z.H., Wang, J., Fang, N.F., Wu, G.L., Zhang, H.Y., 2014. Rainfall kinetic energy controlling erosion processes and sediment sorting on steep hillslopes: A case study of clay loam soil from the Loess Plateau, China. *Journal of Hydrology*, **512**, 168-176. 10.1016/j.jhydrol.2014.02.066.

220. Watt, S.F.L., Pyle, D.M., Mather, T.A., Martin, R.S., Matthews, N.E., 2009. Fallout and distribution of volcanic ash over Argentina following the May 2008 explosive eruption of Chaiten, Chile. *Journal of Geophysical Research-Solid Earth*, **114**. 10.1029/2008jb006219.

221. Watt, S.F.L., Pyle, D.M., Naranjo, J.A., Rosqvist, G., Mella, M., Mather, T.A., Moreno, H., 2011. Holocene tephrochronology of the Hualaihue region (Andean southern volcanic zone, ~42° S), southern Chile. *Quaternary International*, **246**(1-2), 324-343. 10.1016/j.quaint.2011.05.029.

222. Waythomas, C.F., Pierson, T.C., Major, J.J., Scott, W.E., 2013. Voluminous ice-rich and water-rich lahars generated during the 2009 eruption of Redoubt Volcano, Alaska. *Journal of Volcanology and Geothermal Research*, **259**, 389-413. 10.1016/j.jvolgeores.2012.05.012.

223. Waythomas, C.F., 2014. Water, ice and mud: lahars and lahar hazards at ice- and snow-clad volcanoes. *Geology Today*, **30**(1), 34-39. 10.1111/gto.12035.

224. Williams, R., Stinton, A.J., Sheridan, M.F., 2008. Evaluation of the Titan2D two-phase flow model using an actual event: Case study of the 2005 Vazcun Valley Lahar. *Journal of Volcanology and Geothermal Research*, **177**(4), 760-766. 10.1016/j.jvolgeores.2008.01.045.

225. Wischmeier, W., Smith , D., 1978. Prediciting rainfall erosion losses - A guide to conservation planning. Agricultural Handbooks (USA) No. 537. US Department of Agriculture, Washington DC.

226. Witham, C.S., 2005. Volcanic disasters and incidents: A new database. *Journal of Volcanology and Geothermal Research*, **148**(3-4), 191-233. 10.1016/J.Jvolgeores.2005.04.017.

227. Woods, S.W., Balfour, V.N., 2010. The effects of soil texture and ash thickness on the post-fire hydrological response from ash-covered soils. *Journal of Hydrology*, **393**(3-4), 274-286. 10.1016/j.jhydrol.2010.08.025.

228. Worni, R., Huggel, C., Stoffel, M., Pulgarín, B., 2011. Challenges of modeling current very large lahars at Nevado del Huila Volcano, Colombia. *Bulletin of Volcanology*, **74**(2), 309-324. 10.1007/s00445-011-0522-8.

229. Yamakoshi, T., Suwa, H., 2000. Post-eruption characteristics of surface runoff and sediment discharge on the slopes of pyroclastic-flow deposits, Mt Unzen, Japan. *Transactions, Japanese Geomorphological Union*, **21**, 469-497.

230. Yu, B., Rose, C.W., Coughlan, K.J., Fentie, B., 1997. Plot-Scale rainfall-runoff characteristics and modeling at six sites in Australia and Southeast Asia. *Transactions of the American Society of Agricultural Engineers*, **40**(5), 1295-1303. 10.13031/2013.21387.

231. Zanchetta, G., Sulpizio, R., Pareschi, M.T., Leoni, F.M., Santacroce, R., 2004. Characteristics of May 5–6, 1998 volcaniclastic debris flows in the Sarno area (Campania, southern Italy): relationships to structural damage and hazard zonation. *Journal of Volcanology and Geothermal Research*, **133**(1-4), 377-393. 10.1016/s0377-0273(03)00409-8.

232. Zhao, N., Yu, F., Li, C., Wang, H., Liu, J., Mu, W., 2014. Investigation of rainfall-runoff processes and soil moisture dynamics in grassland plots under simulated rainfall conditions. *Water*, **6**(9), 2671-2689. 10.3390/w6092671.

233. Zobin, V.M., Plascencia, I., Reyes, G., Navarro, C., 2009. The characteristics of seismic signals produced by lahars and pyroclastic flows: Volcán de Colima, México. *Journal of Volcanology and Geothermal Research*, **179**(1-2), 157-167. 10.1016/j.jvolgeores.2008.11.00.